Spatial and Temporal Distribution of a Rhyolite Compositional Continuum from Wet-oxidizing to Dry-reducing Types Governed by Lower-Middle Crustal P-T-fO_2-fH_2O Conditions in the Taupo Volcanic Zone, New Zealand

A thesis submitted in fulfilment of the requirements for the degree of
Doctor of Philosophy in Geology
at the University of Canterbury
by

Chad D. Deering

University of Canterbury
2009

"It is not the critic who counts: not the man who points out how the strong man stumbles or where the doer of deeds could have done better. The credit belongs to the man who is actually in the arena, whose face is marred by dust and sweat and blood, who strives valiantly, who errs and comes up short again and again, because there is no effort without error or shortcoming, but who knows the great enthusiasms, the great devotions, who spends himself for a worthy cause; who, at the best, knows, in the end, the triumph of high achievement, and who, at the worst, if he fails, at least he fails while daring greatly, so that his place shall never be with those cold and timid souls who knew neither victory nor defeat."

Theodore Roosevelt *(1858-1919)*

ABSTRACT

A continuum of rhyolite compositions has been observed throughout the Taupo Volcanic Zone (TVZ) over the past 550 kyr. reflecting changes in the $fH2O$, fO_2, and P-T conditions in a lower crustal 'hot-zone' (10-30 km) where these evolved melts are generated by crystal fractionation of successively intruded basaltic magmas. The rhyolite compositional continuum is bound by two distinct end-member types: R1 is characterized by hydrous minerals (hornblende ± biotite), low FeO*/MgO (calc-alkaline series), low MREE, Y, and Zr, and high Sr; and R2 is characterized by anhydrous minerals (orthopyroxene ± clinopyroxene), high FeO*/MgO (tholeiitic series), high MREE, Y, and Zr, and low Sr.

Slab-derived aqueous fluid components (Ba, Cl) correlate well with oxygen fugacity, and other well defined characteristics of silicic magmas in the Taupo Volcanic Zone (TVZ) between a cold-wet-oxidizing magma type (R1: amphibole ± biotite; high Sr, low Zr and FeO*/MgO, depleted MREE) and a hot-dry-reducing magma type (R2: orthopyroxene ± clinopyroxene; low Sr, high Zr, and FeO*/MgO, less depleted MREE). Oxygen fugacity was obtained from analysis of Fe-Ti oxides and ranges between -0.039 to +2.054 log units (ΔQFM; where QFM = quartz + fayalite + magnetite buffer) and is positively correlated with the bulk-rock Ba/La ratio, indicating that slab-derived fluid is the oxidizing agent in the rhyolites. Chlorine contents in hornblende also correlate with the bulk-rock Ba/La ratio. Hence, high fluid-flux typically correlates with the R1 and low fluid-flux with R2 rhyolite magma types. A geochemical evolution and distribution can be tracked in time and space throughout the central region of the TVZ from 550 ka to present and has revealed two distinct magmatic cycles that vary in length. The first cycle included widespread R1 type magmatism across the central TVZ beginning ca. 550 ka and was directly associated with previously unreported dome-building and ignimbrite-forming volcanism, and led to a voluminous (>3000 km^3) ignimbrite 'flare-up' between ca. 340 and 240 ka. These magmas also display the highest K_2O and Pb isotopic compositions compared to those erupted more recently, and is consistent with a peak in slab-derived sediment input. The second cycle began roughly 180 ka, erupting ca. 800 km^3 of magma, and continues to the present. The duration, rate, and composition of melt production within these cycles appears to be governed by the flux of fluid/sediment released from the subducting slab, while the distribution of melts may be governed more by extension along the central rift axis.

The Matahina Ignimbrite (~160 km^3 rhyolite magma; 330 ka) was deposited during a caldera-forming eruption from the Okataina Volcanic Centre, TVZ. The outflow sheet is distributed primarily from the northeast to southeast and consists of a basal plinian fall member and three ash-flow members. Pumice clasts are separated into three groups defined by differences in bulk geochemistry and mineral contents: high CaO, MgO, Fe_2O_{3T}, TiO_2, and low Al_2O_3, +hornblende (A2), low CaO, MgO, Fe_2O_{3T}, TiO_2, ±hornblende (A1), and a subset to A1, which has high-K, +biotite (B). Two types of crystal-rich mafic clasts were also deposited during the final stages of the eruption. The distinct A and B rhyolite magma types are petrogenetically related to corresponding type A and B andesitic magma by up to 50% crystal fractionation under varying fO_2-fH_2O conditions. Further variations in the low- to high-silica rhyolites can be accounted for by up to 25% crystal fractionation, again under distinct fO_2-fH_2O conditions. Reconstruction of the P-T-fO_2-fH_2O conditions of the andesite to rhyolite magmas are consistent with the existence of a compositional and thermal gradient prior to the eruption. Magma mingling/mixing between the basalt to andesite

and main compositionally zoned rhyolitic magma occurred during caldera-collapse, modifying the least-evolved rhyolite at the bottom of the reservoir and effectively destroying the pre-eruptive gradients.

A detailed examination of the diverse range of calcic-amphibole compositions from the ca. 330 ka Matahina eruption (ca. 160 km^3 rhyolitic magma) of the Okataina Volcanic Complex, Taupo Volcanic Zone, including crystal-rich basalt to dacite pumice from post-collapse deposits, reveals several pre- and syn-eruption magmatic processes. (1) Amphibole phenocrysts in the basaltic-andesite and andesite crystallized at the highest pressures and temperatures (P: up to 0.6±0.06 GPa and T: up to 950°C), equivalent to mid-crustal depths (13-22 km). Inter- and intra-crystalline compositions range from Ti-magnesiohornblende → Ti-tschermakite → tschermakite → magnesiohornblende and some display gradual decreases in T from core to rim, both consistent with magma differentiation by cooling at depth. (2) The largest amphibole crystals from the basaltic-andesite to andesite display several core to rim increases in T (up to 70°C), indicating new hotter magma periodically fluxed the crystal mush. (3) The dominant population of amphibole (magnesiohornblende) from the rhyolite is small and bladed and crystallized at low P-T conditions (P: 0.3 GPa, T: 765°C), equivalent to the eruptive P-T conditions. Amphibole (tschermakite-magnesiohornblende) from the dacitic and low-silica rhyolitic pumice form two distinct populations, which nucleated at two different T (High: 820°C and Low: 750°C). These compositional variations, governed primarily by differences in T conditions during crystal growth, record the mixing of two distinct amphibole populations that approached a thermal equilibrium at the eruptive T. Therefore, the diversity in amphibole compositions can be reconciled as an exchange of crystals+liquid between the basaltic-andesite to dacite from the mid-crust and rhyolite from the upper-crust, which quenched against one another, modifying the dacite to low-silica rhyolite compositions as the eruption progressed.

ACKNOWLEDGEMENTS

I would like to thank my wife Heather and my children Dakota, Kiska, and Hudson for their patience and understanding throughout the duration of this endeavour. They have sacrificed the most for this pursuit of knowledge. Heather also helped develop my writing skills, which became invaluable for professional publications. Jim Cole provided excellent support for logistics and important background information from his extensive knowledge of volcanic processes and, in particular, the volcanic history of the Taupo Volcanic Zone rhyolites. Tom Vogel helped to refine and expand hypotheses throughout the evolution of this work through in-depth discussions of the geochemistry. Ian Nairn's help with fieldwork from the inception of this study was crucial to laying the foundation for strong geochemical models.

The following is a list of staff and colleagues that contributed to this research project, from helping with graphical development and sample preparation to insightful discussions on the scientific hypotheses and models. Without the contributions from the above mentioned people and those listed below this project would never have been completed.

John Valley
Mike Spicuzza
Darren Gravley
Rob Spiers
Phil Shane
Rose Turnbull
Colin Wilson
Hugh Bibby
Susan Ellis
Joe Dufek
Steve Brown
Dave Szymanski
Tyrone Rooney
Olivier Bachmann
Dean Podolsky
Steve Weaver
Stu Brown
Graham Leonard
Martin Reyners
Grant Caldwell
Jennifer Jackson
Bob Weibe
Travis Horton

Financial support for analyses was generously provided through the Marsden Fund administered by the Royal Society of New Zealand and the Department of Geological Sciences, University of Canterbury, Mason Trust Fund. Direct PhD funding was administered through a University of Canterbury Doctoral Scholarship.

CONTENTS

LIST OF FIGURES

LIST OF TABLES

CHAPTER 1

Introduction

1.1 INTRODUCTION

The origin of large-volume silicic/rhyolitic systems has remained a topic of spirited debate in the geosciences for decades because it leads to an understanding of how the Earth differentiates. A recent review collection emphasizes the importance of these systems (Large Silicic Systems, JVGR, V. 167, 2007). Silicic magmas are generated in a variety of settings: mantle plume-continents, continental rifts, and mature oceanic and continental arcs. Thus their origin is considered to be important in the generation of continental crust.

The Taupo Volcanic Zone (TVZ) is currently the most active rhyolitic volcanic zone on Earth (15,000 km^3 erupted over the past 1.6 Ma; Wilson et al., 1995) and the petrogenesis of the rhyolite has remained a topic of debate for more than 40 years (e.g. Ewart, 1967a,b; Reid, 1983; Graham et al., 1992; McCulloch et al., 1994; Price et al., 2005). Specifically, the contributions from the mantle and continental crust have not been quantified, which is crucial to understanding whether or not new continental crust is being added (via new melts from the mantle) or existing crust is being simply melted (recycled).

1.2 OBJECTIVES

The overall aim of this research was to compile an extensive geochemical database, which could be used to develop a characterization of the rhyolitic magma types from the Taupo Volcanic Zone (TVZ), New Zealand, and conditions under which they were derived in order to develop models for their petrogenesis. The geochemical database that existed prior to this research consisted primarily of major element data and some trace elements obtained by X-ray fluorescence (XRF) analysis with fewer than 50 analyses using higher precision methods such as inductively

coupled plasma – mass spectrometry (ICP-MS). In this study, over 450 bulk-rock samples were analyzed using XRF and MR-ICP-MS for major and trace elements, including rare-earth elements (REE), to compile a dataset that is statistically significant for rigorously testing hypotheses. Eruptive units were chosen to represent the spatial and temporal extent of TVZ volcanism over the past 600 kyrs. In addition, over 5000 mineral analyses were used to determine equilibrium P-T-fO_2-fH_2O conditions and for characterizing the range of rhyolitic magma types originally outlined by Ewart (1967a,b) based on the following ferromagnesian assemblages: 1) orthopyroxene, 2) orthopyroxene + amphibole, and 3) biotite ± amphibole ± orthopyroxene. This extensive new geochemical database was used to reach the following specific objectives:

1. Develop a geochemical framework, through multivariate statistical analysis of major and trace element bulk rock chemistry, for characterizing the continuum of magma types observed in the TVZ.
2. Determine the underlying physical conditions and processes governing the generation of the continuum of rhyolite compositions from cold-wet-oxidizing to hot-dry-reducing types.
3. Determine the spatial relationship between the different magma types to the central rift axis and volcanic front.
4. Determine the relationship between mineral types, abundance, and chemistry and the host melt.
5. Quantify the physical conditions under which the rhyolites are generated (P-T-fO_2-fH_2O).
6. Develop a 3-D spatial and temporal model for magma evolution in the TVZ over the past ~600 kyrs.

1.3 ORGANIZATION AND OVERVIEW

The chapters in this dissertation are organized to present the testing of hypotheses in a logical progression. **Chapter 2** presents interpretations of the bulk geochemical dataset compiled from previous studies and supplemented with over 450 new major and trace elements (including rare earth elements) that represent the spatial and temporal range of the Taupo Volcanic Zone rhyolitic compositions from seven of the nine caldera complexes active over the past 1.6 Myrs. Polytopic vector analysis (PVA), a multivariate statistical tool, was used to evaluate the extensive dataset to investigate the origin of bulk-rock chemical variations. This analysis led to a modification and refinement of existing rhyolite petrogenetic models proposed by others through the identification of a continuum of rhyolite compositions that occur between two distinct end-members – one wet-oxidizing and the other dry-reducing. This manuscript was published in 2008 in the *Journal of Petrology*..

Chapter 3 tests the temporal magmatic evolution inferred by the model developed in Chapter two, which suggested that eruption of wet-oxidizing magmas would precede that of dry-reducing magmas. Collaboration with Graham Leonard (GNS) allowed for the Ar-Ar dating of specific samples that detail the volcanic, and, thereby, magmatic evolution in key areas to improve the temporal and spatial representation/resolution of the geochemical evaluation. The temporal and spatial distribution of the different magma types were evaluated for the past 600 kyrs., linking contributions from slab-derived fluid/sediment components to the types of rhyolite erupted at the surface. Magmatic cycles were identified, as wet-oxidizing magmas precede dry-reducing ones. Importantly, the type of magma erupted (wet-oxidizing or dry-reducing) is correlated with the volume of rhyolite erupted, suggestive of a direct link between the amount of flux melting in the mantle, induced

by slab-fluids, and the amount of rhyolite produced and erupted. The results of this model bear on the underlying processes governing flare-up volcanism and have led to further hypotheses and research addressed in the 'continued research' section of Chapter 6. This manuscript was prepared for submission to *Contributions to Mineralogy and Petrology*.

Chapter 4 investigates the relationship between crystal-rich, amphibole-bearing basalt to dacite magmas and the co-magmatic rhyolite in a case study of the 330 ka Matahina eruption. The objective of this detailed evaluation of amphibole compositions from this unique suite of rocks was to further characterize the P-T-fO_2-fH_2O conditions of the mid-crustal 'mush' zone and determine the timing of processes occurring pre- and syn-eruption. This manuscript is in press at *American Mineralogist*.

Chapter 5 presents a case study of the 330 ka Matahina eruption in the context of the previously developed petrogenetic models. A chemical and physical profile from crystal-rich andesite to crystal-poor rhyolite is established, providing a more detailed understanding of the spatial and temporal variability that can arise within a single volcanic complex. This manuscript was prepared for submission to *Contributions to Mineralogy and Petrology*.

Chapter 6 summarizes the important contributions that this research has made to our understanding of silicic magmatic systems in the TVZ. This chapter also includes a list of manuscripts in preparation that are pending submission to journals, which contain additional data compiled in this research project used to continue testing hypotheses.

1.4 REFERENCES

Ewart. A. (1967a). The Petrography of the Central North Island Rhyolitic Lavas: Part 1-Correlations between the phenocryst assemblages. *New Zealand Journal of Geology and Geophysics* **10**, 182-197.

Ewart. A. (1967b). The Petrography of the Central North Island Rhyolitic Lavas: Part 2-Regional petrography including notes on associated ash-flow pumice deposits. *New Zealand Journal of Geology and Geophysics* **11**, 478-545.

Graham, I.J., Gulson, B., Hedenquist, J.W., Mizon, K. (1992). Petrogenesis of Late Cenozoic rocks from the Taupo Volcanic Zone, New Zealand; in the light of new Pb isotopic data. *Geochimica et Cosmochimica Acta* **56**, 2797-2819.

McCulloch, M.T., Kyser, T.K. Woodhead, J.D., Kinsley, L. (1994). Pb-Sr-Nd-O isotopic constraints on the origin of rhyolites from the Taupo volcanic zone of New Zealand; evidence for assimilation followed by fractionation from basalt. *Contributions to Mineralogy and Petrology* **115**, 303-312.

Price, R.C., Gamble, J.A., Smith, I.E.M., Stewart, R.B., Eggins, S., Wright, I.C. (2005). An integrated model for the temporal evolution of andesites and rhyolites and crustal development in New Zealand's North Island. *Journal of Volcanology and Geothermal Research* **140**, 1-24.

Wilson, C.J.N., Gravley, D.M., Leonard, G.S. & Rowland, J.V. (in press). Volcanism in the central Taupo Volcanic Zone, New Zealand: tempo, styles and controls. *Geological Society London Special Publication*.

CHAPTER 2

A Rhyolite Compositional Continuum Governed by Lower Crustal Source Conditions in the Taupo Volcanic Zone, New Zealand

A Rhyolite Compositional Continuum Governed by Lower Crustal Source Conditions in the Taupo Volcanic Zone, New Zealand

C.D. Deering[1*], J.W. Cole[1], T.A. Vogel[2]

[1]Dept. of Geological Sciences, University of Canterbury, PB 4800, Christchurch 8020, New Zealand
[2]Dept. of Geological Sciences, Michigan State University, 206 Natural Sciences Bldg., East Lansing, Mi, 48824-1115, USA

Published in the Journal of Petrology, vol. 49, no. 12, pgs. 2245-2275, 2008.

Contributions

Jim Cole contributed useful discussion regarding the volcanic history and early models of the Taupo Volcanic Zone. Collaboration with Tom Vogel provided discussion of general rhyolite petrogenetic modeling from a global perspective.

2.1 ABSTRACT

Rhyolites generated in the modern Taupo Volcanic Zone (TVZ), New Zealand, have previously been interpreted as having evolved by a combination of extensive fractional crystallization and limited crustal assimilation (up to 25%). Polytopic vector analysis (PVA), a multivariate statistical analysis of over 475 basaltic to rhyolitic bulk-rock samples (24 analytes each) representing over 600 kyr. of volcanism from along the entire TVZ, has provided a robust platform for rhyolite characterization and new insight on rhyolite petrogenesis in the TVZ. With these analyses a continuum of compositions between two rhyolite end-member magma types (EM1 and EM2) has been identified that consist of distinct petrological and geochemical characteristics: EM1) crystal-rich (up to 45%), hydrous phases (± hornblende ± biotite ± cummingtonite), high Aluminum Saturation Index [molar $Al_2O_3/(CaO + Na_2O + K_2O)$], low FeO*/MgO (calc-alkaline series), depleted middle rare-earth elements (MREE) and Y, and high Sr, and EM2) crystal-poor (<10%), anhydrous phases (orthopyroxene ± clinopyroxene), high FeO*/MgO (tholeiitic series), low Aluminum Saturation Index, less depleted MREE and Y, and low Sr.

The range of Aluminum Saturation Indices and relative depletions in MREE and Y in the rhyolites are consistent with experiments involving the partial melting of amphibolites. In general, major and trace element modelling are consistent with 50-60% equilibrium crystallization of a contaminated, hornblende-bearing andesite to produce the TVZ rhyolites. Distinct variations in the compositions along the continuum between the two rhyolite end-member types can also be effectively modelled with major and trace elements by simulating changes in the P-T-fO_2-fH_2O conditions in the lower crustal source zone. Low P-T and high fO_2 and fH_2O in the source region promote abundant hornblende crystallization while suppressing

plagioclase crystallization, which produces the EM1 type rhyolite that is characterised by hydrous minerals (hornblende±biotite), low FeO*/MgO (calc-alkaline series) high Sr, high Aluminum Saturation Index, low MREE and low Y. By increasing the P-T and/or lowering fO_2, fH_2O in the source region plagioclase becomes more dominant while suppressing hornblende crystallization, producing more EM2 magma types (anhydrous (orthopyroxene ± hornblende), high FeO*/MgO (tholeiitic series), low Sr, lower Aluminum Saturation Index, less-depletion of the MREE, and Y).

Keywords: *rhyolite, magma genesis, water, Taupo Volcanic Zone, Polytopic Vector Analysis*

2.2 INTRODUCTION

The New Zealand tectonic regime is characterized by oblique subduction of the Pacific Plate oceanic crust beneath the continental crust of the Indo-Australian Plate. The central extent of the TVZ is defined by a thinning, rifted crust behind the volcanic front to the east. In this central region, the volcanism is overwhelmingly bi-modal rhyolitic and basaltic, with subordinate intermediate types. Rhyolite is volumetrically dominant in the modern (1.6 Ma to present) central Taupo Volcanic Zone (TVZ), representing over 90% of the deposits (Fig. 2.1) (Wilson *et al.* (1995). Twenty-five caldera-forming eruptions of rhyodacitic to rhyolitic composition have erupted over 6000 km^3 of magma over this period. For a comprehensive review of the eruptive activity see Wilson *et al.* (1995, in press).

Early workers (Ewart and Stipp 1968; Cole 1979) proposed that voluminous rhyolitic magma in the TVZ originated from anatexis of metasedimentary crust. This was widely accepted at the time, and Reid (1983) concluded that production of rhyolitic magmas by anatexis of metasedimentary crust was more consistent with trace element modelling than partial melting or fractional crystallization of a primary, mantle-derived basaltic parent. These ideas were later advanced as new isotopic, trace element, and experimental data became available and were summarized by Graham *et al.* (1995). They concluded that binary mixing between a metasedimentary melt and mantle-derived basaltic melt, followed by advanced fractional crystallization or a combined process of AFC, was consistent with the available isotopic (Sr-Nd-Pb-O), major-trace element, and geophysical evidence. However, details of these processes remain to be well constrained with uncertainties regarding "end-member compositions, contamination rate, bulk crystal-liquid distribution coefficients and, especially, the differentiation process operating" [Graham *et al.* (1995) pg. 81].

We present new evidence based on an expanded bulk-rock geochemical database, mineral chemistry and Sr-Nd isotopes, representing ca. 600 kyr of the 1.6 Ma modern volcanism, which is broadly consistent with the conclusions of Graham *et al.* (1995). We develop a revised, integrated model for the evolution of the TVZ rhyolites. To analyze this large chemical database, Polytopic Vector Analysis (PVA) (Johnson *et al.*, 2002; Vogel *et al.*, 2008), a powerful multivariate statistical tool, is used to characterize and evaluate the chemical variation of TVZ rhyolites. This analysis estimates rhyolitic end-member compositions and provides a guide for investigating petrogenesis, because it establishes strict constraints for major and trace element modelling.

In this study, we demonstrate that the TVZ rhyolitic magmas are genetically related to primary, mantle-derived basaltic melts. These basaltic magmas are intruded into the lower continental crust (20-30 km), where they assimilate metasedimentary crust and crystallize in a 'hot-zone'. Evolved andesitic melts are produced by fractional crystallization of these magmas and accumulate and fractionate at ca. 15-20 km depth, forming a mushy accumulation and ascent zone at the top of this 'hot-zone' under water-saturated or near-saturated conditions. Extraction of evolved low-silica rhyolitic magma, under varying P-T, fH_2O, and fO_2 conditions, leads to production of a continuum of rhyolitic magma types. We characterize both the end-members and the continuous variations of these rhyolitic magmas, providing new insight into both the petrogenetic evolution of the rhyolites and the geochemical diversity that occurs within them.

2.3 ANALYTICAL TECHNIQUES

Pumice and lava samples used for this study were trimmed using a diamond grinder and saw to remove any weathered rind or organic matter. Sample fragments were then cleaned in a sonic bath of distilled water for 10 minutes to remove any surface contaminants from the grinder and saw, then placed in an oven at 100ºC for a minimum of 24 hours. These dry fragments were rough crushed using a tungsten-carbide, pneumatic press. Any additional weathered fragments were removed from the sample aggregate prior to milling in a Frisch Planetary agate mill.

For the XRF and ICP analyses, three grams of the milled rock powder and 9.0 g of lithium tetraborate ($Li_2B_4O_7$), along with 0.5 g of ammonium nitrate (NH_4NO_3; used as an oxidizer), were fused in platinum crucibles at 1000 °C for 20-30 minutes on an orbital mixing stage. The melt was then poured into platinum molds, making a glass disk that was analyzed using a Bruker S-4 X-ray fluorescence (XRF) spectrograph. XRF major-element analyses were reduced by a fundamental parameter data reduction method using Bruker Spectra Plus® software, while XRF trace-element (Rb, Sr, and Zr) data were calculated using standard linear regression techniques using the ratio of the element peak to the Rh Compton peak, which corrects for mass absorption. Prior to any calculations, the background signal was subtracted from the standards and samples. Major- and trace-element concentrations in the samples were calculated based on a linear regression method using BHVO, W-2, STM-1, MRG-1, SY-2, SY-3, DNC-1, PCC-1 JA-2, JA-3, BIR, QLO-1, and RGM-1 standards.

The rare-earth elements Nb, Ta, Hf, Ba, Y, Th, U and Pb were analyzed by laser ablation inductively coupled plasma mass spectrometry (LA ICP-MS) on the same glass disks as used for XRF analyses. A Cetac LSX200+ laser ablation system was used coupled with a Micromass Platform ICP-MS, using strontium determined by

XRF as an internal standard. Trace element data reduction was done using MassLynx software. Element concentrations in the samples were calculated based on a linear regression method using well-characterized standards. All major- and trace-element whole rock analyses reported here were conducted at Michigan State University. Precision and accuracy of both XRF and LA-ICP-MS chemical analyses are reported in Vogel *et al.*, 2006.

Hornblende and plagioclase compositions were determined using a Cameca SX 100 EPMA at the University of Michigan equipped with five wavelength spectrometers using an accelerating potential of 15 kV, a focused beam with a 0 μm spot size, counting time of ~3 min/ mineral, and a 10 nA beam current. Standards used were natural fluor-topaz (FTOP), natural jadeite (JD-1), natural grossular, Quebec (GROS), natural adularia, St. Gothard, Switzerland (GKFS), synthetic apatite (BACL), synthetic Cr_2O_3, and synthetic $FeSiO_3$ (FESI).

The $^{87}Sr/^{86}Sr$ and $^{143}Nd/^{144}Nd$ isotopic ratios were measured on the Victoria University Geochemistry Laboratory Nu-Plasma Multi-Collector ICP-MS (MC-ICP-MS), Wellington, New Zealand. Mass spectrometric and laboratory techniques used are a modified version of those described in detail in Waight *et al.* (2002). The ratios were corrected for mass spectrometric fractionation using exponential law and normalized to $^{86}Sr/^{87}Sr = 0.710248$ (SRM987) and $^{143}Nd/^{144}/Nd = 0.512980$ (BHVO-2). Precision (2σ) is ±0.00002.

2.4 GEOCHEMICAL DATASET

Our dataset consists of 404 bulk-rock major and trace element analyses from this study and an additional 1200 from published papers (Table 2.1). Representative data are given in Table 2.2, and the complete dataset is available in Electronic

Appendix 2.1. For simplification and to reduce the clutter in diagrams, the samples have been separated by volcanic centre and appropriate time segment. Table 2.1 also displays the symbols used throughout this paper in the figures for each volcanic centre including each respective, major episode.

The mineralogy (composition and modal percent) of basalt-rhyolite clasts from the Matahina Ignimbrite and post-caldera collapse deposits (~330 ka; Manning, 1995) were analyzed to investigate physical conditions of crystallization (e.g. pressure-temperature) and for modelling crystal fractionation. The mafic (basalt to andesite) clasts were specifically selected, as will be outlined later in the paper, to best represent potential parental magma compositions. The microprobe data for these clasts are available in Electronic Appendix 2.2.

2.4.1 Secondary hydration and alteration

Samples analyzed for this study were all single pumice-clasts, vitric fiamme or lava samples. Loss on ignition (LOI) provides an approximation of secondary hydration of the glass. Because the samples are fused for analyses all water is driven off during this fusion process. LOI was calculated during the XRF major element data reduction by determining the initial weight loss and then applying the correction for reduced oxygen concentration to the calculated major element concentrations. This process is repeated until no changes occur in the calculated major element concentrations. In comparing samples where LOI values are measured by classical techniques and calculated by XRF, the calculated LOI values are within 10% of measured values (Dr. T.A. Vogel pers. comm. 2007).

Glass and hydrous phenocryst contents are highly variable within such a large dataset. Hydrous phenocrysts generally make up <1 wt % of the samples; however,

some of the more crystal-rich rocks contain up to 10 wt % hydrous phenocrysts. Therefore, the water contributions from these are considered variable, but relatively low, contributing much less than 1 wt % to LOI values in almost all cases. LOI values are dominated by glass hydration. Consequently low crystallinity samples tend to have the higher LOI, which is consistent with hydrated glass controlling LOI values. In some cases, secondary alteration (hydrous minerals) has occurred, which will increase the LOI values. These alteration products can be seen in thin section.

Several petrological and geochemical observations are important when scrutinizing such a large dataset. First, if the alkali values contain petrologic information, the alkali concentrations in the pumice should not be correlated with measured LOI. Volcanic glass is susceptible to hydration, and once the glass is fully hydrated, ion exchange between the H_2O and glass may occur (Noble, 1967). Fig. 2.2a shows the wide range in LOI values relative to the Na/K ratio. A direct relationship is not observed between Na/K and LOI for any of the volcanic sample suites individually, although highly variable ratios are observed. Na_2O is correlated with SiO_2 for most of the sample suites, and some distinct individual groups are also observed (Fig. 2.2b). The more mafic samples have been removed from Fig. 2.2b to clarify this relationship. As Na_2O does not correlate with LOI, the variability in Na_2O does not reflect secondary hydration processes. Although there has undoubtedly been some alkali mobility, the lack of a strong correlation with LOI within the individual datasets indicates to us that this exchange is insignificant. Second, samples with Ce anomalies (relative to La and Pr) must be removed from the dataset because this anomaly has been associated with weathering and REE mobility (Patino *et al.*, 2003). A number of samples were removed from this dataset prior to LOI screening. Third, available thin sections were screened for the occurrence of zeolites and other

secondary alteration minerals. Some pumice-clast and lava samples were analyzed within individual studies using XRD to determine the presence of secondary alteration minerals. These samples were removed from the dataset before our initial screening of the entire dataset. Numerous other studies (Schmitz and Smith 2004; Wilson *et al.* 2005; Shane *et al.* 2007) have reported pumice with LOI between 4.0-5.0% and glass with up to 6.0 wt.% by difference in studies of more recent TVZ volcanics. Therefore, on this basis, we have employed a cut-off of analytical totals <95 wt. % regardless of whether or not any secondary alteration minerals were seen in the thin sections.

2.4.2 Bulk-rock and selected mineral chemistry

Mafic (basalt to andesite) samples

Bulk geochemistry

Our study considers the potential genetic relationship between mafic magmas with high water contents (as reflected by the presence of hornblende) and the rhyolites of the TVZ. In the context of this paper, we explore this relationship based on both bulk-rock geochemistry and mineral chemistry. Hornblende-bearing samples are presented in this section along with currently active basaltic to andesitic volcanoes, hereafter referred to as 'modern', for comparison (Brown 1994; Wilson 2005; this study). These eruptive deposits range from calc-alkaline to tholeiitic in composition (Fig. 2.3a). Hornblende-bearing samples are similar to modern mafic samples in most major element oxides (Fig. 2.3c,e,f); however, several have distinctly different TiO_2 and CaO contents (Fig. 2.3b,d). Trace element contents also have a similar range for both hornblende-bearing and modern types (Fig. 2.4a-e), with the exception of Zr, for which several hornblende-bearing samples contain much higher contents at similar SiO_2 (Fig. 2.4f) to the modern mafic samples. Hornblende-bearing samples are

metaluminous to peraluminous with Aluminum Saturation Index [molar $Al_2O_3/(CaO + Na_2O + K_2O)$] values ranging between 0.6 to 1.4 (Fig. 2.5). Published $^{87}Sr/^{86}Sr$ are plotted against an indice of differentiation (SiO_2) for the modern mafic samples, with a few in the low-dacite range, and hornblende-bearing mafic samples (Fig. 2.6). Strontium isotopic compositions range from 0.707905 to 0.702560 and neodymium from 0.513129 to 0.512615.

Selected mineral chemistry: hornblende-bearing mafic rocks

In this section, we present mineral analyses representing the hornblende-bearing mafic plutonic/volcanic rocks. The modal abundance, size and shape of the plagioclase and hornblende vary considerably in each of these suites of rocks. Brown (1994) described the Atiamuri dolerite as medium to fine grained (1-2mm), highly crystalline (>95%) with strongly zoned plagioclase laths (An_{83} to An_{36}), abundant euhedral/subhedral hornblende, anhedral clinopyroxene, and rare olivine. Some large Tschermakitic-hornblende have partially replaced clinopyroxene. A lack of resorption or other disequilbrium textures led him to suggest that these represented primary crystallization, not partial melts.

A suite of hornblende-bearing mafic samples exhumed as part of the 26.5 ka, 500 km^3, caldera-forming Oruanui eruption are also included in our evaluation. These samples are described by Wilson *et al.* (2005) as fine-grained and crystal-poor (<13%), with a mineral assemblage of plagioclase + clinopyroxene ± orthopyroxene ± olivine ± hornblende + magnetite ± ilmenite. Plagioclase compositions are variable and show signs of disequilibrium.

Hornblende-bearing samples from a post-caldera collapse deposit, which followed the Matahina Ignimbrite emplacement, *sensu stricto*, at ~330 ka, also reflect chemical disequilibrium in the phenocryst contents. These mafic samples are crystal-rich (up to 50%) with mineral assemblages of plagioclase + hornblende ± orthopyroxene ± clinopyroxene + magnetite ± ilmenite. Phenocrysts are highly variable in shape, size, and abundance in this suite of rocks. Many samples show obvious signs of mingling between a mafic and felsic melt composition. However, we selected only a few of the most mafic samples to include as relevant to this study.

In general, all of these samples together have plagioclase compositions ranging from An_{94} to An_{31}, with a corresponding increase in FeO from ~0.2 to 0.8 wt % (Fig. 2.7a,b). Amphiboles are magnesio-hastingsite hornblende, tschermakitic-hornblende, and magnesio-hornblende (Fig. 2.7c,d), using the classification of Leake *et al.* (1997), and range from 0.6 to 2.4 Al^T (afpu).

Rhyodacite-rhyolite samples

The TVZ rhyolites are tholeiitic to calc-alkaline (Fig. 2.8a), projecting the Miyashiro (1974) FeO*/MgO ratio into the rhyolite field. TVZ rhyolites are slightly to moderately peraluminous to slightly metaluminous with Aluminum Saturation Index values ranging between 0.9 to 1.75 (Fig. 2.5). Major element oxides (TiO_2, CaO, MgO, Fe_2O_3, K_2O and Al_2O_3) display coherent trends correlated with SiO_2 (Fig. 2.8b-h), but with considerable scatter. The Al_2O_3 shows a widening in the data array as SiO_2 decreases. Oxides MgO, Na_2O, and P_2O_5 (not shown) show the most scatter with a slight inflection apparent in some of the Na_2O data at ~75 wt. % SiO_2.

Pumice-clast and lava samples show significant variations in trace elements (Zr: 345-61 ppm; Sr: 193-33 ppm; Rb: 222-56 ppm; Ba: 1180-587 ppm). In trace element

plots, Rb, Ba, and Y display an increase with increasing SiO_2 (Fig. 2.9a-f). The slight differences in slope indicate the relative degree of incompatibility of these elements. Trace elements Rb and Ba are more incompatible than Y. Strontium (Sr) and Zr both decrease with increasing SiO_2 and are compatible; however, Zr shows more scatter than the Sr. All samples are LREE enriched and variably depleted in MREE and HREE relative to chondrite (Fig. 2.10).

We selected samples from our dataset for isotopic analyses to represent the continuum of geochemical variations between the two end-member rhyolite types characterized. This characterization will be described below. The plot of Sr-Nd for TVZ rhyolites demonstrates the narrow range of compositions ($^{87}Sr/^{86}Sr$ 0.705130 to 0.706271 and $^{143}Nd/^{144}Nd$ 0.512744 to 0.512563) reported by both this and previous studies (Fig. 2.11). Modern mafic samples are plotted for comparison. Note the overlapping rhyolite field with some of the andesite compositions.

2.5 DATA TREATMENT: POLYTOPIC VECTOR ANALYSIS

To understand the petrogenesis of the modern TVZ (600 ka to present) rhyodacitic-rhyolitic volcanism, we used a subset of the larger database, consisting of more than 400 bulk rock analyses from both published literature and those acquired in this study. This subset was selected to represent the range of rhyolite compositions that have a complete suite of trace-element data available, thereby providing a more robust statistical evaluation of the data. The mafic series of samples selected were from hornblende-bearing magmas, erupted following the caldera collapse of the Matahina eruption within the central TVZ where the rhyolitic volcanism occurs. We chose these clasts instead of modern mafic samples, erupted outside of the central

TVZ, as they represented intermediate compositions most likely genetically related to the rhyolites.

Unravelling the complex processes that influence the composition of a melt/magma from source to subvolcanic reservoir, just prior to eruption, can be difficult as many of these processes occur simultaneously. This has the effect of overprinting the final eruptive products with a number of geochemical 'signatures'. Recently Vogel *et al.* (2008) have reviewed the use of polytopic vector analysis and the following discussion is taken from this paper. Polytopic vector analysis is a type of principal component procedure that can be used to evaluate mixing or unmixing (fractional crystallization) in geologic systems using all of the major and trace elements simultaneously. It differs from other principal component techniques in that it not only determines the number of end-members and their compositions, but also partitions the relative proportions of the end-members into each sample. The proportions of end-members can be used as input in other multivariate analyses to evaluate magmatic processes. Polytopic Vector Analysis is used to determine three essential parameters in a mixing system: 1) the minimum number of end-members (sources), 2) the geochemical signature of each source, and 3) the relative proportions of each source in all samples. In Polytopic Vector Analysis, a very useful parameter is the coefficient of determination, which evaluates the predicted concentration versus the actual concentration of an analyte (element) in a sample. This allows the researcher to evaluate and eliminate samples that may have poor analyses or are altered. Data screening involves removal of extreme outlier samples that may reflect secondary alteration, sample contamination, analytical detection, or simply samples that are geochemically distinct from the bulk of the dataset. Although these samples can be important in evaluating processes in an individual dataset, the purpose of this

study is a broad characterization, and extreme outliers were noted, but removed from consideration. For a complete review of the development of Polytopic Vector Analysis, see Johnson *et al*. (2002).

2.5.1 Application of the Polytopic Vector Analysis

Twenty-four major and trace elements obtained from XRF and ICP-MS analyses for >400 basaltic-rhyolitic samples were evaluated using the coefficient of determination (CD) to screen the sample set to determine number of sources or end-members (EM) that are sufficient to explain the variation in the samples. Once the minimum number of end-members were defined, the Polytopic Vector Analysis was applied to characterize the sources and establish the relative proportions of these end-members in each sample. It is important to note that defining the relative proportions of end- members in each sample is just another way of looking at the chemical composition of the samples, except in this manner all of the chemical components in the samples are captured in the proportion of end-members in each sample.

Results of the Polytopic Vector Analysis output are provided in Tables 2.3 and 2.4 and in Electronic Appendix 2.3 (end-member proportions). Table 2.3 provides the correlation coefficient (CD) for each analyte relative to the number of end-members in a solution. As a general rule, CD values >0.5 support a particular end-member solution, >0.7 strong support, and >0.9 very strong support. Correlation coefficients for a three end-member solution provide support to very strong support for nearly all the analytes. We observe a wide variation in Na_2O in this study and our other studies of volcanic rocks, and although a four end-member solution would improve the correlation in this dataset, we accept this variability recognizing that the Na_2O content does not have an impact on the overall correlation among end-members. Similarly, the low Zr CD results from a high variability of accessory zircons in individual samples

and may reflect non-representative sampling. Therefore, a three end-member solution is preferred as the four end-member solution does not provide a significant improvement in CD for most analytes.

Polytopic Vector Analysis characterization of hornblende- bearing mafic rocks and TVZ rhyolites

The compositions and proportions of the three end-members (EM1 and EM2 are rhyolitic and EM3 is basaltic) are provided in Table 2.4 and Electronic Appendix 2.3, respectively. Hornblende-bearing mafic samples are defined by EM3, which is similar in composition to a high alumina basalt with respect to most trace elements, and are also similar to those of modern mafic samples (Fig. 2.4) (with the exception of Zr). In plots of the proportions of EM3 vs. EM1 and EM2 (Fig. 2.12a,b), the linear array of hornblende-bearing andesitic-dacitic samples is clearly projected towards the EM1 rhyolite type. (Fig. 2.12b). This linear array defines an actual mixing relationship between the Matahina rhyolite (Table 2.1) samples and the hornblende-bearing andesite samples to form the dacitic compositions from the post-caldera collapse deposit described earlier.

Plots of the proportions of EM1 versus the proportions of EM2 in each sample define a continuum of rhyolite compositions ranging between the two end-member types (Fig. 2.12a), which can generally be interpreted in two ways: 1) The compositional variation reflects a systematic change in the *source* composition. This can be accomplished by systematically changing the source conditions (P-T-fH_2O, fO_2) or source composition (metasedimentary crust), which will have the effect of changing the composition of any derivative melts removed; or 2) A rhyolite-rhyolite *mixing* relationship among samples that results from upper-crustal, vertical or lateral

magma migration and mixing. Although both would require some variation in the source composition, the latter would allow for very distinct end-member type magmas (i.e. EM1 and EM2) to be produced under distinctly different conditions (one of these end-members could also occur as a mid-upper crustal metasedimentary melt - assimilant), which are mixed in the *upper crust*. In contrast, the former would call for more systematic changes in the *lower crustal* source zone, prior to melt removal, which produces the compositional continuum.

2.6 RHYOLITE PETROGENESIS

2.6.1 Upper crustal mixing of rhyolite genetically related to primary mantle-derived melts and metasedimentary rhyolite melts?

Previous work on rhyolite petrogenesis by McCulloch *et al.* (1994) and Blattner & Reid (1982) focused on Pb-Sr-Nd-O isotope systematics. These studies concluded, based on isotopic evidence (Sr-Nd-Pb-O), that crustal melting of one or both of the two dominant basement lithologies does not produce rhyolites with suitable isotopic ratios. McCulloch *et al.* (1994) provided evidence to support a model for the generation of TVZ rhyolites by fractionation following contamination of a mantle-derived basalt. They demonstrate that the relatively constant level of contamination, was produced by ~15-25% contamination of a basalt by Torlesse-type basement rock followed by ~70% crystal fractionation with a minimal amount of further contamination. Graham *et al.* (1995) summarize the interpretations/data from their and other studies, pointing out that the range of rhyolite and potential assimilants were not well represented. Despite these uncertainties, they concluded that either AFC of mantle-derived HAB (Graham *et al.,* 1992) or binary mixing followed by

prolonged crystal fractionation (McCulloch *et al.,* 1994) were consistent with the available data.

Although the new Sr-Nd isotope values presented in this study are within the range for rhyolites from previous studies (Fig. 2.11), we tested the hypothesis that one of these EM rhyolite types might be a rhyodacitic-rhyolitic metasedimentary melt that mixed with rhyolite melt, genetically related to primary, mantle-derived basalt to form a mixing continuum of rhyolite compositions. The proportion of EM2 in each of the samples against $^{87}Sr/^{86}Sr$ is shown in Fig. 2.13. EM2 does not correlate with the $^{87}Sr/^{86}Sr$ isotopes, precluding a simple binary mixing of crustal melt and rhyolites genetically related to primary, mantle-derived basalt. Therefore, we interpret the variation among the isotopes to be a consequence of variable degrees of assimilation, types of assimilant, or AFC processes either inherited from the source region or as the rhyolite resides in the mid to upper-crust prior to eruption.

2.6.2 Rhyolite genetically related to primary, mantle-derived basalt: P-T-fO_2-fH_2O, phase assemblages, and mafic compositions

The Aluminium Saturation Index (ASI) [molar $Al_2O_3/(CaO + Na_2O + K_2O)$] provides an important measure of the relationship between the total Al, and Ca+Na+K. Because the conditions (fH_2O, fO_2, P-T) and composition of the source have a significant influence on the Aluminum Saturation Index of derivative melts, we evaluated the Aluminum Saturation Index for this new dataset. Early workers (e.g. Conrad *et al.*, 1988; Nicholls *et al.*, 1992), based on a relatively small number of samples representing the more recent deposits (22 ka to present), reported that the dominant composition of the TVZ rhyolites are metaluminous (ASI < 1.0). In contrast, the more extensive dataset compiled in this study of over 1500 rhyolite

samples representing all of the major eruptions from the TVZ during the past 600 kyr are dominated by peraluminous (ASI > 1.0) compositions (Fig. 2.5), with only a subordinate population of metaluminous samples.

Experimental studies have established the origin of evolved peraluminous melts (Kushiro & Yoder, 1972; Conrad *et al.*, 1988; Beard & Lofgren, 1991; Sisson & Grove, 1993a; Müntener *et al.*, 2001; Prouteau & Scaillet, 2003; Sisson *et al.*, 2005), and these studies provide constraints on the source composition and conditions for the formation of these peraluminous magmas. In general, peraluminous melts can be produced in one or a combination of three ways: 1) melting of pelitic crust, 2) hornblende fractionation at low pressures, or 3) partial melting or fractionation under H_2O near-saturated or saturated conditions.

As has been previously shown (Graham *et al.*, 1995), melting of pelitic crust is unsuitable for producing the rhyolites on the basis of Sr-Nd-Pb-O isotopic evidence. Fractionation of hornblende will produce only mildly peraluminous melts, which would not account for the range in Aluminum Saturation Index observed in the TVZ rhyolites. Therefore, we consider the critical parameter to be H_2O - partial melting or fractionation under H_2O near-saturated or saturated conditions.

Müntener *et al.* (2001) concluded in their experiments that high H_2O contents in calc-alkaline melts were a prerequisite for producing peraluminous derivative magmas. They also documented that even small variations in the H_2O content had significant effects on the crystallization sequence, which suppressed the crystallization of plagioclase, producing peraluminous liquids. A necessary consequence of these experiments is to leave a hornblende-bearing or pyroxenite ultramafic plutonic restite, which are commonly found in subduction zone settings.

Other experimental studies (Beard & Lofgren, 1991; Sisson *et al.*, 2005; Wolf & Wyllie, 1994; Rapp *et al.*, 1991; Rapp, 1995) have also shown that a wide range of rhyolitic, peraluminous melt compositions can be produced by partial melting of a gabbroic (amphibolite) protolith under varying P-T-fO_2-fH_2O conditions. In general, these experiments highlight the importance of H_2O saturation and K/Na in the starting material, which has a significant impact on the Aluminum Saturation Index and K/Na of the derivative melts, respectively. Fig. 2.14 compares the experimental results of Beard & Lofgren (1991) and Sisson *et al.* (2005) with the TVZ rhyolites. Note the Aluminum Saturation Index range of the dacitic-rhyolitic melts produced by melting hornblende-bearing protoliths of varying compositions and the agreement with the observed Aluminum Saturation Index range of the TVZ rhyolites.

Beard & Lofgren (1991) experiments performed under H_2O-saturated conditions produce the most peraluminous melts. Residual phases in equilibrium with the H_2O saturated melts always contain hornblende and clinopyroxene in varying abundances at pressures >3.0 kbar. In contrast, H_2O under-saturated experiments only at pressures >3.0 kb and temperatures <900°C contain hornblende. Water-saturated runs also display an overall lower modal abundance of plagioclase when compared to the dehydration runs, reflecting the suppression of plagioclase crystallization with high water contents (Fig. 2.15a). Furthermore, variations in the temperature have the effect of changing the modal hornblende/orthopyroxene-clinopyroxene ratios in the residual (Fig. 2.15b,c). Sisson *et al.* (2005) controlled the fO_2, using different oxygen buffers in their dehydration melting experiments. A correlation between the fO_2 and FeO*/MgO of the derivative melts (glass) demonstrates the effects of fO_2 on melt compositions (Fig. 2.15d). In summary, variations in the compositions of the derivative melts and the equilibrium phases in these experiments are affected by T,

fO_2, and fH_2O conditions: 1) changes in T affect the modal proportions of the residual phases, 2) changes in fO_2 affect the FeO*/MgO of the derivative melts, and 3) changes in fH_2O produce variability in the Aluminum Saturation Index of the derivative melts (Fig. 2.14).

2.6.3 Lower crustal source zone

Geophysical considerations

Experimental studies, discussed above, provide important geophysical constraints on our petrogenetic model, indicating that lower crustal P-T-H_2O conditions are likely to produce the observed geochemical variations seen in the rhyolites. This is important for two key reasons: 1) fractionation at the base of the crust alleviates the spatial problem of accommodating a large amount of parental residuum in the mid-upper crust, for which there is no evidence, and 2) higher temperatures in the lower crust provide sufficient heat for crustal assimilation (Jackson *et al.*, 2003; Dufek & Bergantz, 2005; Annen *et al.*, 2006).

Harrison & White (2004) presented a crustal cross-section of the TVZ, interpreted from wide-angle seismic experiments, that defines the lower 15-30 km as a heavily intruded mafic crust with ≥2% partial melt. Other studies by Ogawa *et al.* (1999) and Bannister *et al.* (2004) interpret low S-wave velocities to represent a very conductive zone between 15-20 km in the central TVZ. Numerical modelling of rhyolitic melt generation and segregation by Jackson *et al.* (2003), concluded that repeated injection of basaltic sills into the lower crust would facilitate the development of an accumulation and ascent zone. Their model also predicted that the solid matrix of the primitive still molten rock would remain in the source region. Later, similar models were developed defining a lower crustal 'hot-zone' that

controlled the composition of evolved melts (Dufek & Bergantz, 2005 and Annen *et al.*, 2006). We suggest that these numerical models of intermediate to evolved melt production in lower crustal 'hot zones' are consistent with geophysical observations of the TVZ and that basaltic intrusions at between 20-30 km may be capped by a mushy accumulation and ascent zone between 15-20 km. Notably, Jackson *et al.* (2003) also demonstrated that significant volumes of rhyolitic melt could be produced within geologically short timescales (10^4-10^6 yr), which is a requisite in the TVZ where rhyolite melt production is very high (0.1-0.2 m^3 s^{-1}; Wilson, 1993).

Petrological observations

Determining the water content in subduction-related magmas has been the focus of many studies (e.g. Sisson & Layne, 1993; Blatter & Carmichael, 1998, 2001; Moore & Carmichael, 1998, Benjamin *et al*., 2007). Although the importance of the role of water in subduction zone environments is well established, few high-H_2O content (as indicated by the presence of hornblende) mafic eruptions have been reported worldwide (e.g. Cerro La Pilita, Western Mexico, Luhr & Carmichael (1985); Mount Lamington, Papua New Guinea, Arculus *et al.* (1983). In a comprehensive study of the Izu-Bonin Arc volcanics, Tamura & Tatsumi (2002) concluded that the negative slope of the water-saturated liquidi for calc-alkaline melts caused these 'wet' mafic magmas to stall in the mid-crust. This arresting of 'wet' magmas is consistent with the observations that hornblende-bearing gabbros are commonly found as part of exhumed subduction zone lithologies and in the lower crust (Blundy & Sparks, 1992; Sisson *et al.*, 1996). Barclay & Carmichael (2004) concluded, based on water-saturated fractionation experiments on hornblende-bearing basalts from Western Mexico, that ascent of hydrous basalts at the *base* of the crust is

retarded by the high crystallinity resulting in a stalling and subsequent 'stock-piling' of these magmas.

The TVZ has erupted mafic magmas over the past 600 kyr; however, the current focus of mafic volcanism occurs outside of the central TVZ. Basalts represent <1% of the total erupted volume within the central TVZ, and even fewer examples of hornblende-bearing mafic samples have been documented (Brown, 1994; Leonard *et al.*, 2002; Wilson *et al.*, 2005; this study). Interestingly, these are all co-eruptive pumice clasts associated with major caldera-forming rhyolitic eruptions. Hornblende-bearing gabbro/diorite has also been reported as exhumed xenoliths from several eruptions from the TVZ (Brown, 1994; Beresford, 1997; Burt *et al.*, 1998). The depletion in MREE relative to chondrite observed in all of the TVZ rhyolites (Fig. 2.16) illustrates the presence of hornblende in the source phase assemblage and suggests a potential genetic relationship between these hornblende-bearing mafic magmas and the rhyolites.

The chemical composition of the hornblende and plagioclase from the Matahina post-caldera collapse deposits (this study) and Oruanui calc-alkaline mafic pumice clasts (Wilson *et al.*, 2005) are unique within the TVZ. Some of the hornblendes have high-Al_2O_3 (>9.5 wt.%) and Mg# (>65) hornblende, and high-An plagioclase (>An_{85}) (Fig. 2.7). Al in hornblende has been used by some as a geobarometer under SiO_2 saturated conditions (e.g. Johnson & Rutherford 1989a). Although we are not seeking a quantitative measure of the pressure for depth estimates, a semi-quantitative estimate can be obtained by comparing the hornblende from the crystal-rich, mafic samples of the Matahina post-caldera collapse deposits with those from the rhyolite ignimbrite.

Experimental studies that have focused on the Al-hornblende as a geobarometer (Johnson & Rutherford, 1989; Thomas & Ernst, 1990; Schmidt, 1992; Ernst & Liu, 1998) demonstrated that increasing pressure favoured a coupled Al-Tschermak substitution ($^{T}Si + {}^{M1\text{-}M3}Mg = {}^{T}Al + {}^{M1\text{-}M3}Al$). In contrast, temperature variations do not favour the Al-Tschermak substitution (Spear, 1981). Instead, temperature favours the edenite exchange [$^{T}Si + {}^{A}\square = {}^{T}Al + A(Na + K)$] (Spear, 1981; Blundy & Holland, 1990) and also correlates with Ti-content. Fig. 2.17a shows the positive correlation between Ti-content and ^{T}Al in the Matahina hornblende and associated andesitic samples. This suggests that some of the hornblende variation is the result of changes in temperature. However, the plot of ^{T}Al vs. $^{M1\text{-}M3}Al$ also shows a positive correlation, suggesting that the variation in Al^{total} is also governed by changes in pressure (Fig. 2.17b). Calculations using the methods of Schmidt (1992) yield pressures for hornblende cores consistently greater than 4.0 kbar, which are also consistent with the semi-quantitative study of calcic-amphibole in MORB by Ernst & Liu (1998). High Al_2O_3 (>9.5 wt. % Al_2O_3; >1.75 Al^{total} apfu) in hornblende are also reported in numerous crystallization/melting experiments under variable T-fO_2-fH_2O conditions (Conrad *et al.*, 1988; Beard & Lofgren, 1991; Prouteau & Scaillet, 2003; Sisson *et al.*, 2005), consistent with pressures greater than 4.0 kbar. Hence, we estimate that these magmas crystallized at, or close to 15-20 km depth, which corresponds with our proposed accumulation and ascent zone.

Geochemical evaluation of basalt to andesite magmas

Price *et al.* (2005) evaluated the potential genetic relationship between modern andesites and the TVZ rhyolites. They demonstrated that the andesites have Sr-Nd isotopes that extend into the rhyolite field as shown in Fig. 2.11 and that rhyolitic melt

inclusions in some were similar to TVZ rhyolite compositions. This led them to conclude that a 'pre-conditioning' of the lower crust with andesite was a prerequisite for rhyolite production.

Modern basalts and andesites show evidence of contamination, which can be evaluated by incompatible element behaviour. If mafic samples are contaminated in the lower crust via. binary mixing accompanied by equilibrium crystallization and batch melt removal prior to eruption, we expect incompatible elements (K_2O, Rb) to occur on a mixing hyperbola. Fig. 2.18a shows a simple binary mixing model between the least-evolved basaltic composition and an average metasedimentary crust composition (from Reid, 1983). The K_2O/Rb ratio of the mafic samples decrease significantly with small amounts of change in Rb, indicating that the first 20% of assimilation, accompanied by only a negligible degree of crystal fractionation, can explain the data array. Compositions that fall off of the mixing hyperbola, dominantly andesite, may be derived from a combination of assimilation and fractional crystallization (AFC) (see Graham *et al.*, 1995). .

Hornblende-bearing, andesitic-clasts investigated in this study have similar K_2O/Rb ratios, occurring close to the binary mixing line (Fig. 2.18a), and isotopic compositions as the rhyolites, suggestive of open-system assimilation with a limited degree of crystal fractionation (Fig. 2.18a,b). The nearly flat K_2O/Rb data array of the hornblende-bearing andesite to rhyolite series of the TVZ is consistent with near closed-system crystallization as the dominant process producing the rhyolites from a contaminated andesite source magma (Fig. 2.18a). Trace element (La, Y, Yb) variation with increasing silica contents are also consistent with lower-middle crustal hornblende-bearing mafic fractionation (not shown), not amphibolite melting, in

accordance with a REE modelling study by Brophy (2008). Therefore, we prefer a crystallization, as opposed to partial melting, origin for the rhyodacite-rhyolite melts.

Annen *et al.* (2006) calculated melt fraction of crustal (e.g. pelite, greywacke) assimilation to basaltic magmas at lower crustal temperatures. These numerical models show that the temperature gradient above the uppermost basaltic emplacement decreases rapidly, and as a consequence, the amount of assimilation decreases substantially. This suggests that very little assimilation will occur once the evolved melt has been removed. The small range in rhyolite isotope values and overlap with the modern andesite field (Fig. 2.18b) support this interpretation that the isotopic overlap is governed by the thermal limits on crustal melts.

Bachmann & Bergantz (2004) investigated the chemical and physical constraints of generating rhyodacitic-rhyolitic melts expelled from an intermediate crystal mush. Their model suggests that once the intermediate magma reaches ~45-50 vol. % crystals chaotic convection ceases, which allows the interstitial rhyodactic-rhyolitic melt to be extracted along a horizon above the solidifying base. The results of these numerical models suggest that thermal, chemical and physical conditions require: 1) the bulk of assimilation to occur in the lower crust, and 2) the rhyodacitic-rhyolitic melt to remain in mechanical and chemical equilibrium with the crystallizing andesite prior to extraction.

Consequently, we propose a two stage process: 1) open-system contamination of intruded basalt by the surrounding metasedimenatary crust with concomitant fractional crystallization and andesitic melt extraction, followed by 2) near closed-system (with respect to metasedimentary crustal assimilation, but open to primary andesite recharge) equilibrium crystallization and batch rhyodacitic-rhyolitic melt extraction.

2.7 MAJOR AND TRACE ELEMENT MODELLING

2.7.1 Major elements

The distinct characteristics of the two end-member rhyolite types provide a guide for geochemical modelling of fractionation/melting from a primitive magma. EM1 rhyolite is defined by a high Aluminum Saturation Index, low FeO*/MgO, and an abundance of hydrous ferromagnesian phases. In contrast, EM2 is defined by low Aluminum Saturation Index, high FeO*/MgO and anhydrous ferromagnesian phases. The experimental analogs discussed above provide important constraints on modal assemblages that are in equilibrium with melts of these two end-member types. Based on these constraints, we chose to model crystal fractionation using a mineral assemblage of plagioclase + hornblende + orthopyroxene + magnetite + ilmenite ± clinopyroxene. This assemblage is consistent with the residual phases in the experiments at appropriate pressures (3.0-7.0kbar), considered reasonable estimates for the lower crust. Least-evolved mineral compositions that occur in the selected parental rock (UC1100) (hornblende + orthopyroxene + clinopyroxene + magnetite + ilmenite) were used for the modelling (Electronic appendix 2.4). These compositions were fixed for major element modelling runs. As the composition of plagioclase can vary greatly in a given melt evolution, we chose to use generic plagioclase end-member compositions (An_{98} and An_2; Deer *et al.*, 1992), which allowed the regression calculation to find a 'best-fit' composition. Samples used in modelling were chosen to represent eruptive products most similar to the two rhyolitic end-member types along the compositional continuum. The least-evolved calc-alkaline, hornblende-bearing andesite (UC1100) that was used as the source rock meets all of our criteria for a potential parent: 1) K_2O/Rb ratio is similar to that of the TVZ rhyolites, 2) Sr-Nd

isotopic ratios are similar to the TVZ rhyolite, and 3) hornblende-bearing andesitic rock. In addition, this rock has a crystallinity, estimated to be ca. 50% based on modal analysis, a peraluminous rhyodacitic-rhyolitic glass composition, and was erupted with an EM1 rhyolite magma type.

Equilibrium crystallization of the primitive andesite to produce the representative EM1 and EM2 rhyolites was evaluated using multiple linear regression analysis of major elements. An important feature of this modelling is that it would occur under equilibrium crystallization conditions, where the melt remains in contact with the crystals until conditions (e.g. buoyancy, deformation) allow the melt to separate. This could take place by crystallization or melting processes and the results would be identical. The sum of the squares (Σr^2) of the residual provides a measure of the similarity between measured and theoretical chemical parameters tested. In modelling equilibrium crystallization directly from the andesite to representative rhyolite types, a Σr^2 residual < 0.1 was set as a cut-off.

Results of the analyses are presented in Table 2.7. The results of this exercise demonstrate that both EM1 and EM2 could be produced by 50-60% liquid-crystal separation from a contaminated andesite – EM1 by hornblende-dominant fractionation; EM2 by orthopyroxene/clinopyroxene dominant fractionation. Although we first modelled equilibrium fractionation for the EM2 magma type using the hornblende/orthopyroxene assemblage, the Σr^2 residual was greater than our cut-off so we tried modelling with the orthopyroxene/clinopyroxene assemblage. The respective assemblages modelled produce liquid compositions consistent with the TVZ rhyolite end-member types. For simplification, apatite was not used in these regressions so the P_2O_5 disparity was expected. The K_2O has the highest residual due to an apparently low parental (1.00 K_2O wt. %) content. We tested this using an

artificially higher K_2O (1.25 K_2O wt. %) content in the parent and were able to improve results for the samples analyzed. This suggests that the source rock has a K_2O content slightly greater than the parent used here for the rhyolite modelling. However, modern andesites and those found within the Matahina post-caldera collapse deposits have similar K_2O contents to those which we modelled artificially.

Several important observations can be made of the modal mineral assemblages predicted by the regression analyses. First, the hornblende/orthopyroxene ratio predicted for the EM1 type rhyolite is similar to the water-saturated, low –temperature amphibolite melting experiments of Beard & Lofgren (1991) and that observed in the actual sample (UC1100). These variations in the hornblende/orthopyroxene ratio are consistent with changes in experimental phase proportions discussed earlier in this paper, which are controlled by T-P-fH_2O conditions. Second, the EM2 rhyolite type predicted assemblage is clinopyroxene-orthopyroxene dominant. Only the amphibolite dehydration experiments at high temperatures (>925°C) produce residual melts with anhydrous phase assemblages, suggesting that the EM2 melts were produced under similar conditions. Third, the lower modal proportions of plagioclase in the predicted EM1 assemblage is suggestive of high H_2O pressures. This is consistent with the abundant hydrous phases and higher Aluminum Saturation Index characterizing EM1.

2.7.2 Trace elements

Trace-element concentrations of melts are controlled by the phase assemblages in equilibrium with the melts and the original concentrations of trace elements in the source, as well as other intensive parameters (P, T, fO_2, fH_2O). Therefore, we chose to apply trace element modelling to test the validity of our major

element fractionation model for a hornblende-orthopyroxene/clinopyroxene bearing source. Our objective was to determine if the predicted modal assemblages modelled by regression analyses could produce the distinct concentrations of key trace elements (Rb, Sr, Ba, Y, REE) that occur in EM1 and EM2. An average of the trace element concentrations for several of the mafic compositions was used to represent trace element abundances observed in potential source rocks. In these calculations we used the predicted modal mineral assemblages obtained from the major element regression modelling.

Trace-element concentrations for the melt were calculated for equilibrium crystallization using published partition coefficients (GERM online database and Rollison, 1993) and are provided in Electronic Appendix 5. Equilibrium fractionation was preferred rather than Rayleigh fractionation because, as discussed above, major-element modelling requires the source to remain in equilibrium with the melt until the melt is extracted. Low-silica rhyolite or rhyolitic liquid partition coefficients (Kd) were preferred over high-silica rhyolite to be consistent with the andesite-rhyolite major element modelling. In addition, experimental or calculated Kd's, which account for T, P, and/or X dependence, were preferred over those determined from phenocryst-matrix partitioning.

Rb-Sr-Zr-Ba-Y

The predicted concentrations of Rb do not vary significantly between the two end member compositions, but are slightly lower than the actual rhyolite (Table 2.7). This value is on the lower end of the spectrum of compositions observed in the TVZ rhyolites (Rb: 56-222 ppm); however, few low-silica rhyolites (SiO_2 < 74.0 wt. %) exceed Rb-120 ppm. As Rb is an incompatible element and there is such a wide range

of concentrations observed in the natural rhyolites, we suggest that a wide range of Rb source contents is dictating this variation, probably controlled by early assimilation. Modern andesites in the TVZ display a wide range of Rb concentrations (Fig. 2.4b) at similar SiO_2 as our andesite parent, which is also consistent with considerable variation in the source. Furthermore, the higher Rb concentrations (>120 ppm) are restricted to the high-silica rhyolites and are interpreted to represent upper crustal fractionation/assimilation following removal from the source zone. Predicted Sr concentrations are highly dependent on the modal proportion of plagioclase in the fractionating assemblage. Our modelling closely estimates Sr concentrations in the liquids for both end-member types. A comparison of the Sr between the two end-members shows that EM1 is enriched in Sr relative to EM2. This disparity is consistent with the ca.10% modal variation in plagioclase between the two assemblages modelled. Partition coefficients available for Zr in hornblende in rhyolite vary considerably (0.27 – 4.0), but are always greater than those from the same studies relative to pyroxene. As a result, we expect that in melts where hornblende is dominant over pyroxene in the fractionating assemblage the melts will be depleted in Zr, relative to those where pyroxene is the dominant fractionating phase. A significant disparity between the predicted and observed concentrations of Zr in the EM2 model suggests that either the starting composition does not accurately represent that for the rhyolites modelled, similar to Rb a large variation exists in andesite Zr concentrations, or the partition coefficient used is lower than the actual for this system. Regardless, the model accurately predicts the variation in Zr concentrations between EM1 and EM2 rhyolites.

The concentrations of Ba and Y are particularly useful in this modelling as Ba behaves incompatibly and Y is highly compatible in hornblende; behaving similar to

the MREE. Figure 2.19 displays the Ba and Y concentrations predicted in our model. Both the Ba and Y are in excellent agreement with the modelled representative rhyolites and the overall low-silica TVZ rhyolites. The slope can be used to illustrate the dominance of hornblende in the fractionating assemblage. Ytrium is partitioned into hornblende, which consequently controls the slope of Ba versus Y of the melts derived from the source. The slope of the line produced by EM1, Ba relative to Y, projected back to our source rock is negative. This illustrates the dominance of hornblende in the source. In contrast, a positive slope is observed projecting from the source to EM2 and illustrates the dominance of pyroxene in the source mineral assemblage. We consider the separate, but positive sloping, trends observed in the *rhyolites* to represent similarities in the fractionating assemblages as the magma is removed from the source zone and stored in the upper crust (Fig. 2.15). Similar to the positive sloping trend observed in modelling fractionation in the source zone, the rhyolitic examples used here have trends consistent with orthopyroxene+hornblende fractionation. Other samples (not shown) illustrate a diversity of slopes in Ba-Y space that reflect variations in the upper crustal fractionating assemblages.

Rare earth elements

The predicted melt concentrations of the REE are in excellent agreement with trends formed by the natural rhyolites (Fig. 2.20a). Hornblende dominant fractionation effectively produces the more depleted MREE-HREE trend over opx dominant fractionation, with an enrichment in LREE. Conversely, the opx dominant fractionation shows a relative enrichment in MREE and enriched LREE. Another distinct difference between the two modelled liquids is the Eu anomaly (Eu/Eu*), which is much more pronounced in the EM2 trend. This depletion is consistent with

the higher modal plagioclase in equilibrium with this end-member. Fig. 2.20b shows several examples of EM1 and EM2 magma types (EM1: Rotoiti and Lake Okataina pyroclastics; EM2: Mangaone and Mamaku pyroclastics) with full suites of REE plotted separately for clarity. The MREE depletion, high Sr, and moderate Eu anomaly of the EM1 rhyolite emphasizes the importance of the coupled nature of hornblende crystallization under high H_2O conditions, which consequently suppresses plagioclase crystallization.

2.7.3 Petrologic evidence (Restite)

The FC/melting model would predict the occurrence of both hornblende-dominant and pyroxene-dominant gabbroic restite. Over the modern volcanic history of TVZ, both of these types of xenoliths have been reported in lithic lag deposits and within host pyroclastic deposits. Hornblende-rich gabbros have been described from the Kaingaroa ignimbrite (Beresford, 1997), and Whakamaru ignimbrite (Brown, 1994) and pyroxene-rich gabbros occur as lithics in the more recent Kaharoa pyroclastic deposits (Leonard, 2002). Brown (1994) reported strongly zoned An_{83-36} plagioclase in the gabbros with rhyolitic, peraluminous glass. Plagioclase analyzed in this study have even more An-rich cores (An_{94}). The observed strongly zoned plagioclase of Brown (1994) reflect in-situ changes in melt composition as the magma crystallized and the high-An cores require high H_2O activity, both consistent with the proposed model.

2.8 CONCLUSION

Using Polytopic Vector Analysis (PVA) of our comprehensive dataset, we have been able to identify a continuum of rhyolite compositions between two distinct

end- member types in the TVZ. We have been able to evaluate these end-members by major and trace element modelling. Variation in the major and trace element compositions of the rhyolite end-members (EM1 and EM2) is best explained by differences in lower crustal source conditions (P-T-fO_2-fH_2O) that dictate the fractionating mineral assemblages and, as a result, produce a continuum of evolved melt compositions between the two contrasting rhyolite end-members. Saturated to near-saturated H_2O conditions and/or hornblende in the source are important in producing the observed range of metaluminous to peraluminous rhyolites. Under water-saturated conditions, hornblende was always present at pressures ≥3 kb and, in dehydration experiments, only in trace amounts (Beard & Lofgren, 1991). In addition, the modal assemblage of orthopyroxene-clinopyroxene/hornblende changed with variations in fO_2, fH_2O, P-T. Specifically, the temperature increased the modal abundance of orthopyroxene-clinopyroxene, and in dehydration experiments at T > 925ºC hornblende is completely absent. In contrast, hornblende is always present in the 7.0 kb (Sisson *et al.*, 2005) dehydration experiments regardless of variations in T-fO_2, thereby, emphasizing the importance of the starting composition on the phases in equilibrium with the melt. These experiments highlight the importance of source conditions in producing distinct melt compositions.

Hence, the distinct geochemical and petrological characteristics of the TVZ rhyolites are summarized as follows in the context of an end-member continuum.

EM1 magma types are produced under low P-T and high fO_2-fH_2O conditions, promoting the fractionation of hornblende and suppressing that of plagioclase, resulting in: 1) the depletion of MREE and Y; 2) an increase in Sr; 3) a decrease in Zr; 4) less pronounced depletion of Eu; 5) oxidizing conditions, which reduce the compatibility of Fe and produce liquids with lower FeO*/MgO (calc-alkaline) ratios;

6) abundant crystallization of hydrous phases; and 7) moderately peraluminous melts. In contrast, EM2 magma types are produced under higher P-T and/or lower fO_2-fH_2O, or more reducing conditions, promoting the fractionation of clinopyroxene-orthopyroxene over hornblende, resulting in: 1) an enrichment of MREE and Y; 2) a decrease in Sr; 3) an increase in Zr; 4) large Eu anomaly; 5) reducing conditions producing high FeO*/MgO (tholeiitic) ratios; 6) low crystallinity, dominated by anhydrous phases; and 7) slightly-moderately peraluminous melts. Subtle changes in the source P-T conditions (Δ1.0-2.0 kbar - Δ50-100ºC) can change the modal proportions in equilibrium with the evolved melt. Consequently, subtle changes in melt composition will be produced. More dramatic changes in the source P-T or fH_2O/fO_2 conditions (i.e. exhausting the H_2O) produce a distinctly different melt composition closer to the extreme EM2.

We have shown that the diversity of magma compositions found within the TVZ are primarily governed by differences in the source conditions and slight variations in the composition/isotopic character of the surrounding metasedimentary crust that is assimilated into the crystallizing basalt. The overall amount of crustal contamination is dictated by the thermal limits of the emplaced basaltic magma. As the temperature and composition of the mantle is not thought to have changed over this short time frame, a near constant assimilation rate is sufficient to explicate the observed isotopic shifts. Therefore, we suggest that to satisfy the thermal, physical, and geochemical constraints developed in this study, a wet basaltic pre-conditioning in a 'hot-zone' is continuously rejuvenated by successive basalt emplacement.

Our model is similar to those conceptualized, by Charlier *et al.* (2005) and Smith *et al.* (2005) for TVZ rhyolite production; however, we emphasize the importance of the lower crustal environment in governing the compositions or

rhyodacite-rhyolite. We propose a scenario, illustrated in Fig. 2.21, where primitive basaltic magmas produced in the mantle wedge intrude into the lower metasedimentary crust as a series of sills (20-30 km) (Jackson *et al.*, 2003; Dufek & Bergantz, 2005; Annen *et al.*, 2006). These hot, wet intrusions assimilate metasedimentary basement lithologies, probably greywacke, then undergo rapid crystallization. Batches of andesitic melt are removed and coalesce near 15-20 km forming an accumulation and ascent zone. Initially, in the andesitic melts,, hornblende dominates the fractionating assemblage under water-saturated, high fO_2, low P-T conditions, and consequently, the melt composition is driven towards a peraluminous EM1 rhyolite type [low FeO*/MgO (calc-alkaline), depleted MREE and Y, abundant hydrous phases]. Once crystallinity reaches 45-50 vol. %, in the fractionating andesite, batches of evolved rhyolitic melt ascend and are stored in the mid to upper-crust prior to eruption. However, if melt production continues within the mantle wedge, a progressive inverted stacking of the basaltic sills can continue in the source zone. This will have the effect of raising the P-T in the source zone, changing the ratio of hydrous/anhydrous phases in the intruding basaltic sills, as well as in the intermediate melt at the accumulation and ascent zone. Consequently, the composition of the evolved melts will shift towards the EM2 rhyolite type [high FeO*/MgO (tholeiitic), non-depleted MREE and Y, anhydrous phases]. If H_2O flux from the mantle wedge decreases, the change will become more dramatic until conditions are dry in the source zone. One potential consequence of the proposed model is that there could be a geochemical temporal progression as successive basalts are emplaced and/or the flux of H_2O changes over time. The temporal variation of the TVZ magmatic system will be explored in a companion paper.

2.9 ACKNOWLEDGEMENTS

We would like to thank the Marsden Fund administered by the Royal Society of New Zealand (UOC0508) and the Department of Geological Sciences, University of Canterbury, Mason Trust Fund for financial support. Electron microprobe analysis at the University of Michigan was supported by NSF grant #EAR-9911352. The thorough and constructive reviews from Ian Graham, Kurt Knesel, and an anonymous reviewer are greatly appreciated.

2.10 REFERENCES

Annen, C., Blundy, J.D., Sparks, R.S.J. (2006). The Genesis of Intermediate and Silicic Magmas in Deep Crustal Hot Zones. *Journal of Petrology* **47**, 505-539.

Arculus, R.J., Johnson, R.W., Chappell, B.W., McKee, C.O., Sakai, H. (1983). Ophiolite-contaminated andesites, trachy-basalts and cognate inclusions of Mount Lamington, Papua New Guinea: anhydrite-amphibole-bearing lavas and the 1951 cumulodome. *Journal of Volcanology Geothermal Research* **18**, 215-258.

Bachmann, O. & Bergantz, G.W. (2004). On the Origin of Crystal-poor Rhyolites: Extracted from Batholithic Crystal Mushes. *Journal of Petrology* **45**, 1565-1582.

Bannister, S., Bryan, C.J., Bibby, H.M. (2004). Shear wave velocity variation across the Taupo Volcanic Zone, New Zealand, from receiver function inversion. *Geophysical Journal International* **159**, 291-310.

Barclay, J. & Carmichael, I.S.E. (2004). A Hornblende Basalt from Western Mexico: Water-saturated Phase Relations Constrain a Pressure-Temperature Window of Eruptibility. *Journal of Petrology* **45**, 485-506.

Beard, J.S. & Lofgren, G.E. (1991). Dehydration Melting and Water-Saturated Melting of Basaltic and Andesitic Greenstones and Amphibolites at 1, 3, and 6.9 kb. *Journal of Petrology* **32**, 365-401.

Benjamin, E.R., Plank, T., Wade, J.A., Kelley, K.A., Hauri, E.H., Alvarado, G.E. (2007). High water contents in basaltic magmas from Irazú Volcano, Costa Rica. *Journal of Volcanology and Geothermal Research* **168**, 68-92.

Beresford, S.W. (1997). Volcanology and Geochemistry of the Kaingaroa Ignimbrite, Taupo Volcanic Zone, New Zealand. *Unpublished PhD thesis*, *University of Canterbury Library*.

Bignall, G., Browne, P.R.L., Kyle, P.R. (1996). Geochemical characterisation of hydrothermally altered ignimbrites in active geothermal fields from the central Taupo Volcanic Zone, New Zealand. *Journal of Volcanology and Geothermal Research* **73**, 79-97.

Blatter, D.L. & Carmichael, I.S.E. (1998). Plagioclase-free andesites from Zitacuaro (Michoacan), Mexico: petrology and experimental constraints. *Contributions to Mineralogy and Petrology* **132**, 121-138.

Blatter, D.L. & Carmichael, I.S.E. (2001). Hydrous phase equilibria of a Mexican high-silica andesite: a candidate for mantle origin? *Geochimica et Cosmochimica Acta* **65**, 4043-4065.

Blattner, P. & Reid, F. (1982). The origin of lavas and ignimbrites of the Taupo Volcanic Zone, New Zealand, in the light of oxygen isotope data. *Geochimica et Cosmochimica Acta* **46**, 1417-1430.

Blundy, J.D. & Sparks, R.S.J. (1992). Petrogenesis of mafic inclusions in granotoids of the Adamello Massif, Italy. *Journal of Petrology* **33**, 1039-1104.

Blundy, J.D. & Holland, T.J.B. (1990). Calcic amphibole equilibria and a new amphibole-plagioclase geothermometer. *Contributions to Mineralogy and Petrology* **104**, 208-224.

Brophy, J.G. (in press). A study of rare earth element (REE)-SiO_2 variations in felsic liquids generated by basalt fractionation and amphibolite melting: a potential test for discriminating between the two different processes. *Contributions to Mineralogy and Petrology, DOI 10.1007/s00410-008-0289-x*.

Brown, S.J.A., (1994). Geology and geochemistry of the Whakamaru Group ignimbrites, and associated rhyolite domes, Taupo Volcanic Zone, New Zealand. *Unpublished PhD thesis*, *University of Canterbury Library*.

Brown, S.J.A., Wilson, C.J.N., Cole, J.W., Wooden, J.L. (1998). The Whakamaru Group ignimbrites, Taupo volcanic zone, New Zealand: evidence for reverse tapping of a zoned silicic magmatic system. *Journal of Volcanology Geothermal Research* **84**, 1-37.

Burt, R.M., Brown, S.J.A., Cole, J.W., Shelley, D., Waight, T.E. (1998). Glass-bearing plutonic fragments from ignimbrites of the Okataina caldera complex, Taupo Volcanic Zone, New Zealand: remnants of a partially molten intrusion associated with preceding eruptions. *Journal of Volcanology and Geothermal Research* **84**, 209-237.

Charlier, B.L.A., Wilson, C.J.N., Lowenstern, J.B., Blake, S., van Calsteren, P.W., Davidson, J.P. (2005). Magma generation at a large, *hyperactive* silicic volcano (Taupo, New Zealand) revealed by U-Th and U-Pb systematics in zircons. *Journal of Petrology* **46**, 3-32.

Cole, J.W. (1979). Structure, petrology and genesis of Cenozoic volcanism, Taupo Volcanic Zone, New Zealand – a review. *New Zealand Journal of Geology and Geophysics* **22**, 631-657.

Conrad, W.K., Nicholls, I.A., Wall, V.J. (1988). Water-saturated and undersaturated melting of metaluminous and peraluminous crustal compositions at 10 kb; evidence for the origin of silicic magmas in the Taupo Volcanic Zone, New Zealand, and other occurrences. *Journal of Petrology* **29**, 765-803.

Deer, W.A., Howie, R.A., Zussman, J.(1992). An Introduction to the Rock-Forming Minerals. *Longman Scientific & Technical*, 438-439.

Dufek, J. & Bergantz, G.W. (2005). Lower Crustal Magma Genesis and Preservation: a Stochastic Framework for the Evaluation of Basalt-Crust Interaction. *Journal of Petrology* **46**, 2167-2195.

Ernst, W.G. & Liu, J. (1998). Experimental phase-equilibrium study of Al- and Ti-contents of calcic amphibole in MORB—A semiquantitative thermobarometer. *American Mineralogist* **83**, 952-969.

Ewart, A. & Stipp, J.J. (1968). Petrogenesis of the volcanic rocks of the Central North Island, New Zealand, as indicated by a study of $^{87}Sr/^{86}Sr$ ratios, and Sr, Rb, K, U and Th abundances. *Geochimica et Cosmochimica Acta* **32**, 699-736.

Gamble, J.A., Smith, I.E.M., McCulloch, M.T., Graham, I.J., Kokelaar, B.P. (1993). The geochemistry and petrogenesis of basalts from the Taupo Volcanic Zone and Kermadec Island Arc, S.W. Pacific. *Journal of Volcanology and Geothermal Research* **54**, 265-290.

Graham, I.J., Cole, J.W., Briggs, R.M., Gamble, J.A., Smith, I.E.M (1995). Petrology and petrogenesis of volcanic rocks from the Taupo Volcanic Zone: a review. *Journal of Volcanology Geothermal Research* **68**, 59-87.

Graham, I.J., Gulson, B.L, Hedenquist, J.W., Mizon, K. (1992). Petrogenesis of late Cenozoic volcanic rocks from the Taupo volcanic zone, New Zealand, in the light of new lead isotope data. *Geochimica et Cosmochimica Acta* **56**, 2797-2819.

Gravely, D.M. (2004). The Ohakuri pyroclastic deposits and the evolution of the Rotorua-Ohakuri volcanotectonic depression. *Unpublished PhD thesis, University of Canterbury Library.*

Harrison, A.J. & White, R.S. (2004). Crustal structure of the Taupo Volcanic Zone, New Zealand; stretching and igneous intrusion. *Geophysical Research Letters* **31**, 1-4.

Jackson, M.D., Cheadle, M.J., Atherton, M.P. (2003). Quantitative modelling of granitic melt generation and segregation in the continental crust. *Journal of Geophysical Research* **108**, 1-21.

Johnson, G. W., Ehrlich, R., Full, W. (2002). Principal Components Analysis and Receptor models in environmental forensics, in *An Introduction to Environmental Forensics*, edited by B. L. Murphy and R. D. Morrison, pp. 461-515, Academic Press, San Diego.

Johnson, M.C. & Rutherford, M.J. (1989). Experimental calibration of the aluminium-in-hornblende geobarometer with application to Long Valley Caldera (California) volcanic rocks. *Geology (Boulder)* **17**, 837-841.

Karhunen, R.A. (1993). The Pokai and Chimp Ignimbrites of NW Taupo Volcanic Zone. *Unpublished PhD thesis, University of Canterbury Library*.

Kushiro, I. & Yoder, H.S. Jr. (1972). Origin of Calc-Alkalic Peraluminous Andesites and Dacites. *Year Book - Carnegie Institution of Washington* **71**, 411-413.

Leake, B.E., Wooley, A.R., Arps, C.E.S., Birch, W.D., Gilbert, M.C., Grice, J.D., Hawthrone, F.C., Kato, A., Kisch, H.J., Krivovichev, V.G., Linthout, K., Laird, J., Mandarino, J.A., Maresch, W.V., Nickel, E.H., Rock, N.M.S., Schumacher, J.C., Smith, D.C., Stephensen, N.C.N., Ungaretti, L., Whittaker, E.J.W., and Youzhi, G. (1997). Nomenclature of amphiboles: Report of the Subcommittee on Amphiboles of

the International mineralogical Association, Commission on New Minerals and Mineral Names. *American Mineralogist* **82**, 1019-1037.

Leonard, G.S., Cole, J.W., Nairn, I.A., Self, S. (2002). Basalt triggering of the c. AD 1305 Kaharoa rhyolite eruption, Tarawera Volcanic Complex, New Zealand. *Journal of Volcanology and Geothermal Research* **115**, 461-486.

Leonard, G.S. (2003). The evolution of Maroa Volcanic Centre, Taupo Volcanic Zone, New Zealand. *Unpublished PhD thesis, University of Canterbury Library*.

Luhr, J.F. & Carmichael, I.S.E. (1985). Jorullo Volcano, Michocoan, Mexico (1759-1774): the earliest stages of fractionation in calc-alkaline magmas. *Contributions to Mineralogy and Petrology* **90**, 142-161.

Manning, D.A. (1995). Late Pleistocene tephrostratigraphy of the Eastern Bay of Plenty region, New Zealand. Unpublished PhD thesis, Victoria University.

McCulloch, M.T., Kyser, T.K., Woodhead, J.D., Kinsley, L. (1994). Pb-Sr-Nd-O isotopic constraints on the origin of rhyolites from the Taupo volcanic zone of New Zealand; evidence for assimilation followed by fractionation from basalt. *Contributions to Mineralogy and Petrology* **115**, 303-312.

Milner, D.M., Cole, J.W., Wood, C.P. (2001). Mamaku Ignimbrite: a caldera-forming ignimbrite erupted from a compositionally zoned magma chamber in Taupo Volcanic Zone, New Zealand. *Journal of Volcanology Geothermal Research* **122**, 243-264.

Miyashiro, A. (1974). Volcanic rock series in island arcs and active continental margins. *American Journal of Science* **274**, 321-355.

Moore, G.M. and Carmichael, I.S.E. (1998). the hydrous phase equilibria (to 3 kbar) of an andesite and basaltic andesite from Western Mexico: constraints on water content and conditions of phenocryst growth. *Contributions to Mineralogy and Petrology* **130**, 304-319.

Müntener, O., Kelemen, P.B., Grove, T.L. (2001). The role of H2O during crystallisation of primitive arc magmas under upper-most mantle conditions and genesis of igneous pyroxenites: an experimental study. *Contributions to Mineralogy and Petrology* **141**, 643-658.

Nairn, I.A., Shane, P.R., Cole, J.W., Leonard, G.J., Self, S., Pearson, N. (2004). Rhyolite magma processes of the ~AD 1315 Kaharoa eruption episode, Tarawera volcano, New Zealand. *Journal of Volcanology and Geothermal Research* **131**, 265-294.

Nicholls, I.A., Oba, T., Conrad, W.K. (1992). The nature of primary rhyolitic magmas involved in crustal evolution: Evidence from an experimental study of cummingtonite-bearing rhyolites, Taupo Volcanic Zone, New Zealand. *Geochimica et Cosmochimica Acta* **56**, 955-962.

Noble, D.C. (1967). Sodium, potassium, and ferrous iron contents of some secondarily hydrated natural silicic glasses. *American Mineralogist* **52**, 280-286.

Ogawa, Y., Bibby, H.M., Caldwell, T.G., Takakura, S. Uchida, T., Matsushima, N., Bennie, S.L., Tosha, T., Nishi, Y. (1999). Wide-band magnetotelluric measurements across the Taupo volcanic zone, New Zealand; preliminary results. *Geophysical Research Letters* **26**, 3673-3676.

Patino, L.C., Velbel, M.A., Price, J.R., Wade, J.A. (2003). Trace element mobility during spheroidal weathering of basalts and andesites in Hawaii and Guatemala. *Chemical Geology* **202**, 343-364.

Price, R.C., Gamble, J.A., Smith, I.E.M., Stewart, R.B., Eggins, S., Wright, I.C. (2005). An intergrated model for the temporal evolution of andesites and rhyolites and crustal development in New Zealand's North Island. *Journal of Volcanology and Geothermal Research* **140**, 1-24.

Prouteau, G. & Scaillet, B. (2003). Experimental Constraints on the Origin of the 1991 Pinatubo Dacite. *Journal of Petrology* **44**, 2203-2241.

Rapp, R.P. (1995). Amphibole-out phase boundary in partially melted metabasalt, its control over liquid fraction and composition and source permeability. *Journal of Geophysical Research* **100**, 15,601-15,610.

Rapp, R.P., Watson, E.B., Miller, C.F. (1991). Partial melting of amphibolite/eclogite and the origin of Archean trondhjemites and tonalites. *Precambrian Research* **51**, 1-25.

Reid, F.W. (1983). Origin of the rhyolitic rocks of the Taupo Volcanic Zone, New Zealand. *Journal of Volcanology Geothermal Research* **18**, 191-214.

Rollison, H.R. (1993). Using geochemical data: evalution, presentation, interpretation. *Prentice Hall*, 108-111.

Schmidt, M.W. (1992). Amphibole composition in tonalite as a function of pressure: an experimental calibration of the Al-in-hornblende barometer. *Contributions to Mineralogy and Petrology* **110**, 304-310.

Schmitz, M.D. & Smith, I.E.M. (2004). The Petrology of the Rotoiti Eruption Sequence, Taupo Volcanic Zone: an Example of Fractionation and Mixing in a Rhyolitic System. *Journal of Petrology* **45**, 2045-2066.

Shane, P. Martin, S.B., Smith, V.C., Beggs, K.F., Darragh, M.B., Cole, J.W., Nairn, I.A. (2007). Multiple rhyolite magmas and basalt injection in the 17.7 ka Rerewhakaaitu eruption episode from Tarawera volcanic complex, New Zealand. *Journal of Volcanology and Geothermal Research* **164**, 1-26.

Sisson, T.W. & Grove, T.L. (1993). Experimental investigations of the role of H2O in calc-alkaline differentiation and subduction zone magmatism. *Contributions to Mineralogy and Petrology* **113**, 143-166.

Sisson, T.W. & Layne, G.D. (1993). H2O in basalt and basaltic andesite glass inclusions from four subduction-related volcanoes. *Earth and Planetary Science Letters* **117**, 619-635.

Sisson, T.W., Ratajeski, K., Hankins, W.B., Glazner, A.F. (2005). Voluminous granitic magmas from common basaltic sources. *Contributions to Mineralogy and Petrology* **148**, 635-661.

Sisson, T.W., Grove, T.L., Coleman, D.S. (1996). Hornblende gabbro sill complex at Onion Valley, California, and a mixing origin for the Sierra Nevada Batholith. *Contributions to Mineralogy and Petrology* **126**, 81-108.

Smith, V.C., Shane, P., Nairn, I.A. (2005). Trends in rhyolite geochemistry, mineralogy, and magma storage during the last 50 kyr at Okataina and Taupo volcanic centres, Taupo volcanic zone, New Zealand. *Journal of Volcanology and Geothermal Research* **148**, 372-406.

Smith, V.C., Shane, P., Nairn, I.A. (2004). Reactivation of a rhyolitic magma body by new rhyolitic intrusion before the 15.8 Rotorua eruptive episode: implications for magma storage in the Okataina Volcanic Centre, New Zealand. *Journal of the Geological Society* **161**, 757-772.

Smith, V.C., Shane, P., Smith, I.E.M. (2002). Tephrostratigraphy and geochemical fingerprinting of the Mangaone Subgroup tephra beds, Okataina Volcanic Centre, New Zealand. *New Zealand Journal of Geology & Geophysics* **45**, 207-219.

Spear, F.S. (1981). An experimental study of hornblende stability and compositional variability in amphibolite. *American Journal of Science* **281**, 697-734.

Sun, S. & McDonough, W.F. (1989). Chemical and isotopic systematics of oceanic basalts: implications for mantle compositions and processes. In: Norry MJ (ed) Magmatism in the Ocean Basins. *Geological Society Special Publications*, 313–345.

Sutton, A.N., Blake, S., Wilson, C.J.N. (1995). An outline geochemistry of rhyolite eruptives from Taupo volcanic centre, New Zealand. *Journal of Volcanology and Geothermal Research* **68**, 153-175.

Tamura, Y. & Tatsumi, Y. (2002). Remelting of an Andesitic Crust as a Possible Origin for Rhyolitic Magma in Oceanic Arcs: an Example from the Izu-Bonin Arc. *Journal of Petrology* **43**, 1029-1047.

Thomas, W.M. & Ernst, W.G. (1990). The aluminium content of hornblende in calc-alkaline granitic rocks: a mineralogic barometer calibrated experimentally to 12kbars. *Special Publication – Geochemical Society* **2**, 59-63.

Vogel, T.A., Flood, T.P., Patino, L.C., Wilmot, M.S. Maximo, R.P.R, Arpa, C.B., Arcilla, C.A, Stimac, J.A. (2006). Geochemistry of silicic magmas in the Macolod Corridor, SW Luzon, Philippines: evidence of distinct, mantle-derived, crustal sources for silicic magmas. *Contributions to Mineralogy and Petrology* **151**, 267-281.

Vogel, T. A., Hidalgo, P.J., Patino, L.C., Tefend, K.S., and Ehrlich, R. (2008). Evaluation of magma mixing and fractional crystallization using whole-rock chemical analyses: Polytopic vector analyses, Geochemistry Geophysics Geosystems **9**, doi:10.1029/2007GC001790.

Waight, T.E., Baker, J.A., Peate, D.W. (2002). Sr isotope ratio measurements by double-focusing MC-ICPMS: techniques, observations and pitfalls. *International Journal of Mass Spectrometry* **221**, 229-244.

Wilson, C.J.N., 1993. Stratigraphy, chronology, styles and dynamics of late Quaternary eruptions from Taupo Volcano, New Zealand. *Philosophical Transactions Royal Society of London. Series* A, **343**, 205-306.

Wilson, C.J.N., Blake, S., Charlier, B.L.A., Sutton, A.N., 2006. The 26.5 ka Oruanui Eruption, Taupo Volcano, New Zealand: Development, Characteristics and Evacuation of a Large Rhyolitic Magma Body. *Journal of Petrology* **27**, 35-69.

Wilson, C.J.N., Gravley, D.M., Leonard, G.S. & Rowland, J.V. (in press). Volcanism in the central Taupo Volcanic Zone, New Zealand: tempo, styles and controls. *Geological Society London Special Publication*.

Wolf, M.B. & P.J., Wyllie (1994). Dehydration-melting of amphibolite at 10kbar: the effects of temperature and time. *Contributions to Mineralogy and Petrology* **115**: 369-383.

2.11 FIGURES

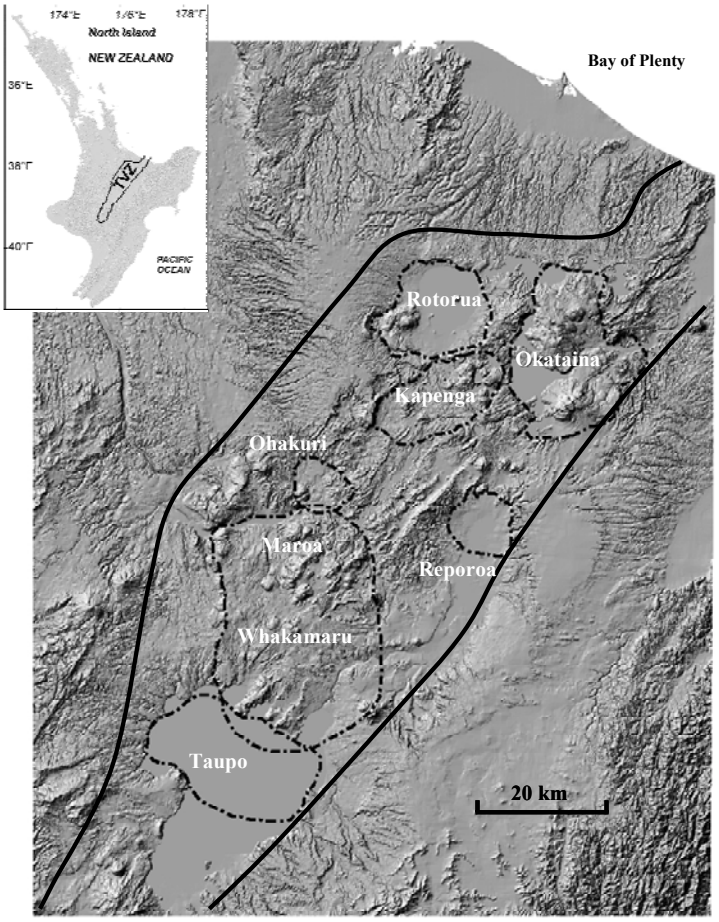

Fig. 2.1. Topographical/structural map showing the Taupo Volcanic Zone (TVZ) in the North Island, New Zealand. Inferred caldera boundaries are outlined in bold dashed lines.

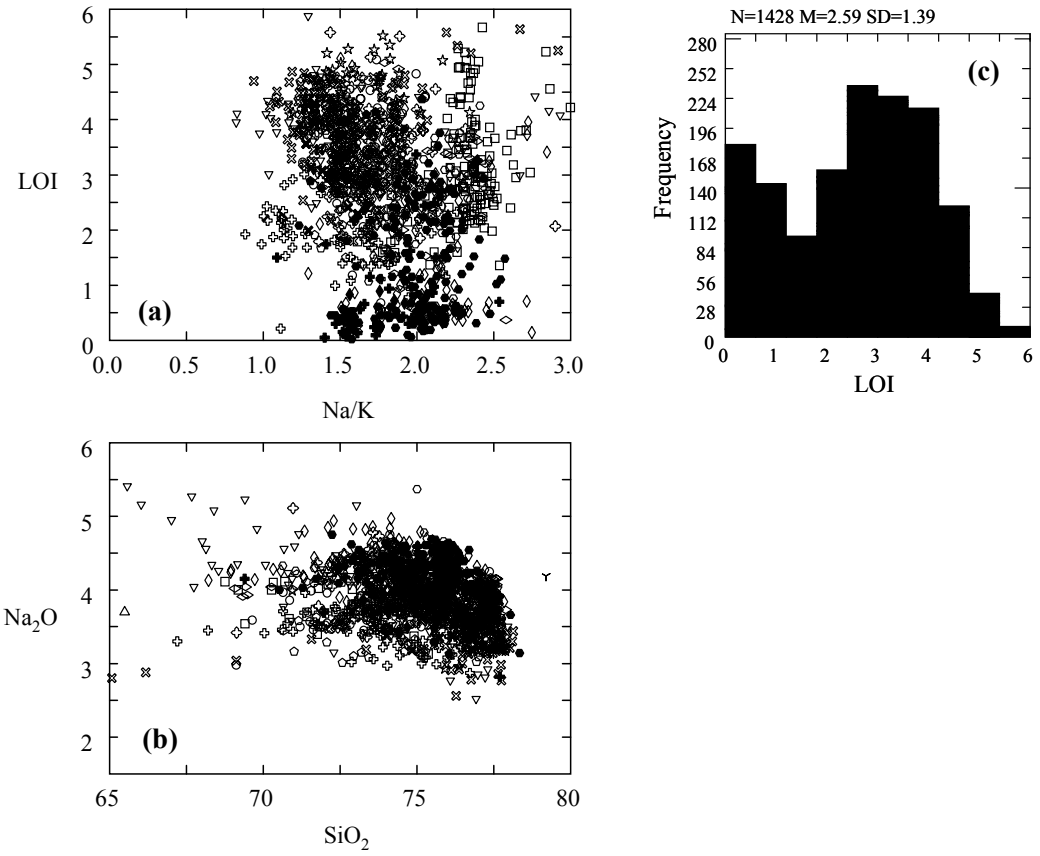

Fig. 2.2. Alkali variability in pumice and lava clasts of the TVZ. (a) LOI vs. K/Na ratio. (b) Na_2O vs. SiO_2.

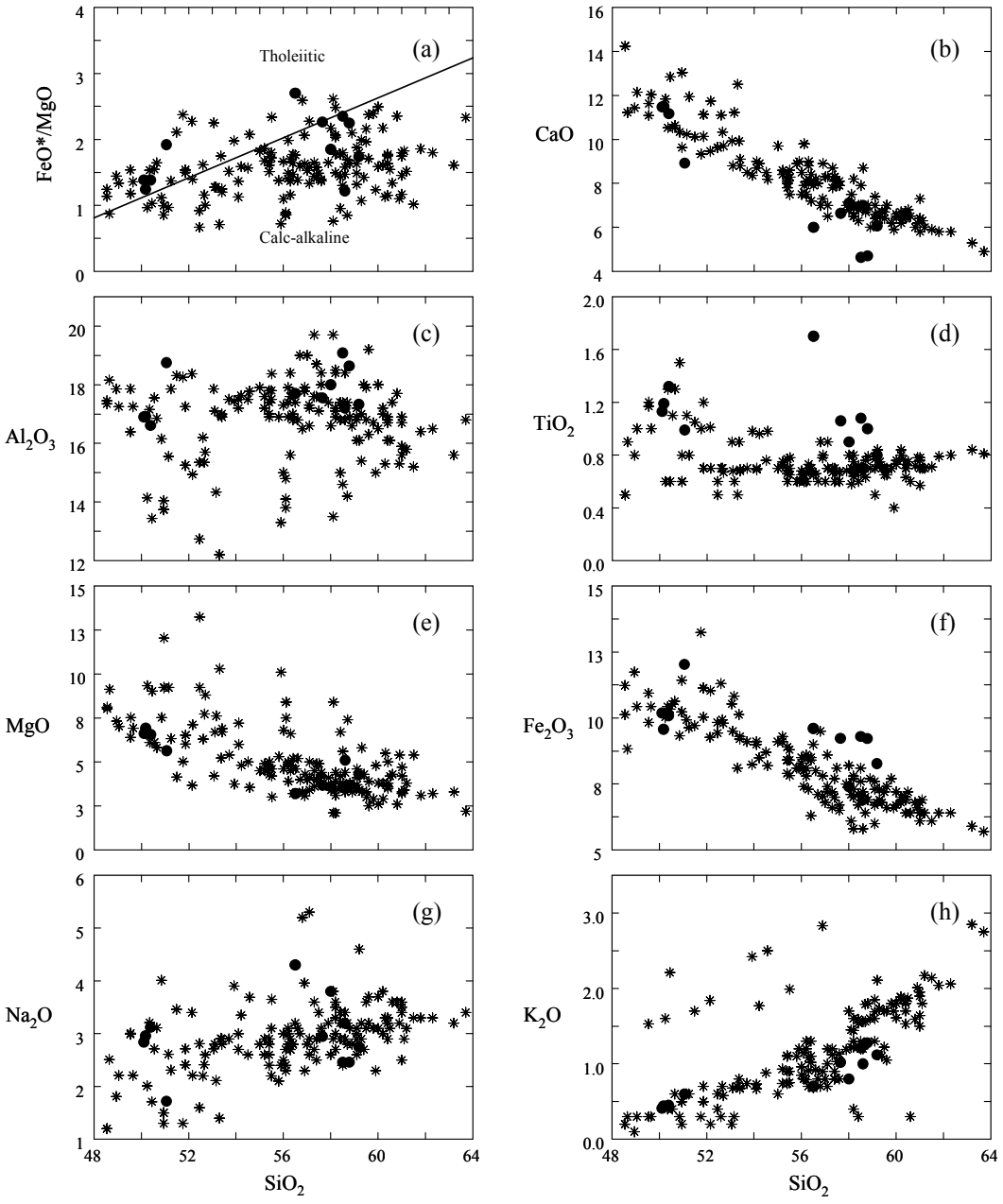

Fig. 2.3. (a) FeO*/MgO vs. SiO_2 with divisions for tholeiitic and calc-alkaline rocks (Miyashiro 1974). (b-f) Plots of selected major element oxides against silica for the TVZ modern basalt-andesites and selected hornblende-bearing mafic samples. Modern basalt-andesites are asterisks and hb-bearing mafic samples are filled circles.

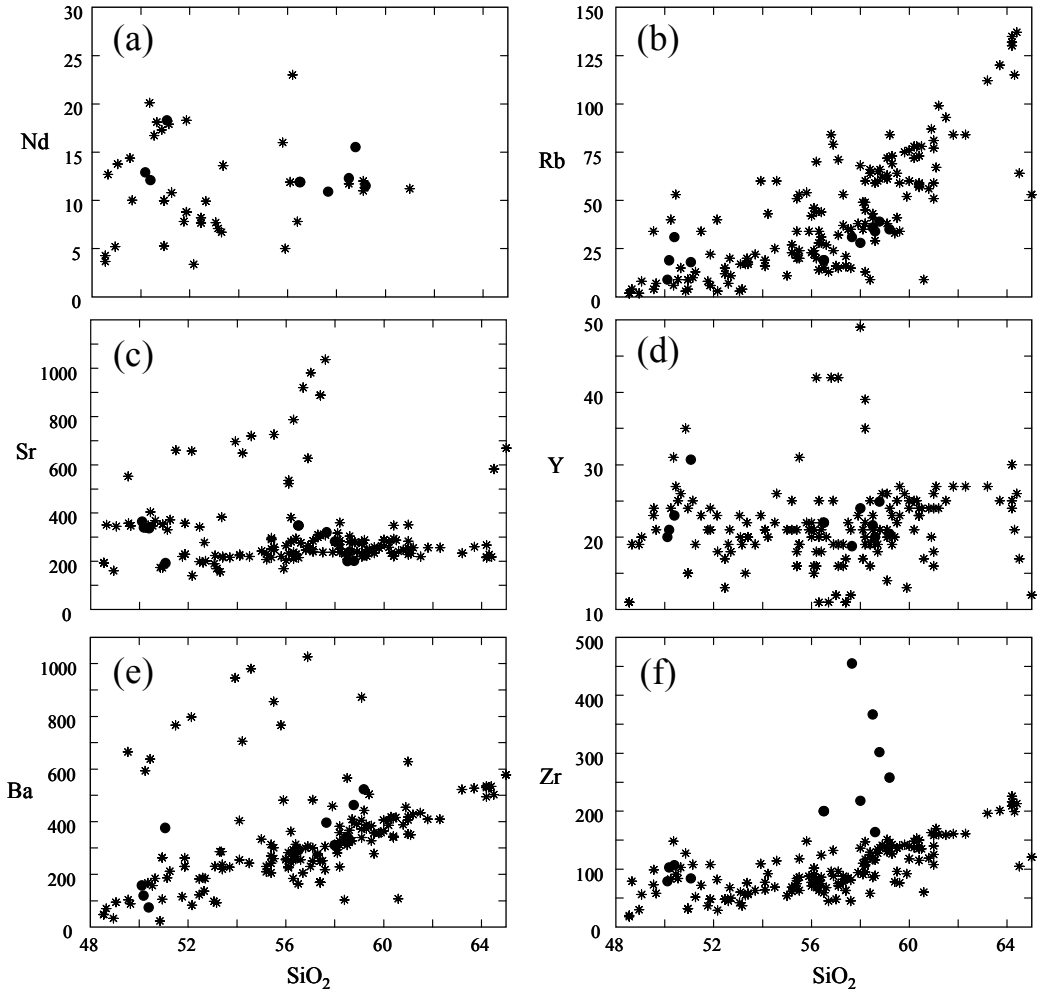

Fig. 2.4. Selected trace elements vs. SiO_2 for the TVZ modern basalt-andesites and selected hornblende-bearing mafic samples. Symbols as for Fig. 2.3.

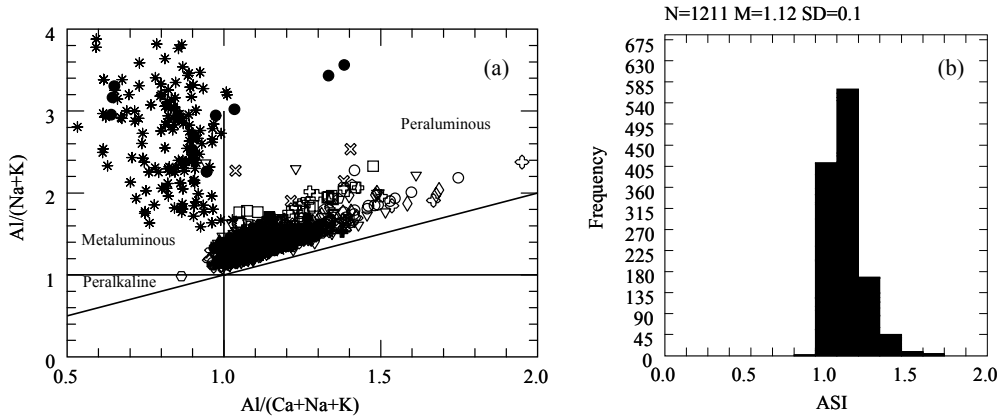

Fig. 2.5. Aluminum saturation index (ASI) for TVZ rhyodacite/rhyolites and associated hornblende-bearing mafic rocks considered in this study; divisions per Shands index. Frequency distribution of the 1211 rhyodacite/rhyolite samples in this dataset have a mean: 1.12. Symbols as for Table 2.1.

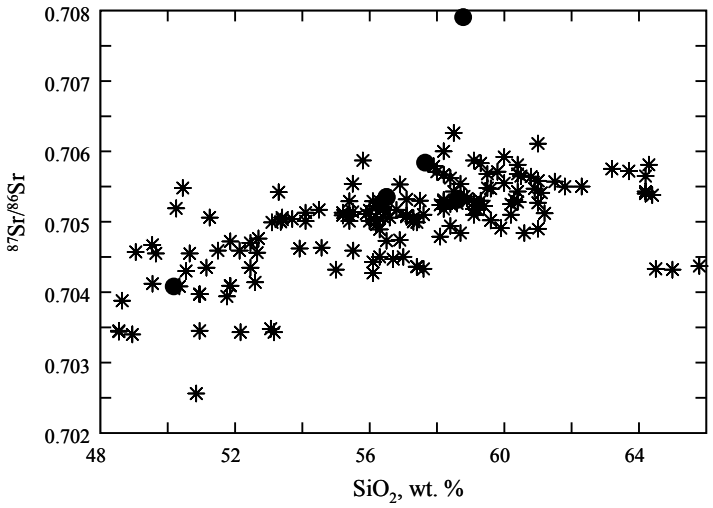

Fig. 2.6. $^{87}Sr/^{86}Sr$ ratio vs. SiO_2 for TVZ modern basalt-andesites and hornblende-bearing mafic clasts. Symbols as for Fig. 2.3.

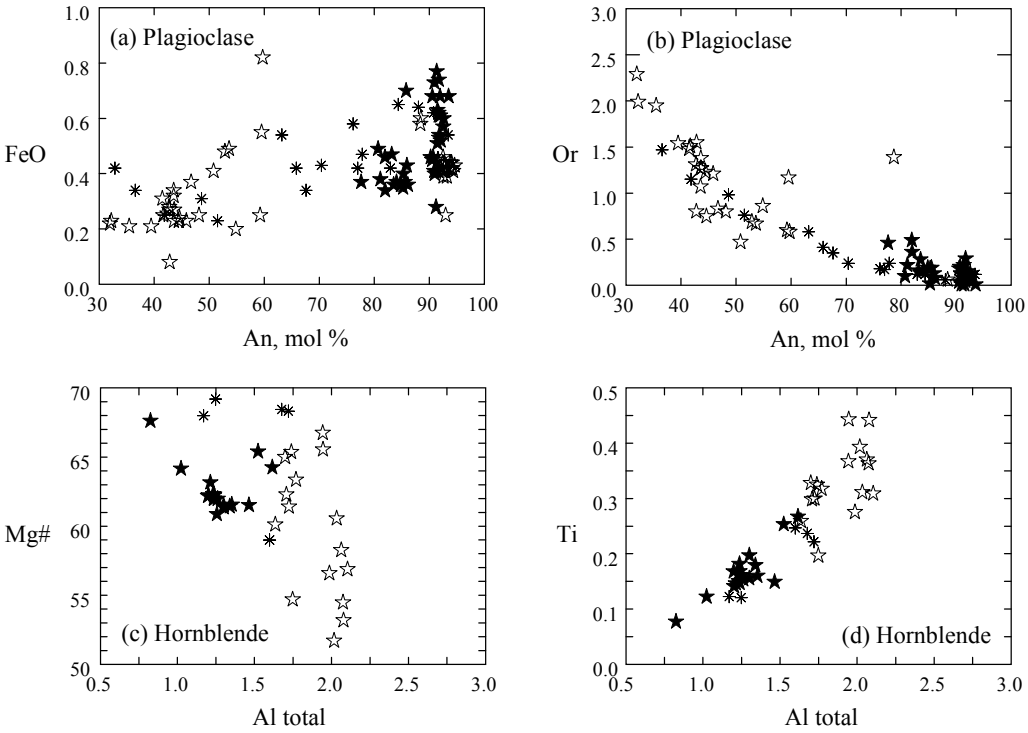

Fig. 2.7. Selected mineral compositions of hornblende-bearing mafic clasts. Closed stars are hornblende-bearing basalt and mingled andesite clasts from Matahina post-collapse deposits, open stars are hornblende-bearing basaltic-andesite/andesite clasts from Oruanui eruption, asterisks are hornblende-bearing gabbro from Whakamaru eruption.

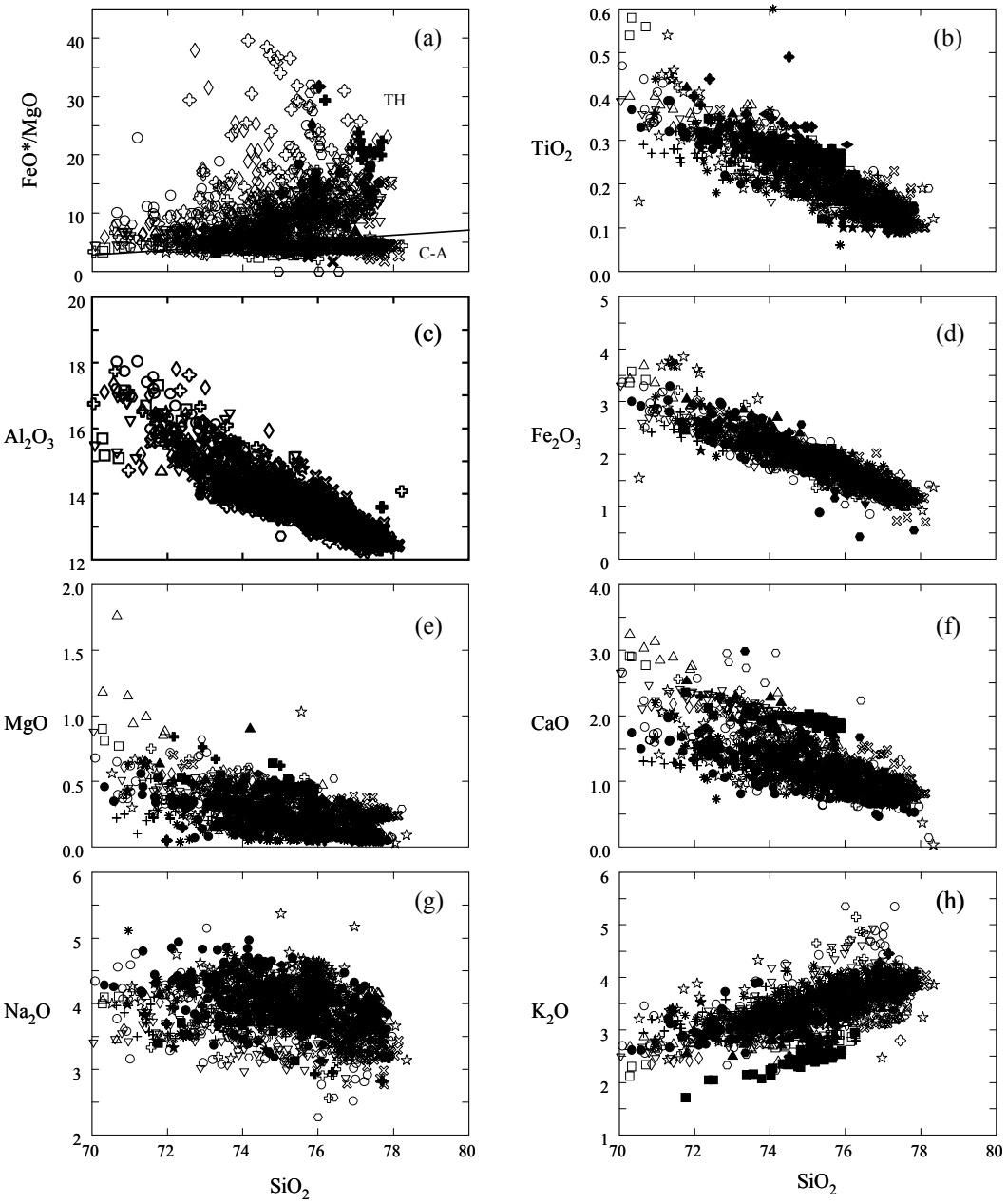

Fig. 2.8. (a) Projection of the FeO*/MgO divisions for tholeiitic and calc-alkaline rocks (Miyashiro 1974) into the rhyolitic field. (b-g) Selected major element oxides vs. silica for the TVZ rhyodacite-rhyolites.

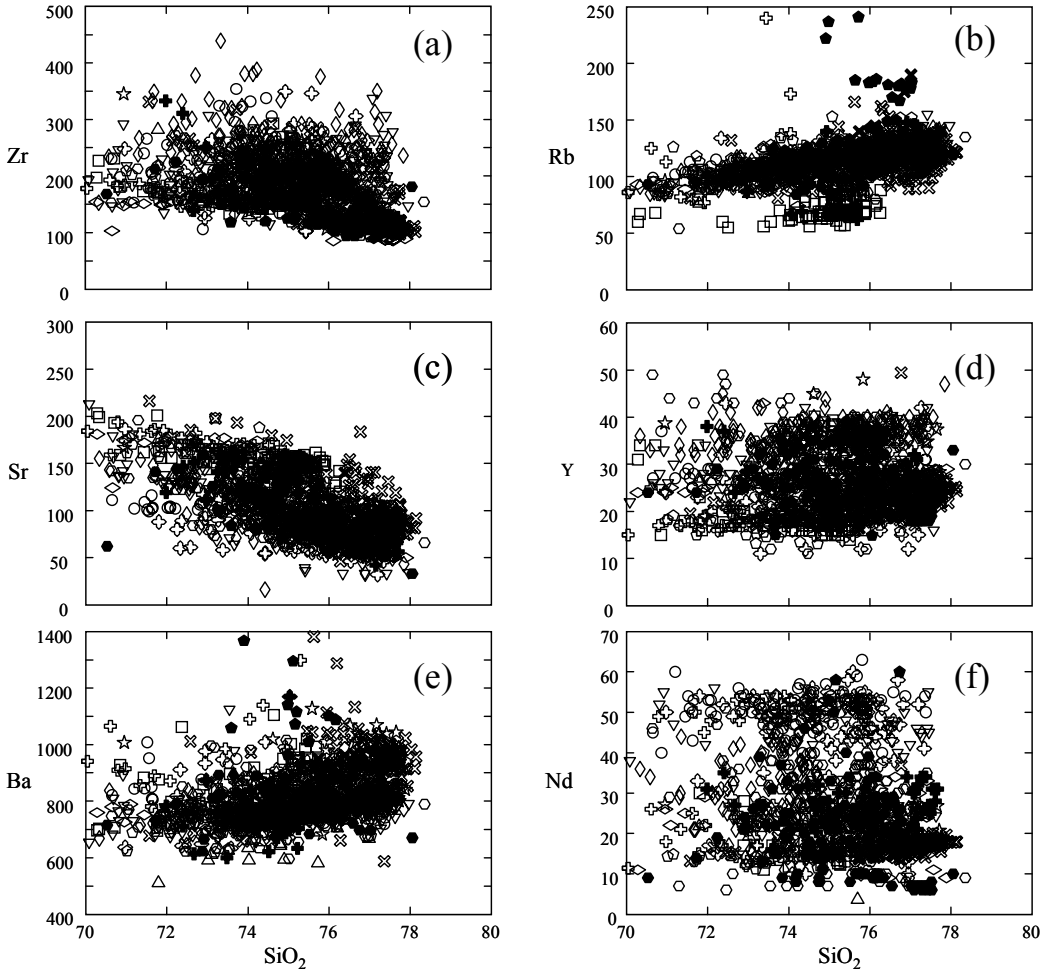

Fig 2.9. Selected trace elements vs. silica for the TVz rhyodacite/rhyolites. Symbols as for Table 2.1.

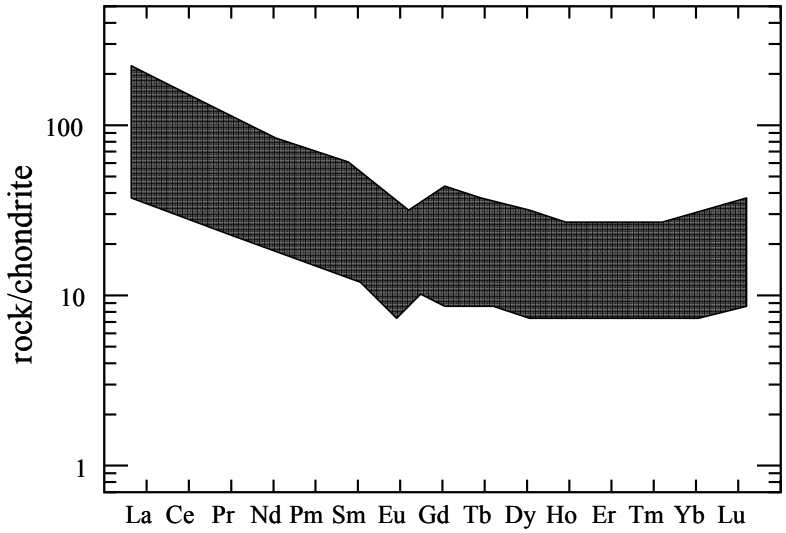

Fig. 2.10. Field representative REE data for the TVZ rhyodacite-rhyolite samples. Normalised to C1 chondrite from Sun and McDonough (1989).

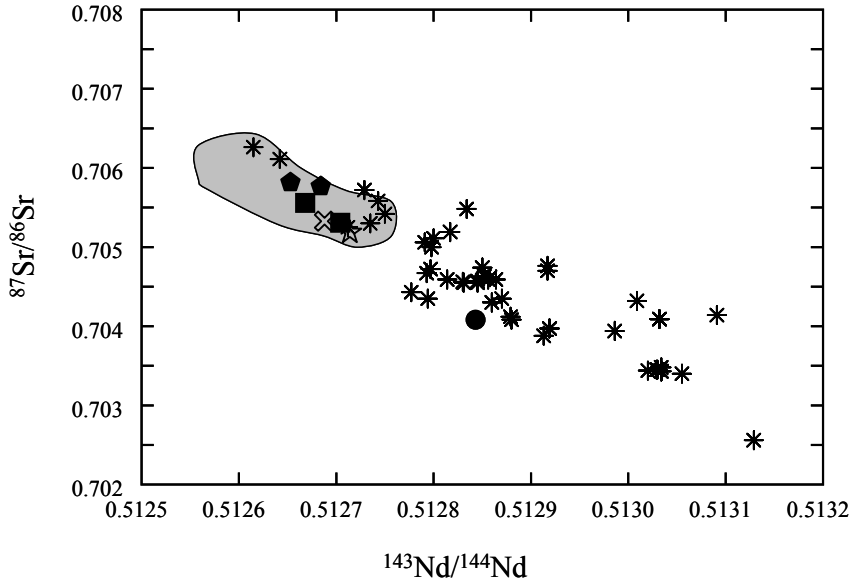

Fig. 2.11. $^{87}Sr/^{86}Sr$ vs. $^{143}Nd/^{144}Nd$ values for TVZ rhyodacite-rhyolites (field) and modern basalt-andesites (asterisks).

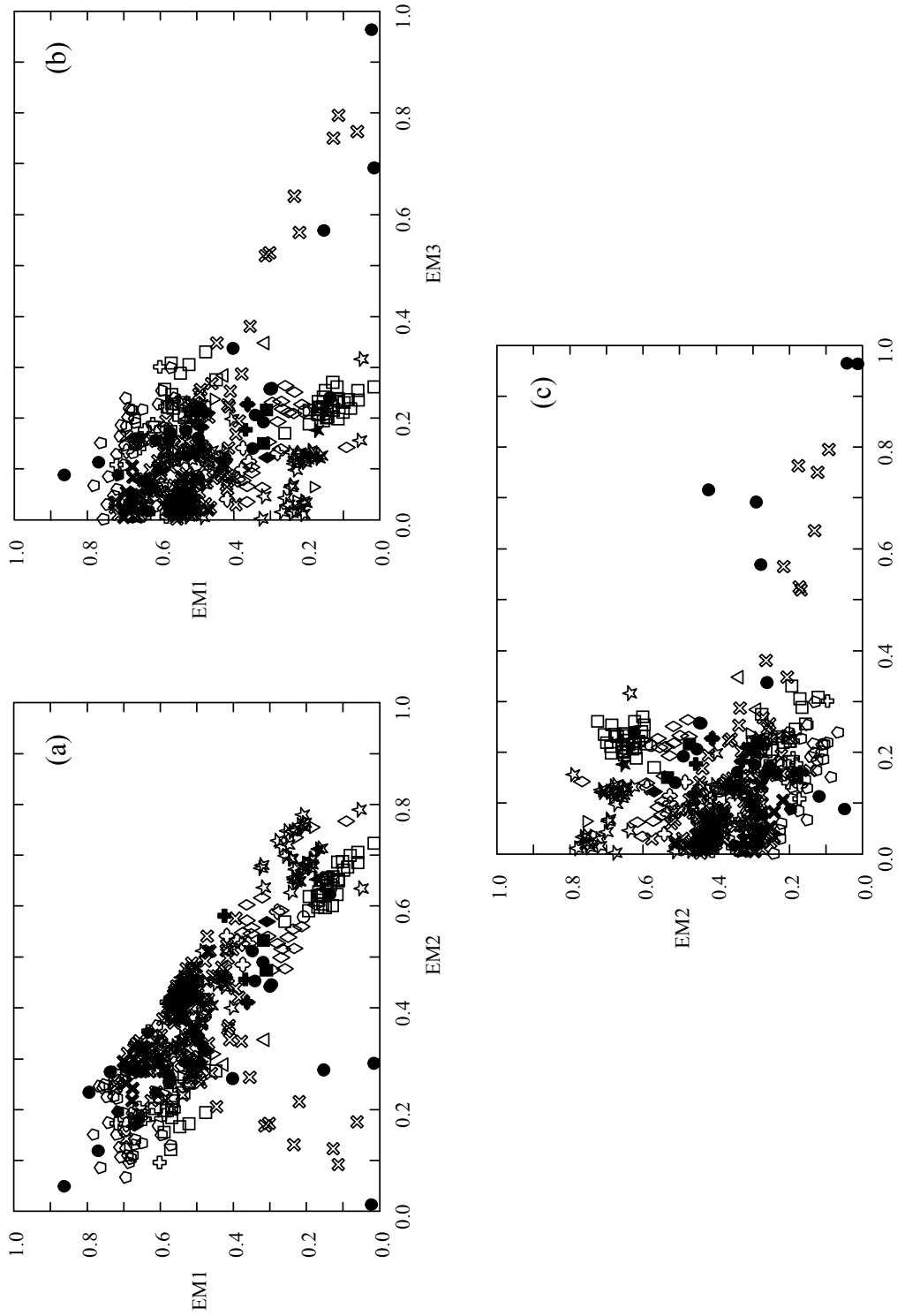

Fig. 2.12. Proportions of end-members (EM1-3) in individual samples. Symbols as for Table 1.

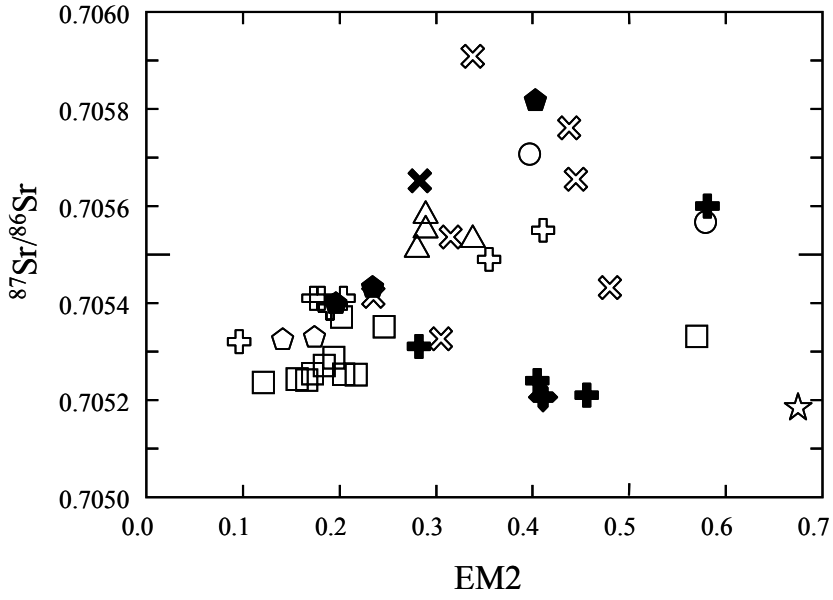

Fig. 2.13. $^{87}Sr/^{86}Sr$ vs. rhyolite end-member EM2. Symbology as for Table 2.1.

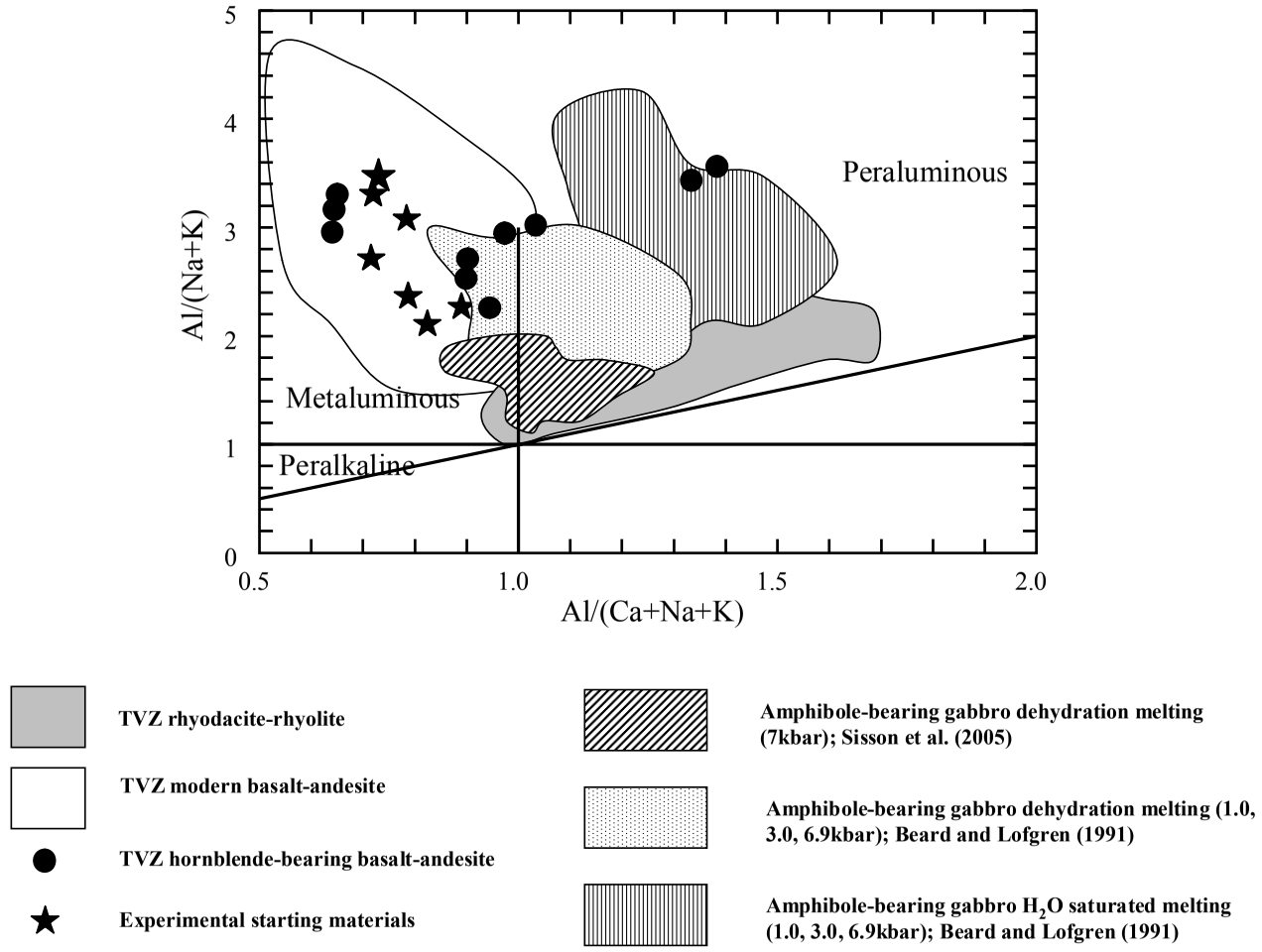

Fig. 2.14. Experimental melting of hornblende-bearing gabbroic rock under various P-T-fO_2-fH_2O conditions.

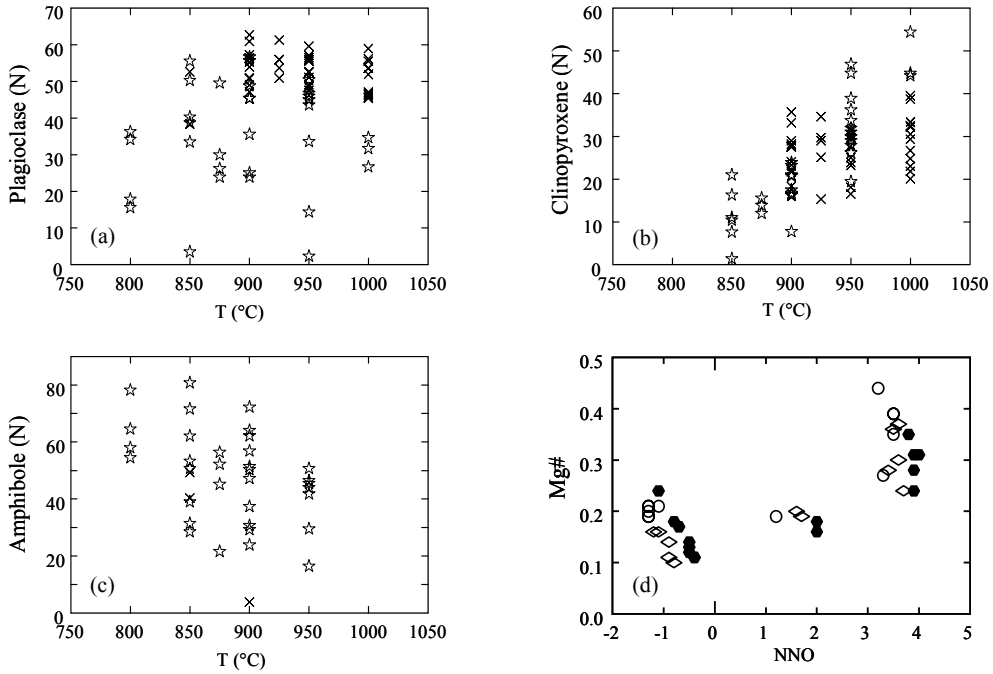

Fig. 2.15. Modal mineral assemblages and Mg# of evolved melts, produced by partial melting of amphibolite, in equilibrium with the starting material at various P-T-fO_2-fH_2O (Beard and Lofgren, 1991; Sisson et al., 2005). (a-c) Modal assemblage of plagioclase, clinopyroxene, and amphibole vs. temperature (Beard and Lofgren, 1991); stars are water-saturated experiments and crosses are under-saturated expermiments. (d) Dehydration melting experiments of (Sisson et al., 2005), Mg# (molar Mg/[Mg+Fe^{2+}]) of evolved melts vs. nickel-nickel oxide (NNO) buffer; different symbols represent different starting materials.

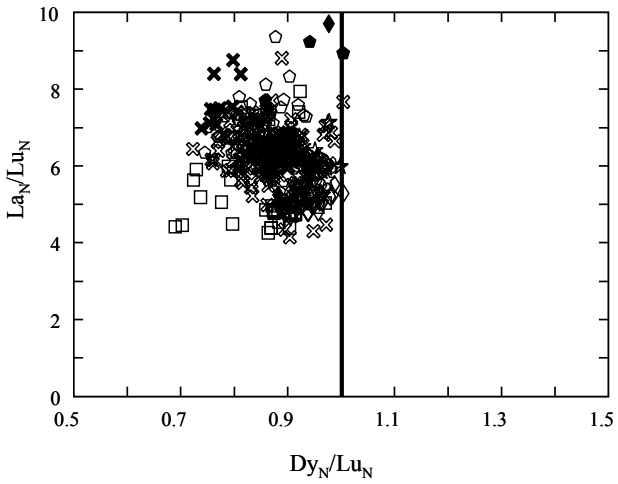

Fig. 2.16. Chondrite normalised La/Lu (LREE/HREE) vs. Dy/Lu (MREE/HREE) for TVZ rhyodacites-rhyolites. Dy/Lu <1 indicates amphibole (hornblende) in the source.

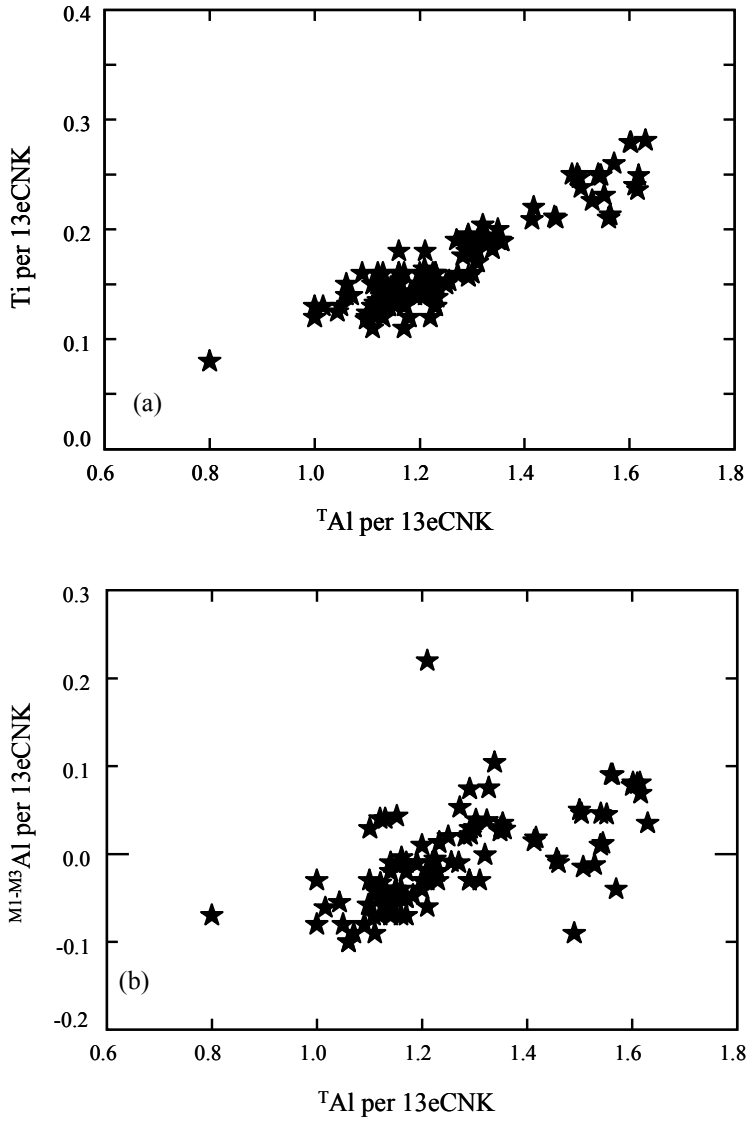

Fig. 2.17. Al-Tschermak and Ti-Tschermak substitutions in hornblende, $^{M1\text{-}M3}$Al per 13eCNK vs. ^{T}Al per 13eCNK and Ti per 13eCNK vs. ^{T}Al per 13eCNK, respectively, illustrating substitution in Matahina rhyolite hornblendes and associated basalts-andesites from post-caldera deposits.

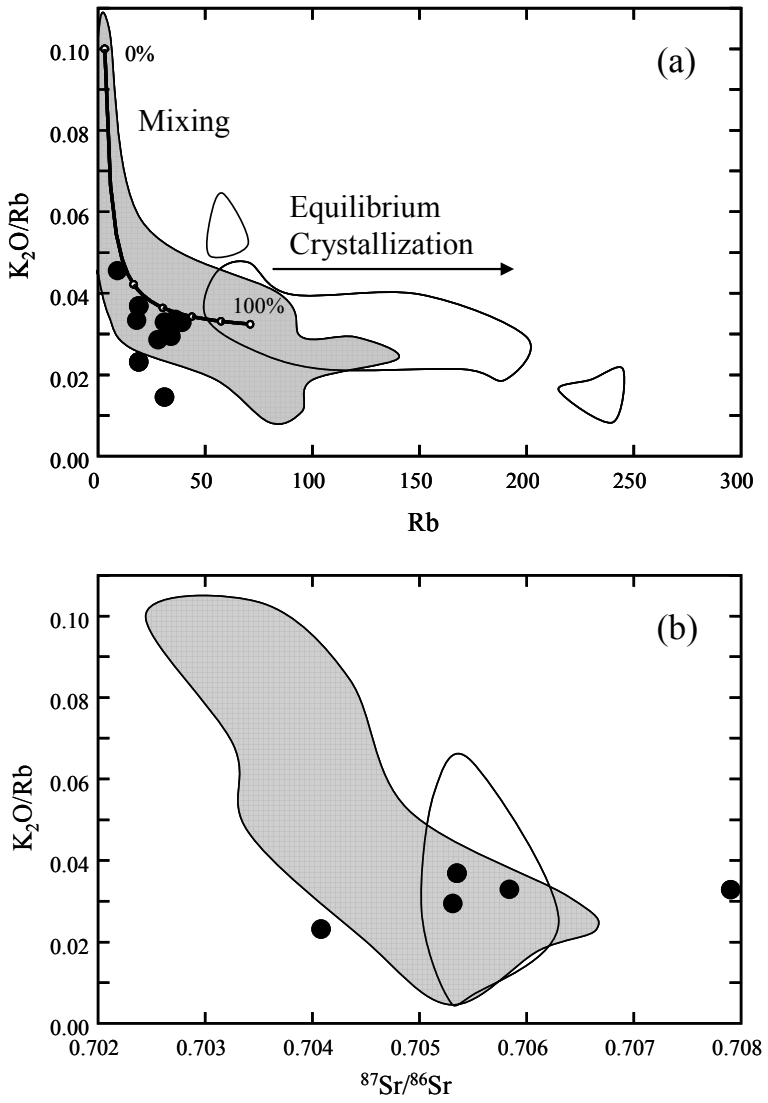

Fig. 2.18. (a) K_2O/Rb vs. Rb. (b) K_2O/Rb vs. Rb vs. $^{87}Sr/^{86}Sr$. Symbols are for Fig. 2.3. Open fields are for TVZ rhyolites and gray field is for modern basalt-andesite.

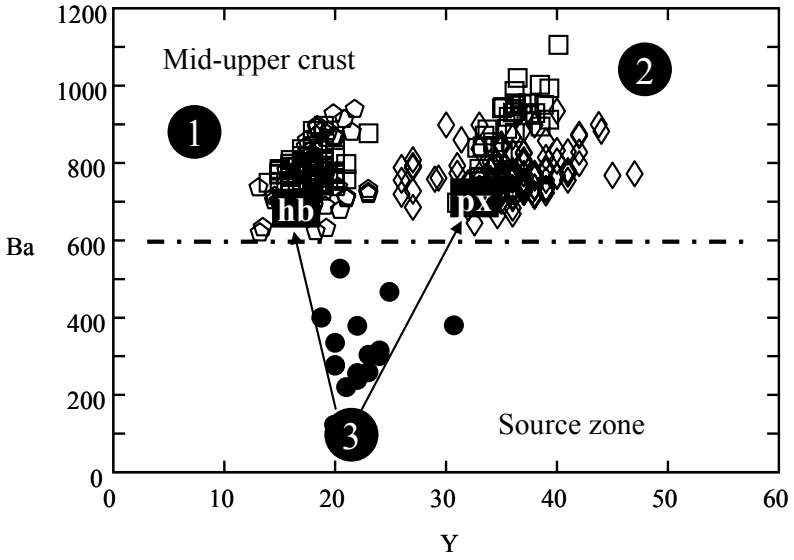

Fig. 2.19. Ba vs. Y for select TVZ rhyolites and hornblende-bearing basalt-andesite clasts. Dash-dot line indicates the theoretical division between processes occurring in a lower crustal source zone and those in the mid-upper crust following source zone extraction of the evolved melt. Circles represent composition of Polytopic Vector Analysis calculated end-members. Hornblende-bearing basalt-andesite samples (filled circles); EM2 samples: Mamaku (open diamonds); Mangaone (open squares); EM1 samples: Rotoiti (open squares); Okataina (open hexagons). Arrows projecting from EM3 (source rock) towards the Ba-Y values calculated in trace element modeling for each end-member type; either hornblende (hb) dominant fractionation or pyroxene (px) dominant fractionation.

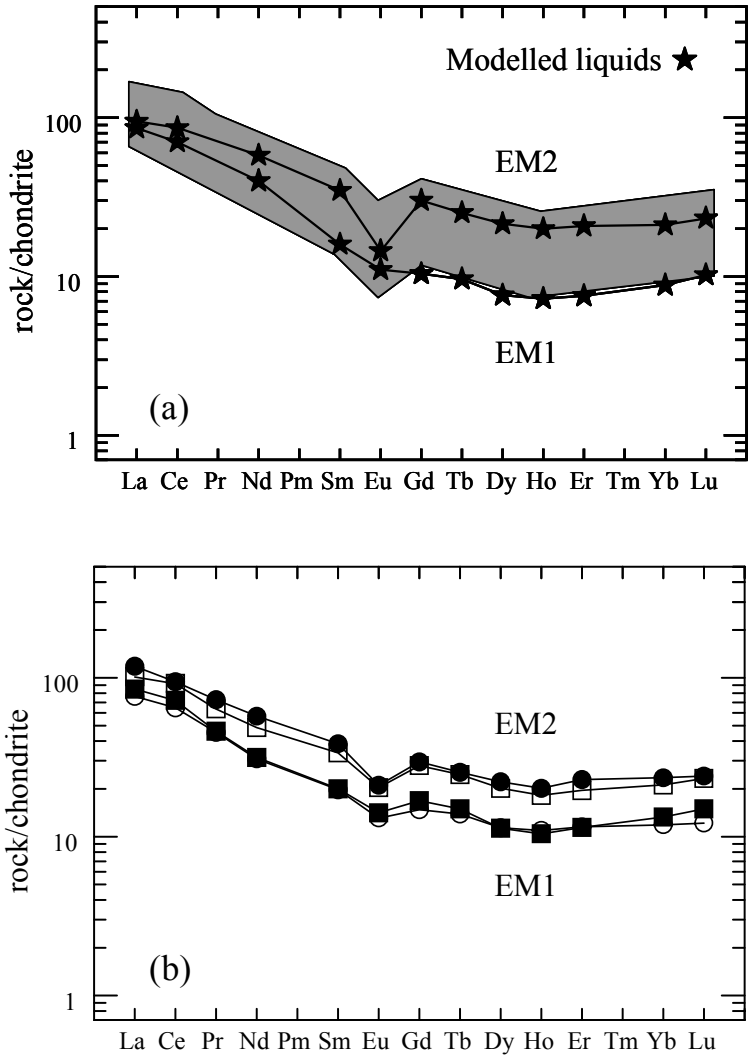

Fig. 2.20. (a) Modeled REE concentrations normalized to chondrite (Sun and McDowell 1989) for liquid compositions predicted by fractionation/melting of hb-bearing andesite. Shaded field represents all of the TVZ rhyolites. (b) REE concentrations of representative rhyolites that are compositionally more like the two extreme EM. EM2 rhyolites: Mamaku (filled circles) and Mangaone (open squares); and EM1 rhyolites: Lk. Okataina (open circles) and Rotoiti (filled squares).

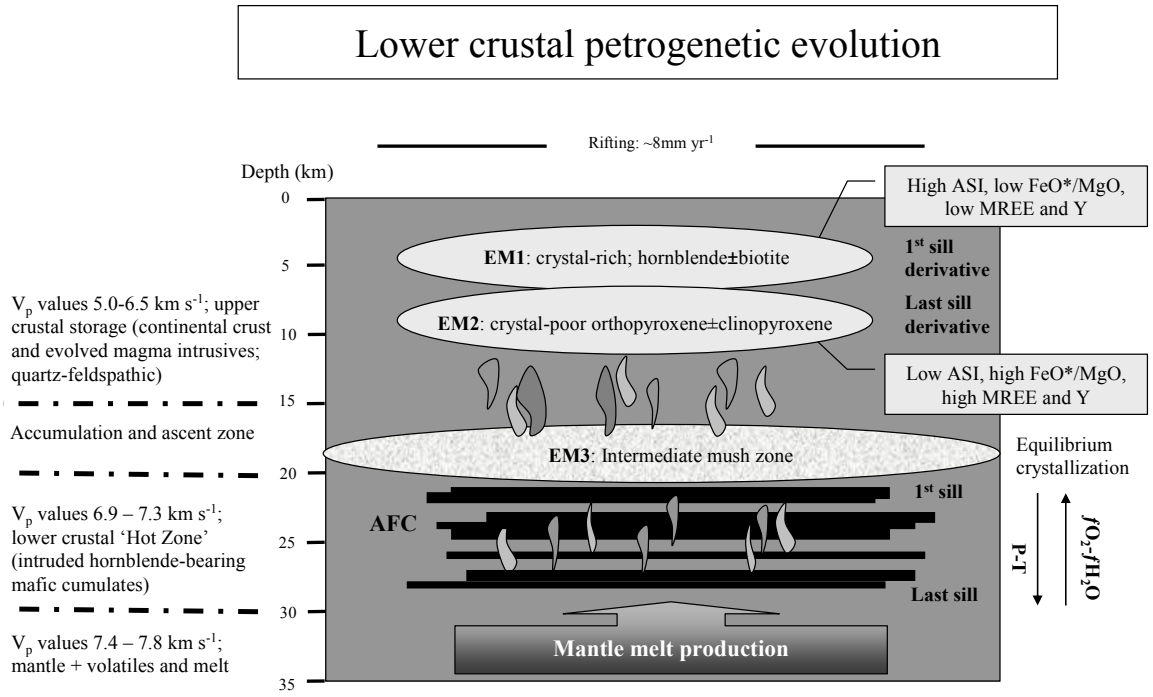

Fig. 2.21. Representative cross-section depicting the subsurface of the Taupo Volcanic Zone, using seismic velocity profiles of Harrison & White (2004). 'Wet' mantle derived calc-alkaline basalts pond and fractionate/assimilate at the base of the crust as a series of sills emplaced at low pressure and temperature. The emplacement depth of the first sill will vary along the TVZ as the subsurface of the thinning crust will be irregular; however, is roughly constrained over this time period to 15-20 km depth. The successive emplacement of basalt sills in the subcrustal region has the effect of thickening the existing crust with the underplated material. This 'artificial' thickening causes the next sills to be emplaced at greater and greater depths within a P-T-fO_2-fH_2O gradient. Further fractionation ±assimilation can then occur in the upper crustal reservoirs following the rhyolite melt extractions from the accumulation and ascent zone.

2.12 TABLES

Table 2.1 Volcanic Complexes

Volcanic Complex	*Major eruptives and associated doming*	*Previous Studies / § this study*	***Symbol*** *pyroclastics*	***Symbol*** *doming*
Okataina				
600ka - 367ka	Okataina pyroclastics/associated doming	§	⬠	⬟
367ka - 325ka	Murupara Subgroup (includes the Matahina)	§	⨻	✖
325ka - 236ka	Onuku*, Pikowai* and Pokopoko doming/associated pyroclastics	§	☆	★
236ka - 28ka	Doming and Rotoiti(+Earthquake Flat) and Mangaone pyroclastics	Schmitz & Smith (2004); Smith et al. (2002)§	□	■
28ka - present	Rotorua Subgroup; doming/pyrocolastics	Shane et al. (2007); Smith et al. (2004); Nairn et al. (2004)§	◇	◆
Whakamaru				
340ka	Whakamaru Group and Northwestern Dome Complex(NWDC)	Brown (1994); Brown et al. (1998); Bignall et al. (1996)	✜	✚
320ka - present	Maroa pyroclastics/associated doming	Leonard (2003); Milner et al. (2001)	⬡	⬢
Rotorua				
>240ka - 240ka	Endean and Hamurana doming; Mamaku pyroclastics/associated doming	Milner et al. (2001)§	◊	⧫
Reporoa				
230ka	Kaingaroa pyroclastics	Beresford (1997)§	○	●
Ohakuri				
240ka	Ohakuri pyroclastics	Gravley (2004)§	▽	
Kapenga				
275ka	Tumunui and Horohoro doming; Chimp and Pokai pyroclastics	Karhunen (1993)§	✣	✤
Taupo				
250ka - present	Oruanui, Taupo pyroclastics/associated doming	Sutton et al. (1995); Wilson et al. (2005)	△	▲
Basalt-andesite	Taranaki, Ruapehu, Rotokawa, Rolles Peak, Motuhora, Karangahape, Kakaramea+Tihia, Clark	Gamble et al. (1993); Graham et al. (1995)	✳	

* Onuku and Pikowai pyroclastics are here grouped with Okataina pyroclastic deposits of similar age; however, the sourcing to the Okataina Volcanic Complex is tentative.

Table 2.2. Representative bulk geochemical analyses

Sample	**UC199**	**UC928**	**UC933**	**UC555**	**UC650**	**UC181**
Lithology	Quartz-biotite	Murupara	Murupara	Matahina	Matahina	Matahina
Deposit description	pyroclastic flow	tephra	tephra	plinian airfall	pinkish tuff	pinkish tuff
Location	Parapara Rd.	Bonisch Rd.	Bonisch Rd.	Pahekeheke Rd.	SH38	Reihana Rd.
Grid reference	V16/291148	V16/310207	V16/310207	V16/356186	V16/113141	U17/092099
Source association	Okataina	Okataina	Okataina	Okataina	Okataina	Okataina
SiO_2	73.51	74.50	76.88	76.74	77.07	74.58
TiO_2	0.27	0.25	0.17	0.11	0.19	0.27
Al_2O_3	14.92	14.07	13.25	13.46	12.62	13.60
Fe_2O_3	2.01	1.85	1.24	1.38	1.48	2.26
MnO	0.04	0.05	0.05	0.04	0.04	0.06
MgO	0.56	0.49	0.28	0.16	0.23	0.52
CaO	1.94	1.72	1.04	0.86	1.07	2.07
Na_2O	3.61	3.88	3.86	3.19	3.53	3.69
K_2O	3.13	3.13	3.18	4.06	3.77	2.92
P_2O_5	0.01	0.04	0.04	0.01	0.01	0.01
LOI	3.08	4.37	4.57	3.47	3.74	4.80
Total	96.79	95.50	95.30	96.38	96.13	95.05
Sc	-	-	-	-	-	-
V	**33.93**	**18.26**	**4.61**	**1.30**	**1.93**	**14.77**
Cr	**12.52**	**3.27**	**2.80**	**5.15**	**2.61**	**3.25**
Ni	16	16	16	17	16	17
Cu	34	6	6	2	2	3
Zn	35	32	36	35	30	41
Rb	114	95	98	114	115	87
Zr	168	151	139	109	158	291
Sr	**157**	**143**	**101**	**85**	**97**	**180**
Y	**19.2**	**18.04**	**26.18**	**25.71**	**19.71**	**24.40**
Nb	**8.52**	**9.19**	**10.17**	**10.15**	**8.45**	**7.76**
Ba	**631**	**866**	**909**	**972**	**838**	**659**
La	**20.38**	**20.94**	**24.59**	**23.81**	**21.76**	**18.98**
Ce	**43.59**	**45.49**	**57.99**	**59.32**	**46.06**	**39.97**
Pr	**4.33**	**4.12**	**5.52**	**5.19**	**4.17**	**4.39**
Nd	**14.91**	**13.43**	**19.65**	**18.69**	**14.52**	**16.11**
Sm	**2.91**	**2.69**	**4.02**	**4.13**	**2.88**	**3.33**
Eu	**0.66**	**0.72**	**0.86**	**0.80**	**0.63**	**0.91**
Gd	**3.31**	**3.03**	**4.63**	**4.23**	**3.35**	**3.80**
Tb	**0.48**	**0.48**	**0.67**	**0.63**	**0.51**	**0.58**
Dy	**2.78**	**2.52**	**3.70**	**3.68**	**2.91**	**3.52**
Ho	**0.56**	**0.54**	**0.76**	**0.76**	**0.58**	**0.71**
Er	**1.71**	**1.70**	**2.40**	**2.31**	**1.84**	**2.18**
Tm	-	-	-	-	-	-
Yb	**1.90**	**1.92**	**2.67**	**2.45**	**2.04**	**2.43**
Lu	**0.30**	**0.35**	**0.43**	**0.40**	**0.35**	**0.41**
Hf	**4.05**	**3.88**	**3.95**	**3.63**	**4.05**	**6.36**
Ta	**1.39**	**1.14**	**1.54**	**2.40**	**1.64**	**1.09**
Pb	**25.97**	**27.57**	**33.33**	**32.25**	**32.15**	**22.82**
Th	**13.92**	**12.39**	**12.20**	**13.79**	**13.26**	**9.45**
U	**3.92**	**3.52**	**3.62**	**4.67**	**4.36**	**2.46**
$^{87}Sr/^{86}Sr$	-	0.705414	0.705432	0.705655	0.705326	0.705908
$^{143}Nd/^{144}Nd$	-	-	-	-	0.512688	-
Eu/Eu*	**0.68**	**0.78**	**0.64**	**0.60**	**0.64**	**0.81**

Samples are normalized to 100% anhydrous. Major elements given in wt. % and trace elements (ppm).
Trace elements in bold analyzed by ICP-MS. LOI values are calculated by weight difference. n.d. = not detected.
Grid references refer to sample localities on the New Zealand NZMS 1:50,000 maps.
Eu/Eu* (Eu anomaly) is calculated from the two linear equations $\log10(Sm_N) = a*(62+b)$ and $\log10(Tb_N) = a*(65+b)$

Table 2.2 cont.

UC888	**UC839**	**UC474**	**NT213-12F**	**UC971**	**UC1099**	**UC1093**
Matahina	Matahina	Matahina	Wairua dome complex	Whakapoungakau	Maungawhakamana	Lake Rotoma
lithic lag breccia	post collapse	post collapse	lava dome	lava dome	lava dome	lava dome
Te Weta Rd.	Te Weta Rd.	Te Weta Rd.	Wairua Rd.	Lake Okataina	SH30-(2)/Otangiwai Pt.	Lake Rotoma
V16/300301	V16/300301	V16/300301	U16/086222	U15/092382	V15/238433	V15/249473
Okataina	Okataina	Okataina	Okataina	Okataina	Okataina	Okataina
76.61	51.29	77.37	74.41	76.12	77.29	75.78
0.16	0.99	0.11	0.31	0.29	0.13	0.24
13.02	18.69	12.84	14.11	14.15	12.63	13.34
1.39	11.85	1.15	2.29	1.34	1.42	1.70
0.05	0.20	0.04	0.03	0.01	0.04	0.05
0.34	5.63	0.24	0.56	0.23	0.19	0.49
1.02	8.88	0.89	1.49	1.04	1.02	1.40
3.33	1.77	3.43	3.42	3.16	3.91	3.93
4.07	0.60	3.92	3.37	3.64	3.36	3.06
0.00	0.09	0.01	0.02	0.02	0.01	0.02
3.91	3.28	3.94	1.80	1.79	3.46	2.55
95.97	96.61	95.94	98.05	98.07	96.42	97.32
-	-	-	-	-	-	-
10.98	**324.69**	**11.58**	**32.46**	**12.37**	**-**	**19.19**
2.96	**21.99**	**9.97**	**12.77**	**4.35**	**6.9**	**4.05**
17	21	17	21	17	16	17
6	0	7	1	4	10	1
27	98	30	41	25	35	31
133	18	118	124	128	103	86
121	84	107	194	183	126	147
85	**193**	**95**	**136**	**103**	**102**	**114**
18.60	**30.70**	**22.99**	**19.15**	**14.88**	**22.99**	**18.60**
9.76	**2.65**	**10.55**	**9.42**	**8.94**	**9.12**	**9.43**
963	**376**	**926**	**836**	**878**	**871**	**1051**
23.69	**11.74**	**22.90**	**22.17**	**20.57**	**21.87**	**23.37**
53.30	**19.51**	**58.18**	**44.17**	**44.58**	**49.44**	**50.01**
4.59	**4.12**	**5.11**	**4.38**	**4.20**	**4.73**	**4.54**
14.72	**18.29**	**16.83**	**14.56**	**13.88**	**16.34**	**15.65**
2.86	**4.62**	**3.65**	**2.88**	**2.67**	**3.55**	**2.96**
0.57	**1.12**	**0.93**	**0.64**	**0.60**	**0.77**	**0.66**
3.21	**4.43**	**4.10**	**3.04**	**2.85**	**3.66**	**3.30**
0.48	**0.71**	**0.63**	**0.48**	**0.43**	**0.58**	**0.49**
2.62	**4.86**	**3.29**	**2.65**	**2.25**	**3.30**	**2.70**
0.56	**0.90**	**0.71**	**0.46**	**0.46**	**0.67**	**0.51**
1.81	**2.82**	**2.19**	**1.69**	**1.40**	**2.13**	**1.67**
-	**-**	**-**	**-**	**-**	**-**	**-**
2.04	**2.88**	**2.41**	**1.89**	**1.50**	**2.34**	**1.82**
0.34	**0.44**	**0.42**	**0.31**	**0.24**	**0.37**	**0.29**
3.58	**2.32**	**3.70**	**4.52**	**4.48**	**3.77**	**3.89**
1.73	**0.18**	**3.51**	**1.71**	**1.74**	**1.87**	**1.43**
29.53	**2.76**	**28.23**	**23.48**	**32.59**	**33.99**	**27.86**
15.89	**1.49**	**13.10**	**13.04**	**14.10**	**12.16**	**10.43**
5.25	**0.45**	**6.79**	**3.42**	**3.66**	**4.28**	**2.93**
0.705652	-	-	0.705432	0.705399	0.705817	0.705556
-	-	-	-	-	0.512653	0.512644
0.60	**0.75**	**0.75**	**0.67**	**0.68**	**0.65**	**0.67**

Table 2.2 cont.

UC812	**UC999**	**UC1028**	**UC1072**	**UC1200**	**UC1173**	**UC1174**
Onuku	Pikowai	Onuku	Ohakuri	Ohakuri	Mamaku	Mamaku
pyroclastic flow	plinian airfall	tephra	pyroclastic flow	pyroclastic flow	pyroclastic flow	pyroclastic flow
Lake Okataina	Pikowai Reserve	Reihana Rd.	-	-	Hippo Rd.	Hippo Rd.
U16/079355	V15/326651	V16/093100	T16/693182	T16/693182		
Okataina	Unknown	Okataina	Ohukuri	Ohakuri	Rotorua	Rotorua
76.60	76.11	76.02	77.42	74.95	73.84	76.96
0.13	0.22	0.21	0.15	0.26	0.29	0.16
13.27	13.62	13.16	12.33	13.37	14.38	13.07
1.37	1.89	1.72	1.43	2.20	2.33	1.44
0.05	0.04	0.05	0.05	0.07	0.08	0.06
0.22	0.24	0.34	0.16	0.33	0.29	0.09
0.89	1.25	1.14	0.71	1.40	1.38	0.70
3.12	3.12	3.56	3.64	3.85	4.23	3.67
4.34	3.50	3.80	4.09	3.53	3.16	3.83
0.01	0.01	0.01	0.01	0.03	0.03	0.01
3.23	4.73	4.85	4.61	3.72	3.20	3.25
96.65	95.22	95.15	95.27	96.15	96.66	96.63
-	-	-	-	-	-	-
5.74	**8.97**	**3.18**	**2.17**	**14.35**	**1.64**	**4.78**
5.82	**6.74**	**1.73**	**2.88**	**4.45**	**5.14**	**6.05**
17	101	16	16	-	-	-
2	191	7	1	12	-	-
28		39	39	47	-	-
140	110	117	126	114	95	114
109	191	204	155	252	275	170
69	**106**	**104**	**57**	**120**	**124**	**59**
22.27	**20.25**	**26.97**	**39.99**	**38.54**	**37.27**	**35.33**
9.36	**8.56**	**9.86**	**12.14**	**14.23**	**10.93**	**12.88**
788	**770**	**825**	**858**	**849**	**745**	**758**
24.62	**21.29**	**23.78**	**27.34**	**27.47**	**27.95**	**27.01**
54.82	**44.10**	**58.88**	**70.59**	**65.90**	**57.79**	**64.33**
4.80	**4.39**	**5.59**	**6.90**	**6.79**	**6.91**	**7.13**
16.02	**15.22**	**19.60**	**26.03**	**26.44**	**26.82**	**26.23**
3.06	**3.32**	**4.02**	**5.49**	**5.89**	**5.88**	**5.66**
0.53	**0.67**	**0.80**	**0.80**	**1.34**	**1.22**	**0.87**
3.43	**3.67**	**4.30**	**5.76**	**6.29**	**6.07**	**5.99**
0.51	**0.61**	**0.66**	**0.88**	**0.93**	**0.95**	**0.98**
2.92	**3.07**	**3.79**	**5.45**	**5.67**	**5.62**	**5.50**
0.55	**0.63**	**0.76**	**1.10**	**1.19**	**1.14**	**1.23**
1.83	**2.01**	**2.34**	**3.34**	**3.41**	**3.78**	**3.76**
-	**-**	**-**	**-**	**-**	**-**	**-**
2.18	**2.26**	**2.50**	**3.70**	**3.81**	**3.99**	**3.71**
0.37	**0.36**	**0.40**	**0.58**	**0.59**	**0.61**	**0.55**
3.29	**4.88**	**5.09**	**4.72**	**6.22**	**6.52**	**4.38**
1.89	**1.23**	**1.55**	**2.24**	**1.45**	**1.13**	**1.45**
25.56	**30.44**	**35.28**	**42.34**	**27.76**	**35.59**	**35.97**
17.71	**13.22**	**14.00**	**13.56**	**11.21**	**11.52**	**13.92**
5.83	**3.93**	**3.74**	**4.14**	**3.60**	**3.11**	**3.90**
0.705536	-	-	-	-	-	-
0.512668	-	-	-	-	-	-
0.52	**0.59**	**0.60**	**0.44**	**0.69**	**0.63**	**0.45**

Table 2.2 cont.

UC1233	**UC533**	**UC1189**	**UC1191**	**UC1212**	**UC1211**	**UC216**
Endean Dome	Mangaone	Kaingaroa	Kaingaroa	Pokai	Pokai	Pokopoko
lava dome	plinian airfall	pyroclastic flow	pyroclastic flow	pyroclastic flow	pyroclastic flow	pyroclastics/doming
Endean Rd.	Near Matahina Dam	Old Waitapu Rd.	Old Waitapu Rd.	Pokai Rd.	Pokai Rd.	Millar Rd.
U15/845359	V16/449366	U16/085108	U16/085108	682268	682268	U16/038326
Rotorua	Okataina	Reporoa	Reporoa	Kapenga	Kapenga	Okataina
73.64	75.72	75.63	75.70	77.28	75.49	76.22
0.31	0.25	0.21	0.21	0.12	0.18	0.20
14.11	13.49	13.30	13.40	12.32	13.88	12.85
2.33	1.78	1.83	1.83	1.56	1.98	1.79
0.05	0.08	0.05	0.05	0.05	0.06	0.06
0.37	0.32	0.24	0.23	0.12	0.17	0.33
1.80	1.22	1.22	1.13	0.76	0.93	1.03
3.91	4.22	3.92	3.74	3.68	3.63	4.16
3.42	2.89	3.60	3.70	4.09	3.65	3.35
0.06	0.02	0.01	0.01	0.00	0.01	0.02
2.83	3.30	3.10	3.36	3.12	1.09	2.66
97.05	96.51	96.77	96.51	96.75	98.78	97.22
-	-	-	-	-	-	-
32.03	**2.99**	**11.41**	**10.94**	**5.79**	**6.98**	**9.50**
5.53	**5.06**	**6.09**	**5.49**	**5.25**	**3.96**	**4.42**
-	18	-	-	-	-	16
3	n.d.	6	5	9	18	6
35	62	39	38	37	41	47
125	95	125	124	137	123	107
180	262	213	213	171	247	224
143	**140**	**113**	**104**	**65**	**89**	**88**
16.46	**39.30**	**28.78**	**28.92**	**34.47**	**33.83**	**36.95**
9.43	**12.04**	**13.21**	**13.13**	**13.83**	**14.95**	**11.90**
894	**993**	**910**	**892**	**915**	**890**	**712**
23.43	**26.70**	**26.16**	**25.66**	**29.65**	**28.62**	**25.45**
46.15	**66.95**	**61.81**	**58.96**	**69.79**	**68.31**	**59.97**
4.53	**6.93**	**5.86**	**5.72**	**6.99**	**6.57**	**6.31**
16.01	**26.13**	**21.31**	**21.21**	**26.12**	**24.60**	**23.32**
3.16	**5.62**	**4.60**	**4.50**	**5.50**	**5.24**	**4.92**
0.73	**1.33**	**0.97**	**0.94**	**0.94**	**1.03**	**0.94**
3.42	**6.06**	**5.03**	**5.13**	**6.17**	**6.01**	**5.46**
0.48	**0.93**	**0.72**	**0.75**	**0.90**	**0.86**	**0.85**
2.53	**5.46**	**4.21**	**4.21**	**5.20**	**4.95**	**5.27**
0.55	**1.12**	**0.89**	**0.89**	**1.08**	**1.05**	**1.10**
1.60	**3.30**	**2.61**	**2.64**	**3.18**	**3.11**	**3.34**
-	**-**	**-**	**-**	**-**	**-**	**-**
1.67	**3.74**	**2.95**	**2.94**	**3.56**	**3.40**	**3.46**
0.26	**0.60**	**0.45**	**0.46**	**0.53**	**0.53**	**0.58**
4.52	**6.29**	**5.41**	**5.45**	**4.94**	**6.29**	**5.59**
1.19	**1.63**	**1.57**	**1.65**	**1.87**	**1.87**	**2.34**
21.78	**32.30**	**26.81**	**25.88**	**32.07**	**29.83**	**33.82**
13.06	**10.24**	**13.52**	**14.28**	**14.49**	**14.84**	**12.02**
3.62	**2.94**	**4.78**	**4.87**	**4.83**	**4.38**	**3.46**
-	**-**	**-**	**-**	**-**	**-**	0.705184
-	-	-	-	-	-	0.512714
0.71	**0.71**	**0.65**	**0.63**	**0.52**	**0.59**	**0.57**

Table 2.3. Klovan/Miesch Coefficient of Determination (CD)

No. of EMs	*2*	***3***	***4***	*5*	*6*
Analyte					
SiO_2	0.90	**0.90**	**0.89**	0.93	0.98
TiO_2	0.92	**0.94**	**0.93**	0.94	0.95
Al_2O_3	0.67	**0.68**	**0.72**	0.85	0.85
Fe_2O_3	0.86	**0.86**	**0.85**	0.90	0.94
MnO	0.76	**0.82**	**0.82**	0.84	0.87
MgO	0.70	**0.69**	**0.75**	0.80	0.88
CaO	0.79	**0.81**	**0.83**	0.83	0.90
Na_2O	0.00	**0.17**	**0.21**	0.76	0.76
K_2O	0.78	**0.79**	**0.81**	0.87	0.89
Rb	0.52	**0.55**	**0.56**	0.67	0.69
Zr	0.28	**0.38**	**0.69**	0.69	0.96
Sr	0.75	**0.78**	**0.79**	0.81	0.82
Y	0.00	**0.92**	**0.94**	0.94	0.95
Ba	0.46	**0.49**	**0.49**	0.49	0.50
La	0.25	**0.56**	**0.61**	0.61	0.63
Ce	0.21	**0.70**	**0.74**	0.76	0.76
Nd	0.02	**0.78**	**0.85**	0.85	0.91
Sm	0.00	**0.83**	**0.88**	0.88	0.93
Eu	0.00	**0.61**	**0.89**	0.90	0.96
Yb	0.00	**0.84**	**0.88**	0.89	0.89
Pb	0.25	**0.54**	**0.55**	0.69	0.74
Th	0.44	**0.45**	**0.50**	0.74	0.74

Polytopic Vector Analysis solutions for end-members from 2-6.

CD values provide a measure of how well a solution is supported:

>0.5 = support; >0.7 strong support; >0.9 very strong support

End-members in bold represent those considered best for the multivariate statistical solution.

Table 2.4. Compositions of PVA generated end-members (EM).

	EM 1	*EM 2*	*EM 3*
Analyte			
SiO_2	77.50	79.20	52.00
TiO_2	0.12	0.02	1.28
Al_2O_3	13.10	12.00	21.20
Fe_2O_3	0.87	0.48	9.90
MnO	0.02	0.05	0.21
MgO	0.04	0.01	3.68
CaO	1.02	0.01	7.66
Na_2O	3.14	4.19	3.94
K_2O	4.11	3.83	0.01
Rb	138	115	0.01
Zr	85.9	181	461
Sr	101	42.8	417
Y	7.55	47.5	21.3
Ba	893	1050	128
La	19.3	33.6	7.85
Ce	37.4	84.4	16.5
Nd	8.93	31.6	13.5
Sm	1.41	7.04	3.14
Eu	0.37	4.15	1.88
Yb	0.91	4.55	2.30
Lu	0.53	0.47	0.53
Pb	18.50	50.40	0.01
Th	14.50	14.40	0.01

Table 2.5. Rhyolite end-member (EM) geochemical and petrological characteristics

	EM1	EM2
Geochemical	low FeO*/MgO	high FeO*/MgO
	low Y	high Y
	low MREE	high MREE
	high ASI	low ASI
	high Sr; low Eu/Eu*	low Sr; high Eu/Eu*
	low Zr	high Zr
Petrological	crystal-rich (10 to 45%)	crystal-poor (<10%)
	dominantly hydrous mineral phases:	dominantly anhydrous mineral phases:
	hornblende±cummingtonite±biotite	orthopyroxene±clinopyroxene

Table 2.6. Crystal contents and modal phenocryst assemblages of end-member types along the compositional spectrum.

Sample	*EM2*	*Whole rock SiO_2*	*Vol% crystals*	*Crystal content*
Okataina	0.15	73.62	15-20	plag+bt+qtz+mt+hb±il
Rotoiti	0.22	74.74	16-28	plag+qtz+cmgt+mt+il±bt
Whakamaru (Type A)	0.19	72.09	35-40	plag+qtz+opx±bt±hb+mt+il
Oruanui	0.30	74.89	<5	plag+opx+qtz+hb±mt+il
Matahina	0.40	76.56	<10	plag+qtz+opx±hb+mt+il
Kaingaroa	0.39	70.89	<5	plag+opx+mt+il±hb
Mamaku	0.56	73.84	<10	plag+qtz+opx+mt+il±cpx±hb
Pokai	0.53	75.83	<10	plag+opx+mt+il±qtz

Plagioclase (plag); quartz (qtz); hornblende (hb); cummingtonite (cmgt); biotite (bt); magnetite (mt); ilmenite (il)

Table 2.7a Linear regression analysis (EM1; hornblende-orthopyroxene)

PARENT	UC1100
DAUGHTER	Okataina (UC1108)

Min/rock	% phase	Modal
Anorthite	17.3	30.9
Albite	11.5	20.6
Hornblende	19.5	34.8
Orthopyroxene	3.9	7.1
Magnetite	3.2	5.7
Ilmenite	0.5	0.9
Liquid remaining	44.0	

Sum of the squares of the residual = 0.078

	Daughter	Observed: UC1100	Calculated: UC1100	Residual
SiO_2	71.22	58.18	57.96	0.09
TiO_2	0.41	1.07	1.05	0.02
Al_2O_3	17.06	17.71	17.76	0.02
Fe_2O_3	2.57	8.38	8.36	0.02
MnO	0.05	0.18	0.16	0.02
MgO	0.62	3.70	3.74	0.03
CaO	2.20	6.70	6.68	0.03
Na_2O	3.17	2.98	3.02	0.04
K_2O	2.69	1.03	1.28	0.25
P_2O_5	0.01	0.06	0.00	0.06

	Calculated	Observed	Difference
Rb	69	85	16
Ba	657	623	34
Zr	192	209	17
La	20.39	18.13	2.26
Ce	43.03	39.59	3.44
Nd	18.65	14.36	4.29
Sr	153	161	8
Sm	2.44	3.02	0.58
Eu	0.64	0.76	0.12
Gd	2.14	3.04	0.90
Tb	0.36	0.52	0.16
Dy	1.94	2.89	0.95
Ho	0.41	0.62	0.21
Y	16.15	18.24	2.09
Er	1.25	1.91	0.66
Yb	1.50	2.02	0.52
Lu	0.26	0.31	0.05

Table 2.7b. Linear regression analysis (EM2; hornblende-orthopyroxene)

PARENT	UC1100
DAUGHTER	Mamaku (UC1173)

Min/rock	% phase	Modal
Anorthite	24.8	41.5
Albite	10.1	16.9
Hornblende	9.6	16.2
Orthopyroxene	10.9	18.3
Magnetite	3.2	5.4
Ilmenite	0.9	1.6
Liquid remaining	40.4	

Sum of the squares of the residual = 0.126

	Daughter	Observed: UC1100	Calculated: UC1100	Residual
SiO_2	73.84	58.18	57.86	0.13
TiO_2	0.29	1.07	1.04	0.03
Al_2O_3	14.38	17.71	17.76	0.02
Fe_2O_3	2.33	8.38	8.35	0.03
MnO	0.08	0.18	0.21	0.03
MgO	0.29	3.70	3.74	0.04
CaO	1.38	6.70	6.67	0.04
Na_2O	4.23	2.98	3.03	0.06
K_2O	3.16	1.03	1.34	0.31
P_2O_5	0.03	0.06	0.01	0.05

	Calculated	Observed	Difference
Rb	75	95	20
Ba	680	745	65
Zr	272	275	3
La	22.07	27.95	5.88
Ce	49.05	57.79	8.74
Nd	23.25	26.82	3.57
Sr	135	124	11
Sm	3.53	5.88	2.35
Eu	0.74	1.22	0.48
Gd	3.31	6.07	2.76
Tb	0.53	0.95	0.42
Dy	2.95	5.62	2.67
Ho	0.62	1.14	0.52
Y	22.95	37.27	14.32
Er	1.89	3.78	1.89
Yb	2.17	3.99	1.82
Lu	0.37	0.61	0.24

Table 2.7c. Linear regression analysis (EM2; orthopyroxene-clinopyroxene)

PARENT	UC1100
DAUGHTER	Mamaku (UC1173)

Min/rock	% phase	Modal
Anorthite	25.8	42.6
Albite	11.9	19.6
Clinopyroxene	4.2	7.0
Orthopyroxene	13.8	22.8
Magnetite	3.8	6.3
Ilmenite	1.1	1.8
Liquid remaining	39.4	

Sum of the squares of the residual = 0.089

	Daughter	Observed: UC1100	Calculated: UC1100	Residual
SiO_2	73.84	58.18	57.92	0.10
TiO_2	0.29	1.07	1.05	0.02
Al_2O_3	14.38	17.71	17.7	0.01
Fe_2O_3	2.33	8.38	8.36	0.02
MnO	0.08	0.18	0.23	0.05
MgO	0.29	3.70	3.73	0.03
CaO	1.38	6.70	6.69	0.01
Na_2O	4.23	2.98	3.04	0.06
K_2O	3.16	1.03	1.29	0.26
P_2O_5	0.03	0.06	0.01	0.05

	Calculated	Observed	Difference
Rb	77	95	18
Ba	680	745	65
Zr	414	275	139
La	22.45	27.95	5.50
Ce	52.78	57.79	5.01
Nd	26.99	26.82	0.17
Sr	126	124	2
Sm	5.32	5.88	0.56
Eu	0.84	1.22	0.38
Gd	6.18	6.07	0.11
Tb	0.94	0.95	0.01
Dy	5.46	5.62	0.16
Ho	1.13	1.14	0.01
Y	31.56	37.27	5.71
Er	3.44	3.78	0.34
Yb	3.59	3.99	0.40
Lu	0.59	0.61	0.02

CHAPTER 3

Origin of cold-wet-oxidizing to hot-dry-reducing rhyolite magma cycles and distribution in the Taupo Volcanic Zone, New Zealand

Origin of old-wet-oxidizing to hot-dry-reducing rhyolite magma cycles and distribution in the Taupo Volcanic Zone, New Zealand

C.D. Deering[1], D.M. Gravley[2], T.A. Vogel[3], J.W. Cole[1], G.S. Leonard[4]

[1]Dept. of Geological Sciences, University of Canterbury, PB 4800, Christchurch 8020, New Zealand
[2]Institute of Earth Science and Engineering (IESE), University of Auckland, PB 92019, Auckland 1142, New Zealand
[3]Dept. of Geological Sciences, Michigan State University, 206 Natural Sciences Bldg., East Lansing, Mi, 48824-1115, USA
[4]Institute of Geological & Nuclear Sciences, PO BOX 30368, Lower Hutt 6315, New Zealand
[1]cdd21@student.canterbury.ac.nz

Manuscript prepared for submission to Contributions to Mineralogy and Petrology.

Contributions

Concepts and model constraints were discussed with Jim Cole and Tom Vogel. Jim Cole provided insight into the volcanic history of the Taupo Volcanic Zone. Darren Gravley helped with sampling and field interpretations that led to construction of a comprehensive coastal stratigraphic history for deposits up to 600 kyrs. old. Graham Leonard performed Ar-Ar experiments on plagioclase separates from samples collectively obtained over the duration of the project, which also contributed to tephra correlations and construction of the pre-300 ka TVZ history.

3.1 ABSTRACT

Slab-derived aqueous fluid components (Ba, Cl) correlate well with oxygen fugacity, and other well defined characteristics of silicic magmas in the Taupo Volcanic Zone (TVZ) between a cold-wet-oxidizing magma type (R1: amphibole ± biotite; high Sr, low Zr and FeO*/MgO, depleted MREE) and a hot-dry-reducing magma type (R2: orthopyroxene ± clinopyroxene; low Sr, high Zr, and FeO*/MgO, less depleted MREE). Oxygen fugacity was obtained from analysis of Fe-Ti oxides and ranges between -0.039 to +2.054 log units (ΔQFM; where QFM = quartz + fayalite + magnetite buffer) and is positively correlated with the bulk-rock Ba/La ratio, indicating that slab-derived fluid is the oxidizing agent in the rhyolites. Chlorine contents in hornblende also correlate with the bulk-rock Ba/La ratio. Hence, high fluid-flux typically correlates with the R1 and low fluid-flux with R2 rhyolite magma types. A geochemical evolution and distribution can be tracked in time and space throughout the central region of the TVZ from 550 ka to present and has revealed two distinct magmatic cycles that vary in length. The first cycle included widespread R1 type magmatism across the central TVZ beginning ca. 550 ka and was directly associated with previously unreported dome-building and ignimbrite-forming volcanism, and led to a voluminous (>3000 km^3) ignimbrite 'flare-up' between ca. 340 and 240 ka. These magmas also display the highest K_2O and Pb isotopic compositions compared to those erupted more recently, and is consistent with a peak in slab-derived sediment input. The second cycle began roughly 180 ka, erupting ca. 800 km^3 of magma, and continues to the present. The duration, rate, and composition of melt production within these cycles appears to be governed by the flux of fluid/sediment released from the subducting slab, while the distribution of melts may be governed more by extension along the central rift axis. Shorter cycles have also

been identified and are unrelated to subduction processes, but occur following large, caldera-forming events. These perturbations in the subduction zone driven long cycles are related to volatile exsolution induced by decompression during caldera collapse, and are evidenced by a decrease in Cl contents of hornblende. Although these magmas are still classified as hot-dry-reducing, some geochemical parameters are also closely related to the caldera-forming rhyolite.

Keywords: *Taupo Volcanic Zone, magma distribution, Ba/La, K_2O, water*

3.2 INTRODUCTION

The Taupo Volcanic Zone (TVZ) in the North Island of New Zealand is a rifted arc (Wilson et al., 1995) and can be divided into segments of dominantly andesitic cone-forming volcanism in the north and south, and a central region characterised by rhyolitic caldera-forming and dome-building eruptions (Healy, 1962; Wilson et al., 1984). In fact, since its 1.6 Ma inception, the central TVZ has erupted > 6,000 km^3 of rhyolitic magma (70-77wt. % SiO_2), which is equivalent to 90% of the total erupted volume (Wilson et al., 2009). Caldera structural boundaries and regional tectonic fault structures define the central TVZ as a ca. 120 km long and up to 60 km wide envelope (Houghton et al., 1995; Fig. 3.1). In total, 25 caldera-forming eruptions have been recognised from eight rhyolitic centres that have been active over the 1.6 Myr volcanic history of the central TVZ. However, our focus in this study is a period of magmatism from ca. 550 ka to present that has led to caldera-forming and dome-building volcanism from seven of the eight rhyolitic centres (Fig. 3.1). During this period more than 4,000 km^3 of the rhyolitic magma generated at depth was erupted (cf. Wilson et al., 2009).

Previous evaluation of a large database of bulk-rock and Sr-Nd isotopic data representing volcanism over the past 550 ka by Deering et al. (2008) led to a model that accounts for the geochemical diversity of the rhyolites. A continuum of rhyolite compositions was characterized between two distinct end-members that are referred to as R1 and R2 in this paper (cf. EM1 and EM2; Deering et al., 2008). R1 contains dominantly hydrous ferromagnesian minerals (hornblende ± biotite) and is crystal-rich, with low FeO*/MgO (calc-alkaline series), enriched Sr, and depleted Zr, Y, and middle rare-earth elements (MREE); and R2 contains dominantly anhydrous

ferromagnesian minerals (orthopyroxene ± clinopyroxene ± hornblende) and is crystal-poor, with high FeO*/MgO (tholeiitic series), depleted Sr, and enriched Zr, Y, and MREE (Table 3.1). Deering et al. (2008) interpreted these differences in the rhyolite magma chemistry to reflect changes in the fH_2O, fO_2, P-T conditions within a mid-lower crustal (15-30 km) 'hot-zone' where these evolved melts are generated via fractionation of successively intruded basalts. Specifically, the systematic variations in the rhyolite geochemistry are governed by variable proportions of amphibole-orthopyroxene-clinopyroxene in equilibrium with the source melt.

Ewart (1967a,b) described a significant correlation between the ferromagnesian phenocryst assemblages and both total crystal contents and plagioclase/quartz ratios of TVZ rhyolites. This correlation was examined using the experimental 'granite system' of Tuttle and Bowen (1958) and led to the conclusion that each group of magma was derived from a distinct source. These groups are defined by their ferromagnesian contents: 1) orthopyroxene, 2) orthopyroxene + hornblende, and 3) biotite ± hornblende ± orthopyroxene, where 1) and 3) essentially correspond to the dominant phases of end-members bounding the spectrum of rhyolite compositions determined by Deering et al. (2008). Ewart (1967a,b) also suggested that the orthopyroxene group (low in quartz or quartz-free) residual liquid had not reached the quartz-feldspar boundary curve, indicating higher liquidus temperatures than the other hornblende- and biotite-bearing rhyolites. To quantify the pre-eruptive temperature (T) and oxygen fugacity (fO_2) conditions of the different magmas we have compiled mineral chemical data in the context of the aforementioned petrogenesis models of Ewart (1967a,b) and Deering et al. (2008).

An important feature of the Deering et al. (2008) model was that it predicted, as the system evolved, that a temporal variation in the rhyolite compositions would

occur with earlier magmas dominated by a hydrous end-member (R1) and later magmas dominated by an anhydrous end-member (R2). This progression was produced by successive intrusions of basaltic magma into the mid-lower crust (15-30 km) that fractionated under continuous changes in the source conditions and implies that a P-T-fH_2O-fO_2 gradient, which varies with depth, develops in the lower crust.

In this paper, we put the hypotheses of that model to the test by examining the spatial and temporal variations of the relative proportions of R1 and R2 using the mineral content and chemistry of dome lavas and pyroclastic deposits. Based on the proportion of R1 vs. R2 magma types, we divide the last 550 kyrs into 4 distinct magmatic time periods: T1 (550 to 330 ka), T2 (330 to 180 ka), T3 (180 to 30 ka), and T4 (30 ka to present). By comparing these time periods and the magma types across the central TVZ, a pattern has emerged with broadscale (time and space) cycling of wet (R1) to dry (R2) magmatism. Superimposed on top of these time periods and cycles are episodes of volcanism that wax and wane with respect to erupted volumes. It is important to note that in this paper we treat the volcanics as the eruptable portions of the magmatic systems such that relatively quiescent volcanic episodes do not necessarily correlate with subdued magmatism. To evaluate rates of magmatism to a first order, we examine the contribution of slab-derived components (slab sediment fluid/melt: K, Rb, Ce and Pb and slab fluid: Ba, Cl) to the inferred source zone. A strong correlation between Ba/La and FeO*/MgO highlights the importance of the source fH_2O and fO_2 in controlling the melt compositions. Temporal variations in the slab fluid/sediment contributions appear to control the time-dependent relationship between subduction zone processes and the type and volume of magma generated. This is particularly evident in the last 550 kyrs. with different types of magma (i.e. R1 and R2) and their eruptive volumes correlating

closely with variable rates of fluid/sediment being fluxed from the subducting slab beneath the central TVZ.

3.3 REGIONAL TECTONICS AND GEOLOGIC SETTING

The central North Island, New Zealand, tectonic regime is characterized by an oblique (~20º) convergence of the Pacific and Australian plates at ca. 42 mm/yr (DeMets et al., 1994). Accommodation of this convergence is through subduction of the Pacific plate (includes Hikurangi Plateau) along the Hikurangi Margin, coupled with deformation of the overlying Australian Plate. A southward increase in the interseismic coupling at the seismogenic zone indicates a clockwise rotation of the forearc as several discrete tectonic blocks (Reyners, 1998; Wallace et al., 2004). This clockwise rotation of the forearc has governed the rifting of the TVZ arc which has been concentrated in the central portion.

Basement lithologies consist of terranes accreted onto the Gondwana supercontinent during the Mesozoic (Mortimer, 2004). The Torlesse and Waipapa greywacke are the dominant lithologic formations underlying the TVZ. The axial ranges are the actively uplifting regions of the North Island, with the North Island Dextral Fault Belt (Beanland, 1995) cutting obliquely through them. Onshore basins along the Hikurangi forearc, east of the axial ranges, are separated from the offshore accretionary prism (Lewis and Pettinga, 1993) by rapidly uplifting Coastal Ranges (Cashman et al., 1992). The rapid uplift and intense associated erosion has created an efficient mechanism for supplying dominantly Mesozoic Torlesse metasediments to the Hikurangi Trough and Kermadec Trench systems (Carter et al., 1996).

Volcanism in the central TVZ is dominantly rhyolitic and overwhelmingly caldera-forming in terms of erupted volume (Wilson et al., 1995; 2009). Caldera

volcanism has been divided broadly into 3 time periods with a relatively prolonged period of volcanic quiescence between the end of the second period (~680 ka) and beginning of the third period (340 ka; cf. Houghton et al., 1995). More recent field investigations (this study and Gravley et al., in prep) and Ar-Ar age determinations (Leonard et al., in prep) have shown that in fact this perceived gap in caldera volcanism was not totally quiet and included the eruption of an ignimbrite at ~550 ka that had previously been correlated by Nairn (2002; i.e. quartz-biotite ignimbrite) with a much younger group of ignimbrites (the 340 to 320 ka Whakamaru-group; Houghton et al., 1995; Brown et al., 1998). The Whakamaru-group eruptions kicked off the most intensive period of caldera volcanism in the central TVZ, the 340 to 240 ka ignimbrite flare-up (Wilson et al., 2009; Gravley et al., in prep). During the flare-up ~3,000 km^3 of magma erupted, forming most of the modern day geologic footprint (Gravley et al., in prep) that has been subsequently overprinted by tectonic and volcanic events primarily in the last 60 kyrs.

3.4 ANALYTICAL METHODS

Bulk geochemical analyses are from Deering et al. (2008) and references therein. Mineral data was compiled from published works, unpublished theses, and over 1800 additional mineral analyses were obtained for this study. Analyses were performed on a Cameca SX 100 EPMA at the University of Michigan equipped with five wavelength spectrometers using an accelerating potential of 15 kV, a focused beam with a 0 μm spot size, counting time of ~3 min/ mineral, and a 15 nA beam current. Precision and accuracy were tracked using measurements of FTOP, ALBL, PX69 standards for amphibole, orthopyroxene, and biotite and GRSQ, PX69, Cr_2O_3, V_2O_5, ilmenite-magnetite (USNM), BHRH for the oxides.

3.5 RESULTS

For simplification, we will refer to the collection of parameters that are found within the rhyolites in the context of R1 (hydrous) or R2 (anhydrous) as outlined in Table 3.1; these end-members were previously termed EM1 and EM2 by Deering et al. (2008), but we adopt the prefix R here to eliminate any confusion with the well established enriched-mantle (EM) definition. As we are evaluating the magmatic variations on a regional scale this is reasonable; however, we recognize that smaller variations do occur that are of interest on a more localized scale (i.e. within individual caldera complexes), making up the complete spectrum of rhyolites between R1 and R2. In several cases, eruptive units that are compositionally near the mid-point of the spectrum are referred to as R1+2. A more robust evaluation of volcanic eruptions within all of the complexes is beyond the scope of this paper; however, where the variations are statistically significant, an assessment of individual complexes is made.

3.5.1 **Data analysis**

The most effective way to evaluate the temporal/spatial dependency of the geochemical trends of rhyolite from intra- and inter-volcanic complexes is to plot abundances against time-geographic coordinates. However, given the range of rhyodacite to high-silica rhyolite compositions that exist both within a single erupted magma and between more than one erupted magma, this was clearly not feasible. Because the chemical variation within individual eruptive units is large, one way to systematically compare the chemical variation among units with time is to use the mean and standard deviations of the variables (provided that the data are normally distributed). Another way would be to apply the method of Plank and Langmuir

(1988) and Straub (2003), which estimates a specific variable's value based on regression analyses from a given indicator of differentiation (e.g. K_2O at 4% MgO). This method produces a single value, which has been 'corrected' for the crystal fractionation effect. Each method will provide a measure of the 'bulk' arc flux and/or an extrapolated value for comparison among eruptive units.

We analyzed the data using both methods, the results of which are provided in Table 3.2. For the method of 'correction' to an indicator of differentiation, we use K_2O as there is little or no inflection in the trend with increasing SiO_2. The K_2O values used for correction were 3.0 and 3.5 (referred to as: $K_{3.0}$ and $K_{3.5}$), which correspond to distinct average compositions for groups of eruptions and will be discussed in detail in a later section. Although each method has its advantages and disadvantages, the analytical results of each are very similar for all element oxides/parameters evaluated (Table 3.2). We first chose to display the results in the form of mean and confidence intervals (95%) for each eruptive episode for comparing the full range of geochemical variability and the signficance of the differences among parameters.

The dominant range in SiO_2 of TVZ rhyolites falls between a relatively restricted range (73.0 and 76.0 wt. %), but we evaluated the entire dataset of rhyolite for the TVZ to ensure that the subordinate, high-silica rhyolite (> 76.0 wt. % SiO_2) eruptive episodes were not excluded. We consider the comparison of fractionation dependent parameters for these high-silica eruptives with the rest of the TVZ only reasonable in cases where the differences between populations are significant and cannot be explained by simple fractionation.

Before we calculated mean values for each parameter, the normality of each eruptive episode was evaluated. This normality test allows for identification of

spurious outliers or bimodal populations that might influence the comparison among individual eruptive deposits. Outliers are presumed to represent analytical error, sample contamination, or possibly anomalous accessory phase concentrations. Extreme outliers were removed and the mean recalculated on the screened dataset.

A grand mean (average for all data combined) was calculated for each parameter and the units compared to this value as a reference. Results of these statistical analyses are presented in Table 3.2 and illustrated graphically in Figure 2a-f. The significance of the variance among populations is quantified graphically by differences in the spaces between confidence intervals. In other words, the further apart the 95% confidence intervals limits (apexes of the diamonds), the greater the variance among populations. Individual parameters are discussed in detail in the following section.

3.5.2 **End-member characteristics*: FeO*/MgO, Sr, Y, Zr***

In this section, we present compositional characteristics of the major effusive dome-building and explosive volcanic events based on their end-member affinity. The temporal-spatial relationship is hereafter presented in four time segments, which were divided up to reflect overall differences in mineral phase equilibria, in accordance with the end-member divisions of Deering et al. (2008), prior to the geochemical evaluation: T1: 550-330 ka; T2: 330-180 ka; T3: 180-30 ka; T4: 30 ka to present. Eruptions occurring during the T1 time segment [Okataina Caldera Complex (OCC), eastern side of the Kapenga Caldera Complex (KCC), and Whakamaru Caldera Complex (WCC)] are of R1 type lavas and pyroclastics with high Sr and low FeO*/MgO, Zr, and Y (Fig. 3.2a-d). The eruptive activity that follows T1 is dominantly comprised of R2 lavas and pyroclastics from: [Northwestern Dome

Complex (Nwdc), Western Dome Complex (Wdc), Reporoa Caldera (ReC), Rotorua Caldera (RoC), Maroa Dome Complex (Mdc), Ohakuri (OhC), Kapenga Caldera (KaC), Okataina Caldera Complex (OCC), with high Y, FeO*/MgO, Zr, and low Sr (Fig. 3.2a-d). The Pokopoko pyroclastics of the OCC have the lowest FeO*/MgO ratio of any of the R2 eruptions (Fig. 3.2a). Only the Matahina ignimbrite, erupted at 322 ± 7 ka (Leonard et al., in prep) from the OCC, is an R1+2 magma type.

Volcanic activity from 240 ka to present began with a period of relative quiescence until the large caldera-modifying Rotoiti eruption at 61 ka from the OCC. This event was accompanied by a subordinate eruptive event, the Earthquake Flat ignimbrite-forming eruption from the northerneastern-most part of the KCC - both are R1 rhyolite types with high Sr and low Y, Zr, and FeO*/MgO (Fig. 3.2a-d). Interestingly, the Mangaone Subgroup of eruptions that would follow have characteristics of both end-members, displaying a high Sr and low FeO*/MgO, similar to the R1 type and high Zr and Y, similar to the R2 type (Fig. 3.2a-d). Eruptions within the past 30 ka are dominantly R1 and R1+2 type pyroclastics with high Sr and low Y, Zr, and FeO*/MgO (Fig. 3.2a-d). These eruptions include the Rotorua Subgroup (R1) of the OCC and the large, caldera-forming Oruanui eruption (R1+2) from the Taupo Caldera Complex (TCC). A notable exception is the post-Oruanui pyroclastics, which are consistent with R2 type (high Y, Zr, FeO*/MgO and moderate Sr; Table 3.2).

3.5.3 **Ba/La and K_2O**

Statistical analysis of the K_2O content (as a proxy for sediment input from the slab; e.g. Straub, 2003; Tamura et al., 2007) of the rhyolites reveals a clear bimodal distribution of the data (Fig. 3.2e). T1 and T2 magmas contain notably higher K_2O

than those from T3 and T4. Hence, the division by averages between T1-T2 and T3-T4 into $K_{3.5}$ and $K_{3.0}$, respectively, in calculating the 'corrected' values for comparing geochemical parameters (Table 3.2). The K_2O increases slightly from the Rotoiti eruption during T3 to the Mangaone and Rotorua Subgroup of eruptions within T4.

The temporal trends displayed by the Ba/La ratios (as a proxy for slab-derived fluid; e.g. Davidson, 1987; Hawkesworth et al., 1993a, Woodhead et al., 2001; Wade et al., 2006) are highly variable over the studied time period (Fig. 3.2f). Ba/La ratios of eruption products from T1 are higher than those from the T2 period. Following several large-caldera forming eruptions at ca. 240 ka (Mamaku, Ohakuri and Kaingaroa ignimbrites), the Ba/La ratio increases within the OCC during T3-T4 (e.g. Rotoiti, Earthquake Flat, and Mangaone Subgroup pyroclastics). The small trace element dataset available for the Taupo eruptions precludes a rigorous statistical comparison for within the volcanic complex; however, the ratio is less than all other eruptions over T4. Notably, the average Ba/La ratios also correlate well with average FeO*/MgO of the bulk rocks (Fig. 3.3), a key geochemical marker for distinguishing between R1 and R2 magma types, demonstrating a direct relationship between the subduction zone contribution of Ba (slab-derived fluid component) and FeO*/MgO (see discussion below for details). The Mamaku and Pokai ignimbrites fall off the dominant trend (Fig. 3.3), but have lower Ba/La ratios than most R1 magma types.

3.5.4 **Ferromagnesian mineral content and chemistry**

Mineral chemical data were compiled from previous studies and supplemented in this study to further characterize the eruptive products. The ferromagnesian content of the major eruptions and key domes are provided in Table 3.2. Orthopyroxene is ubiquitous among all TVZ rhyolites with less than 75 wt.% SiO_2 and is found in both

R1 and R2 types, ranging from dominant to trace proportions. Histograms (Figure 3.4a,b) illustrate a disparity between the means of the two end-member opx populations: R2 (En_{45}) and R1 (En_{52}). This En relationship, exemplified as FeO*/MgO variance, is inversely correlated with the FeO*/MgO ratio observed in the bulk-rock (Fig. 3.5). Hornblende and biotite are dominantly found in R1 rhyolite types and hornblende have only been reported in the R2 rhyolite type as rare and in trace amounts (i.e. Milner, 2001; Karhunen, 1993; Beresford, 1997). Biotite compositions span a wide range between $Mg\#_{20\text{-}45}$ (Fig. 3.4c). In contrast, hornblende compositions span a narrow range between $Mg\#_{40\text{-}50}$ (Fig. 3.4d). Hornblende Cl contents are positively correlated with bulk-rock Ba/La ratios, whereas F contents show no correlation (Fig. 3.6). In general, the ferromagnesian chemistry broadly reflects the bulk-rock chemistry with respect to the FeO*/MgO; however, the orthopyroxene is the best representative with a much narrower range of compositions found in each eruptive unit. This relationship is consistent with the dominant ferromagnesian mineral populations being, at some stage of the magma evolution, in equilibrium with the melt formed in the source zone and can therefore be used as a proxy for bulk-rock FeO*/MgO contents.

3.5.5 **Pre-eruptive and estimated source intensive parameters**

Carmichael (1967) identified a relationship between the temperature, oxygen fugacity and ferromagnesian silicate phase assemblages of silicic magmas. In quartz-bearing rhyolites, the ferromagnesian assemblages are related to specific oxidation states and can be divided into three groups in order of increasing redox state (Carmichael, 1967): 1) fayalite-bearing, 2) orthopyroxene-bearing, and 3) biotite ±

hornblende ± sphene (no orthopyroxene or olivine). Later, Carmichael (1991) concluded, using the experimentally calibrated relationship between natural silicate liquids and oxygen fugacity and temperature, that the redox state of both basic and acidic magmas was inherited from their sources. A comparison between the fO_2 calculated from Fe-Ti oxide pairs of co-magmatic andesite (parental rock used in Deering et al., 2008) and rhyolite are +1.401 and +1.379 log units (ΔQFM; where QFM is quartz-fayalite-magnetite buffer) respectively, consistent with the Carmichael (1991) conclusions. We, therefore, examine the oxygen fugacity of the end-member types assuming that the rhyolite erupted at the surface closely reflects the redox state of the source zone.

Iron-titanium oxides were analyzed in order to calculate pre-eruptive temperatures and oxygen fugacity. Our Fe-Ti oxide data augment the existing data compiled from previous studies (Table 3.1) and were also used to calibrate the measurements from those studies where available data were insufficient. For internal consistency, we tested for Fe-Ti oxide equilibrium and calculated T-fO_2 for all of the data using the algorithm of Ghiorso and Sack (1991). Oxide pairs were first tested for equilibrium using the Mg/Mn test of Bacon and Hirschmann (1988). Oxygen fugacity is pressure dependent – although only slightly - in geothermometry calculations. Therefore, for consistency, we used 2.5 kbar for all fO_2 calculations - based on average P-estimates of TVZ rhyolites from Smith et al. (2005). The averages of the results are presented in Table 3.2.

Figure 3.7 illustrates the significant difference between the fO_2 of the R1 and R2 rhyolite types. R2 rhyolite types clearly formed under more reducing conditions [$fO_{2avg.}$ = +0.536 log units (ΔQFM)] relative to the R1 rhyolite types [$fO_{2avg.}$ = +1.17 log units (ΔQFM)], regardless of temperature. Oxygen fugacity is positively

correlated with both the orthropyroxene enstatite [En = Mg/(Mg + Fe + Ca)] composition and the bulk-rock Ba/La ratio (Fig. 3.8). The correlation between orthopyroxene Mg content and oxygen fugacity (Fig. 3.8a) is consistent with the amphibolite/meta-basalt melting experiments of Beard and Lofgren (1991), Rapp and Watson (1995), and Sisson et al. (2005), where oxygen fugacity is controlled. The strong positive correlation between the slab-derived fluid indicator (Ba/La ratio) and oxygen fugacity (Fig. 3.8b) suggests that the subducting component is the oxidizing agent involved in the generation of the rhyolites.

Geothermometry calculations on Fe-Ti oxides suggest eruptive temperatures range between 720ºC and 850ºC (Fig. 3.9). We used the glass CaO content of fresh pumice and calculated eruptive temperatures to extrapolate along an experimentally derived liquidus to estimate a 'source' T using the method of Blake et al. (2002) and Wilson et al. (2006). The bulk-rock CaO from the least-evolved (lowest SiO_2 wt.%) rhyolite of each eruption was used to encompass the full range of cooling for each magma body. A considerable disparity exists between the average 'source' T of the R2 rhyolites (938ºC) compared to R1 rhyolites (832ºC). These estimations are broadly consistent with experimentally determined stability fields for the appropriate hydrous (biotite + hornblende) and anhydrous (clinopyroxene + orthopyroxene) phases, at isobaric equilibration temperatures, 800-900°C and 900-1000°C, respectively, in melting of amphibole-bearing mafic rocks (Beard and Lofgren, 1991; Sisson et al., 2005; Parat et al., 2008). In particular, clinopyroxene is only found in the R2 magmas, and hence, indicative of a higher source T affinity.

Christiansen (2005), Christiansen and McCurry (2008), and Bachmann and Bergantz (2008) postulated that rhyolites could be divided into two categories: hot-dry-reducing and cold-wet-oxidizing types. Granites have been similarly

characterized based on Zr and T_{Zr} variations, (e.g. Clemens et al., 1986; Frost and Frost, 1997; King et al., 2001; Miller et al., 2003) and appear analogous to the active rhyolitic systems (Bachmann and Bergantz, 2008). High Zr contents are associated with rhyolites derived from intermediate magmas at high temperatures under zircon undersaturated conditions – despite having become zircon-saturated late in their evolution in the upper crust - whereas low Zr contents are associated with those derived under low temperature zircon saturated conditions. The TVZ R2 magmas have consistently higher Zr than R1 magmas indicating higher source temperatures, as observed in Fig. 3.2c, which is consistent with estimates from extrapolating along experimentally derived liquidi.

3.6 MAGMATIC EVOLUTION IN TIME AND SPACE

Using the results of the Deering et al. (2008) statistical analysis and the establishment of rhyolite end-member compositions, we explore the magmatic relationship between volcanic units sourced from caldera complexes across the central TVZ by integrating crystal content/chemistry and key geochemical parameters (refer to Table 3.1) through time (i.e. T1 through T4). The ages given are eruption ages, unless specified otherwise, and thus represent a minimum age for magmatism.

3.6.1 T1: 550 to 330 ka

Eruptive units, mineral content and chemistry

Mineral content and chemistry of the dome-building and pyroclastic events during this period are characteristic of R1 rhyolite types. The average orthopyroxene composition for all of the eruptions during this period is En_{53}, which reflects the low

FeO*/MgO (calc-alkaline series) bulk rock compositions. However, mineral assemblages vary in hydrous phase abundances and contents as illustrated in Fig. 3.10a.

Several volcanic units found within and north of the Okataina Caldera Complex (OCC) have recently been dated at 550 ka (see Leonard et al., in prep) and include the quartz- and biotite-bearing ignimbrite from Nairn (2002). Because the new age for this ignimbrite removes any volcanic association with the much younger Whakamaru-group ignimbrites, we formalise its new identity by assigning it a name, the Utu ignimbrite. The type section for the Utu ignimbrite is near Mangawhio Stream south of the OCC and Figure 1 shows where the ignimbrite was sampled for this study. A more detailed study is required to confirm the source for this ignimbrite, but Nairn (2002) has suggested an origin within the OCC. Mineralogically, the ferromagnesian phase assemblage (biotite + hornblende + opx) and modal abundance (15-25%) of juvenile pumice clasts from the Utu ignimbrite are similar to other recently dated volcanics including the Whakapoungakau rhyolite dome (531±5 ka), exposed along the margin of the OCC and two plinian-style airfall deposits found near the coast north of the OCC (unit 6: 551±4 ka, and unit 8: 537±5 ka; see Gravley et al., in prep). In addition, immediately overlying unit 8 in the coastal stratigraphy are greater than 40 metres of pumice outwash gravels (some pumice >20cm in diameter and an order of magnitude greater in size than the pumice found in the unit 8 airfall) that are inferred to be the epiclastic equivalent of the Utu ignimbrite (Gravley et al., in prep). Unit 8 is therefore inferred to be the plinian airfall equivalent of the Utu ignimbrite.

The abundance of biotite and the common occurrence of large hornblende in this assemblage distinguish these pyroclastics and associated lavas from eruptions at

other calderas and caldera complexes [i.e. Whakamaru Caldera Complex (WCC), Rotorua Caldera (RoC), Reporoa Caldera (ReC)]. Crystallinity varies from 15-25 vol. %. Dissected dome remnants along the margins of the RoC (450 ka) and ReC (490 ka) (Leonard et al. in prep.) are also crystal-rich, 10-27 vol. %, and have a ferromagnesian assemblage of hornblende + orthopyroxene + biotite (Fig. 3.10a). Although geochemically very similar, the relative abundance and large size of the orthopyroxene in these domes distinguishes them from lavas and pyroclastics from the OCC.

The Whakamaru-group ignimbrites (340 to 320 ka) represent a diverse group of volcanics ranging in crystal content from orthopyroxene + hornblende to orthopyroxene + biotite + hornblende to biotite only assemblages (Fig. 3.10a). However, of note is that whenever present, orthopyroxene is always the dominant ferromagnesian mineral (Brown, 1994). The Paeroa group of ignimbrites, which outcrop along the Paeroa Fault scarp on the eastern side of the Kapenga Caldera Complex (KCC), are the same age as the Whakamaru ignimbrites (Houghton et al., 1995). However, their volcanic source has been suggested to be outside the inferred Whakamaru caldera boundary and may be adjacent to the Paeroa Fault scarp and/or the eastern side of the KCC (cf. Keall 1988; Wilson et al., 1995). Similarities in the ferromagnesian assemblages (orthopyroxene + biotite + hornblende) and their order of abundance are consistent with the Paeroa group ignimbrites being from a similar magmatic origin as the Whakamaru ignimbrites.

Ba/La, fO_2-T, and eruptive volumes

In general, the Ba/La ratio of all of the eruptions is similar with the exception of the Hamurana dome located on the northern side of the RoC (Fig. 3.11a). Estimates of source T average 837ºC with an average fO_2 of +1.33 log units (ΔQFM) (Fig. 11a). Notably, the eruptive temperature and fO_2 are some of the lowest and highest estimates for any of the pyroclastics over the 550 kyrs. of volcanism. If the assigned OCC source for the Utu ignimbrite is correct, it represents a substantial eruptive volume that likely induced caldera collapse (Nairn, 2002). Exposure and thickness of deposits proximal to the caldera margins support volume estimates totaling >90 km^3, as suggested by Nairn, 2002 (Fig. 3.1). Although the volume of OCC-derived fall and flow deposits (Manning, 1996; Nairn, 2002) and their volcanic sources are not well for this time period established because proximal deposits are buried by younger volcanics, minimum estimates exceed 150 km^3 of magma.

Further to the south and punctuating the T1 period, more than 2,000 km^3 magma was erupted predominately as ignimbrite-forming events that led to the collapse of the Whakamaru Caldera Complex (WCC) and heralded the beginning of the 340 to 240 ka ignimrite flare-up (Wilson et al., 1986; Brown et al., 1998; Wilson et al., 2009; Gravley et al., in prep). Together, estimates of the volume of magma erupted during the T1 period certainly exceeds 2200 km^3.

3.6.2 T2: 330 ka to 180 ka

Eruptive units, mineral content and chemistry

In contrast to the eruptions that occurred during the period of 550 to 330 ka, volcanic activity following the Whakamaru group ignimbrite eruptions (340 to 320 ka) is exemplified by R2 magma types (Fig. 3.10b); however magma output was

sustained for most of this period (i.e. the ignimbrite flare-up; Gravley et al, in prep). The first eruptions to occur during this period were dome-building events around the western (Wdc) and northwestern (Nwdc) margins of the WCC and within the central to northern part of the WCC (i.e. the Maroa Dome Complex, Mdc). From drill hole data, Ar-Ar age determinations, and volume calculations, Leonard (2003) estimated that the Whakamaru caldera was 85% filled (predominately from rhyolite dome volcanism) within 35 kyr of the Whakamaru-group ignimbrite eruptions. Mdc rhyolite dome-building and to a lesser extent, explosive pyroclastic eruptions, persisted from ca. 305 to 181 ka (Leonard, 2003) and are exclusively orthopyroxene-bearing until ~181 ka when the first orthopyroxene + hornblende-bearing eruptions occur. The Wdc and Nwdc volcanics are rhyolitic (R1+2/R2 and R2 respectively) and are characterized by orthopyroxene + hornblende mineral abundances with some minor biotite + orthopyroxene + hornblende varieties.

Volcanic activity soon after the Whakamaru-group ignimbrites is also recorded outside of the WCC. Within the OCC, both minor dome building and pyroclastic eruptions culminated in the caldera-forming Matahina eruption (322 ka) which are R1+2 magma types and have a mineral suite similar to the Nwdc volcanic (orthopyroxene + hornblende). Between Okataina and Whakamaru, major caldera-forming eruptions occurred from the KCC (Chimp ignimbrite: 300 to 275 ka and Pokai ignimbrite: 275 ka), RoC (Mamaku: 240 ka), OhC (Ohakuri ignimbrite: 240 ka), and ReC (Kaingaroa ignimbrite: 230 ka). All of these volcanic deposits are characterized by orthopyroxene ± clinopyroxene-bearing rhyodacite-rhyolite magmas. Minor volumes of orthopyroxene + hornblende-bearing rhyolite dome building was occurring within and around the geographic expression of what later became the TCC. In addition to the marked difference in mineral contents of the rhyolites erupted

during this time period, a noticeable change in Mg# of orthopyroxene is apparent (Fig. 3.10b).

Ba/La, fO_2-T, and eruptive volumes

The Ba/La ratio of eruptions during this period is measurably lower than the previous 230 kyrs., with the exception of the 322 ka Matahina eruption from the OCC (Fig. 3.11b). Dome and pyroclastic flow deposits within the Mdc display a progressive decrease in the Ba/La ratio from the centre out to the NW and SE (Fig. 3.11b). Some of the Wdc and Nwdc along the inferred Whakamaru caldera boundary also have high Ba/La ratios (Fig. 3.11b) relative to adjacent domes and active calderas (e.g. OhC and KCC). The Horohoro dome, which outcrops along the SW margin of the KCC (Fig. 3.11b), displays a higher Ba/La ratio than any of the eruptions sourced from this region (e.g. Chimp ignimbrite, Pokai ignimbrite, Pokopoko pyroclastics). Estimates of the source T average 893ºC, with an average fO_2 of +0.625 log units (ΔQFM) for the major caldera-forming ignimbrites (Mamaku, Ohakuri, Kaingaroa, and Pokai), which also display the lowest Ba/La ratios (Fig. 3.11b). The source T and fO_2 of the Matahina ignimbrite are 860ºC and +0.764 log units (ΔQFM), respectively. The four caldera-forming eruptions with the low Ba/La and low fO_2 have a combined total volume approaching 500 km^3, while the single high Ba/La and moderate fO_2 Matahina eruption has a volume > 160 km^3.

3.6.3 T3: 180 to 30 ka

Eruptive units, mineral content and chemistry

Although the tempo of volcanic activity throughout the TVZ decreased considerably, crystal-rich, hydrous (R1) magma types re-emerge at ca. 180 ka in the northern TVZ (Fig. 3.10c). Magmatism is distributed intermittently along the central TVZ, but the dominant type and volume erupted is within the OCC. Dome building in the northern TVZ is hydrous with biotite + hornblende bearing lavas and pyroclastics from the Okataina and Kapenga calderas. Rhyolite domes around the southern margin of the OCC, dated at 188 ka and 96 ka (Leonard et al., in prep), and a small biotite + hornblende + cummingtonite dome to the northeast provide the only evidence of volcanism prior to the orthopyroxene + hornblende + cummingtonite ± biotite-bearing, caldera-forming Rotoiti eruption. The Rotoiti eruption at 61 ka punctuated a period of relative quiescence within the OCC that had probably lasted over 150 kyrs. Eruption of the Earthquake Flat pyroclastics from within the inferred Kapenga Caldera Complex (KCC) margin (Fig. 3.10c) accompanied the Rotoiti eruption, probably within weeks to months (Schmitz and Smith, 2004). Minor dome building within the Maroa Dome Complex (Mdc)/WCC region (Fig. 3.10c) would continue as orthopyroxene-bearing (R2 type) rhyolite early in this time segment until the emergence of hornblende, and later hornblende + biotite bearing, (R1 type) rhyolite lava at 152 ka (Leonard, 2003). Sutton et al. (1995) also documented some of the earliest known orthopyroxene ± hornblende ± fayalite-bearing domes and associated pyroclastics around Lake Taupo, a volcano-tectonic depression formed later primarily during the 26.5 ka Oruanui eruption (Wilson, 2001).

Ba/La, fO_2-T, and eruptive volumes

The dominant activity along the TVZ is focused within the OCC as minor effusive volcanism, which led up to the voluminous (120 km^3) 61 ka caldera-forming Rotoiti eruption (Fig. 3.11c). The Ba/La ratio of this magma and others in the north-central TVZ is relatively high compared to the sparse domes to the south (Fig. 3.11c). Estimates of average source T and fO_2 of the Rotoiti eruption are 885ºC and +1.63 log units (ΔQFM), respectively.

3.6.4 T4: 30 ka to present

Eruptive units, mineral content and chemistry

Volcanic activity during this time period is predominantly focused within the OCC and TCC (Fig. 3.10d). The largest eruption from the TCC during this period was the hornblende + orthopyroxene-bearing, 26.5 ka Oruanui ignimbrite (Sutton et al., 1995; Wilson, 2001). Post-Oruanui (20.5 to 1.8 ka) eruptions (Wilson, 1993; Sutton et al., 1995) are orthopyroxene ± clinopyroxene-bearing dacite-rhyolites. OCC activity continued with the eruption of the Mangaone Subgroup pyroclastics from ca. 45 to 26.5 ka (Wilson et al., 2009), representing a marked difference in mineral content (orthopyroxene + clinopyroxene + hornblende) from the 61 ka Rotoiti (orthopyroxene + hornblende + cummingtonite ± biotite). The Rotorua Subgroup consists of extensive, orthopyroxene + hornblende ± cummingtonite ± biotite-bearing, domes and associated pyroclastics erupted within the OCC beginning at ca. 21 ka and continuing to present (Smith et al., 2005).

Ba/La, fO_2-T, and eruptive volumes

Similar to the previous 150 kyrs., the Ba/La ratio displays a bi-modal distribution of high values in the north and low in the south (Fig. 3.11d). A concommitant decrease in Ba/La and fO_2 in OCC magmas occurs immediately following the Rotoiti eruption (61 ka). Estimated source T and fO_2 of the Old Mangaone (44 to 35 ka) pyroclastics are 950ºC and +1.39 log units (ΔQFM), respectively. The following Young Mangaone and Rotorua Subgroup events display a relatively slight increase in Ba/La, with no change in fO_2; however, the T decreases considerably (815ºC). A similar progression is observed within the TCC, which displays an increasing source T [840ºC to 1060ºC; ~+0.715 log units (ΔQFM)] and decreasing Ba/La. Source T of the rhyolitic eruptions to present day in TCC, following the high T dacite (1060ºC), decreases slightly to 940ºC (Smith et al., 2005). As illustrated by Smith et al. (2005), a distinct contrast in fO_2 exists between the OCC and TCC and was interpreted as representing significant differences in the sources and is shown here to correspond with differences in the Ba/La ratio. The apparent correlation between eruptive volumes and Ba/La ratio between 550 to 180 ka is not found from 180 ka to present – in fact, they are inversely correlated (Fig. 3.11d).

3.7 DISCUSSION

3.7.1 Fluid and sediment contributions to the rhyolite magma source zone

The volatile content of arc volcanics has been recognized as a central variable in the de-volatilization of the subducting slab and cycling of volatile elements within the earth (e.g. Dixon et al., 2002; Hieronymus and Baker (2004). The sub-arc mantle, where primitive arc basalts are generated, is substantially enriched in volatiles

compared with a typical MORB mantle (Fischer and Marty, 2005; Wallace, 2005). These magmas also display enrichments in large ion lithophile elements (LILE) and Pb compared to high field strength elements (HFSE) (Gill, 1981; McCulloch and Gamble, 1991; Hawkesworth et al., 1993a; Miller et al., 1994). Some of these elements are not fractionated significantly during either partial melting or differentiation processes and are, therefore, particularly useful for tracking slab dehydration and/or melting contributions to arc magmas (e.g. Tatsumi et al., 1986; McCulloch and Gamble, 1991; Hawkesworth et al., 1993a; Stopler and Newman, 1994). Other studies (e.g. Plank and Langmuir, 1993; Elliott et al., 1997; Turner et al., 1997) have focused on identifying specific contributions from either oceanic crust or sediment and the process of transport through the upper mantle. In particular, the Ba/La ratio is routinely used to quantify fluid contributions derived from slab dehydration (Davidson, 1987; Hawkesworth et al., 1993a, Woodhead et al., 2001; Wade et al., 2006). However, distinguishing between aqueous fluid and sediment melt contributions can be challenging without knowledge of the subducting sediment composition and P-T conditions at the slab-mantle interface.

Dehydration and melting experiments on subducted sediments by Johnson and Plank (1999) showed that with increasing temperature, Rb and K became incompatible in sediment, which corresponds to mica breakdown at 800 and 900ºC at 2-3 GPa Tamura et al. (2007) effectively utilized this phase instability to demonstrate that the enriched K in the back-arc, at the Torishima volcano, Izu-Bonin, resulted from mica breakdown at greater depths on the slab, which correlates with a greater distance *across* arc.

In contrast, within our study region, Gamble et al. (1996) demonstrated that basalts erupted *along* the Kermadec-Hikurangi margin, from north to south, became

progressively more radiogenic with respect to Pb isotopes, and concluded that K-rich basalts recorded an increase in fluid/sediment flux derived from the slab, not through secondary assimilation. High-alumina basalts and hornblende-bearing gabbroic xenoliths erupted within the central TVZ have similar K contents and Pb isotopes to the aforementioned offshore K-rich basalts (Fig. 3.12). Specifically, Gamble et al. (1996) also highlighted that the transition from oceanic to continental crust did not record a difference in the Sr-Nd isotopes or trace elements (Fig. 3.12). They also concluded that the distinct change in sediment input along the margin is directly related to the back-arc rifting along the TVZ, which is accompanied by rapid uplift of the continental crust to the east. Significant erosion, followed by deposition along the Hikurangi trench, results in subducting sediments that are compositionally and isotopically similar to the bulk of the continental crust (Gamble et al., 1996). Importantly, McCulloch et al. (1994) had also pointed out a significant discrepancy among the radiogenic isotope compositions of rhyolite. While Sr-Nd isotopes could roughly constrain continental crust assimilation between 15-25%, the Pb isotopes model up to 100% assimilation. Therefore, we suggest that this discrepancy can be reconciled by input from sediment prior to additions from the continental crust, and that, where Pb isotopic variations coincide with differences in K_2O, K_2O can be used as a proxy for sediment input.

A positive correlation among K/Hf and Rb/Hf, Pb/Hf, Ba/Hf, Th/Hf illustrates the relationship among slab-derived components (Rb, Pb, Ba, Th) and K (Fig. 3.13). In contrast to the Ba/Hf ratio, the Ba/La ratio displays more scatter compared to K/La, which is interpreted as variable coupling of Ba and other slab-derived components (K, Rb, Pb, Th) (Fig. 3.14a,b). The strong correlation between K/Hf and other slab-flux indicators (Rb/Hf, Pb/Hf, and Th/Hf) supports a collective contribution of K, Rb, Th,

and Pb from a slab-derived sediment component. In summary, the Ba/La ratio appears to be a good indicator of aqueous fluid input, while mobile elements: K, Rb, Th, and Pb are good indicators of subducting sediment contributions.

Study of volatile contents of lavas along the Kermadec Arc and Harve Trough back-arc (offshore of the TVZ) has revealed distinct signatures associated with subduction fluids (Wysoczanski et al., 2006). Flourine contents did not correlate with any subduction indicators, agreeing with trace modeling that shows their concentrations can be explained by partial melting of the depleted mantle (Wysoczanski et al., 2006). Alternatively, Cl concentrations were ten-times elevated over expected depleted mantle values and correlate strongly with trace element indicators of fluid addition to the mantle wedge (e.g. Ba/La). H_2O and some halogens are partitioned towards the vapour phase during magma degassing, which has been observed in many effusive and explosive volcanics (e.g. Montagne Pelèe volcano; Villemant and Boudon, 1999; Soufrière Hills volcano; Villemant et al., 2008), where fluorine remains in the melt, but H_2O and other halogens (Cl, Br, I) become strongly depleted. Therefore, assuming that the parental basalts will transfer their existing fluid-volatile contents, derived from the mantle wedge, during second boiling as crystallization progresses, the Cl contents of derivative melts should record variations in slab-derived flux. Similar to the correlation between fO_2 and the Ba/La ratio, Cl contents of hornblende correlate strongly with Ba/La (Fig. 3.7a). In contrast, F contents show no correlation (Fig. 3.7b), which is consistent with the results of Wysoczanski et al. (2006), where F did not correlate with slab-derived fluid indicators. Importantly, the two post-caldera collapse rhyolites (Onuku and Mangaone), which are more R2-like compared to the caldera forming eruptions that preceded them (Matahina and Rotoiti), have lower Cl contents and fall off the

dominant trend defined by slab-derived fluids. These low Cl contents can, therefore, be explained by degassing of the magma prior to hornblende crystallization in a relatively volatile depleted magma.

3.7.2 Comparing T1+T2 and T3+T4

The continuous production of hydrous, R1 rhyolite melts throughout the entire volcanic zone was initiated ca. 550 ka and continued through ca. 330 ka. High Ba/La and K is consistent with a significant sustained pulse of both fluid and sediment melt released from the subducting slab; the highest observed over the entire 550 kyrs. This intense fluid-sediment fluxing drove extensive melt production in the mantle during this period, providing mass and enthalpy to the source zone and consequently produced > 2250 km^3 of rhyolite magma. These melts were dominantly located along the central rift axis suggesting to us that not only was the fluid flux important in determining the volume of parental melt generated in the mantle wedge, but also fluid and melt were probably initially distributed within crustal segments undergoing the greatest degree of extension at that time. The rhyolite eruptive volume between 550 and 330 ka corresponds with a peak in fluid-sediment release from the slab interface compared to the past 180 kyrs. (Figs. 3.2f and 3.11a).

We postulate that the early volcanism concentrated within the OCC, is not restricted to this region (RoC: 450 ka and ReC: 490 ka dome building; Leonard et al. in prep), and is indicative of a much more extensive, hydrous magmatic flux that extended south along the central rift axis to the southern extent of the WCC. The 550 ka age determined for dome lavas, several plinian-style airfall deposits, and the Utu ignimbrite (Leonard et al., in prep) found within and north of the OCC correlates well with the timing of emplacement of an intrusive diorite (~550 ka) intercepted in the

Ngatamariki geothermal drill-hole towards the southern end of the central TVZ (Arehart et al., 2002) and zircon age spectra from Whakamaru-group pumice that record the assembly of magma over a >200 kyr. period prior to the catastrophic eruptions (Brown and Fletcher, 1999), which totalled more than 2,000 km^3 of magma (Wilson et al., 2009).

Further support for a peak in magmatic flux initiated around 550 ka lies in the lack of significant hydrothermal alteration of the overlying Whakamaru ignimbrite, which lead Arehart et al. (2002) to conclude that the geothermal system associated with emplacement of the Ngatamariki diorite was at a peak from ~550 to before the Whakamaru-group ignimbrites were erupted (340 to 320 ka).

Brown (1994) reported a diverse range of rhyolite groups that ranged from an early more hydrous (biotitite + hornblende bearing) to a later, more anhydrous (orthopyroxene ± hornblende) phase of eruptions. Our interpretation is that the magmatic system recorded recharge into the reservoir(s) that may have begun under more hydrous source conditions than those seen just prior to eruption. This might explain the differences in mineral assemblages within the Type A pumice from the earlier part of the eruption to those in the late stage where hydrous phases become less abundant to absent, reflecting recharge into the system from the source by a comparatively drier rhyolitic magma. The geochemical and mineralogical diversity in the Whakamaru ignimbrites is, thereby, considered in the context of the evolution of the magmatic system to be, not only the product of fractional crystallization as Brown (1994) suggested, but the result of having accumulated over a period of time that probably allowed flux of magmas progressively depleted in volatiles into the subvolcanic magma reservoir prior to eruption, for greater than 200 kyrs.

The geographic distribution of the hot-dry-reducing compared to the cold-wet-oxidizing magmas (Figs. 3.10a,b and 3.11a,b) reflects a more widespread distribution to include several extra-rift calderas (RoC, ReC, OhC). We interpret the overall decrease in Ba/La ratios in these extra-rift magmas erupted from 330 to 180 ka (Fig. 3.11b), to reflect an overall decrease in fluid flux, which results in lower melt production in the mantle and consequently a decrease in the total volume of magma erupted (ca. 600 km^3; Fig. 3.11b). The spatial distribution of the wet to dry magmas in relation to the central rift axis (Fig. 3.11a,b) and the correlation between the rhyolite type generated, Ba/La, and volume support a model for magmatic evolution where more buoyant wet magmas are focused within the zones of greatest extension/transtension that are closer to the central rift axis, followed by more extensive distribution away from the rift axis through time (Figs. 3.10a,b and 3.11a,b). The significant disparity in eruptive volumes between the two periods emphasizes the importance of fluid released from the slab in driving voluminous melting in the mantle. A correlation between type of magma generated, cold-wet-oxidizing vs. hot-dry-reducing, and the total volume of eruptable magma also emphasizes the *direct* influence that slab-derived fluid has on the efficiency of rhyolite melt production in the source zone within the lower crust (15-30 km). Interestingly, the K_2O remains elevated during the dry period of melt production (Fig. 3.2e). Hence, fluid flux may have decreased, but the sediment derived component appears to have remained relatively constant.

This de-coupling of the two subduction zone components may be due to one or any combination of the following: 1) exhaustion of the dehydrating phase within the subducting slab with continued sediment melting; 2) heterogeneities in the thickness of the slab and/or sediment package subducted; 3) rate of dehydration

exceeds the rate of subduction; in effect drying the slab before replenishment of more hydrated slab; 4) variability with depth (P-T conditions) in the phase dehydration-melting reactions. Tamura et al. (2007) suggested differences in K_2O content of basalts from the Torishima Volcano, Izu-Bonin Arc, Japan, were the result of variability in the release of slab-derived components with depth. They postulated that the breakdown of phengite at depths greater than 100 km played a dominant role in producing dry, K_2O rich melts in the mantle wedge, exemplified by distinct differences between fore-arc and back-arc distributions of the magma types. Fluid was released during slab dehydration at depths less than 100 km, while higher P-T conditions at greater depths along the slab surface promoted the breakdown of phengite. Our data is consistent with a change in the fluid-sediment partitioning on the slab surface, but the spatial distribution of the magmas precludes an across arc variation in slab sediment-melting and fluid release. Instead, considering the geologically short time scale, we interpret the time-dependent variation as more likely due to a decrease in dehydration of phases at depths greater than 100 km, with continued sediment melting.

Although minor dome building occurred throughout the Mdc and TCC region following the last caldera-forming eruptions of the 330 to 180 ka period at ca. 240 ka (Fig. 3.10c), volcanism appears to have diminished significantly (est. <10 km^3 magma) and a period of relative quiescence ensued for better than 180 kyrs. Interestingly, zircon crystallization ages of the Earthquake Flat ignimbrite (61 ka), from within the inferred KCC, reflect magma assembly beginning greater than 180 ka (Charlier et al., 2003). Crystallization ages of the concomitant Rotoiti ignimbrite are much younger at 70-90 ka, but also predate the eruption age (61 ka) of the magma (Charlier et al., 2003). Although the overall melt production along the TVZ may have

decreased, hydrous melt production appears to have continued within and around the OCC throughout this period (Fig. 3.10c). The apparent disparity between the subduction components (Earthquake Flat ignimbrite has lower Ba/La ratio and higher Th/Yb, Rb/Yb, and K than the Rotoiti ignimbrite) and zircon model age spectra again demonstrates the time-dependency for flux from the slab-mantle interface. Earthquake Flat ignimbrite appears to have recorded a higher sediment melt input relative to the contemporary Rotoiti ignimbrite, but lower than most pre-240 ka eruptions (Fig. 3.2e), possibly recording the higher sediment melt released from the slab at the termination of the 340 to 240 ka 'ignimbrite flare-up', preceding the steep reduction in sediment input that would follow. Interestingly, there is a slight increase in sediment-derived components observed in the Mangaone pyroclastics through to the current Rotorua Subgroup of eruptions (Fig. 3.2e). We interpret this as a progressive increase in sediment melting at the phengite stability depth. Therefore, the magmatism associated with the Rotoiti eruption marked the inception of a H_2O rich fluid released at shallower depths, as subduction progressed, until a new package of metastable sediment reached the critical stability depth and melting was renewed. This significant increase in K_2O within the OCC from ca. 70 ka to present demonstrates that changes in the composition of the fluid flux released at the slab-mantle interface can occur within geologically short time scales, emphasizing the influence sediment distribution has on melt volume input over differing time scales. This also implies a heterogeneous thickness and/or distribution of the sediment pile on the subducting Hikurangi Plateau/Pacific Plate, because a uniform sediment thickness and/or distribution would presumably continue to provide a constant flux of sediment melt.

Recent volcanic activity along the TVZ (180 ka to present) is dominantly focused at the southern and northern extents of the terrestrial expression of the zone (the OCC and TCC; Fig. 3.10d and 3.11d). The melt-sediment ratio of subduction components is distinctly different between these two centres, and as Smith et al. (2005) demonstrated, there are likewise distinct differences in the rhyolite magma characteristics. The persistence of magmas with higher Ba/La ratios observed in the OCC compared to the TCC indicates that the fluid release from the slab-mantle interface along strike or transport along strike is currently discontinuous (Figs. 3.11d). This is in marked contrast to the early magmatic 'flare-up' period (550 to 330 ka), where the fluid flux appeared to be continuous along the length of the central TVZ (Fig. 3.11a), resulting in sustained amounts of hydrous melt production for >200 kyrs. In addition, lower overall sediment flux (low K) is consistent with a heterogeneous distribution of flux from the subducting slab along the strike of the subduction trench, and also a time-dependent variation in the amount of both fluid and sediment melt fluxed from the slab.

The difference in the total volume of magma erupted between 550 to 240 ka and 240 ka to present is significant (ca. 3500 km^3 compared to ca. 750 km^3), which corresponds to an eruption rate of ca. 10.9 km^3/yr. compared to ca. 3.1 km^3/ yr. While the estimates for the volumes of the more recent eruptions (200 ka to present) are probably fairly representative, the 550 to 200 ka eruptive volumes are undoubtedly underestimated. Poor exposure of many of the ignimbrite deposits (i.e. buried deposits) within this time segment results in conservative and minimum estimates. Consequently, the significant difference between the eruption rates during these periods is likely only a minimum.

Assuming that the ratio of erupted volume/magma production remains constant during a given period, there is a pronounced difference in the volume of silicic magma produced following the extensive, 'cold-wet-oxidizing' eruptions that occur between 550 and 330 ka (T1) and that produced following the 'hot-dry-reducing' eruptions that occur between 330 and 180 ka (T2). In addition, from where the eruptions occurred, it appears as if R1-type magmas were focused along the central rift axis (including the OCC) during T1, whereas the R2-type magmas erupted not only within the same centers as the preceding 'cold-wet-oxidizing' eruptions, but also on the periphery of the inferred rift axis. These observations suggest that the fluid was initially focused along the rift axis, not as a gradation extending directly across the volcanic arc as has been found in other arc settings (e.g. Central America; Patino et al., 2000). However, the magmatic history of the OCC is an exception, as relatively hydrous magma types (R1 or R1+2) have been continually produced here for the entire 550 ka. Although a progression along the rhyolite continuum is apparent from R1 towards R2, the compositions rarely appear as 'hot-dry-reducing' (e.g. orthopyroxene + clinopyroxene assemblages; Figs. 3.10 and 3.11) as those found outside of the OCC. This reflects relative differences in the fluid delivered, and subsequently available to produce rhyolite magmas from the northern to southern TVZ. It is also interesting to note that cummingtonite, a hydrous mineral phase rarely found in volcanic rocks, is exclusive to the OCC within the TVZ.

3.7.3 Length of magma cycles

Our observations, as discussed above, show that a prolonged and widespread *magmatic* 'cycle' has occurred from ~550 to 180 ka, progressing from a cold-wet-oxidizing to hot-dry-reducing magmatic system that encompassed an area greater than

4000 km^2. However, this long term cycle can be superimposed over a piecemeal distribution of magmas that represents a temporal offset in the *volcanic* sequence.

At individual caldera complexes, the length of the magma cycle (as recorded by volcanism) can be much shorter. Immediately following the Whakamaru-group caldera-forming ignimbrite eruptions (R1), the rapid infilling of the WCC (Leonard, 2003) by Mdc lavas of an R2 composition suggests little time elapsed between the transition from R1 to R2 magmatism. Shorter cycles have also occurred more recently within the OCC and TCC (Fig. 3.3f). Shane et al. (2005) and Smith et al. (2005) demonstrated that distinct differences in the fO_2, bulk rock composition, and temperature occurred in eruptions from the TCC and OCC following recent caldera-forming eruptions. For instance, within the OCC, the Rotoiti (R1) eruption at 61 ka is followed by the Mangaone Subgroup (R2) of eruptions (45 to 26 ka), which display a decrease in fO_2, concomitant with an increase in T (Table 3.2; Smith et al., 2005). A similar progression within the TCC, beginning with the eruption of the Okaia Subgroup (R1), displays a progressive decrease in fO_2, with concomitant increase in T through the 26.5 ka, Oruanui ignimbrite (R1+2) to the (R2) dacitic-rhyolitic eruptions that proceed to the present day (Table 2). In both centres the geochemical and mineralogical differences reflect a progression from R1 to R2 magma types. However, these changes are not accompanied by significant changes in Ba/La, and are more likely due to perturbations in the melt column within the crustal section induced by caldera-forming eruptions, similar to that seen in the Long Valley region, USA as proposed by Hildreth (2004), rather than direct changes in the fluid flux from the mantle. The notably lower Cl contents in hornblende from post-caldera volcanic deposits (Fig. 3.7a) is consistent with crystallization within a magma with comparatively lower volatile contents, which does support the inference by Hildreth

(2004) that evacuation of the chamber might induce gas exsolution from untapped depths following the climactic depressurization.

The elapsed time (i.e. 10^3 or 10^4 yrs) between the transition from R1 to R2 magmatism at individual caldera complexes indicates differences in subvolcanic magma residence times and potentially a lag between magma production in the source zone, evolved melt ascent, and subsequent removal into upper crustal reservoirs. Regardless of the temporal offset of the eruptions themselves, the volcanism still reflects magmatic cycles where R1 rhyolites are erupted first followed by R2 rhyolites. The apparent changes in slab contributions, coupled with changes in source conditions, are consistent with the conceptual model proposed by Deering et al. (2008), which was adopted from numerical models similar to Annen et al. (2006) and Dufek and Bergantz (2007).

More recent activity indicates that a regional bimodality of volcanism is occurring (Figs. 3.10d and 3.11d). However, modeling by Heise et al. (2007) using magnetotelluric data interpreted a rapid increase in conductivity below the seismogenic zone at ~10 km depth as interconnected melt within the crust along the entire central TVZ. These results demonstrate that although volcanism is currently focused at the southern and northern extremes of the TVZ, magmatism is ongoing throughout.

3.7.4 Geophysical modeling

Slab-mantle interface and mantle wedge

Recent geophysical studies by Reyners et al. (2006) and Eberhart-Phillips et al. (2008) have provided important insights into the structure of the Hikurangi subduction zone in the central North Island, New Zealand. Reyners et al. (2006)

concluded, based on interpretations of Qp and Vp/Vs inversions, that subduction of the Hikurangi Plateau (ca. 17 km thick) would have the effect of fluxing the subduction zone with twice the amount of fluid relative to normal oceanic crust (10-15 km). In addition, they interpret the lowest Vp (7.4 km s-1) and highest Vp/Vs (1.87) at 65 km depth and beneath the TCC as a region of partial melt/fluid. This melt/fluid diminishes along strike within the mantle wedge from the TCC NE to the OCC and is likely the result of lateral flow induced by the thicker crust at the southernmost extent of the TVZ (Reyners et al., 2006). Consequently, the partial melt is focused beneath the TCC. Eberhart-Phillips et al. (2008) 3-D tomographic imaging also shows a difference in partial melt/fluid depth above the slab beneath the TCC (ca. 140 km) compared to the OCC (ca. 80 km).

These geophysical observations are consistent with three important observations from this study: 1) The excessively high heat (Bibby et al., 1995) and mass flow could explain, in particular, the much greater than global average rhyolite production (greater than 10.9 km^3/yr) during the magmatic 'flare-up', driven by flux melting and focusing along the rift axis, 2) The location of the two largest rhyolitic eruptions over the past 550 kyrs., the 26.5 ka Oruanui ignimbrite (530 km^3) and the 340-320 ka Whakamaru ignimbrite (2000 km^3), were at the southernmost extent of the TVZ at the time of the magma accumulation. Therefore, as the crust progressively thins southward (Villamor et al., 2006), the largest volumes of partial (parental) melt, and hence, rhyolitic magmatism will be focused to the SW termination of the TVZ, and 3) Differences in the slab geometry along the trench to the central rift axis from the OCC (NE) to TCC (SW) corresponds with a greater fluid flux, as indicated by high Ba/La and fO_2 in the OCC compared with the TCC. Slab dehydration and flux mantle melting is, therefore, interpreted to be favored at shallower depths beneath the

OCC, whereas flux melting appears diffuse and is accompanied by sediment melting at greater depths beneath the TCC.

3.8 CONCLUSION

Unraveling the contributions from subduction related slab-derived components to evolved arc magmas is inherently difficult due to the influence of crystal fractionation on element behaviour; however, independently determined parameters for the two end-member rhyolite types from the TVZ (fO_2, Cl, Ba/La) correlate well with the cold-wet-oxidizing and hot-dry-reducing magma types. As a result we are able, with some confidence, to identify a correlation between subducting slab-derived fluid and the types of rhyolite that are generated in a 'hot-zone' within the lower continental crust under the TVZ. Changes in the amounts of these slab-derived components also correlate with broad temporal variations in eruptive volumes (550 to 240 ka compared to 240 ka to present), oxidation states, and Cl contents of hornblende. This demonstrates a direct control of rhyolite petrogenesis by the fluid/sediment flux into the mantle wedge. Spatial variations in the distribution of the magma types indicate to us that heterogeneities probably existed in the subcrustal architecture, which influenced the migration of melt/water relative to the central rift axis. Crust:mantle contributions to the rhyolite compositions may be as high as 25:75 based on Sr-Nd isotope studies of the TVZ rhyolites (McCulloch et al., 1994; Graham et al., 1995), but it appears as if the amount and composition of subduction components released from the slab were dominantly governing the type of rhyolite (cold-wet-oxidizing and hot-dry-reducing) ultimately erupted at the surface over long time periods (>10^5 yrs.).

Evaluation of the magmatic distribution over discrete time periods has resulted in a more comprehensive regional model to be superimposed on the existing petrogenetic model. We have demonstrated that, as predicted by the petrogenetic model of Deering et al. (2008), magmatic cycles exist, where successive intrusion of basaltic sills that crystallize-assimilate-fractionate producing rhyolitic melt record a concomitant progression of compositions that reflect the increase in P-T and decrease in fO_2-H_2O. This 'underaccretion' of intruded sills during periods of high melt production can eventually produce more R2 type 'hot-dry-reducing' magmas and extensive distribution of the magmas away from the central rift axis. Alternatively, significant degassing within the crustal melt column following caldera collapse, exemplified by a decrease in Cl contents of hornblende, may explain temporary perturbations in the fluid available in the source zone.

Regardless of the duration and extent of melt production in the mantle wedge, long period magmatic cycles in the back-arc rifted zone were governed by slab-derived fluid. A gradual drying within the lower crustal 'hot-zone', where rhyolitic magmas are proposed to be generated, produces this continuum of compositions that reflects the change in fluid input. The repetition of this 'cycle' is observed along a spectrum of scales dictated by: 1) the duration and composition of the slab-derived components being fluxed to the crust-mantle interface and 2) perturbations in the volatile contents within the mid-upper crust induced by caldera-collapse. Geochemical and petrological variations among the volcanics in the TVZ, along with geophysical observations, support a model whereby cold-wet-oxidizing (R1) magmas have preceded the eruption of hot-dry-reducing (R2) magmas. Cycles have occurred on shorter time scales and these typically reflect only small changes in end-member compositions and correspond with post-caldera volcanism, while longer cycles

typically reflect a greater degree of change (i.e. drying), consequently producing a greater range of compositions from extreme R1 to R2.

The last 550 kyrs. can be divided into two broad cycles each with wet-oxidizing magmatism followed by dry-reducing magmatism. The first of these cycles occurred from ca. 550 to 180 ka and was directly associated with a laterally extensive and voluminous (> 3,000 km^3) ignimbrite flare-up between ca. 340 and 240 ka (Gravley et al., in prep). The second cycle commenced after the last of the ignimbrite flare-up eruptions at ca. 180 ka and has continued to the present. Thus far there has been ca. 800 km^3 of magma erupted during this magmatic cycle, almost all of which came from three caldera-forming eruptions in the last 61 kyr.

3.9 ACKNOWLEDGEMENTS

Thanks to Kate Pedley, Hugh Bibby, and Martin Reyners for insightful discussions regarding the subduction environment and crustal structure. Ian Nairn is thanked for extensive help with field work and Dean Podolsky for contributions to graphic development. Phil Shane and Victoria Smith are also thanked for providing some of their published data. We also acknowledge the Marsden Fund administered by the Royal Society of New Zealand and the Department of Geological Sciences, University of Canterbury, Mason Trust Fund for financial support. Electron microprobe analysis at the University of Michigan was supported by NSF grant #EAR-9911352.

3.10 REFERENCES

Acocella, V., Spinks, K., and Cole, J. (2003) Oblique back arc rifting of Taupo Volcanic Zone, New Zealand. Tectonics 22: doi:10.1029/2002TC001447.

Anderton, P.W. (1981) Structure and evolution of the South Wanganui Basin, New Zealand. New Zealand Journal of Geology and Geophysics 24: 39-63.

Annen, C., Blundy, J.D., Sparks, R.S.J. (2006) The Genesis of Intermediate and Silicic Magmas in Deep Crustal Hot Zones. Journal of Petrology 47: 505-539.

Arehart, G.B., Christenson, B.W., Wood, C.P., Foland, K.A., Browne, P.R.L. (2002) Timing of volcanic, plutonic and geothermal activity at Ngatamarki, New Zealand. Journal of Volcanology and Geothermal Research 116: 201-214.

Bachmann, O. and Bergantz, G.W. (2008) Rhyolites and their Source Mushes across Tectonic Settings. Journal of Petrology 49: 2277-2285.

Bacon, C.R. and Hirschmann, M.M. (1988) Mg/Mn partitioning as a test for equilibrium between coexisting Fe-Ti oxides. American Mineralogist 73: 57-61.

Beanland, S. (1995) The North Island dextral fault belt, Hikurangi subduction margin, New Zealand. Unpublished PhD thesis, Victoria University of Wellington.

Beard, J.S. and Lofgren, G.E. (1991) Dehydration Melting and Water-Saturated Melting of Basaltic and Andesitic Greenstones and Amphibolites at 1, 3, and 6.9 kb. Journal of Petrology 32: 365-401.

Beresford, S.W. (1997) Volcanology and Geochemistry of the Kaingaroa Ignimbrite, Taupo Volcanic Zone, New Zealand. Unpublished PhD thesis, University of Canterbury Library.

Bibby, H.M. Caldwell, T.G., Davey, F.J., Webb, T.H. (1995) Geophysical evidence of the structure of the Taupo Volcanic Zone and its hydrothermal circulation. Journal of Volcanology and Geothermal Research 68: 29-58.

Blake, S., Sutton, A.N., Wilson, C.J.N., Charlier, B.L.A. (2002) The origin of rhyolite magmas and their 'phenocrysts'. Geochimica et Cosmochimica Acta 66: A81.

Brown, S.J.A. (1994) Geology and geochemistry of the Whakamaru Group ignimbrites, and associated rhyolite domes, Taupo Volcanic Zone, New Zealand. Unpublished PhD thesis, University of Canterbury Library.

Brown, S.J.A., Wilson, C.J.N, Cole, J.W., Wooden, J. (1998) The Whakamaru group ignimbrites, Taupo Volcanic Zone, New Zealand: evidence for reverse tapping of a zoned silicic magmatic system. Journal of Volcanology and Geothermal Research 84: 1-37.

Brown, S.J.A and Fletcher, I.R. (1999) SHRIMP U-Pb dating of the preeruptive growth history of zircons from the 340 ka Whakamaru Ignimbrite, New Zealand: evidence for >250 k.y. magma residence times. Geology (Boulder) 27: 1035-1038.

Carmichael, I.S.E. (1967) The iron-titanium oxides of salic volcanic rocks and their associated ferromagnesian silicates. Contributions to Mineralogy and Petrology 14: 36-64.

Carmichael, I.S.E. (1991) The redox states of basic and silicic magmas: a reflection of their source regions? Contributions to Mineralogy and Petrology 106: 129-141.

Carter, L., Carter, R.M., McCave, I.N., Gamble, J.A. (1996) Regional sediment recycling in the abyssal S.W. Pacific Ocean. Geology 24: 735-738.

Cashman, S.M., Kelsey, H.M., Erdman, C.F., Cutten, H., Berryman, K.R. (1992) Strain partitioning between structural domains in the forearc of the Hikurangi subduction zone, New Zealand. Tectonics 11: 242-257.

Charlier, B.L.A., Peate, D.W., Wilson, C.J.N., Lowenstern, J.B., Storey, M., Brown, S.J.A. (2003) Crystallization ages in coeval silicic magma bodies: 238U-230Th disequilibrium evidence from the Rotoiti and Earthquake Flat eruption deposits, Taupo Volcanic Zone, New Zealand. Earth and Planetary Science Letters 206: 441-457.

Christiansen, E.H. (2005) Contrasting processes in silicic magma chambers: evidence from very large volume ignimbrites. Geological Magazine 142: 669-681.

Christiansen, E.H. and McCurry, M. (2008) Contrasting origins of Cenozoic silicic volcanic rocks from the western Cordillera of the United States. Bulletin of Volcanology 70: 251-267.

Clemens, J.D., Holloway, J.R., White, A.J.R. (1986) Origin of an A-type granite; experimental constraints. American Mineralogist 71: 317-324.

Davidson, J.P. (1987) Crustal contamination versus subduction zone enrichment: examples from the Lesser Antilles and implications for mantle source compositions of island arc volcanic rocks. Geochimica et Cosmochimica Acta 51: 2185-2198.

Deering, C.D., Cole, J.W., Vogel, T.A. (2008) A Rhyolite Compositional Continuum Governed by Lower Crustal Source Conditions in the Taupo Volcanic Zone, New Zealand. Journal of Petrology 49: 2245-2276.

DeMets, C., Gordon, R.G., Argus, D.F., Stein, S. (1994) Effect of recent revision to the geomagnetic reveral time scale on estimates of current plate motions. Geophysical Research Letters 21: 2191-2194.

Dufek, J. and Bergantz, G.W. (2005) Lower Crustal Magma Genesis and Preservation: a Stochastic Framework for the Evaluation of Basalt-Crust Interaction. Journal of Petrology 46: 2167-2195.

Eberhart-Phillips, D., Reyners, M., Chadwick, M., Stuart, G. (2008) Three-dimensional attenuation structure of the Hikurangi subduction zone in the central North Island, New Zealand. Geophysical Journal International 174: 418-434.

Elliott, T., Plank, T., Zindler, A., White, W., Bourdon, B. (1997) Element transport from slab to volcanic front at the Mariana Arc. Journal of Geophysical Research 102: 14,991-15,019.

Ewart. A. (1967a) The Petrography of the Central North Island Rhyolitic Lavas: Part 1-Correlations between the phenocryst assemblages. New Zealand Journal of Geology and Geophysics 10: 182-197.

Ewart. A. (1967b) The Petrography of the Central North Island Rhyolitic Lavas: Part 2-Regional petrography including notes on associated ash-flow pumice deposits. New Zealand Journal of Geology and Geophysics 11: 478-545.

Frost, C.D. and Frost, B.R. (1997) Reduced rapakivi granites; the tholeiite connection. Geology 25: 647-650.

Gamble, J.A., Smith, I.E.M., McCulloch, M.T., Graham, I.J., Kokelaar, B.P. (1993) The geochemistry and petrogenesis of basalts from the Taupo Volcanic Zone and Kermadec Island Arc, S.W. Pacific. Journal of Volcanology and Geothermal Research 54: 265-290.

Gamble, J., Woodhead, J., Wright, I., Smith, I. (1996) Basalt and Sediment Geochemistry and Magma Petrogenesis in a Transect from Oceanic Island Arc to Rifted Continental Margin Arc: the Kermadec-Hikurangi Margin, SW Pacific. Journal of Petrology 37: 1523-1546.

Ghiorso, M.S. and Sack, R.O. (1991) Fe-Ti oxide geothermometry: thermodynamic formaulation and estimation of intensive variables in silicic magmas. Contributions to Mineralogy and Petrology 108: 485-510.

Gill, J.B. (1981) Orogenic Andesites and Plate Tectonics. Springer, New York, pg. 390.

Graham, I.J., Gulson, B., Hedenquist, J.W., Mizon, K. (1992) Petrogenesis of Late Cenozoic rocks from the Taupo Volcanic Zone, New Zealand; in the light of new Pb isotopic data. Geochimica et Cosmochimica Acta 56: 2797-2819.

Gravley, D.M., Wilson, C.J.N., Rowland, J.V., Leonard, G.S. (in prep) What is an ignimbrite flare-up? New insight from the hyperactive central Taupo Volcanic Zone, New Zealand.

Harrison, A.J. and White, R.S. (2004) Crustal structure of the Taupo Volcanic Zone, New Zealand; stretching and igneous intrusion. Geophysical Research Letters 31: 1-4.

Hawkesworth, C.J., Gallagher, K., Hergt, J.M., McDermott, F. (1993a) Mantle and slab contributions in arc magmas, Annual Reviews in Earth and Planetary Sciences 21: 175-204.

Healy, J. (1962) Structure and volcanism in the Taupo volcanic zone, New Zealand. Geophysical Monograph 6: 151-157.

Heise, W., Bibby, H.M., Grant, C.T., Bannister, S.C., Ogawa, Y., Takakura, S., Uchida, T. (2007) Melt distribution beneath a young continental rift; the Taupo Volcanic Zone, New Zealand. Geophysical Research Letters 34: 28.

Hildreth, W. (2004) Volcanological perspectives on Long Valley, Mammoth Mountain, and Mono Craters: several contiguous but discrete systems. Journal of Volcanology and Geothermal Research 136: 169-198.

Houghton, B.F. and Wilson, C.J.N. (1995) Volcanic and structural evolution of central Taupo volcanic zone, New Zealand. Australasian Institute of Mining and Metallurgy 9/95: 291-296.

Johnson, M.C. and Plank, T. (1999) Dehydration and melting experiments constrain the fate of subducted sediments. Geochemistry, Geophysics, Geosystems, 1, paper number 1999GC000014.

Jurado-Chichay, Z. and Walker, G.P.L. (2000) Stratigraphy and dispersal of the Mangaone Subgroup pyroclastic deposit, Okataina Volcanic Centre, New Zealand. Journal of Volcanology and Geothermal Research 104: 319-383.

Karhunen, R.A. (1993) The Pokai and Chimp Ignimbrites of NW Taupo Volcanic Zone. Unpublished PhD thesis, University of Canterbury Library.

Keall, J.M. (1988) Volcanology and Ignimbrite Stratigraphy along the Paeroa Fault, Taupo Volcanic Zone. Unpublished MSc thesis, Victoria University of Wellington.

King, P.L., Chappell, B.W., Allen, C.M., White, A.J.R. (2001) Are A-type granites the high-temperature felsic granites? Evidence from fractionated granites of the Wangrah Suite. Australian Journal of Earth Sciences 48: 501-514.

Leonard, G.S. (2003) The evolution of Maroa Volcanic Centre, Taupo Volcanic Zone, New Zealand. Unpublished PhD thesis, University of Canterbury Library.

Leonard, G.S., Calvert, A.T., Wilson, C.J.N., Gravley, D.M., Deering, C.D., (in prep) Taupo Volcanic Zone $^{40}Ar/^{39}Ar$ geochronology illuminates 550 ka volcanism at Okataina Volcanic Centre, coastal uplift and sea level fluctuations.

Lewis, K.B. and Pettinga, J.R. (1993) The emerging, imbricate frontal wedge of the Hikurangi Margin. Sedimentary Basins of the World 2, ed. Balance, P.F., Elsevier, Amsterdam, 225-250.

McCulloch, M.T. and Gamble, J.A. (1991) Geochemical and geodynamical constraints on subduction zone magmatism. Earth and Planetary Science Letters 102: 358-374.

McCulloch, M.T., Kyser, T.K. Woodhead, J.D., Kinsley, L. (1994) Pb-Sr-Nd-O isotopic constraints on the origin of rhyolites from the Taupo volcanic zone of New Zealand; evidence for assimilation followed by fractionation from basalt. Contributions to Mineralogy and Petrology 115: 303-312.

Miller, D.M., Goldstein, S.L., Langmuir, C.H. (1994) Cerium/lead and lead isotope ratios in arc magmas and the enrichment of lead in the continents. Nature 368: 514-520.

Miller, C.F., Meschter McDowell, S., Mapes, R.W. (2003) Hot and cold granites? Implications of zircon saturation temperatures and preservation of inheritance. Geology 31: 529-532.

Milner, D.M., Cole, J.W., Wood, C.P. (2001) Mamaku Ignimbrite: a caldera-forming ignimbrite erupted from a compositionally zoned magma chamber in Taupo Volcanic Zone, New Zealand. Journal of Volcanology Geothermal Research 122: 243-264.

Mortimer, N. (2004) New Zealand's geological foundations. Gondwana Research 7: 261-272.

Nairn, I. A. (2002) Geology of the Okataina Volcanic Centre, scale 1:50,000. Institute of Geological and Nuclear Sciences geological map, 25. 1 sheet + 156 p.: Lower Hutt, New Zealand, Institute of Geological and Nuclear Sciences Limited.

Nairn, I.A., Shane, P.R., Cole, J.W., Leonard, G.J., Self, S. and Pearson, N. (2004) Rhyolite magma processes of the ~AD 1315 Kaharoa eruption episode, Tarawera volcano, New Zealand. Journal of Volcanology and Geothermal Research 131: 265-294.

Parat, F., Holtz, F., Feig, S. (2008) Pre-eruptive Conditions of the Huerto Andesite (Fish Canyon System, San Juan Volcanic Field, Colorado): Influence of Volatiles (C-O-H-S) on Phase Equilibria and Mineral Composition. Journal of Petrology 49: 911-935.

Patino, L.C., Carr, M.J., Feigenson, M.D. (2000) Local and regional variations in Central American arc lavas controlled by variations in subducted sediment input. Contributions to Mineralogy and Petrology 138: 265-283.

Plank, T. and Langmuir, C.H. (1988) An evaluation of global variation in the major element chemistry of arc basalts. Earth and Planetary Science Letters 90: 349-370.

Plank, T. and Langmuir, C.H. (1993) Tracing trace elements from sediment input to volcanic output at subduction zones. Nature 362: 739-742.

Rapp, R.P. and Watson, E.B. (1995): Dehydration melting of metabasalt at 8-32kbar—implications for continental growth and crust-mantle recycling. Journal of Petrology 36: 891-931.

Reyners, M. (1998) Plate coupling and the hazard of large subduction thrust earthquakes at the Hikurangi subduction zone, new Zealand. New Zealand Journal of Geology and Geophysics 41: 343-354.

Reyners, M. Eberhart-Phillips, D., Stuart, G. Nishimura, Y. (2006) Imaging subduction from the trench to 300 km depth beneath the central North Island, New Zealand, with Vp and Vp/Vs. Geophysical Journal International 165: 565-583.

Schmitz, M.D. and Smith, I.E.M. (2004) The Petrology of the Rotoiti Eruption Sequence, Taupo Volcanic Zone: an Example of Fractionation and Mixing in a Rhyolitic System. Journal of Petrology 45: 2045-2066.

Shane, P., Smith, V.C., Nairn, I.A. (2005) High temperature rhyodacites of the 36 ka Hauparu pyroclastic eruption, Okataina volcanic centre, New Zealand; change in a silicic magmatic system following caldera collapse. Journal of Volcanology and Geothermal Research 147: 357-376.

Smith, V.C., Shane, P., Nairn, I.A. (2005) Trends in rhyolite geochemistry, mineralogy, and magma storage during the last 50 kyr at Okataina and Taupo volcanic centres, Taupo Volcanic Zone, New Zealand. Journal of Volcanology and Geothermal Research 148: 372-406.

Sisson, T.W., Ratajeski, K., Hankins, W.B., Glazner, A.F. (2005) Voluminous granitic magmas from common basaltic sources. Contributions to Mineral Petrology 148: 635-661.

Stopler, E. and Newman, S. (1994) The role of water in the petrogenesis of Mariana trough magmas. Earth and Planetary Science Letters 121: 293-325.

Straub, S.M. (2003) The evolution of the Izu Bonin – Mariana volcanic arcs (NW Pacific) in terms of major element chemistry. Geochemistry, Geophysics, Geosystems 4, no. 2, 19 February 2003, 1018, doi: 10.1029/2002GC000357.

Sutton, A.N., Blake, S., Wilson, C.J.N. (1995) An outline geochemistry of rhyolite eruptives from Taupo volcanic centre, New Zealand. Journal of Volcanology and Geoethermal Research 68: 153-175.

Tamura, Y., Tani, K., Chang, Q., Shukuno, H., Kawabata, H., Ishizuka, O., Fiske, R.S. (2007) Wet and Dry Basalt Magma Evolution at Torishima Volcano, Izu-Bonin Arc, Japan: the Possible Role of Phengite in the Downgoing Slab. Journal of Petrology 48: 1999-2031.

Tatsumi, Y., Hamilton, D.L., Nesbitt, R.W. (1986) Chemical characteristics of fluid phase released from a subducted lithosphere and origin of arc magmas: Evidence from high-pressure experiments and natural rocks. Journal of Volcanology and Geothermal Research 29: 293-309.

Turner, S.P., Hawkesworth, C.J, Rogers, N., Bartlett, J., Worthington, T., Hergt, J., Pearce, J., Smith, I. (1997) $^{238}U/^{230}Th$ disequilibria, magma petrogenesis, and flux rates beneath the depleted Tonga-Kermadec island arc. Geochimica et Cosmochimica Acta 61: 4855-4884.

Tuttle. O.F. and Bowen N.L. (1958) Origin of granite in the light of experimental studies in the system $NaAlSi_3O_8$-$KAlSi_3O_8$-SiO_2-H_2O. Geological Society of America Mem 74: 11.

Villamor, P. and Berryman, K. (2006) Evolution of the southern termination of the Taupo Rift, New Zealand. New Zealand Journal of Geology and Geophysics 49: 23-37.

Villemant, B. and Boudon, G. (1999) H_2O and halogen (F, Cl, Br) behaviour during shallow magma degassing processes. Earth and Planetary Science Letters 168: 271-286.

Villemant, B., Mouatt, J., Michel, A. (2008) Andesitic magma degassing investigated through H2O vapour-melt partitioning of halogens at Soufrière Hills Volcano, Montserrat (Lesser Antilles). Earth and Planetary Science Letters 269: 212-229.

Wade, J. A.,Plank, T.Melson, W. G.Soto, G. J., Hauri, E. H. (2006) The volatile content of magmas from Arenal Volcano, Costa Rica. Journal of Volcanology and Geothermal Research 157: 94-120.

Wallace, L., Beavan, J., McCaffrey, R., Darby, D. (2004) Subduction zone coupling and tectonic block rotations in the North Island, New Zealand. Journal of Geophysical Research 109: B12406, doi: 10.1029/2004JB003241.

Wilson, C.J.N. (1993). Stratigraphy, chronology, styles and dynamics of late Quaternary eruptions from Taupo volcano, New Zealand. Philosophical Transactions of the Royal Society of London 343: 205-306.

Wilson, C.J.N. (2001). The 26.5 ka Oruanui eruption, New Zealand: an introduction and overview. Journal of Volcanology and Geothermal Research 112: 133-174.

Wilson, C.J.N., Blake, S., Charlier, B.L.A. Sutton, A.N. (2006) The 26.5 ka Oruanui Eruption, Taupo Volcano, New Zealand: Development, Characteristics and Evacuation of a Large Rhyolitic Magma Body. Journal of Petrology 47: 35-69.

Wilson, C.J.N., Gravley, D.M., Leonard, G.S., Rowland, J.V. (2009). Volcanism in the central Taupo Volcanic Zone, New Zealand: tempo, styles and controls. Geological Society of London Special Publication: Studies in Volcanology: *The Legacy of George Walker*.

Wilson, C.J.N., Houghton, B.F., and Lloyd, E.F. (1986) Volcanic history and evolution of the Maroa-Taupo area, central North Island. In: I.E.M. Smith (Editor), Late Cenozoic Volcanism in New Zealand. Royal Society of New Zealand Bulletin 23: 194-223.

Wilson, C.J.N., Houghton, B.F., McWilliams, M.O., Lanphere, M.A., Weaver, S.D., Briggs, R.M. (1995) Volcanic and structural evolution of Taupo Volcanic Zone, New Zealand: a review. Journal of Volcanology and Geothermal Research 68: 1-28.

Wilson, C.J.N., Rogan, A.M., Smith, I.E.M., Northey, D.J., Nairn, I.A., Houghton, B.F. (1984). Caldera volcanoes of the Taupo volcanic zone, New Zealand. Journal of Geophysical Research 89: 8463-8484.

Woodhead, J.D, Hergt, J.M., Davidson, J.P., Eggins, S.M. (2001) Earth and Planetary Science Letters 192: 331-346.

Wysoczanski, R.J., Wright, I.C., Gamble, J.A., Hauri, E.H., Luhr, J.F, Eggins, S.M., Handler, M.R. (2006) Volatile contents of Kermadec Arc-Havre Trough pillow glasses: Fingerprinting slab-derived aqueous fluids in the mantle sources of arc and back-arc lavas. Journal of Volcanology and Geothermal Research 152: 51-73.

3.11 FIGURES

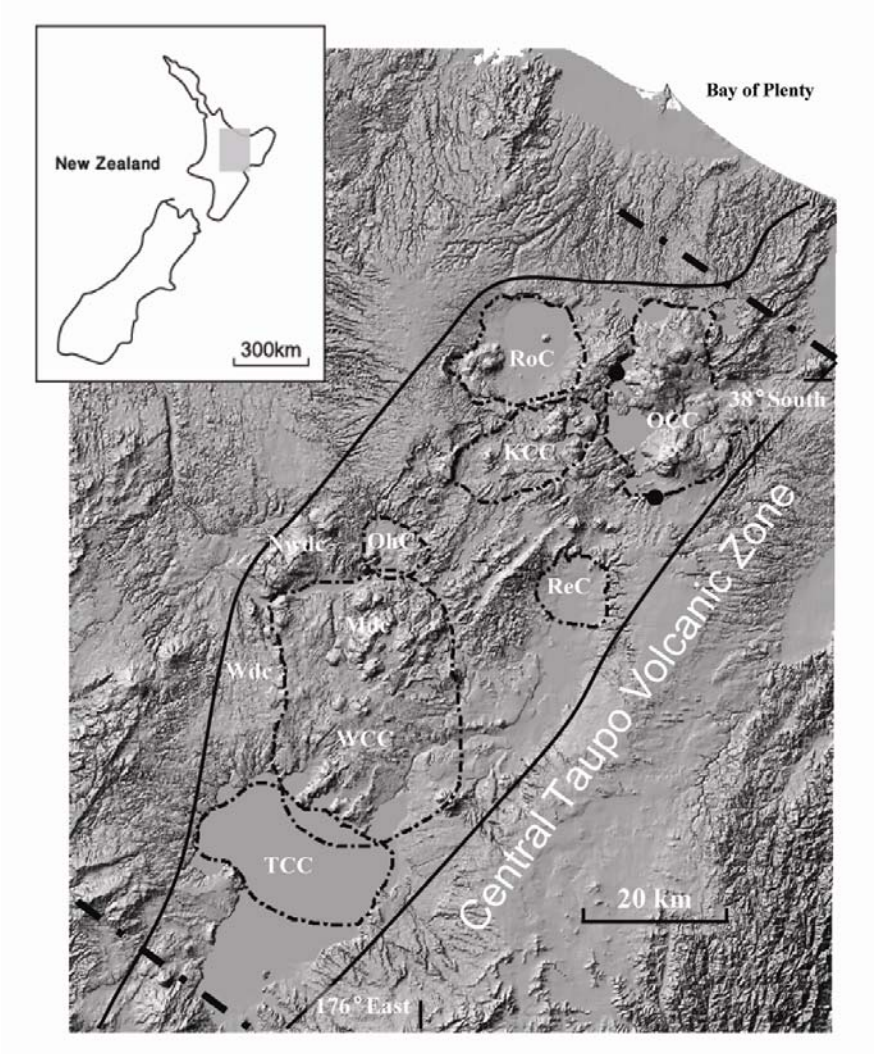

Fig. 3.1. Topographical/structural map showing the Taupo Volcanic Zone (TVZ) in the North Island, New Zealand. Inferred caldera boundaries are outlined in bold dashed lines. Large filled circles are field sampling localities discussed in the text.

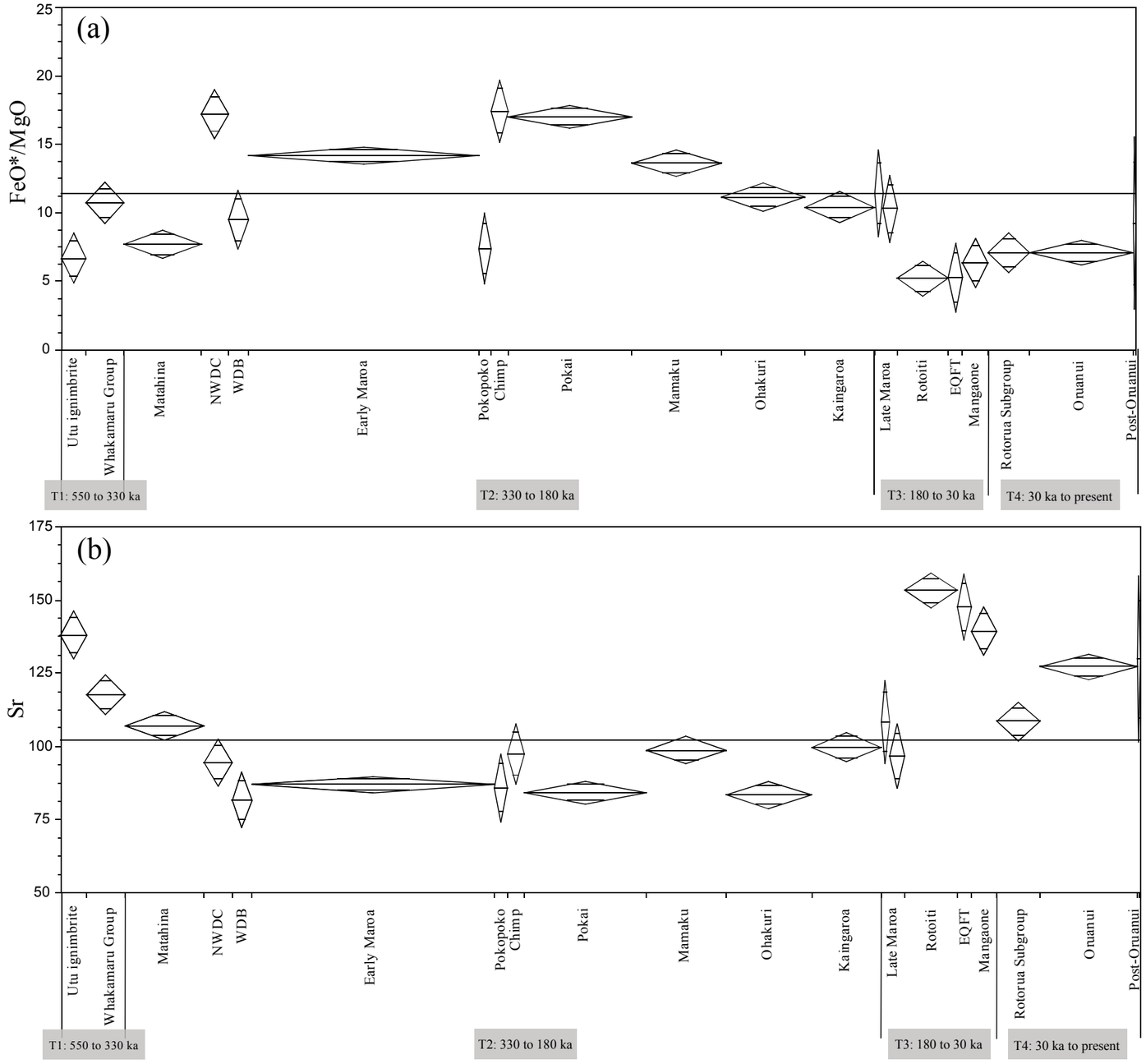

Fig. 3.2. Plot of mean (with 95% confidence intervals) for select geochemical parameters. (a-d) Key end-member geochemical parameters (FeO*/MgO, Sr, Zr, and Y) that are used to characterize representative rhyolite pyroclastics. (e-f) Geochemical parameters indicative of slab-derived fluid (Ba/La) and sediment input (K_2O). The solid horizontal line represents a grand mean, which is equal to the mean of all TVZ rhyolitic eruptive products. Diamond width is proportional to the number of samples and height indicates the 95% confidence interval.

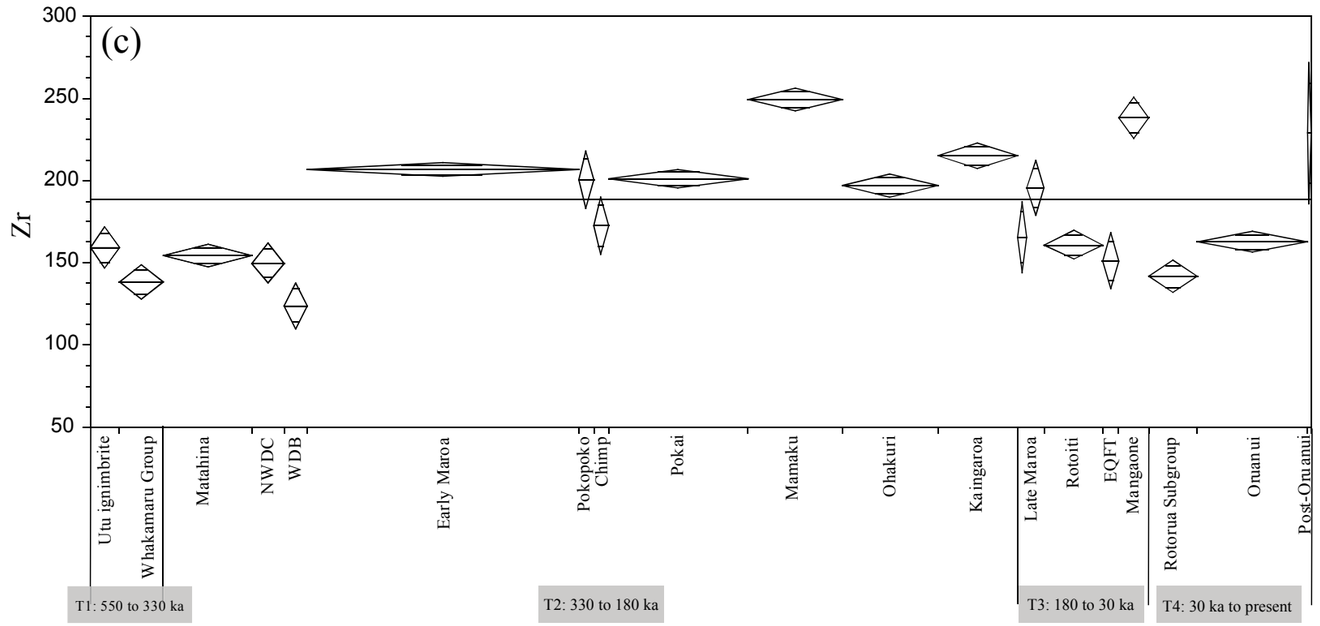
(c)
Zr
300
250
200
150
100
50
Utu ignimbrite
Whakamaru Group
Matahina
NWDC
WDB
Early Maroa
Pokopoko
Chimp
Pokai
Mamaku
Ohakuri
Kaingaroa
Late Maroa
Rotoiti
EQFT
Mangaone
Rotorua Subgroup
Onuanui
Post-Oruanui
T1: 550 to 330 ka
T2: 330 to 180 ka
T3: 180 to 30 ka
T4: 30 ka to present
(d)
Y
40
35
30
25
20
15
10
Utu ignimbrite
Whakamaru Group
Matahina
NWDC
WDB
Early Maroa
Pokopoko
Chimp
Pokai
Mamaku
Ohakuri
Kaingaroa
Late Maroa
Rotoiti
EQFT
Mangaone
Rotorua Subgroup
Onuanui
Post-Oruanui
T1: 550 to 330 ka
T2: 330 to 180 ka
T3: 180 to 30 ka
T4: 30 ka to present

Fig. 3.2 cont.

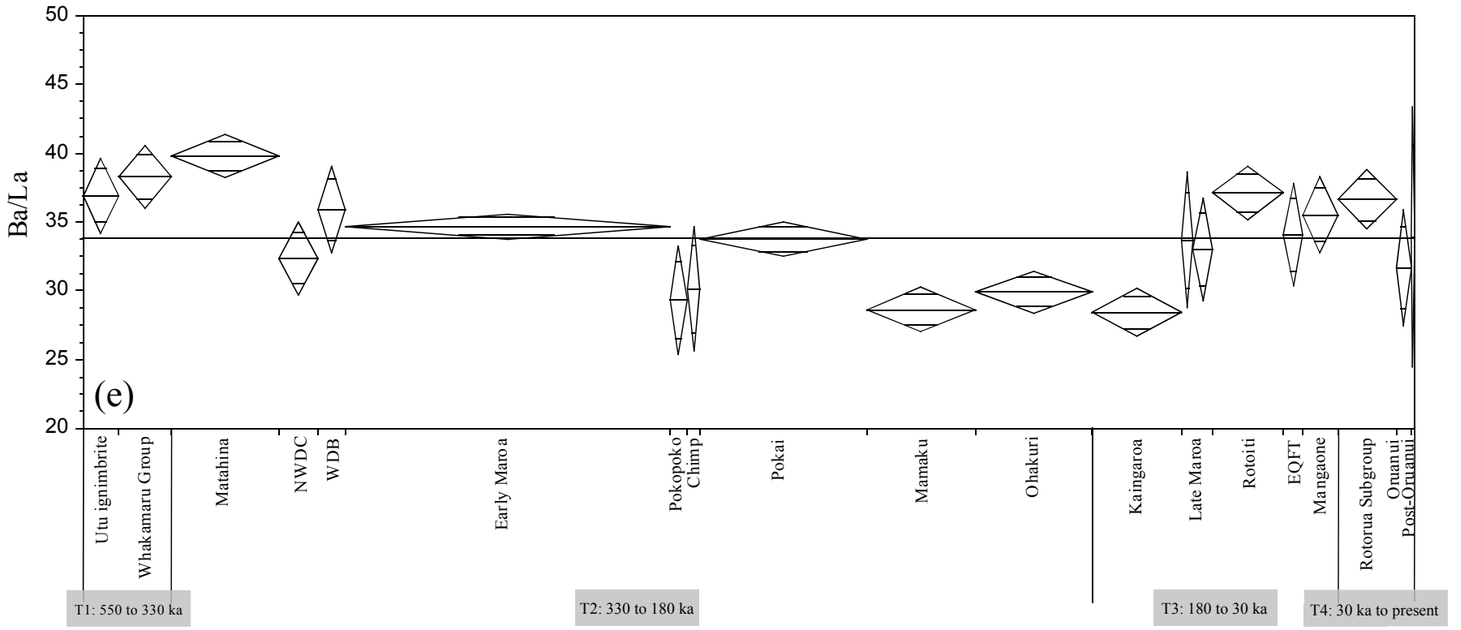
Ba/La
50
45
40
35
30
25
20
(e)
Utu ignimbrite
Whakamaru Group
Matahina
NWDC
WDB
Early Maroa
Pokopoko Chimp
Pokai
Mamaku
Ohakuri
Kaingaroa
Late Maroa
Rotoiti
EQFT
Mangaone
Rotorua Subgroup
Onuanui
Post-Onuanui
T1: 550 to 330 ka
T2: 330 to 180 ka
T3: 180 to 30 ka
T4: 30 ka to present
K2O
4
3.5
3
2.5
2
(f)
Utu ignimbrite
Whakamaru Group
Matahina
NWDC
WDB
Early Maroa
Pokopoko Chimp
Pokai
Mamaku
Ohakuri
Kaingaroa
Late Maroa
Rotoiti
EQFT
Mangaone
Rotorua Subgroup
Onuanui
Post-Onuanui
T1: 550 to 330 ka
T2: 330 to 180 ka
T3: 180 to 30 ka
T4: 30 ka to present

Fig. 3.2 cont.

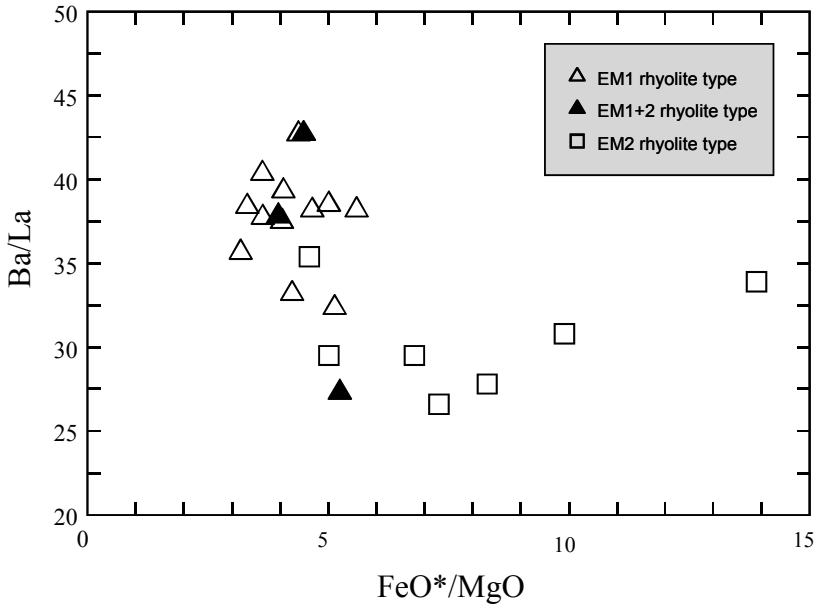

Fig. 3.3. Mean bulk-rock Ba/La vs. FeO*/MgO, representing EM compositions from EM1 to EM2.

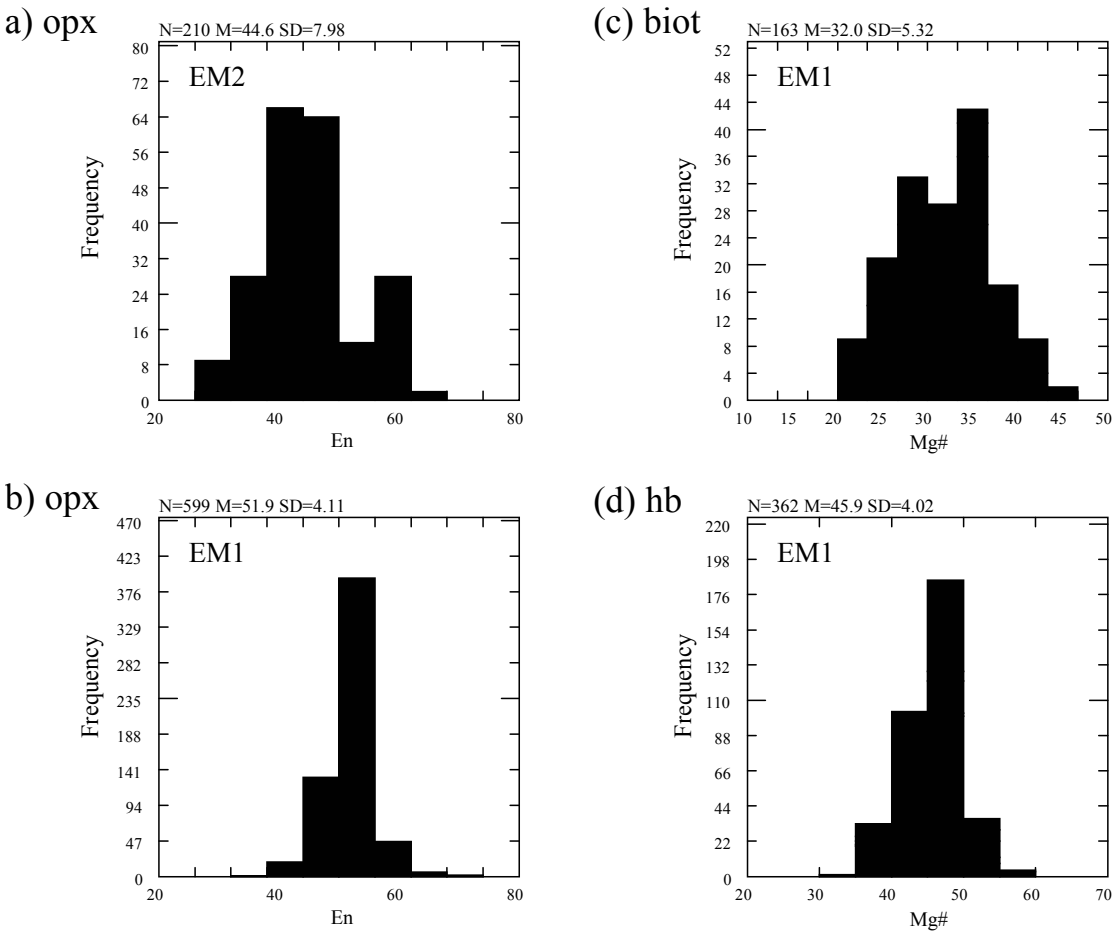

Fig. 3.4. Histograms of Mg# (Mg/Mg+Fe) for ferromagnesian minerals of EM magmas. (a) and (b) illustrate the disparity between EM1 and EM2 orthopyroxene (opx) compositions, means = 51.9 and 44.6, respectively. (c) Biotite (biot) display a wide range of compositions, but are only found in EM1 magma types. (d) Hornblende (hb) compositions range between Mg# 35 to 65, but are predominantly between Mg# 40 and 50.

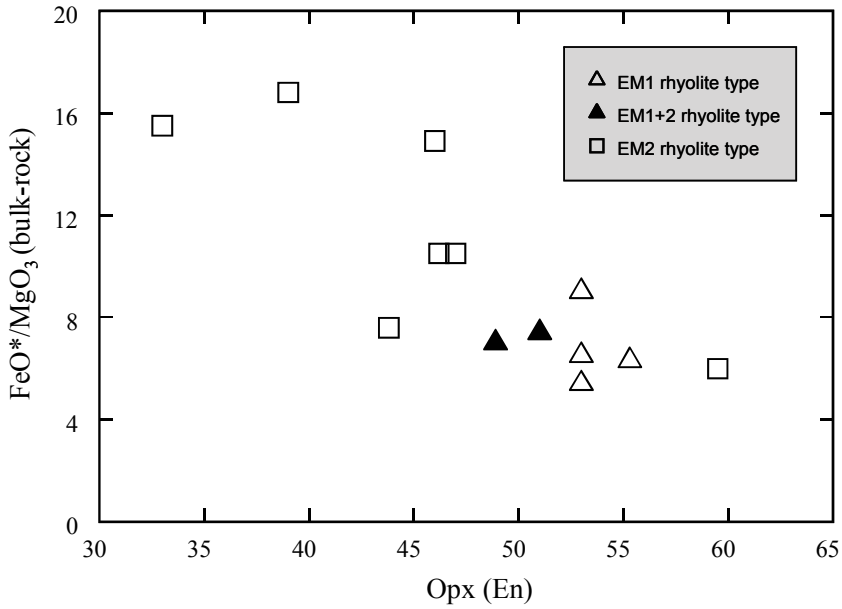

Fig. 3.5. FeO*/MgO_3 (= bulk-rock $K_{3.0\_3.5}$ corrected) vs. mean orthopyroxene (opx) enstatite compositions representing the range of EM compositions.

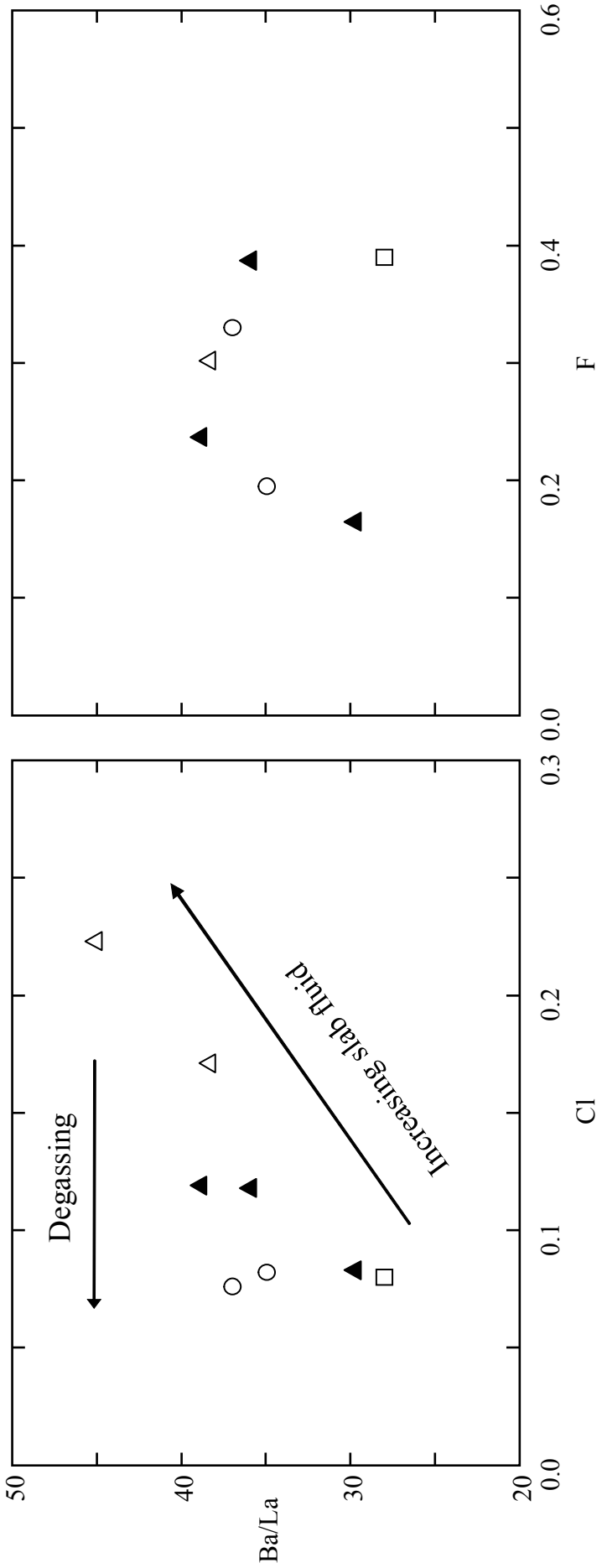

Fig. 3.6. a) Correlation between slab-derived fluid indicator and Cl in hornblende phenocrysts and b) no correlation between slab-derived fluid indicator and F in hornblende phenocrysts (given as averages from eight separate eruptions). Open boxes are hot-dry-reducing, closed triangles are intermediate, open triangles are cold-wet-oxidizing, and open circles are post-caldera collapse eruptions.

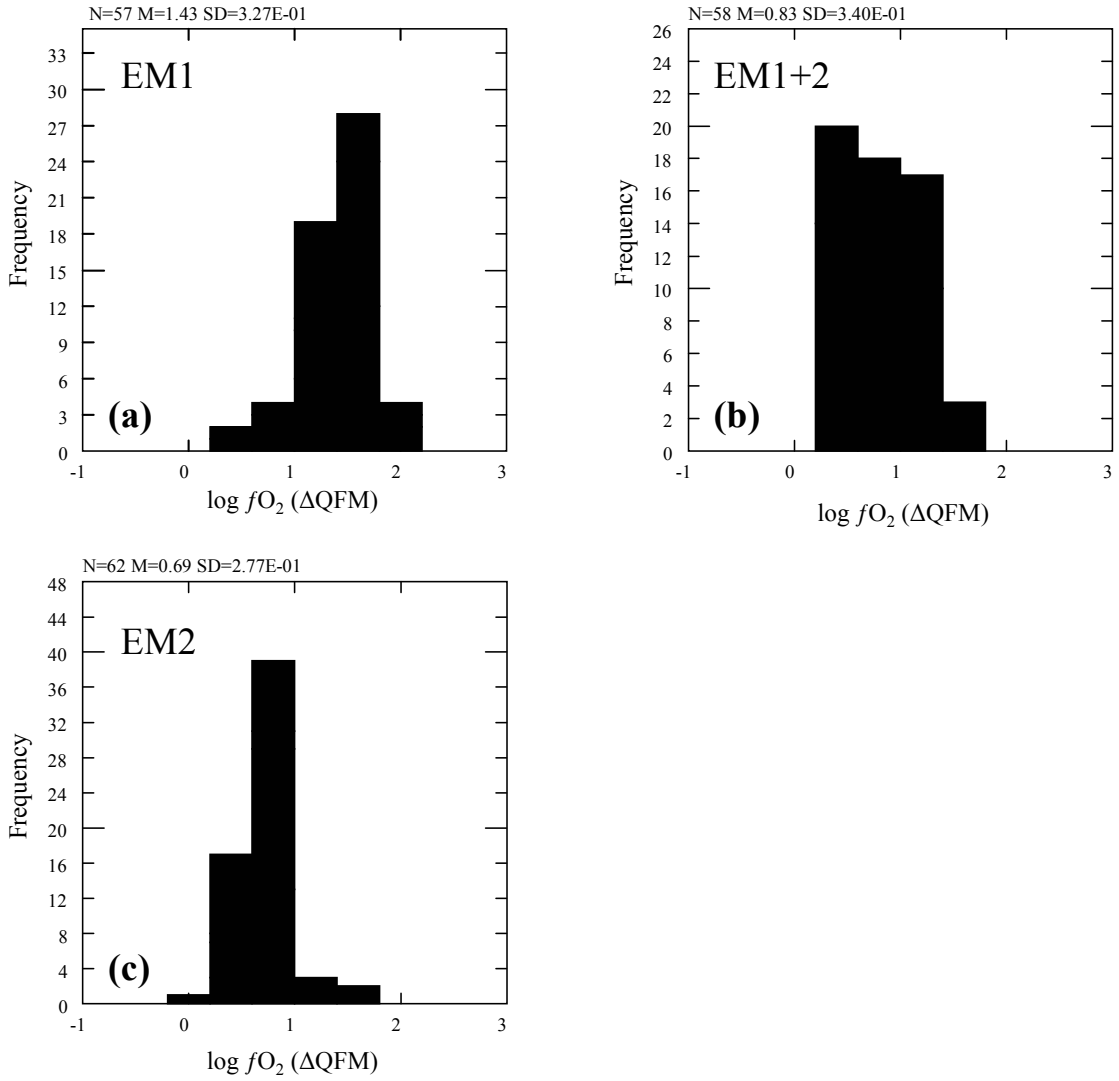

Fig. 3.7. Histograms of oxygen fugacity [log units (ΔQFM)] of representative eruptions illustrating the continuum of rhyolite compositions from EM1 to EM2. A significant disparity is observed between EM1 [mean = +1.17 log units (ΔQFM)] and EM2 [mean = +0.687 log units (ΔQFM)] magma types. EM1+2 eruptives reflect greater variability than either compositional end-member. EM1: Lake Okataina, Paeroa, Whakamaru, Qtz+biotite, pre-Matahina doming, Rotoiti, Rotorua Subgroup; EM1+2: Matahina, Oruanui, Pokopoko; and EM2: Mamaku, Ohakuri, Pokai, Kaingaroa, Mangaone.

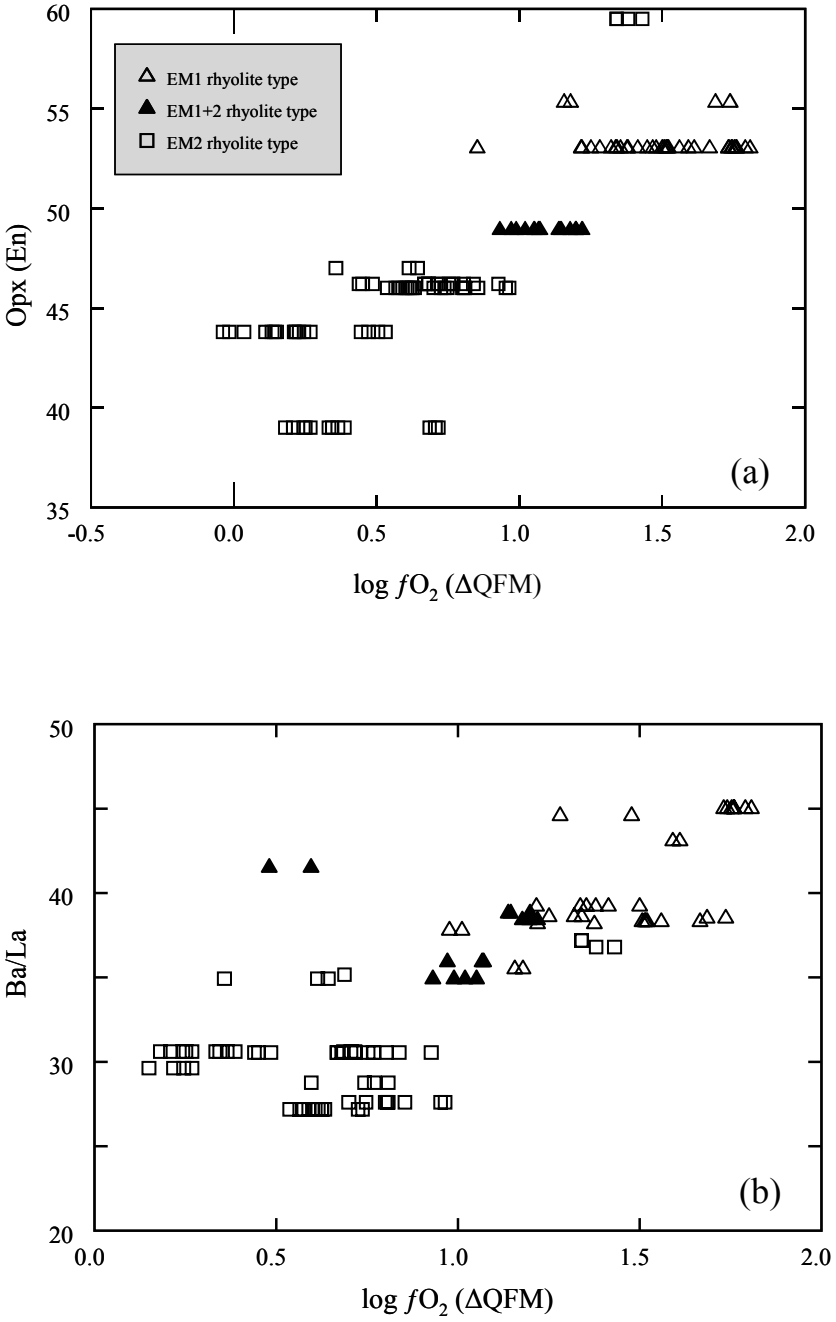

Fig. 3.8. (a) Mean orthopyroxene (opx) enstatite composition and (b) Ba/La vs. mean oxygen fugacity [log units (ΔQFM)], calculated from Fe-Ti oxide pairs, of representative EM compositions.

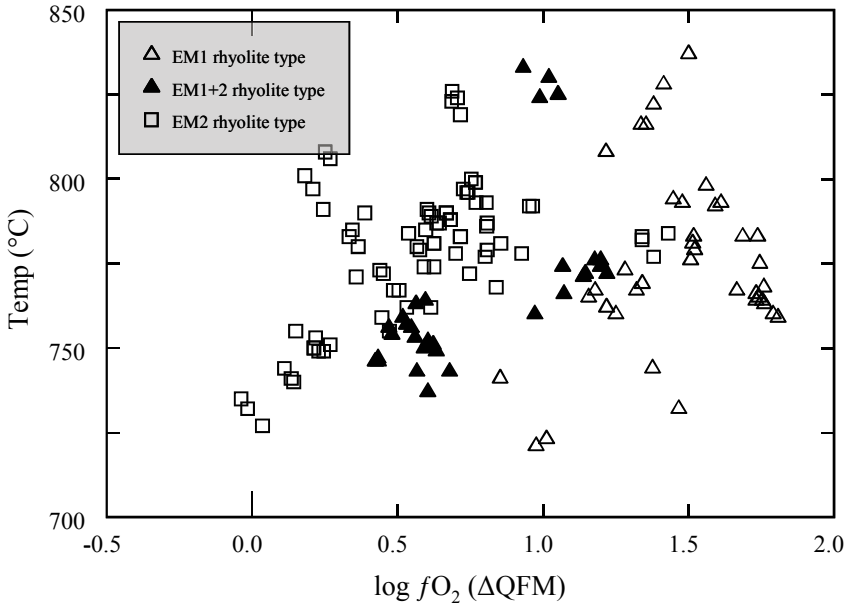

Fig. 3.9. Plot of oxygen fugacity [log units (ΔQFM)] vs. temperature, calculated from Fe-Ti oxide pairs, of representative EM compositions.

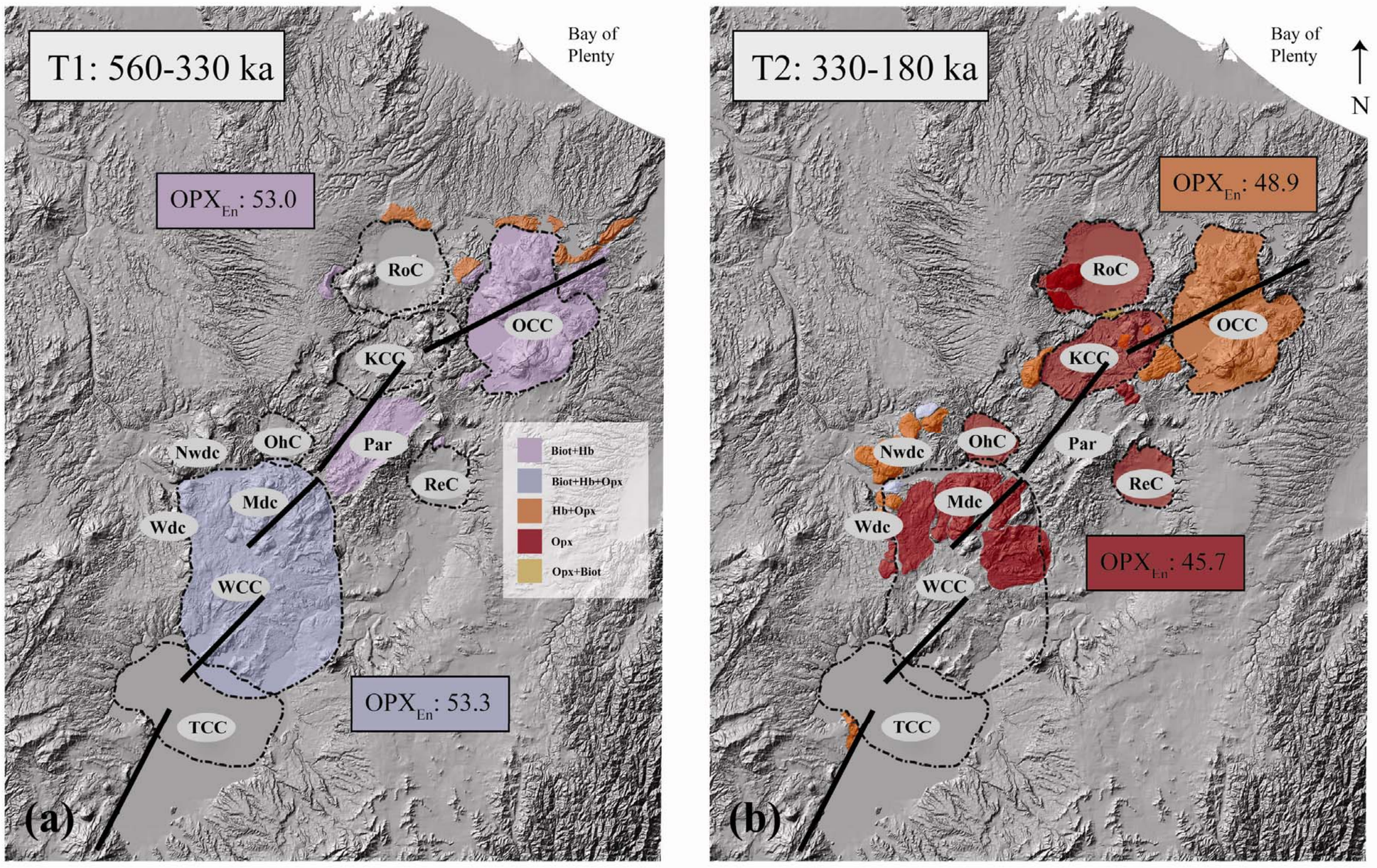

Fig. 3.10. Structural/topographic map of the TVZ showing the ferromagnesian mineral assemblages of domes and caldera-forming rhyolitic eruptions in time segments between (a) 560 to 330 ka and (b) 330 to 180 ka. Orthopyroxene enstatite (En) are for major, caldera-forming events that represent the dominant volumes of magma erupted. Inferred rift axes are from Acocella et al. (2003).

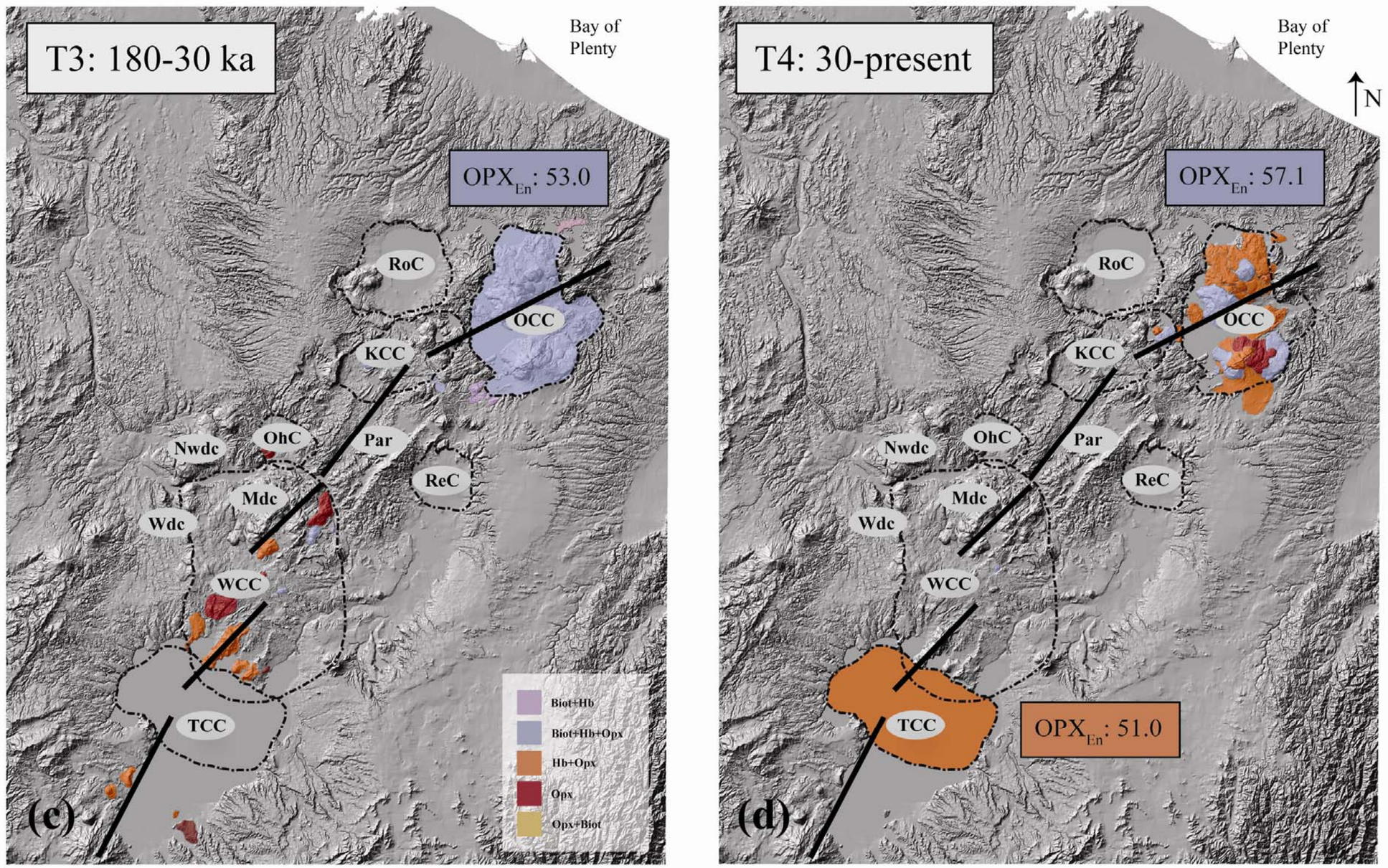

Fig. 3.10cont. Structural/topographic map of the TVZ showing the ferromagnesian mineral assemblages of domes and caldera-forming rhyolitic eruptions in time segments between (c) 180 to 30 ka and (d) 30 ka to present. Orthopyroxene enstatite (En) are for major, caldera-forming events that represent the dominant volumes of magma erupted. Inferred rift axes are from Acocella et al. (2003).

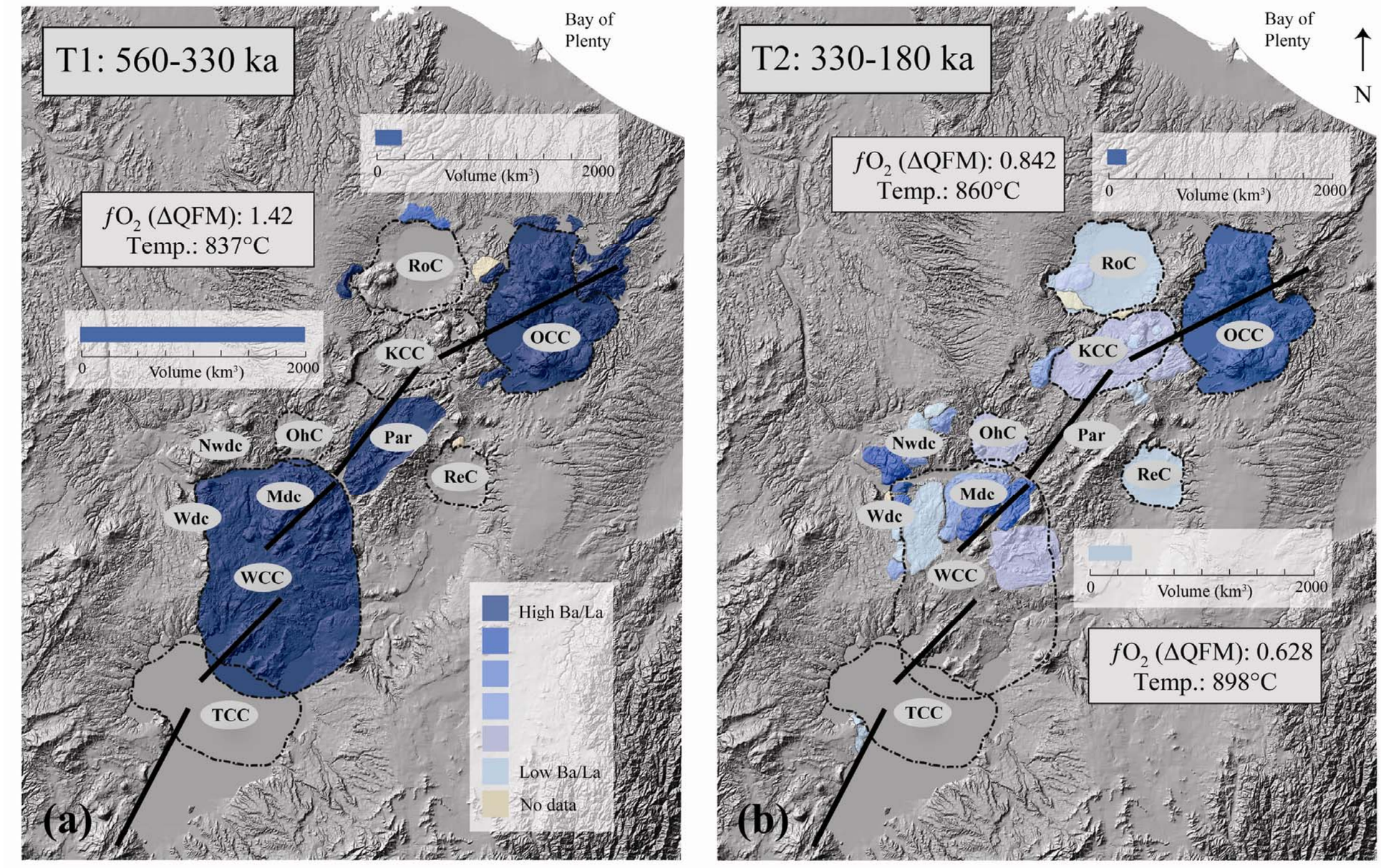

Fig. 3.11. Structural/topographic map of the TVZ with estimated source temperatures and oxygen fugacity [log units (ΔQFM)] calculated from Fe-Ti oxide pairs for major-caldera-forming events that represent the dominant volumes of magma erupted. Color coding for the Ba/La ratio of the bulk-rocks ranges from high (dark) to low (light). Magma volume estimates are compiled for domes and caldera-forming events that are geographically associated and of similar EM affinity. Time segments are (a) 560 to 330 ka and (b) 330 to 180 ka. Inferred rift axes are from Acocella et al. (2003).

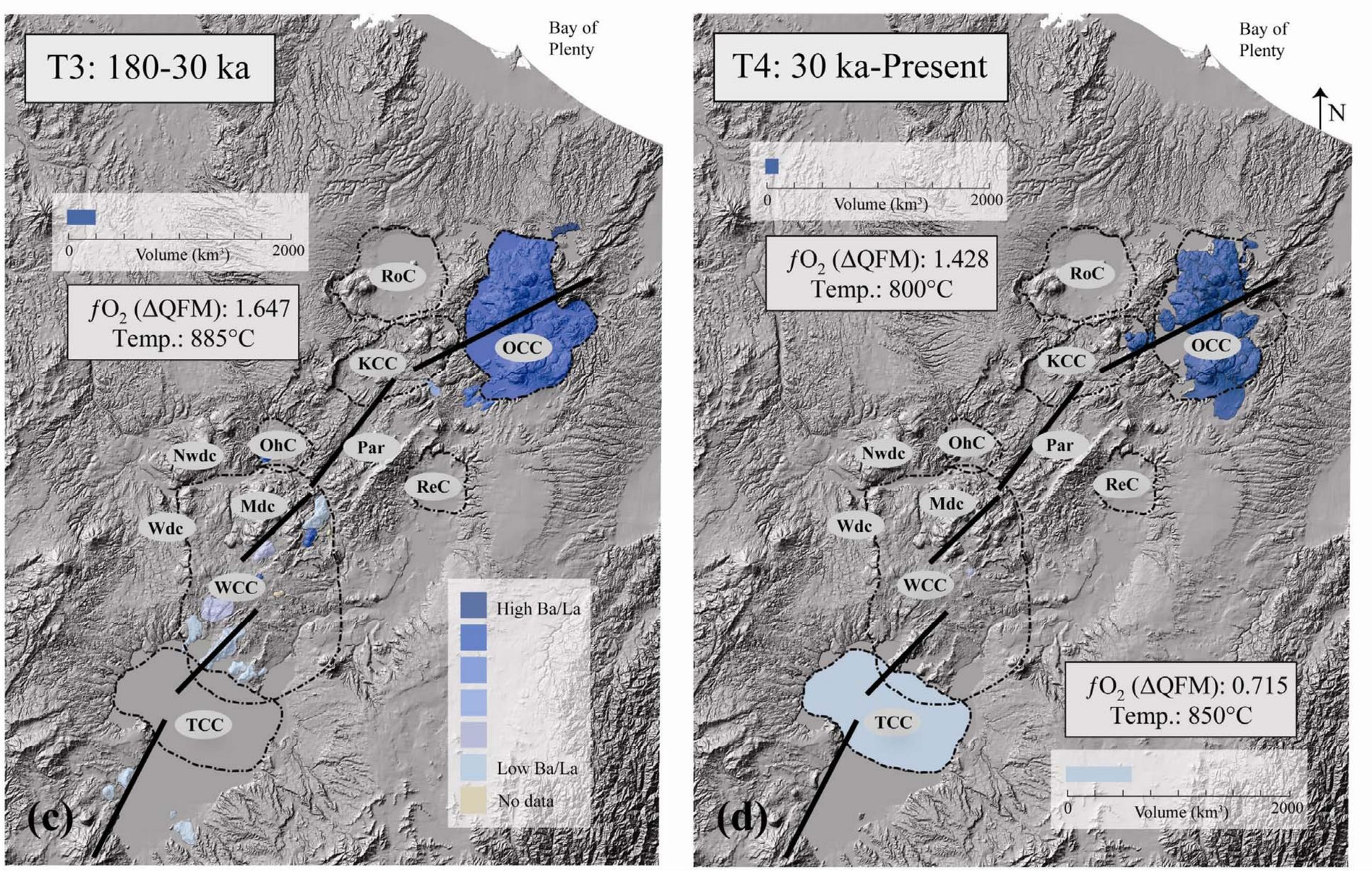

Fig. 3.11cont. Structural/topographic map of the TVZ with estimated source temperatures and oxygen fugacity [log units (ΔQFM)] calculated from Fe-Ti oxide pairs for major-caldera-forming events that represent the dominant volumes of magma erupted. Color coding for the Ba/La ratio of the bulk-rocks ranges from high (dark) to low (light). Magma volume estimates are compiled for domes and caldera-forming events that are geographically associated and of similar EM affinity. Time segments are (c) 180 to 30 k and (d) 30 ka to present. Inferred rift axes are from Acocella et al. (2003).

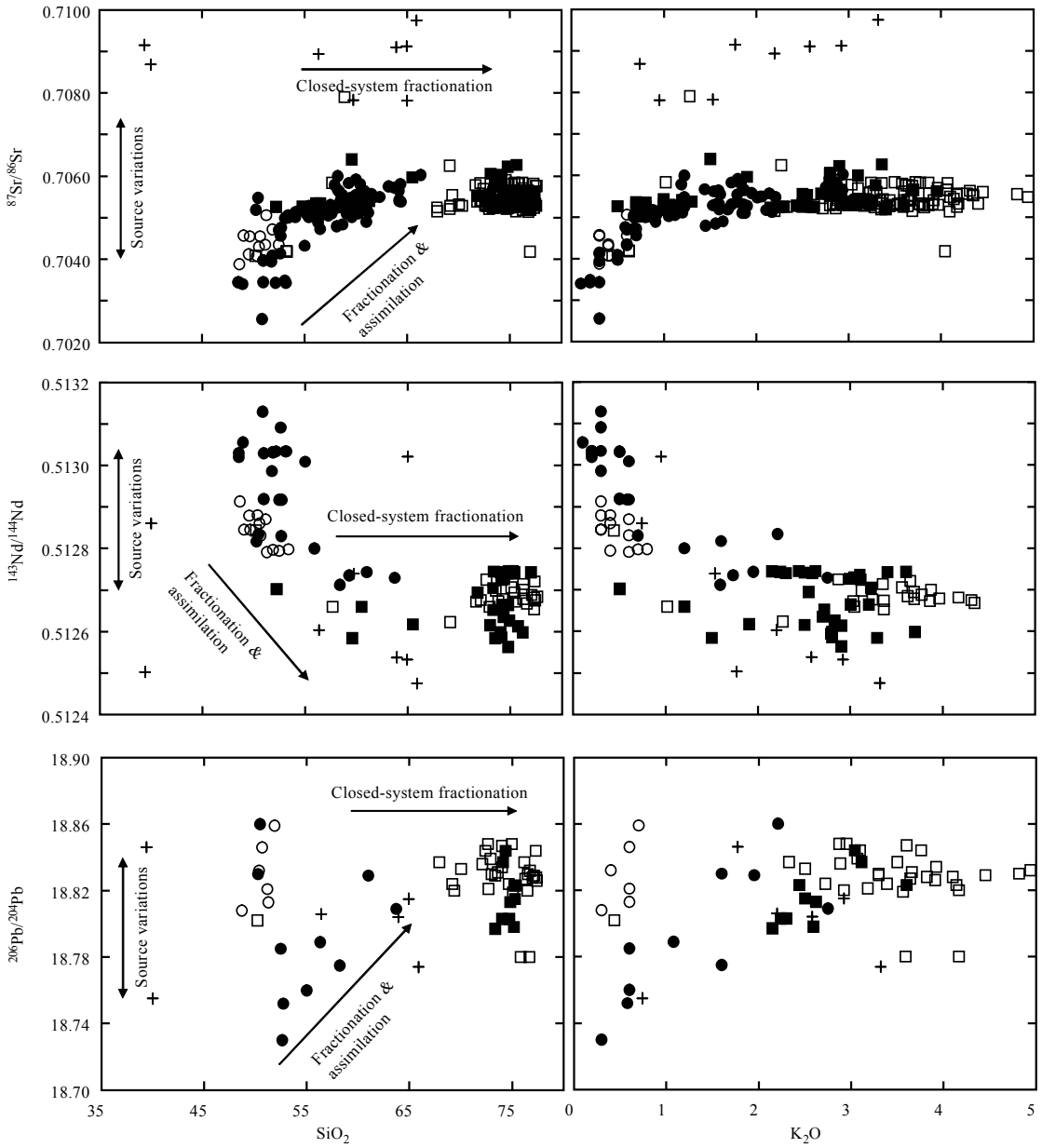

Fig. 3.12. Diagrams of $^{87}Sr/^{86}Sr$, $^{143}Nd/^{144}Nd$, and $^{206}Pb/^{207}Pb$, against SiO_2 and K_2O used to assess the role of crustal contamination versus slab-derived sediment input in Kermedac-Hikurangi and on-shore/off-shore TVZ basalts, select andesites, and rhyolites. Open circles are central TVZ high-alumina basalts; closed circles are Kermedac-Hikurangi basalts and basalts and andesites from outside of the central TVZ; open boxes are samples from T1+T2; closed boxes are samples from T3+T4; crosses are arc sediment. Although some source variation is indicated for all basalts analyzed, the basalt to andesite dominantly follow an assimilation fractionation trend based on the Sr and Nd isotopes. The high-K basalt from the southern Kermedacs lies isotopically and compositionally within the cluster of high-alumina basalt from the central TVZ. In general, the rhyolite form a loose linear trend from the andesite, consistent with predominantly closed system fractionation. T1+T2 rhyolites have higher $^{206}Pb/^{207}Pb$ compared to T3+T4 with the exception of the Earthquake Flat Breccia (61 ka), which has distinctly older zircon model age spectra than the contemporaneous Rotoiti eruption (Charlier et al., 2003). Data from Graham et al. (1992), Gamble et al. (1993, 1996), Karhunen (1993), Sutton et al. (1995), Brown et al. (1998), Leonard (2003), Gravley (2004), Schmitz and Smith (2004),Wilson et al. (2006), Deering et al. (2008).

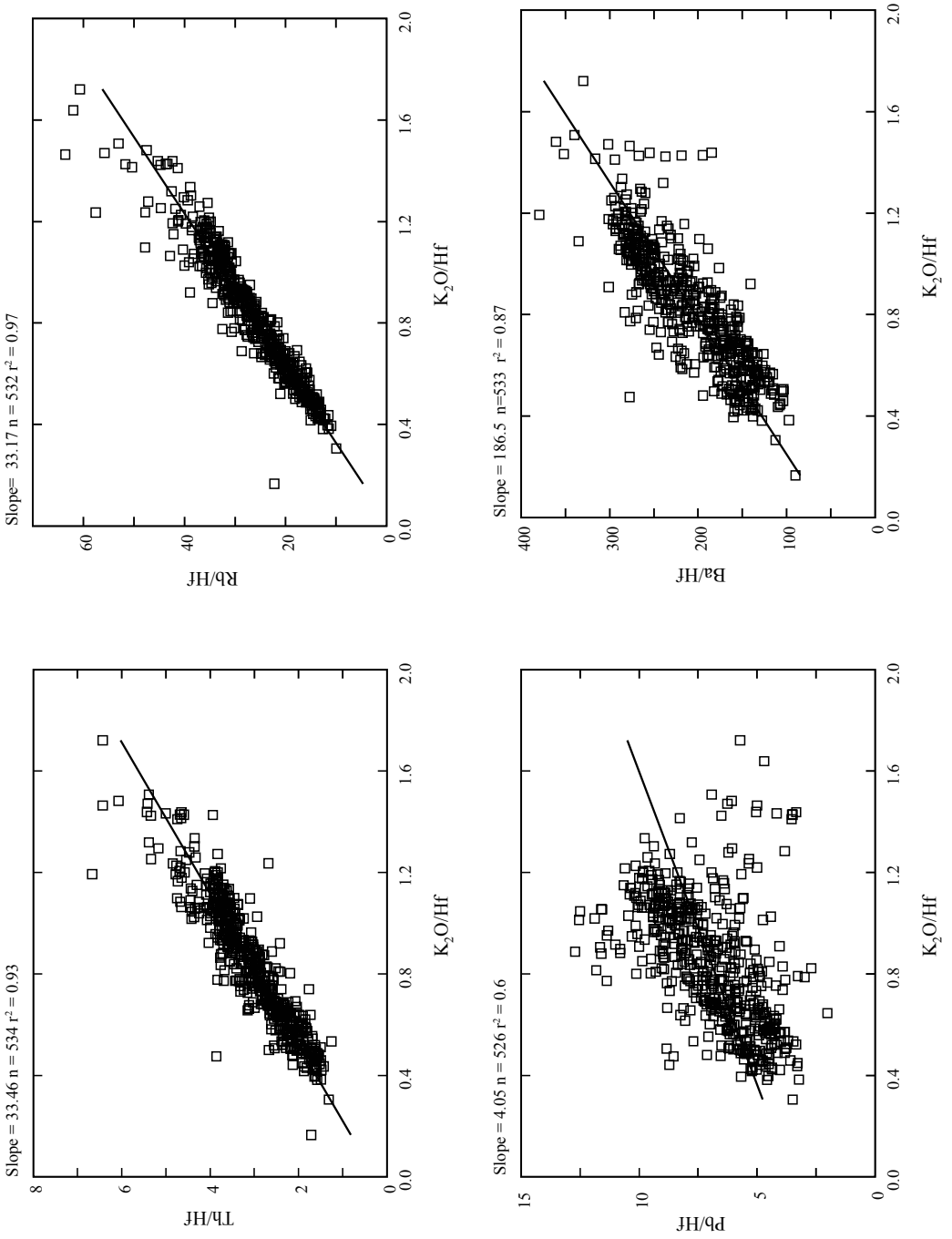

Fig. 3.13. (a-d) Plots of K_2O/Hf against Th/Hf, Rb/Hf, Pb/Hf, and Ba/Hf. Plots illustrate the moderate to strong correlation between K_2O and other slab-derived components (Pb, Th, Rb, Ba).

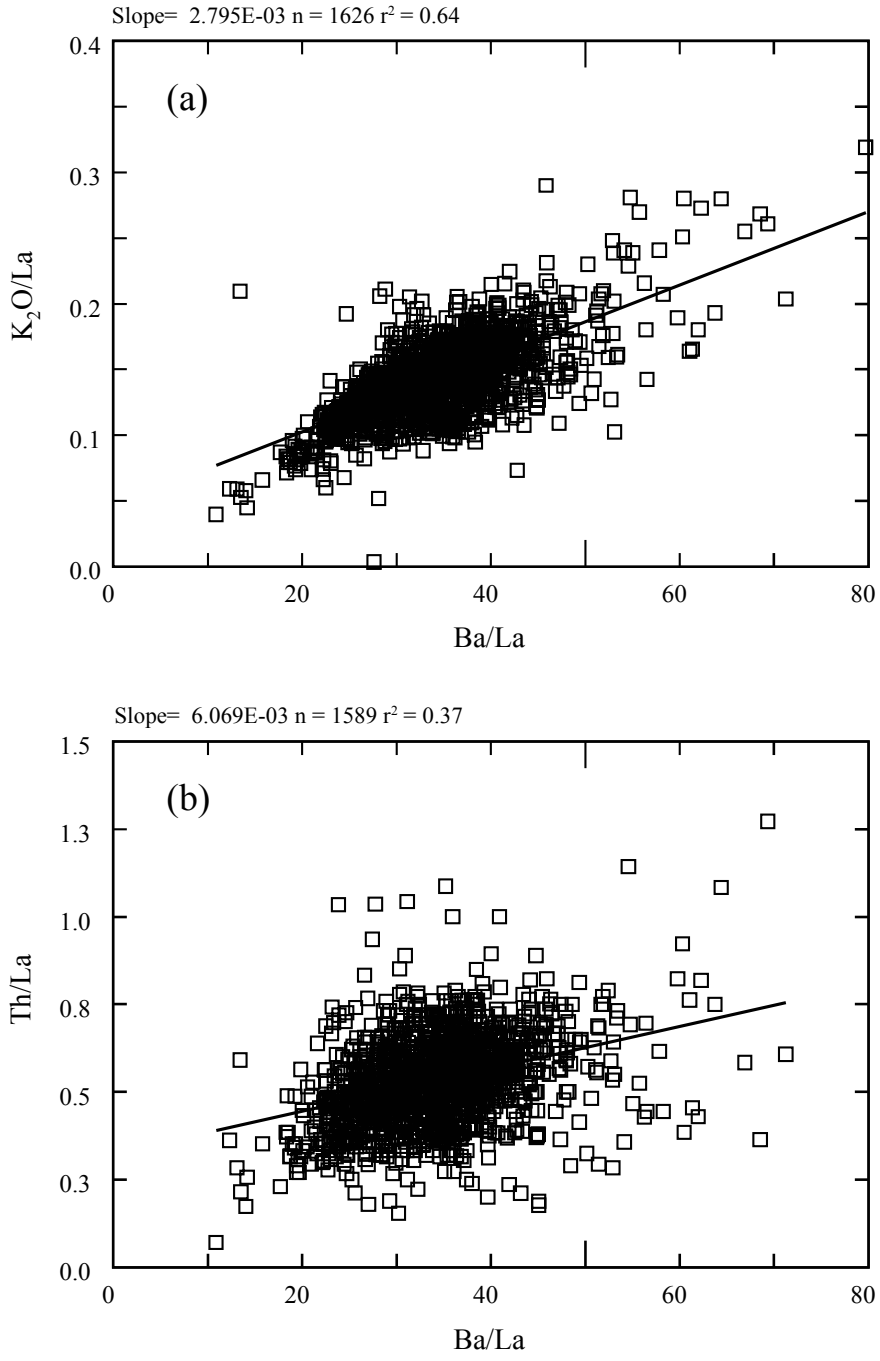

Fig. 3.14. (a) Plot of K_2O/La against Ba/La showing a moderate correlation between K_2O and Ba, relative to La. (b) Plot of Th/La against Ba/La showing a poor correlation between Th and Ba. See text for discussion.

3.12 TABLES

Table 3.1. Taupo Volcanic Zone rhyolite characteristics

	R1	R2
Geochemical	low FeO*/MgO	high FeO*/MgO
	low Y	high Y
	low MREE	high MREE
	high Sr; low Eu/Eu*	low Sr; high Eu/Eu*
	low Zr	high Zr
Petrological	crystal-rich (up to 45%)	crystal-poor (<10%)
	dominantly hydrous mineral phases: amphibole±biotite	dominantly anhydrous mineral phases: orthopyroxene±clinopyroxene

Rhyolite end-members (R1 and R2) characterized by Deering et al. (2008).

Table 3.2. Summary of TVZ rhyolite characteristics from 550 ka to present

Eruptive Unit	*Caldera/Caldera complex*	*Age (ka)*	*Eruptive volume (km^3 magma)*	*Crystal content (%)*	*Ferromagnesian assemblage*	*Wr SiO_2*	Y		Zr	
							mean	$K_{3.0\_3.5}$	*mean*	$K_{3.0\_3.5}$
Utu ignimbrite (including Utu equivalents)	OCC	~549*	>90?	15-25	bt+hbl±opx	74.0 (1.2)	17.8	17.6	156	160
Tephra A	OCC	551±4								
Tephra B	OCC	538±5								
Utu pumice outwash	OCC									
Whakapoungakau Dome	OCC	531±5*		~19	bt+hbl+opx	75.8	16.8	-	183	-
Trig 8566 Dome	ReC	490*		~27	bt+opx+hbl	n.d.	n.d.	-	n.d.	-
Endean Dome	RoC	451*		~28	hbl+opx+biot	73.6	16.5	-	180	-
Hamurana Dome	RoC	>400?		~11	opx+hbl	73.9	25.0	-	243	-
Maungawhakamana Dome	OCC	436±6*		~15	hbl+opx	74.9	23.8	-	116	-
Wairua Dome	OCC	411±5*		~20	bt+hbl	74.4	19.2	-	194	-
Whakamaru Group	WCC	340-320	>2000	35-40	opx+bt+hbl	73.2 (0.6)	21.7	20.8	136	150
Matahina	OCC	322±7*	160	<15	opx±hbl±bt	73.8 (0.9)	23.7	23.2	156	170
Western Dome Complex	WCC	313-141?	15	<7	opx	74.5 (0.5)	23.9	24.1	125	167
Northwestern Dome Complex	WCC	313-141?	15	<8	opx±hbl±bt	76.3 (1.3)	25.1	24.7	188	155
Chimp	KCC	~300	50	<10	opx±hbl	74.4 (1.0)	37.4	38.7	173	172
Pokai	KCC	275	100	<10	opx	74.1 (0.8)	25.6	24.3	202	206
Pokopoko	OCC	~237±4*		~14	opx±hbl	75.8 (0.3)	37.0	36.5	201	197
Ohakuri	OhC	240	100	<10	opx	73.8 (0.8)	27.8	27.9	198	196
Mamaku	RoC	240	145	<10	opx±hbl	73.7 (0.8)	35.7	36.0	246	246
Kaingaroa	ReC	230	100	~5	opx	73.9 (0.8)	28.2	28.1	216	217
Early Maroa	WCC	305-180	51	<9	opx±hbl	74.9 (1.4)	32.1	31.8	208	204
Late Maroa	WCC	180-present	11	~7 -30	opx±hbl±bt	75.0 (1.2)	28.5	26.4	185	192
Rotoiti	OCC	61	80	16-28	cum+hbl+opx±bt	74.2 (0.7)	17.7	18.0	161	160
Earthquake Flat Breccia	KCC	~61	4	<40	bt+hbl+opx	73.9 (0.8)	18.1	18.0	149	149
Mangaone Subgroup (MSg)	OCC	35-30	16	~5	opx+hbl	74.4 (0.7)	35.8	35.0	238	198
Oruanui	TCC	26.5	530	<5	hbl+opx	74.0 (1.3)	23.2	23.3	161	154
Post-Oruanui (OSg)	TCC	26-present	48	<5	opx+cpx	74.3 (0.4)	33.3	37.5	229	242
Rotorua Subgroup	OCC	30-present	80	~5-25	hbl+opx±cum±bt	76.0 (1.3)	25.4	24.4	141	170

Eruptive volumes, crystallinity, ferromagnesian assemblage, and geochemical data are from this study and compiled from the following sources: Wilson et al. (2006; in press), Ewart (1967a,b), Smith et al. (2005; and references within), Leonard (2003), Gravley (2004), Milner et al. (2001), Beresford (1997), Karhunen (1993), Sutton et al. (1995), Nairn et al. (2004), Brown (1994), Schmitz & Smith (2004). Values in parentheses are standard deviations from average calculations. Mg# = $Mg/(Mg+Fe_{tot})$. *New Ar-Ar dates from Leonard et al. (in prep.)

Table 3.2. Cont.

Sr		FeO*/MgO		Ba/La		Opx (En)	Hb (Mg#)	Biot (Mg#)	fO_2 log units (ΔQFM)	*Eruptive T (°C)*	*Est. source T (°C)*	R type
mean	$K_{3.0\_3.5}$	*mean*	$K_{3.0\_3.5}$	*mean*	$K_{3.0\_3.5}$							
137	144	6.9	6.5	37.3	37.4	53.0 (3.7)	59.9 (2.1)	49.4 (5.2)	1.239 (0.098)	762 (8.0)	845	1
108	-	4.4	-	42.7	-	n.d.	63.3 (0.2)	50.9 (0.1)	n.d.	n.d.	-	1
n.d.	-	n.d.	-	n.d.	-	50.0 (0.3)	n.d.	n.d.	n.d.	n.d.	-	1
143	-	6.2	-	38.2	-	51.8 (1.8)	55.5 (1.9)	n.d.	0.558	785	-	1
154	-	5.9	-	32.3	-	54.9 (6.7)	n.d.	n.d.	n.d.	n.d.	-	1
119	-	4.6	-	37.7	-	44.9 (2.1)	60.8 (1.2)	-	n.d.	n.d.	-	1+2
137	-	4.6	-	37.7	-	n.d.	57.9 (2.0)	46.9 (4.0)	n.d.	n.d.	-	1
114	136	11.1	9.0	38.5	40.2	53.3 (2.1)	59.9 (4.0)	42.8 (4.9)	1.601 (0.061)	781 (10)	880	1
108	115	7.8	7.0	39.8	39.4	48.9 (4.7)	57.8 (4.3)	56.2 (0.1)	0.842 (0.078)	751 (7)	860	1+2
122	106	10.4	13.1	30.3	30.3	n.d.	-	-	n.d.	n.d.	-	2
76	100	22.9	20.3	33.0	33.4	n.d.	n.d.	n.d.	n.d.	n.d.	-	1+2/2
98	97	17.5	17.9	29.4	29.1	51.8 (5.5)	57.6 (1.1)	-	0.625	774	830	1+2
84	90	17.4	16.8	32.1	33.3	39.0 (6.8)	-	-	0.663 (0.159)	813 (40)	920	2
86	85	7.4	7.6	29.6	29.8	43.8 (6.2)	57.8 (3.4)	-	0.191 (0.054)	748 (5)	-	2
82	93	11.4	10.5	30.0	29.7	46.0 (6.0)	-	-	0.690 (0.134)	786 (11)	900	2
99	84	14.1	14.9	29.6	28.9	46.0 (5.3)	n.d.	-	0.703 (0.132)	785 (7)	910	2
100	101	10.4	10.5	28.1	28.0	47.0 (2.6)	-	-	0.538 (0.157)	773 (13)	860	2
85	82	14.7	15.5	35.0	33.6	46.0 (0.3)	n.d.	-	0.488 (0.208)	745 (17)	-	2
103	131	10.1	7.1	34.7	37.1	n.d.	n.d.	n.d.	n.d.	n.d.	-	1+2
153	150	5.3	5.4	37.7	37.0	53.0 (6.4)	60.9 (3.7)	49.5 (4.9)	1.647 (0.281)	765 (13)	885	1
146	146	5.3	5.3	33.2	33.2	n.d.	n.d.	n.d.	n.d.	n.d.	-	1
140	132	6.4	6.0	35.6	34.3	59.5 (2.3)	65.5 (1.4)	-	1.389 (0.052)	782 (3)	825	2
126	120	7.2	7.4	28.9	24.2	51.0 (2.9)	58.7 (3.8)	-	0.715 (0.041)	769 (6)	850	1+2
130	60	9.3	8.3	26.6	23.5	52.0	-	-	0.753	830	940	2
106	131	7.3	6.3	37.6	33.9	57.1 (6.41)	58.4 (7.5)	46.9 (2.6)	1.428 (0.442)	760 (17)	800	1

CHAPTER 4

Cannibalization of an amphibole-rich andesitic progenitor induced by caldera-collapse during the Matahina eruption: evidence from amphibole compositions

Cannibalization of an amphibole-rich andesitic progenitor induced by caldera-collapse during the Matahina eruption: evidence from amphibole compositions

Chad D. Deering[1*]

[1]Dept. of Geological Sciences, University of Canterbury, PB 4800, Christchurch 8020, New Zealand

American Mineralogist: article in press

4.1 ABSTRACT

The diverse range of calcic-amphibole compositions from the ca. 330 ka Matahina eruption (ca. 160 km^3 rhyolitic magma) of the Okataina Volcanic Complex, Taupo Volcanic Zone, including crystal-rich basalt-dacite pumice from post-collapse deposits, reveals several pre- and syn-eruption magmatic processes. (1) Amphibole phenocrysts in the basaltic-andesite and andesite crystallized at the highest pressures and temperatures (P: up to 0.6±0.06 GPa and T: up to 950°C), equivalent to mid-crustal depths (13-22 km). Inter- and intra-crystalline compositions range from Ti-magnesiohornblende→Ti-tschermakite→tschermakite→magnesiohornblende and some display gradual decreases in T from core to rim, both consistent with magma differentiation by cooling at depth. (2) The largest amphibole crystals from the basaltic-andesite to andesite display several core to rim increases in T (up to 70°C), indicating new hotter magma periodically fluxed the crystal mush. (3) The dominant population of rhyolite amphibole is small and bladed (magnesiohornblende) and crystallized at low P-T conditions (P: 0.3 GPa, T: 765°C), equivalent to the eruptive P-T conditions. Dacitic and low-silica rhyolitic amphibole (tschermakite-magnesiohornblende) form two distinct populations, which nucleated at two different T (High: 820°C and Low: 750°C). These compositional variations, governed primarily by differences in T conditions during crystal growth, record the mixing of two distinct amphibole populations that approached a thermal equilibrium at the eruptive T. Therefore, the diversity in amphibole compositions can be reconciled as an exchange of crystals+liquid between the basaltic-andesite to dacite from the mid-crust and rhyolite from the upper-crust, which quenched against one another, modifying the dacite to low-silica rhyolite compositions as the eruption progressed.

Keywords: *amphibole, crystal growth, crystal-mush, cummingtonite, geothermometry, geobarometry*

4.2 INTRODUCTION

Determining the processes involved in generating silicic (>65 wt. %) magmas is a topic of active debate for igneous petrologists (for review see: Large Silicic Systems, JVGR, V. 167, 2007). In general, two mechanisms have been proposed for the generation of rhyolites in the Taupo Volcanic Zone, New Zealand: (1) partial melting of crustal material (e.g. greywacke, intermediate igneous rock), and/or (2) fractional crystallization from a mafic parent (McCulloch et al., 1994; Graham et al., 1995; Price et al., 2005; Deering et al., 2008). Although simple anatexis of continental crust has been precluded based on radiogenic isotopes, varying contributions (up to 25 %) have been invoked (e.g. McCulloch et al., 1994). The dominant processes involved in generating the silicic compositions are, therefore, assumed to be either the partial melting of intermediate rock (Price et al., 2005) or fractional crystallization from a mafic progenitor (McCulloch et al., 1994; Deering et al., 2008). Importantly, Deering et al. (2008) concluded, based on bulk rock trace element patterns of the TVZ rhyolites, that amphibole was an important phase crystallizing in the parent magma.

Few amphibole-rich basalt-andesite eruptions are recorded globally (Cerro la Pilita basalt, Western Mexico, Luhr and Carmichael, 1985; Montserrat andesite, Rutherford and Devine, 2003; Huerto Andesite, Parat et al., 2008); however, the importance of their role in generating large silicic magma bodies, as well as providing a mechanism for the remobilization of more evolved magma via gas sparging, has recently been proposed (Sisson and Bacon, 1999; Bachmann and Bergantz, 2004). Therefore, crystal 'mushes' presumably represent the root zone of a magma reservoir or a zone of accumulation and are rarely erupted to the surface as primary magmas.

Post-collapse deposits associated with eruption of the voluminous (~250 km^3) Matahina ignimbrite are basaltic-rhyolitic in composition and represent the

incorporation of exotic magma types in the late stages of the eruption (Deering et al., 2008). These deposits include a suite of crystal-rich (up to 50 vol.%), hornblende-bearing mafic pumice and a felsic biotite-bearing pumice. The foundering of the overlying crust during this event is hypothesized to have induced chaotic mixing in the chamber (e.g. Kennedy et al., 2008), thereby assisting in the withdrawal of comparatively small volumes of these magmas.

This paper presents a detailed evaluation of the temperature and pressure evolution and interaction of a complex suite of magmas, some of which are thought to represent the active, and very productive, mushy accumulation and ascent zone beneath the Taupo Volcanic Zone (TVZ), where rhyolitic magmas are produced (Deering et al., 2008). Chemical variations along amphibole traverses provide clues to the complex relationship among the diverse magma compositions, both from the main rhyolitic magma body and the basalt-dacite exhumed in the late stages of the Matahina eruption (post-caldera collapse). Amphibole chemistry is well suited for evaluating the evolution of this magmatic system due to the early appearance of amphibole on the liquidus in calc-alkaline, arc-related magmas and the availability of appropriate geothermometers and geobarometers (e.g. Holland and Blundy, 1994; Schmidt, 1992; Anderson and Smith, 1995; Féménias et al., 2006).

4.3 GEOLOGIC BACKGROUND

The TVZ in the North Island of New Zealand is a rifted arc (Wilson et al., 1995) and can be divided into segments of dominantly andesitic cone-forming volcanism in the north and south, and a central region characterised by rhyolitic caldera-forming and dome-building eruptions (Healy, 1962; Wilson et al., 1984) (Fig. 4.1). Since the inception of volcanism in this central region, 1.6 Ma, >6,000 km^3 of

rhyolitic magma has erupted from eight major eruptive centres. The Okataina Volcanic Centre (OVC), located at the northern extent of the TVZ, is defined as a complex of coalescing collapse structures, which formed during numerous pyroclastic eruptions over > 400 kyrs. (Nairn, 2002).

The Matahina ignimbrite (ca. 330 ka) was erupted over several weeks or possibly months from the OVC (Fig. 4.1) as a slightly compositionally zoned series of fall and flow deposits (Bailey and Carr, 1994). A ca. 30 km^3, plinian style eruption preceded the voluminous expulsion of greater than 160 km^3 of rhyolitic magma during the catastrophic, caldera-forming event. The ignimbrite lies mainly to the northeast, east, and southeast, extending radially up to 30 km from the caldera margin (Fig. 4.1; Bailey and Carr, 1994).

4.4 MATAHINA PETROLOGY

The Matahina ignimbrite (s.s.) bulk composition varies from 72.2 to 77.8 wt. % SiO_2, but is dominantly from 75.2 to 77.8 wt. % SiO_2, consisting of ash and pumice lapilli (Bailey and Carr, 1994). Juvenile lapilli are crystal poor (2-21 vol. %) and contain phenocrysts of plagioclase, bipyramidal quartz, orthopyroxene, hornblende, Fe-Ti oxides, and rare biotite and clinopyroxene (Table 4.1).

The early, plinian phase of the Matahina eruption is characterized by rhyolitic pumice with a mineral assemblage grading from plagioclase + quartz + orthopyroxene + Fe-Ti oxides to plagioclase + quartz + orthopyroxene + amphibole + Fe-Ti oxides (Table 4.1). Amphibole crystals are almost exclusively small and bladed (<1 mm; Fig. 4.2a), but a few larger tabular types occur. Only in later stages of the eruption does a slightly higher crystal content (up to 15 vol. % compared to <5 vol. %), amphibole

(typically tabular or stubby) +orthopyroxene ± biotite ± sanidine, and a low-silica rhyolite pumice type appear (Table 4.1).

An ignimbrite (PDC deposit), found directly overlying lag breccias on the eastern margin of the caldera (Fig. 4.1; locality 2), consists of a range of pumice types (basalt-rhyolite), which include the dominant rhyolite type (orthopyroxene ± amphibole) from the Matahina ignimbrite. Andesite to dacite pumice clasts are typically crystal-rich (up to 30 vol. %) and porphyritic, and some display obvious macroscopic signs of mingling between a mafic and felsic melt composition. Total crystal contents decrease with increasing bulk rock SiO_2 for clasts within this deposit Table 4.1). Rare, basaltic clasts are fine-grained and crystal-rich, consisting predominantly of amphibole with plagioclase microlites in the groundmass (45 vol. %; Table 4.1). Rhyolitic clasts display a diverse ferromagnesian mineralogy: 1) orthopyroxene-only, 2) orthopyroxene + amphibole, and 3) amphibole + orthopyroxene + biotite.

Along the western margin of the caldera, a lithic-rich ignimbrite (Fig. 4.1; locality 1), containing crystal-rich basaltic-andesite to dacite and crystal-poor rhyodacite to rhyolite clasts, was also erupted following the Matahina (*s.s.)* caldera-collapse. The basaltic-andesite to dacite pumice clasts are similar in composition and mineralogy to those deposited on the eastern margin (Deering et al., 2008), but have comparatively higher crystal contents, which also decrease with increasing bulk rock SiO_2 (Table 4.1). However, the distinctly different, biotite-bearing, co-magmatic, high-silica pumice type is only found at this locality. Other rhyolitic clasts containing biotite are found within exposures to the south of the caldera margin (Fig. 4.1; locality 3) and within the PDC deposit to the east (Fig. 4.1; locality 2), but are distinguished

from the biotite-bearing, high-silica pumice by the presence of orthopyroxene and amphibole.

In general, the basalt to dacite clasts erupted from both sides of the caldera are characterized by a multi-modal mineral distribution of glomerocrysts (Fig. 4.2c) and individual crystals ranging in size up to ca. 4.0 mm. Although the mineral abundances vary, the clasts contain plagioclase + amphibole + orthopyroxene + magnetite + clinopyroxene + ilmenite ± biotite ± quartz (Table 4.1). Individual amphiboles are blocky (Fig. 4.2b), tabular, or stubby and range in size up to ca. 3.5 mm. Adcumulate textures, numerous glomerocrysts, and disequilibrium textures (e.g. resorbed and embayed plagioclase, crystal overgrowths, amphibole reaction rims, mingled mafic and felsic glasses) are ubiquitous (Fig. 4.2c,d).

4.5 ANALYTICAL TECHNIQUES

Amphibole compositions were determined at the University of Michigan, on a Cameca SX 100 EPMA equipped with five wavelength spectrometers using an accelerating potential of 15 kV, a focused beam with a 0 ųm spot size, counting time of ~3 min/ mineral, and a 10 nA beam current. Standards used were natural fluor-topaz (FTOP); natural jadeite (JD-1); natural Grossular, Quebec (GROS); natural adularia, St. Gothard, Switzerland (GKFS); synthetic apatite (BACL); and synthetic $FeSiO_3$ (FESI). Amphiboles typically average ~2 wt.% of (H_2O + F +Cl); therefore, only analyses with anhydrous totals (SiO_2, Al_2O_3, FeO_{tot}, MgO, CaO, Na_2O, K_2O, TiO_2, MnO) of 98±1 wt. % were retained.

4.6 AMPHIBOLE COMPOSITIONS

Over 85 amphibole crystals from 29 samples were analyzed representing a diverse range of bulk-rock compositions (basalt-rhyolite) and stages of the Matahina eruptive sequence. Representative analyses are presented in Table 4.2 and the full geochemical database is available in Electronic Appendix 4.1. Cation distributions for structural formulae were recalculated using the procedure suggested by Leake et al. (1997), which estimates the proportion of ferric iron based on the maximum stoichiometric limits (13eCNK). All Matahina amphibole can be broadly classified as calcic [$Ca_B \geq 1.5$; Ti < 0.50 atoms per formula unit: (apfu)] and divided into two subgroups: 1) $(Na + K)_A \geq 0.50$ apfu and 2) $(Na + K)_A < 0.50$ apfu (Fig. 4.3a). Amphibole with $(Na + K)_A \geq 0.50$ and Si < 6.5 are classified as magnesiohastingsite, rather than pargasite based on the low Al_{vi} content relative to estimated Fe^{3+} (Fig. 4.3a). Additionally, they all classify as magnesian amphibole ranging in X_{Mg} (Mg/Mg + Fe^{2+}) between 0.5 and 1.0 (Fig. 4.3b).

Stubby, small amphibole (<0.5 mm) from the fine-grained basalt are magnesiohornblende and compositionally similar to the rhyolitic hornblende. Basaltic-andesite amphibole range from magnesiohastingsite → tschermakite → magnesiohornblende, whereas andesite and dacite are tschermakite and magnesiohornblende. Some core compositions from amphibole of the basaltic-andesite and andesite also have Ti between 0.25 and 0.49 apfu and are classified as titanian-magnesiohastingsite and titanian-tschermakite progressing from tschermakite to magnesiohornblende or cummingtonite at the rims. Individual cummingtonite crystals (< 250 μm) also occur in the groundmass of one mingled andesite sample (UC1239). The magnesiohastingsite and tschermakite are typically glomerocrysts or large (up to 3.0 mm) blocky phenocrysts (Fig. 4.2c,d). The compositions of individual

phenocrysts in the dacite and low-silica rhyolite are tschermakite to magnesiohornblende, with some displaying a range from tschermakite cores to magnesiohornblende rims. Low-silica rhyolite have a bimodal population of magnesiohastingsite/tschermakite, which are the largest amphibole (up to 1.5 mm), and smaller (less than 1.0 mm) magnesiohornblende. Nearly all the bladed, elongate (up to 1.0 mm; Fig. 4.2a) amphibole from the rhyolite are defined as magnesiohornblende with rare tschermakite.

4.7 GEOTHERMOBAROMETRY

Experimental studies that have evaluated the effects of pressure and temperature on amphibole composition (Johnson and Rutherford, 1989; Thomas and Ernst, 1990; Schmidt, 1992; Spear, 1981; Blundy and Holland, 1990) have concluded that the Al-Tschermak substitution ($Si_T + Mg_{M1-M3} = Al_T + Al_{M1-M3}$) is sensitive to changes in pressure and the Ti-Tschermak ($2Si_T + Mn_{M1-M3} = 2Al_T + Ti_{M1-M3}$) and edenite [$Si_T + \square_A = Al_T + (Na+K)_A$] exchanges in response to changes in temperature. Anderson and Smith (1995) determined that two additional intensive parameters might induce an Al-Tschermak exchange, leading to an overestimation of pressure: 1) decreasing fO_2 lowers Mg (relative to Fe^{2+}) forcing a Tschermak substitution, or 2) low Fe^{3+} relative to total Fe induces a Fe^{3+} Al_{M1-M3} exchange. However, calculated $Fe^{3+}/(Fe^{3+} + Fe^{2+})$ ratios for the Matahina hornblende are similar to those in barometric calibrations and oxygen fugacity calculated using Fe-Ti oxides are higher than the QFM buffer, which precludes a significant effect on hornblende compositions governed by changes in these conditions. Increasing fH_2O, independent of P and T, was shown by Scaillet and Evans (1999) to increase Al_{tot}; however, these changes were small (1.64 to 1.81 Al_{tot}; 5.7 to 7.0 wt. % H_2O, respectively) in relation to the

Al_{tot} range for the Matahina amphibole (0.91 to 1.89) and cannot account for the total variation within the population.

The Al-variations in the Matahina amphibole can be assessed based on the above mentioned preferred substitutions governed by P and T. The $(Na+K)_A$-, Ti-, and Ca-content display good correlations with Al_T (Fig. 4.4a,b,d) and indicate a strong compositional dependency on temperature. In contrast, the Al_T and Al_{M1-M3} (Al-Tschermak exchange) are poorly correlated, but an increasing trend is recognized from rhyolite to basaltic-andesite (Fig. 4.4c), indicating that pressure also influenced this compositional variation in the amphibole.

Many studies have evaluated the parageneses of amphibole in both mafic (Helz 1973, 1976, 1979, 1982; Spear, 1981; Ernst and Liu, 1998) and felsic (Hammarstrom and Zen, 1986; Johnson and Rutherford, 1989; Schmidt, 1992; Anderson and Smith, 1995) igneous rocks. In particular, the Al-hornblende geobarometer has been experimentally calibrated with the buffering assemblage (quartz + alkali feldspar + plagioclase + hornblende + biotite + iron titanium oxide + titanite + melt + fluid). However, this assemblage is only found in some of the rhyolite clasts erupted. These hornblende are used in evaluating the coupled Al-Tschermak exchange (Fig. 4.4c) observed among the entire dataset and are consequently utilized as a relative indicator of pressure. Therefore, the pressure estimates must be evaluated with caution as the geobarometer has not yet been calibrated to higher pressures and temperatures with the coexisting phases present in the mafic magmas.

The Anderson and Smith (1995) experimental calibration is temperature dependent and, at temperatures >800°C, the correction increases and becomes unsuitable for estimating pressure. In fact, similar to the results of Féménias et al.

(2006) at temperatures >800°C, the calculations produce negative results. Independent T-estimates from Fe-Ti oxides and orthopyroxene-clinopyroxene (author unpublished data) yield temperatures consistently >800 °C (Table 4.3), indicating that this method is inappropriate for many of the Matahina hornblende. Estimation of P-T using the semi-quantitative, graphical method devised by Ernst and Liu (1998) is appropriate for the range of P, T, and compositions of the Matahina hornblende and is generally consistent with P estimates from other calibrations (Hollister et al., 1987; Hammarstrom and Zen, 1986; Schmidt et al., 1992). To reduce the uncertainty inherent in graphical estimations, the pressure estimates were obtained using the experimental calibration of Schmidt (1992).

Anderson (1996) and Bachmann and Dungan (2002) evaluated the Al-in-hornblende thermometric algorithms, concluding that the Holland and Blundy (1994) calibration was the most reliable. Based on this assessment, cation distributions for structural formulae were recalculated using the scheme of Holland and Blundy (1994), Appendix B, for applying their thermo-barometric algorithm. The Holland and Blundy (1994B) estimates compare well with temperatures calculated by independent means (Fe-Ti oxides; Table 4.3) for a range of temperatures with well constrained plagioclase compositions that co-exist with, or are included in, dacitic-rhyolitic hornblende. However, the intra- and inter-phenocryst compositional diversity of hornblende and plagioclase in the basaltic-andesite to dacite samples, revealed by detailed traverses (most <20 μm), limits the interpretation of these results for the full range of samples evaluated and, therefore, the Holland and Blundy (1994) estimates were only used on the rhyolites.

According to Helz (1973, 1976, 1979), Otten (1984), Ernst and Liu (1998), and Féménias et al. (2006), Ti solubility appears an acceptable geothermometer

within the P-T envelope (P = 0.1-0.6 GPa; T = 700-950°C) of the Matahina magmas. The Féménias et al. (2006) calculations are within error of the plagioclase-hornblende T estimates by the aforementioned independent geothermometers for well constrained (equilibrated and homogenous) rhyolite samples (Table 4.2). Therefore, considering that the mafic Matahina magma is Ti-saturated (ilmenite present), it is suggested that, in contrast to the felsic compositions, Ti-hornblende is most appropriate for interpreting the thermal evolution of the basalt to dacite magmas.

Most of the amphiboles (Ti-magnesiohastingsite and Ti-tschermakite) in the basaltic-andesite and andesite crystallized at the highest pressures and temperatures (Fig. 4.5c,d; P: up to 0.5±0.06 GPa and T: up to 950°C), but also display the widest range and show a relative decrease in pressure and temperature from core to rim when compared to the dacitic to rhyolitic hornblende. The lowest rim/near-rim temperature estimates (<750°C) are from the mingled andesite sample UC1239 and are considered tenuous as these are from tschermakite with cummingtonite overgrowths, and Ti along these diffuse boundaries are low. Pressure and temperature estimates from dacitic and low-silica rhyolitic amphiboles (tschermakite-magnesiohornblende) show a near bi-modal distribution (Fig. 4.5b; *High*, P: 0.35-0.55 GPa, T: 775-850°C and *Low*, P: 0.2-0.3 GPa, T: 750-775°C) indicative of two distinct crystallization sequences at pressures and temperatures similar to crystallization conditions estimated for the andesite and rhyolite (*s.s.*) (Fig. 4.5a, d). The dominant population of rhyolite amphibole (magnesiohornblende) crystallized under comparatively low P-T conditions (Fig. 4.5a; P: 0.2-0.3 GPa, T: 725-800°C), but a subordinate population encompasses higher P-T (Fig. 4.5a; P: 0.2-0.45 GPa, T: 775-860°C). This subordinate population represents the larger (up to 1.6 mm) phenocrysts (stubby or tabular), while the dominant population are small (< 0.7 mm), bladed phenocrysts.

4.8 AMPHIBOLE PROFILES

Thirty amphiboles from fifteen different samples were chosen to represent the range of bulk rock compositions (basalt-rhyolite) and growth habits (e.g. bladed, stubby, glomerocrysts) for detailed major element traverses (core-rim) to investigate the growth history of the amphiboles. Traverses range from 100 to 1350 μm in length, with most analytical steps less than 15 μm, but one of the largest phenocrysts has 45 μm steps.

In general, the Al_2O_3, is correlated positively with the TiO_2, Na_2O, K_2O, and MgO, whereas the FeO and SiO_2 are inversely correlated and the MnO and CaO remain relatively constant (e.g. Fig. 4.6). As Al_{tot} and Ti appear to be good indicators of P-T changes, these elements were chosen to evaluate the core-rim variations among amphibole.

The Al_{tot} and Ti contents of twenty-three of the amphibole traverses are shown in Figure 4.7, representative of the basalt to rhyolite bulk rock compositions (Deering et al., 2008). Amphibole compositions have been divided into high- and low- Al_{tot} -Ti contents. The low- Al_{tot} –Ti (LAT) category corresponds with the eruptive P-T estimates (P: 0.3 GPa and T: 765°C), respectively, for the Matahina outflow sheet (s.s.). The high- Al_{tot} –Ti (HAT) category encompasses a range in T from 850 to 950°C, but the highest P-T estimates from the basaltic-andesite amphibole are used as a graphical reference (Fig. 4.7).

In the basalt, the small amphibole are LAT with slight oscillations from core to rim (Fig. 4.7a). A Ti element map of the largest phenocyrst found in the basalt displays several distinct zones from a low-Ti core to high-Ti rim (Fig. 4.8a). The one small basaltic-andesite amphibole displays a clear increase from a LAT core towards

a HAT rim (Fig. 4.7b). In contrast, the larger amphiboles from the basaltic-andesite and andesite have HAT core contents and display variable magnitude oscillations with steep decreases to LAT at the rim (Fig. 4.7b,c). The Ti element map of a large glomerocryst (3.0 mm) shows an anhedral orthopyroxene core with distinct bands in the hornblende overgrowth (Fig. 4.8b). Notably, a near rim decrease occurs over the last ~200-250 μm on each amphibole. The smallest andesite amphibole traverses with HAT cores are also ~200-250 μm in length and have steep decreases to a LAT rim, with the exception of one larger traverse (~625 μm) that shows little change from core to rim (Fig. 4.7d). Tschermakite with cummingtonite overgrowths also occur within one mingled andesite clast. Magnesium and Ti element maps clearly show the distinct compositional change along the tschermakite edge up to ~250 μm thick (Fig. 4.9a,b). Small amphibole from the dacite to rhyolite predominantly show two contrasting trends from core to rim: 1) an increase from the lowest Al_{tot} -Ti to the LAT and 2) decrease from HAT to LAT, with two HAT amphibole that show little variation from core to rim (Fig. 4.7e,f).

4.9 DISCUSSION

4.9.1 Magma evolution and recharge

Deering et al. (2008) recently proposed a model for rhyolite petrogenesis in the central TVZ, which highlighted (1) the importance of amphibole in the parent rock, based on bulk rock trace element geochemistry, and (2) the likelihood of in-situ equilibrium crystallization coupled with periodic rhyodacite-rhyolite melt extractions from a crystal mush in an accumulation and ascent zone in the mid-crust. A first order indicator of compositional zoning within the Matahina magmatic system, likely related to crystal fractionation in the mid-crustal reservoir, is the decrease in crystal

contents from andesitic to low-silica pumice from the two PDC deposits (Table 4.1; Fig. 4.1: localities 1 and 2).

Calcic-amphibole phenocrysts/antecrysts and/or groundmass microcrysts appear as the dominant ferromagnesian phase, over clinopyroxene/orthopyroxene, in the basaltic-andesite to dacite bulk rock compositions, but vary in rhyolite bulk rock compositions when orthopyroxene is present. Since amphibole is always present, it remained on the liquidus throughout the magmatic evolution, and compositional variations are hence interpreted to reflect a record of magmatic differentiation (Ti-magnesiohastingsite→Ti-tschermakite→tschermakite→magnesiohornblende), which is correlated with the basaltic-andesite/andesite to rhyolite bulk rock compositions. In particular, amphibole from the crystal-rich basaltic-andesite (UC816) and andesite (UC1100) and some individual phenocrysts (e.g. from samples: UC816, UC1100, UC1283) include the entire range of compositions of the magmatic differentiation trend consistent with in-situ crystallization. The largest Ti-magnesiohastingsite, Ti-tschermakite, and tschermakite are mostly found in the basaltic-andesite to andesite, occur as glomerocrysts or large blocky phenocrysts (Fig. 4.2), and were equilibrated at the highest pressures (0.4 to 0.6 GPa) and temperatures (800-950°C). Some of these amphibole grains display gradual decreases in temperature from core to rim (Fig. 4.10a), indicative of a progressive cooling at mid-crustal depths between 13-22 km, using an average continental crust density of 2.67 g/cm^3.

Experiments (e.g. Beard and Lofgren, 1991; Parat et al., 2008) on amphibole-bearing andesites at conditions similar to those estimated for the Matahina andesitic mush constrain the stability field for co-existing hornblende+orthopyroxene+clinopyroxene between 915°C and 850°C and melt H_2O between 4.3 to 6.0 wt. % (±sulfur). Some of the glomerocrysts of hornblende

originally nucleated as orthopyroxene/clinopyroxene (Fig. 8), but probably reacted with the melt early as either the temperature decreased or aH_2O increased into the hornblende stability field. Several large (>2.5 mm) phenocryst traverses display low frequency (200 to 800 μm apart), high amplitude temperature increases (up to 70°C) interpreted to reflect magma recharge events into the mid-crustal basaltic-andesite to andesite cumulate (Fig. 4.10b). However, temperatures appear to remain within the amphibole stability field. The frequency and amplitude of the temperature variations are relatively broad (Figs. 4.8 and 4.10) and can be constrained within the time required to grow millimeter sized phenocrysts as the magma rehomogenizes and/or cools between recharge pulses (Kuo and Kirkpatrick 1982; Cashman 1992, 1993; Wörner 1996). In addition, the 3-D crystal network, as indicated by glomerocrysts and adcumulate textures (Fig. 4.2) and high crystallinity (~50%) indicates this magma was probably near the rheologial locking point, where convection would have ceased (Bachmann and Bergantz 2004). Differences within and among several crystals in the population indicate that crystallization probably occurred at several discrete depths prior to eruption. These steps in crystallization can be related to the continued evolution of the central, andesitic mush by recharge, prior to exhumation following chaotic mixing in the main magma reservoir.

4.9.2 Magma mingling - quenching

The general relationship between decreasing crystal contents and increasing SiO_2 contents within both the andesite to low-silica rhyolite from the PDC deposits and the main Matahina outflow sheet (s.s.) (Table 4.1) are suggestive of a subtle zoning within the dominant portion of the magma reservoir. However, two important observations indicate that additional processes, other than crystal fractionation

occurred just prior to or during the Matahina eruption: 1) high-silica, crystal-poor rhyolite pumice, which also erupted during the initial plinian phase, occur within the PDC deposits, and 2) the rhyodacite to low-silica rhyolite clasts within the PDC deposits have lower crystal contents than those of comparable bulk rock composition from the main Matahina outflow sheet (Table 4.1; e.g. samples UC813 and UC498) (Fig. 4.1; localities 1 and 2). These features indicate that the evacuation of the chamber was not continuous and normal, but probably piece-meal, incorporating the basalt to dacite compositions only during the final stages of the eruption and that the rhyodacite to low-silica rhyolite from post-collapse deposits resided separately from the main Matahina rhyolitic reservoir.

Some of the basaltic-andesite to low-silica rhyolite clasts from the PDC deposits (Fig. 4.1; localities 1 and 2) show variable signs of macroscopic mingling of a mafic and felsic component. Amphibole grains are characterized by a near bi-modal distribution of large (glomerocrysts, tabular, blocky) and small (stubby and bladed) forms, which correspond to HAT and LAT types, respectively (Fig. 4.7). However, limitations in the pressure estimates based on Al_{tot} variation (as outlined earlier) restrict the interpretation and, therefore, discussion refers to intra-crystalline T, not P changes. The large amphibole from basaltic-andesite to andesite (up to 3.5 mm) have high-T cores with steep decreases to low-T 200-250 μm rims that correspond in thickness and T to rims of the dacite to rhyolite and small fine-grained basalt crystals (Fig. 4.7). In particular, the small amphibole from the andesite with high-T cores also have steep T decreases, consistent with late nucleation and rapid, cooling induced crystallization (Fig. 4.7). Crystals that formed at low-T show an increase from core to rim, indicating heating (Fig. 4.7), but this cannot be quantified as it is within the error of the estimates (±30°C). Overall these trends indicate that two distinct crystal

populations merged and grew, approaching a thermal equilibrium close to the eruptive temperature (~765°C).

Perhaps the most convincing evidence of these distinct episodes of crystallization and mixing are the tschermakite with cummingtonite overgrowths and small individual cummingtonite phenocrysts from a mingled andesite clast (Fig. 4.9) *and* the abundant magnesiohornblende (up to 90% modal) in the fine-grained basalt (Table 4.1). The stability field for cummingtonite in a rhyolitic melt was determined for TVZ rhyolites by Nichols et al. (1992). Their experiments showed that cummingtonite was restricted to pressures less than 0.35 GPa and a temperature of ca. 750°C. Cummingtonite rims on hornblende have also been observed in other silicic eruptions [e.g Pinatubo, 1991; Luhr and Melson, 1996] and attributed to crystallization at low temperatures (< 800°C). Crystallization experiments on mafic inclusions from the Adamello Massif granitoids (Blundy and Sparks, 1992) ascribed the abundance of hornblende, plagioclase, and magnetite to overstepping of the olivine and clinopyroxene nucleation field by rapid quenching below 970°C. Therefore, temperature estimates (~750°C) for the overgrowths (< 250 μm) of cummingtonite on tschermakite from the mingled andesite and the abundant, small (< 250 μm) magnesiohornblende from the basalt, record a dramatic decrease in temperature. Together these features provide further support for rapid quenching as a hot mafic magma mingled with a cool felsic magma upon ascent.

4.10 CONCLUSION

The thorough evaluation of the conditions of amphibole crystallization from the main Matahina outflow sheet and post-collapse deposits provide evidence of diverse magmatic processes that occurred from inception of rhyolite generation

through the eruptive phases. First, the continuum of amphibole compositions from Ti-magnesiohastingsite→Ti-tschermakite→tschermakite→magnesiohornblende in basaltic-andesite/andesite to rhyolite, a decrease in crystal contents with increasing bulk rock SiO_2, and gradual decreases in temperature within the largest individual basaltic-andesite/andesite crystals support a model whereby an andesitic progenitor cools and fractionates at mid-crustal levels, producing rhyolitic magmas. However, the distinct pre-eruptive storage conditions of the basaltic-andesite/andesite (~875°C and 0.6 GPa) and Matahina rhyolite (~765°C and 0.3 GPa) suggest development of discrete thermal zones, which were maintained prior to the catastrophic eruption. Second, the low frequency, high temperature fluctuations recorded within single hornblende crystals in the basaltic-andesite to andesite indicate that periodic fluxing by hot, mafic magma into the mid-crustal accumulation and ascent zone occurred. Third, the steep decreases in temperature observed along the rims of amphibole (qualitatively displayed as cummingtonite overgrowths) from the basaltic-andesite/andesite and slight increases in temperature along some dacite to rhyolite hornblende rims, both to eruptive temperatures (~765°C), indicate that these magmas rapidly reached thermal equilibrium. In addition, crystallization within the amphibole+plagioclase+oxide stability field of the fine-grained basalt reflects a rapid temperature decrease, likely from temperatures greater than 970°C to ~740°C. Hence, chaotic mixing, probably induced by the caldera collapse, initiated the withdrawal of this mush from the base of the reservoir, quenching the hotter basalt to dacite to the cooler rhyolite; this ‘quenching’ probably occurred during ascent and produced the distinct dacite to low-silica rhyolite types erupted at the final eruptive stage.

4.11 ACKNOWLEDGEMENTS

The author would like to thank the Marsden Fund administered by the Royal Society of New Zealand (UOC0508) and the Department of Geological Sciences, University of Canterbury, Mason Trust Fund for financial support. Electron microprobe analysis at the University of Michigan was supported by NSF grant #EAR-9911352. Carl Henderson is also acknowledged for help with EPMA quality control and Eric Essene for insightful discussions that encouraged the author to continuing exploring these minerals in detail. Jim Cole, Olivier Bachmann, and Tom Vogel are also thanked for helpful review of the original manuscript. Reviews by Olivier Féménias and Lawford Anderson helped improve this manuscript. The patience and thoughtful revisions suggested by the associate editor Virginia Peterson are also greatly appreciated.

4.12 REFERENCES CITED

Anderson, J.L. (1996) Status of thermobarometry in granitic batholiths. Transactions of the Royal Society of Edinburgh: Earth Sciences, 87, 125-138.

Anderson, J.L., and Smith, D.R. (1995) The effects of temperature and fO_2 on the Al-in-hornblende barometer. American Mineralogist, 80, 549-559.

Bachmann, O. and Dungan. M.A (2002) Temperature-induced Al-zoning in hornblendes of the Fish Canyon magma Colorado. American Mineralogist, 87, 1062-1076.

Bachmann, O. and Bergantz, G.W. (2004) On the Origin of Crystal-poor Rhyolites: Extracted from Batholithic Crystal Mushes. Journal of Petrology, 45(3), 1565-1582.

Bailey, R.A., and Carr, R.G. (1994) Physical geology and eruptive history of the Matahina Ignimbrite Taupo Volcanic Zone, North Island, New Zealand. New Zealand Journal of Geology and Geophysics, 37, 319-344.

Beard, J.S, and Lofgren, G.E. (1991) Dehydration Melting and Water-Saturated Melting of Basaltic and Andesitic Greenstones and Amphibolites at 1, 3, 6.9 kb. Journal of Petrology, 32(P2), 365-401.

Blundy, J.D., and Holland, T.J.B. (1990) Calcic amphibole equilibria and a new amphibole-plagioclase geothermometer. Contributions to Mineralogy and Petrology, 104(2), 208-224.

Carr, R.G. (1984) The Matahina Ignimbrite: Its Evolution Including its Eruption and Post-Depositional Changes. Unpublished PhD dissertation, University of Auckland.

Cashman, K.V. (1992) Groundmass crystallization of Mount St. Helens dacite, 1980-1986: a tool for interpreting shallow magmatic processes. Contributions to Mineralogy and Petrology, 109, 431-449.

Cashman, K.V. (1993) Relationship between plagioclase crystallization and cooling rate in basaltic melts. Contributions to Mineralogy and Petrology, 113, 126-142.

Deering, C.D., Cole, J.W., Vogel, T.A. (2008) A Rhyolite Compositional Continuum Governed by Lower Crustal Source Conditions in the Taupo Volcanic Zone, New Zealand. Journal of Petrology, 49, 2245-2276.

de Silva, S., Bachmann, O., Miller, C., Yoshida, T., Knesel, K. (2007) Large Silicic Magma Systems. Journal of Volcanology and Geothermal Research, 167(1-4), 1-336.

Ernst, W.G., and Liu, J. (1998) Experimental phase-equilibrium study of Al- and Ti-contents of calcic amphibole in MORB-A semiquantitative thermobarometer. American Mineralogist, 83, 952-969.

Féménias, O., Mercier, J-C. C. Nkono, C., Diot, H. Berza, T., Tatu, M. Demaiffe, D. (2006) Calcic-amphibole growth and compositions in calc-alkaline magmas: Evidence

from the Motru Dike Swarm (Southern Carpathians, Romania). American Mineralogist, 91, 73-81.

Ghiorso, M.S. & Sack, R.O. (1991) Fe-Ti oxide geothermometry: thermodynamic formaulation and estimation of intensive variables in silicic magmas. Contributions to Mineralogy and Petrology, 108, 485-510.

Graham, I.J., Cole, J.W., Briggs, R.M., Gamble, J.A., & Smith, I.E.M. (1995) Petrology and petrogenesis of volcanic rocks from the Taupo Volcanic Zone: a review. Journal of Volcanlogy and Geothermal Research 68, 59-87.

Hammarstrom, J.M., and Zen, E.-A. (1986) Aluminium in hornblende: an empirical igneous geobarometer. American Mineralogist, 71, 1297-1313.

Healy, J. (1962) Structure and volcanism in the Taupo volcanic zone, New Zealand. Geophysical Monograph, 6, 151-157.

Helz, R.T. (1973) Phase relations of basalts in their melting range at PH_2O = 5 kb as a function of oxygen fugacity. Part I: Mafic phases. Journal of Petrology, 14, 249-302.

Helz, R.T. (1976) Phase relations of basalts in their melting range at PH_2O = 5 kb as a function of oxygen fugacity. Part II: Melt compositions. Journal of Petrology, 17, 139-193.

Helz, R.T. (1979) Alkali exchange between hornblende and melt: a temperature sensitive reaction. American Mineralogist, 64, 953-965.

Helz, R.T. (1982) Phase relations and composition of amphiboles produced in studies of the melting behavior of rocks. In D.R. Veblen and P.H. Ribbe Eds. Petrology and experimental phase relations, 9B, p. 279-354. Reviews in Mineralogy, Mineralogical Society of America, Chantilly, Virginia.

Holland, T., and Blundy, J. (1994) Non-ideal interactions in calcic amphiboles and their bearing on amphibole-plagioclase thermometry. Contributions to Mineralogy and Petrology, 116, 433-447.

Hollister, L.S., Grissom, G.C., Peters, E.K., Stowell, H.H., Sisson, V.B. (1987) Confirmation of the empirical correlation of Al hornblende with pressure of solidification of calc-alkaline plutons. American Mineralogist, 72, 231-239.

Johnson, M.C., and Rutherford, M.J. (1989a) Experimentally determined conditions in the Fish Canyon Tuff, Colorado, magma chamber. Journal of Petrology, 30, 711-737.

Kennedy, B.M., Jellinek, A.M., Stix, J. (2008) Coupled caldera subsidence and stirring inferred from analogue models. Nature, 1, 385-389.

Kuo, L.C. and Kirkpatrick, R.J. (1982) Pre-eruption history of phyric basalts from DSDP Legs 45 and 46: evidence from morphology and zoning patterns in plagioclase. Contributions to Mineralogy and Petrology, 79, 13-27.

Leake, B.E., Wooley, A.R., Arps, C.E.S., Birch, W.D., Gilbert, M.C., Grice, J.D., Hawthrone, F.C., Kato, A., Kisch, H.J., Krivovichev, V.G., Linthout, K., Laird, J., Mandarino, J.A., Maresch, W.V., Nickel, E.H., Rock, N.M.S., Schumacher, J.C., Smith, D.C., Stephensen, N.C.N., Ungaretti, L., Whittaker, E.J.W., and Youzhi, G. (1997). Nomenclature of amphiboles: Report of the Subcommittee on Amphiboles of the International Mineralogical Association, Commission on New Minerals and Mineral Names. American Mineralogist, 82, 1019-1037.

Leonard, G.S., Cole, J.W., Nairn, I.A., Self, S. (2002) Basalt triggering of the c. AD 1305 Kaharoa rhyolite eruption, Tarawera Volcanic Complex, New Zealand. Journal of Volcanology and Geothermal Research, 115, 461-486.

Luhr, J.F. & Carmichael, I.S.E. (1985) Jorullo Volcano, Michocoan, Mexico (1759-1774): the earliest stages of fractionation in calc-alkaline magmas. Contributions to Mineralogy and Petrology, 90, 142-161.

Luhr, J.F. & Melson, W.G. (1996) Mineral and Glass Compositions in June 15, 1991, Pumices: Evidence for Dynamic Disequilibrium in the Dacite of Mount Pinatubo. Fire and Mud: Eruptions and Lahars of Mount Pinatubo, Philippines. Editors: Newhall, C.G. & Punongbayan, R.S., 733-750.

McCulloch, M.T., Kyser, T.K., Woodhead, J.D. & Kinsley, L. (1994). Pb-Sr-Nd-O isotopic constraints on the origin of rhyolites from the Taupo volcanic zone of New Zealand; evidence for assimilation followed by fractionation from basalt. Contributions to Mineralogy and Petrology, 115, 303-312.

Nairn, I.A. (2002) Geology of the Okataina Volcanic Centre, scale 1:50000. Institute of Geological & Nuclear Sciences geological map 25. 1 sheet + 156 p. Lower Hutt, New Zealand: Institute of Geological & Nuclear Sciences Limited.

Nichols, I.A., Oba, T., Conrad, W.K. (1992) The nature of primary rhyolitic magmas involved in crustal evolution: Evidence from an experimental study of cummingtonite-bearing rhyolites, Taupo Volcanic Zone, New Zealand. Geochimica et Cosmochimica Acta, 56, 955-962.

Otten, M.T. (1984) The origin of brown hornblende in the Artssjället gabbros and dolerites. Contribution to Mineralogy and Petrology, 86, 185-199.

Parat, F. Holtz, F., Feig, S. (2008) Pre-eruptive Conditions of the Huerto Andesite (Fish Canyon System, San Juan Volcanic Field, Colorado): Influence of Volatiles (C-O-H-S) on Phase Equilibria and Mineral Composition. Journal of Petrology, 49(5), 911-935.

Price, R.C., Gamble, J.A., Smith, I.E.M. Stewart, R.B., Eggins, S. & Wright, I.C. (2005) An intergrated model for the temporal evolution of andesites and rhyolites and

crustal development in New Zealand's North Island. Journal of Volcanology and Geothermal Research, 140, 1-24.

Rutherford, M.J., and Devine, J.D. (2003) Magmatic Conditions and Magma Ascent as Indicated by Hornblende Phase Equilibria and Reactions in the 1995-2002 Soufrière Hills Magma. Journal of Petrology, 44(8), 1433-1454.

Scaillet, B., and Evans, B.W. (1999) The 15 June 1991 eruption of Mount Pinatubo. I. Phase equilibria and pre-eruption P-T-fO_2-fH_2O conditions of the dacite magma. Journal of Petrology, 40(3), 381-411.

Schmidt, M.W. (1992) Amphibole composition in tonalite as a function of pressure; an experimental calibration of the Al-in-hornblende barometer. Contributions to Mineralogy and Petrology, 110(2-3), 304-310.

Shane, P., Martin, S.B., Smith, V.C., Beggs, K.F., Darragh, M.B., Cole, J.W., Nairn, I.A. (2007) Multiple rhyolite magmas and basalt injection in the 17.7 ka Rerewhakaaitu eruption episode from Tarawera volcanic complex, New Zealand. Journal of Volcanology and Geothermal Research, 164, 1-26.

Sisson, T.W., and Bacon, C.R. (1999) Gas-driven filter pressing in magmas. Geology, 27, 613-616.

Spear, F.S. (1981) An experimental study of hornblende stability and compositional variability in amphibolite. American Journal of Science, 281, 697-734.

Thomas, W.M., and Ernst, W.G. (1990) The aluminium content of hornblende in calc-alkaline granitic rocks: A mineralogic barometer calibrated experimentally to 12 kbars. In R.J. Spencer and I-M Chou, Eds., Fluid-mineral interactions: A tribute to H.P. Eugster. Geochemical Society Special Publication, 2, 59-63.

Wilson, C.J.N., Rogan, A.M., Smith, I.E.M., Northey, D.J., Nairn, I.A., Houghton, B.F. (1984) Caldera volcanoes of the Taupo volcanic zone, New Zealand. Journal of Geophysical Research, 89, 8463-8484.

Wilson, C.J.N., Houghton, B.F., McWilliams, M.O., Lanphere, M.A., Weaver, S.D., Briggs, R.M. (1995) Volcanic and structural evolution of Taupo volcanic zone, New Zealand: a review. Journal of Volcanology and Geothermal Research, 68, 1-28.

Wörner, S.W.G. (1996) Crystal-size distribution in Jurassic flows and sills (Victoria Land Antarctica): evidence for processes of cooling, nucleation, and crystallization. Contributions to Mineralogy and Petrology, 125, 1-15.

.

4.13 FIGURES

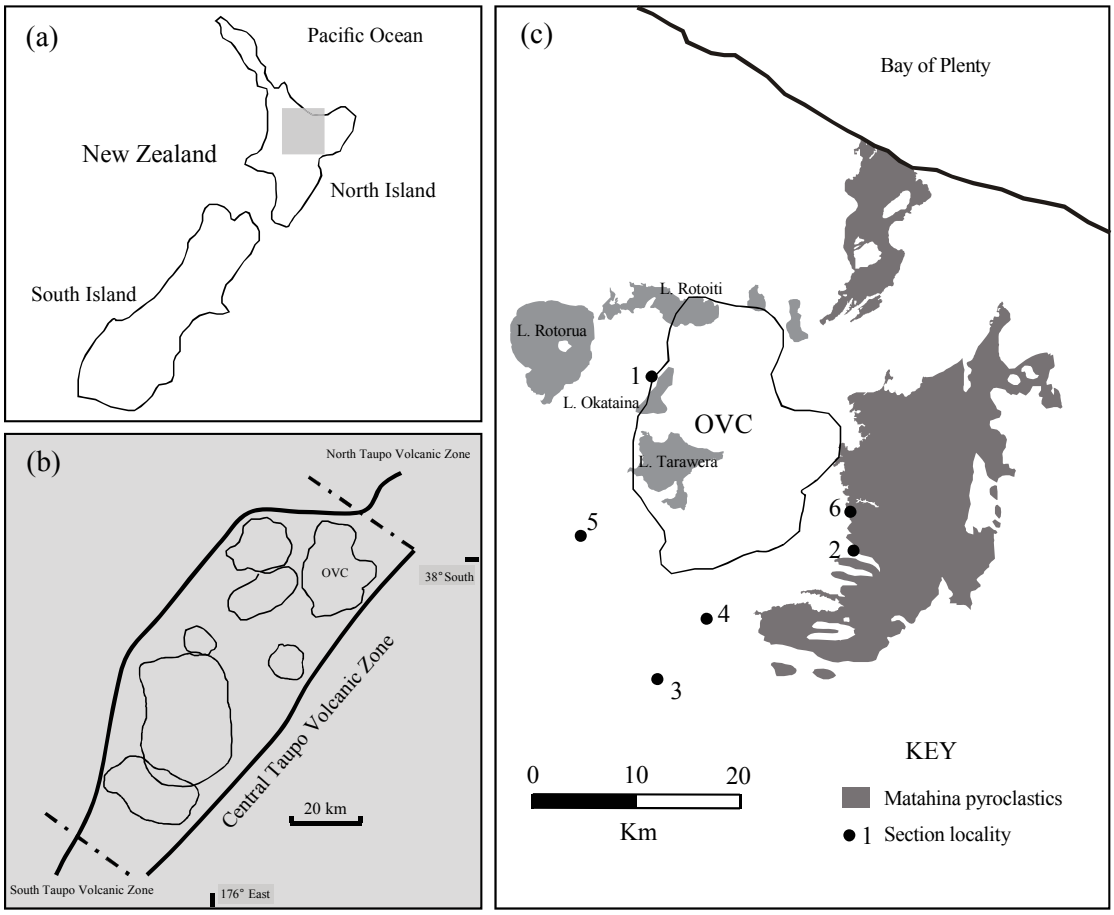

Fig. 4.1. (a) Location of the central Taupo Volcanic Zone (TVZ) North Island, New Zealand. (b) The central Taupo Volcanic Zone and Okataina Volcanic Centre (OVC) as one of seven major caldera-forming volcanic complexes. Inferred caldera boundaries are outlined in bold. (c) Mapped extent of the Matahina outflow sheet (s.s.) surrounding OVC and specific sampling localities discussed in the text. Mapped Matahina outflow after Leonard and Beggs (in prep).

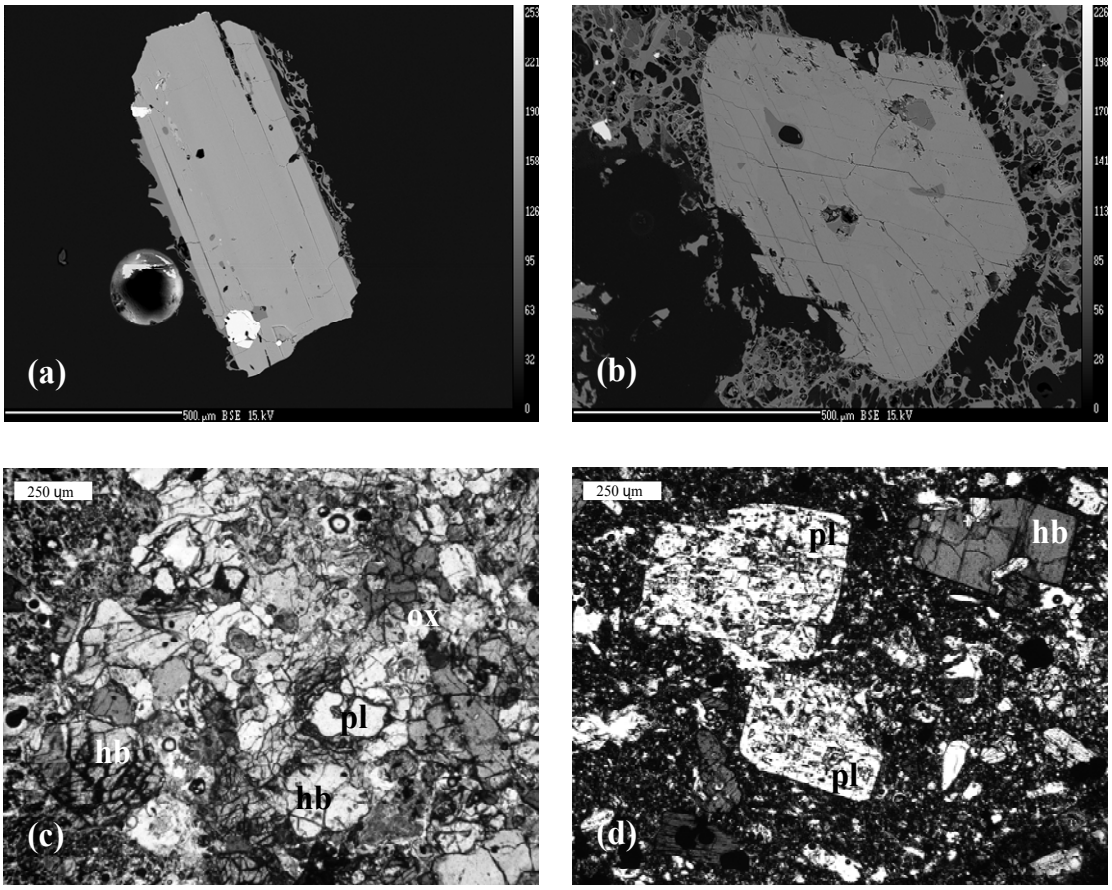

Fig. 4.2. BSE images of (a) typical bladed hornblende crystal found in rhyolite clasts, and (b) blocky hornblende typically found in basaltic-andesite to dacite clasts. Photomicrographs of (c) glomerocrysts of hornblende, plagioclase, and oxides, and (d) resorbed and embayed plagioclase. Hornblende (hb); Plagioclase (pl); and oxides (ox).

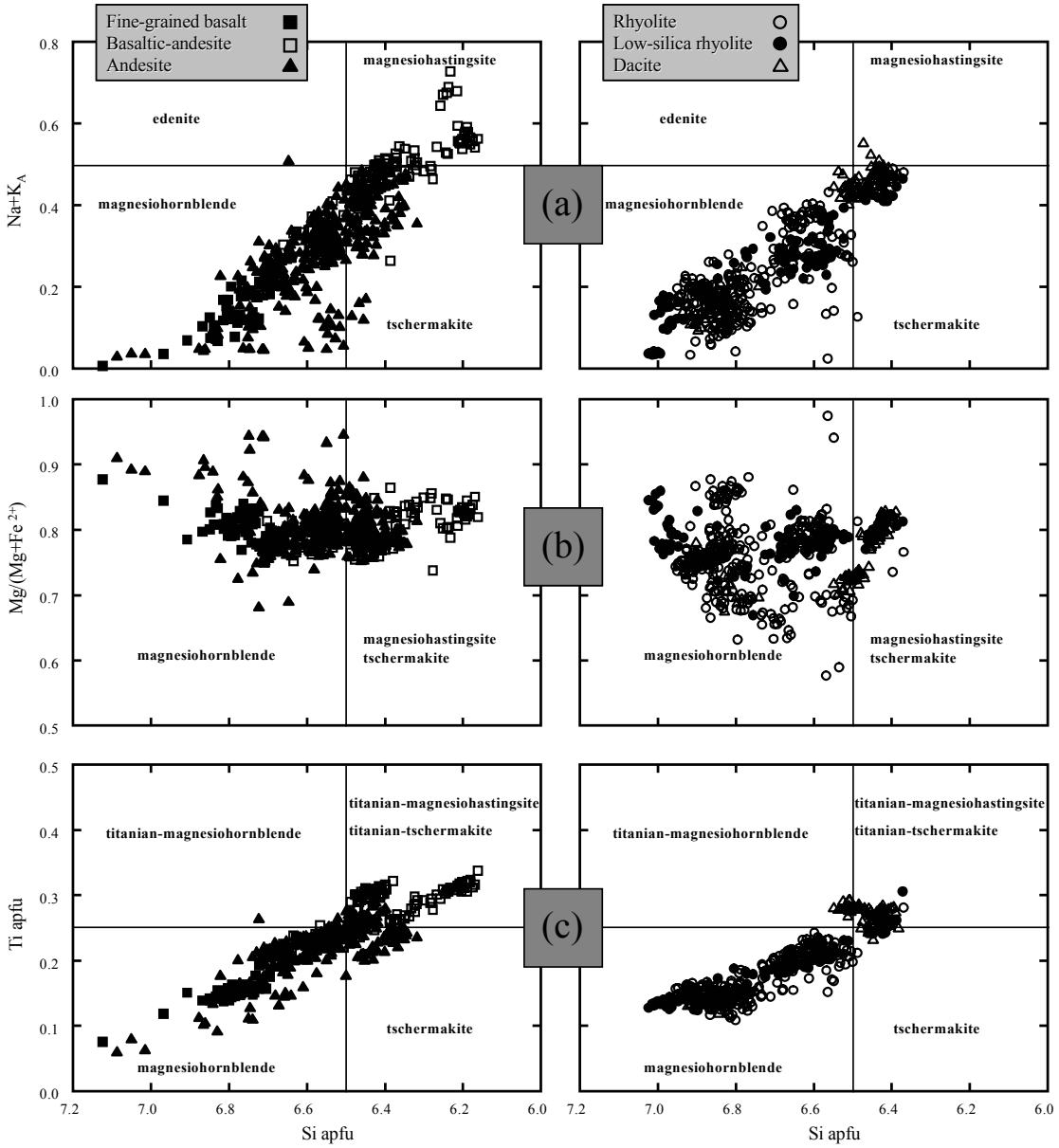

Fig. 4.3. Amphibole classification using structural formulae as recommended by Leake et al., 1997 (13eCNK: 13 cations excluding Ca, Na, and K). (a) $(Na+K)_A$ vs. Si; (b) X_{Mg} vs. Si; and (c) Ti vs. Si for Matahina basalt to rhyolite amphibole.

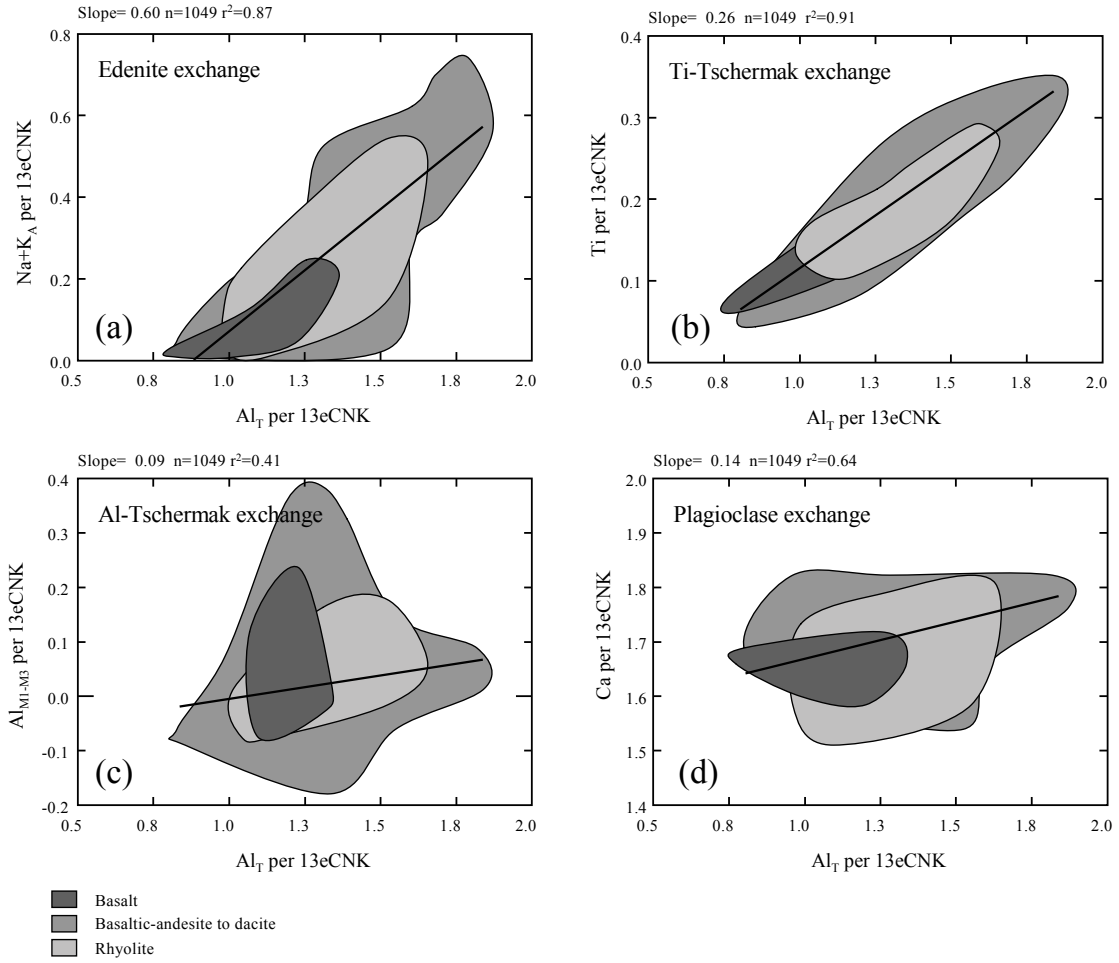

Fig. 4.4. Amphibole substitution mechanisms for Matahina basalt to rhyolite. Plots of Al_T vs. (a) $(Na+K)_A$, (b) Ti, (c) Al_{M1-M3} (note: Al_{M1-M3} is generally <0.15 afpu and negative values were calculated for some), and (d) Ca.

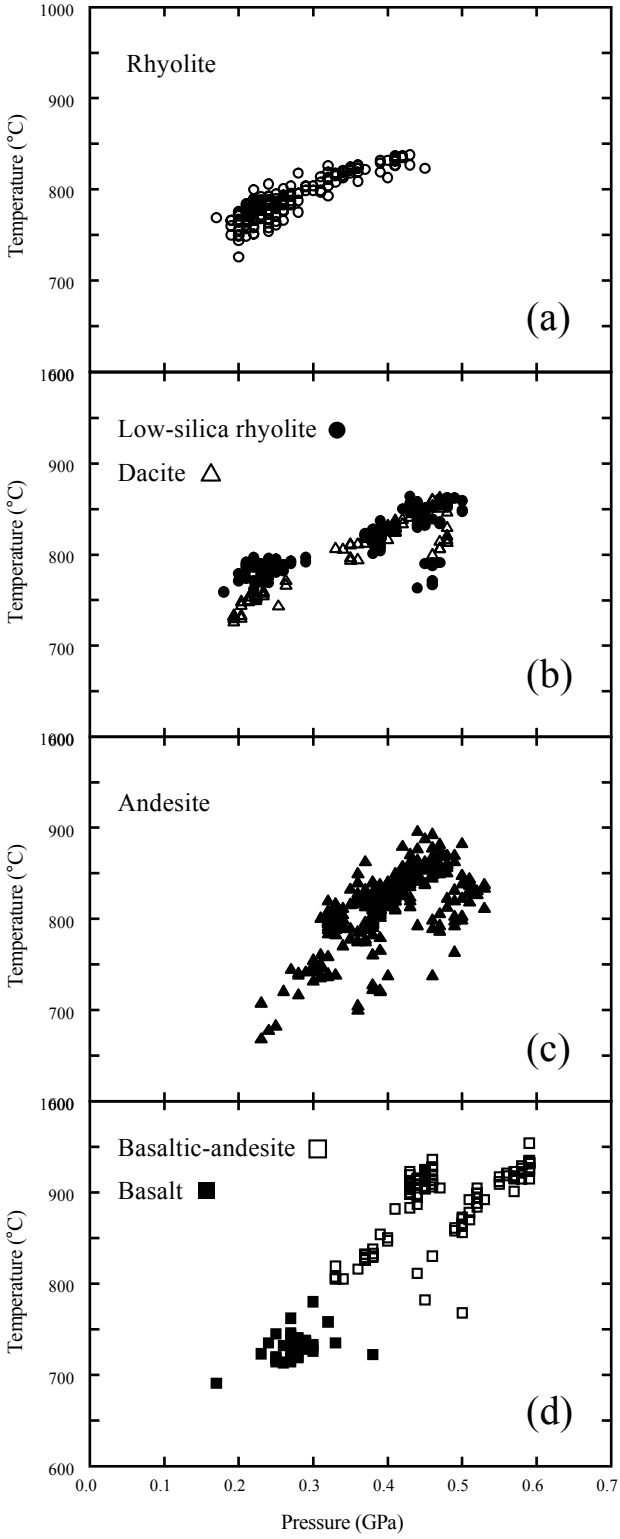

Fig. 4.5. Pressure and temperature distribution of the Matahina basalt to rhyolite. Pressure estimates using the algorithm of Schmidt (1992). Temperature estimates for rhyolite using Holland and Blundy (1994) and basalt-dacite using Féménias et al. (2006). Symbols as in Fig. 4.3.

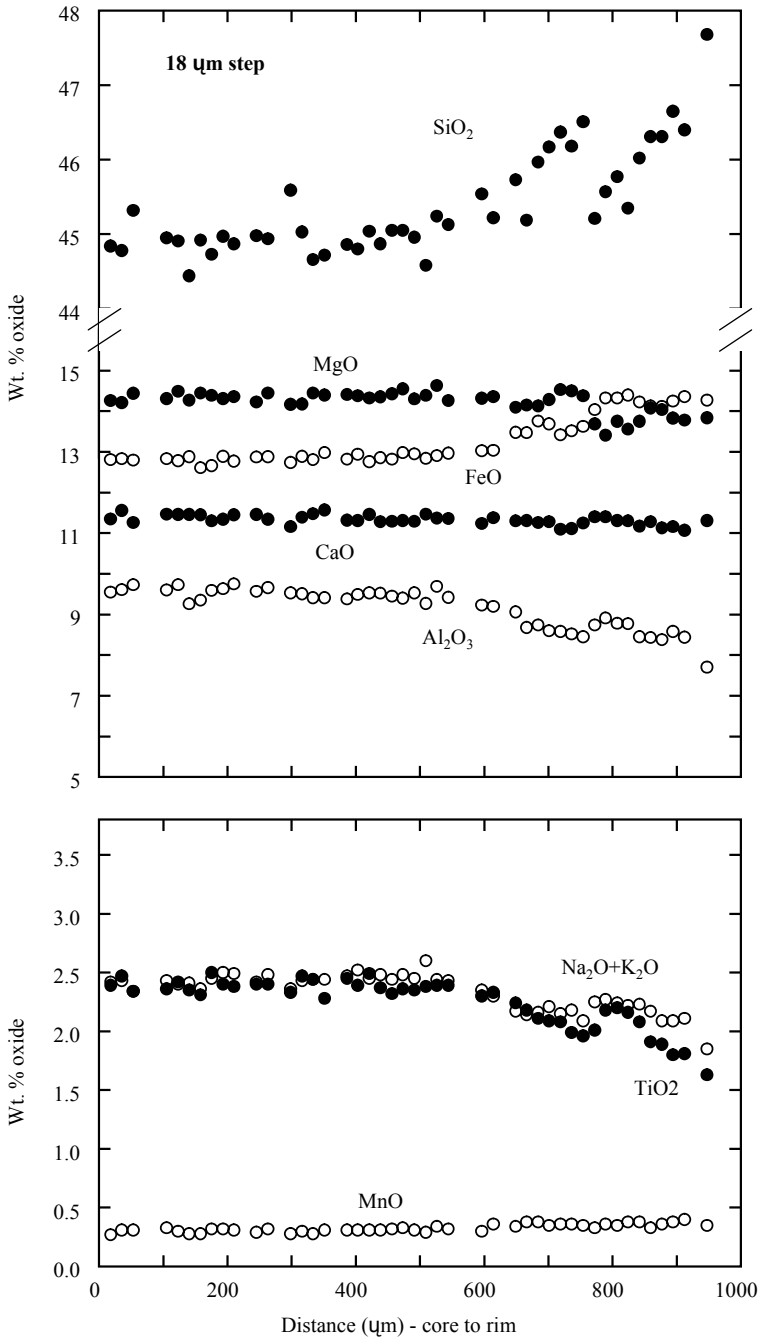

Fig. 4.6. Compositional profile of a representative calcic-amphibole in an andesite.

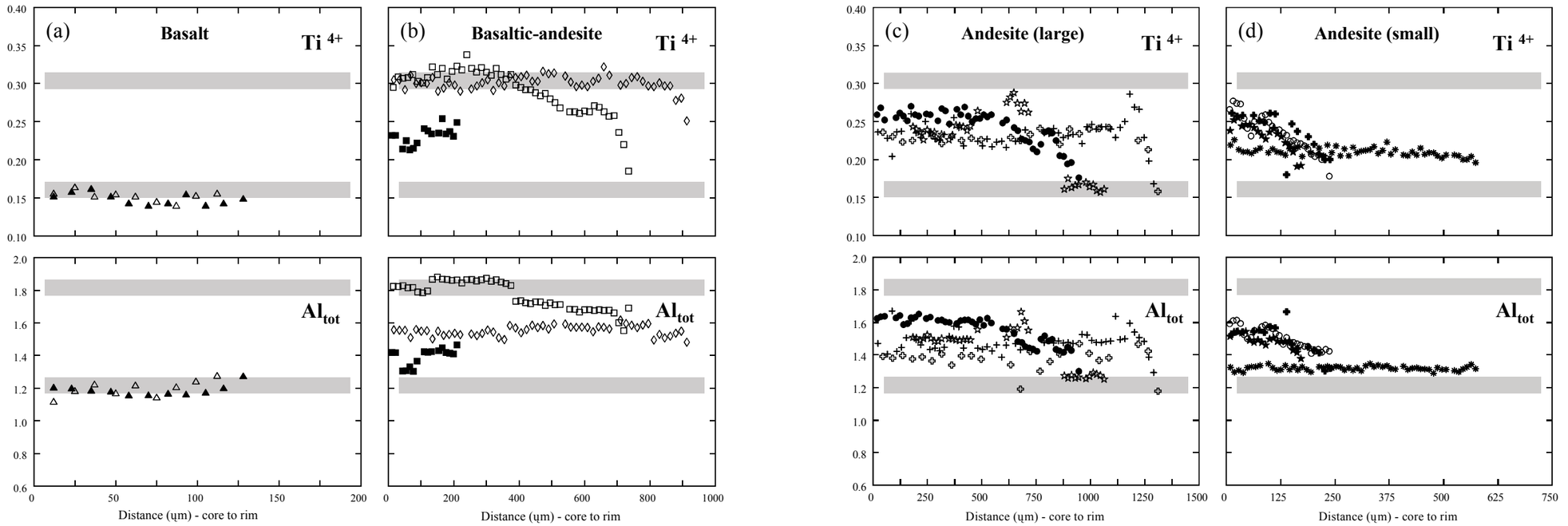

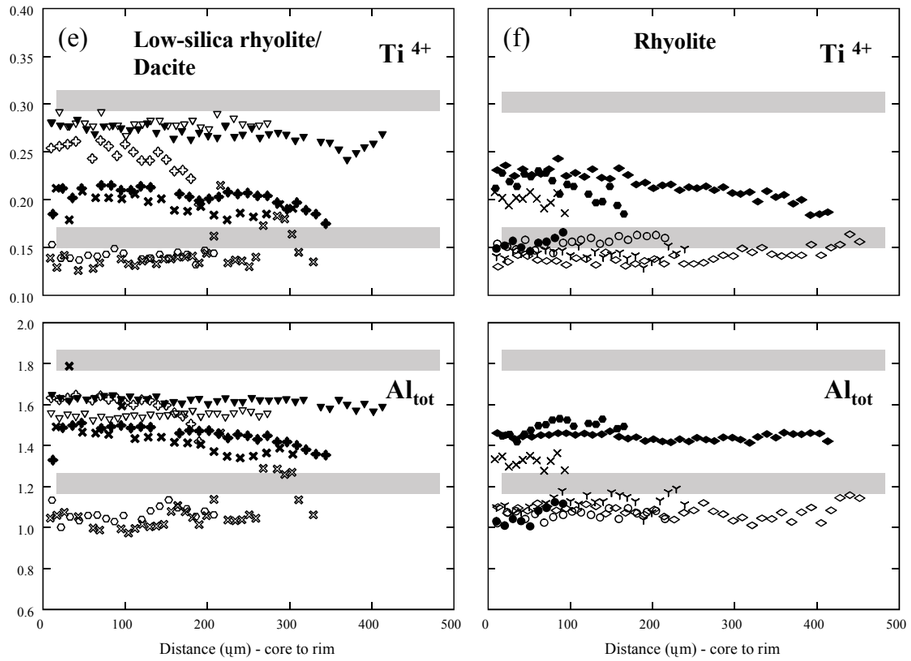

Fig. 4.7. Detailed microprobe traverses performed on the Matahina amphibole representing the suite of magma compositions erupted from basalt to rhyolite (a-f). Gray bars represent the Al_{tot} and Ti contents of high (P: 0.06 GPa and T: 950C) and low [(P: 0.3 GPa and T: 765°C (i.e. eruptive P-T conditions)] P-T categories. Each symbol is a different amphibole. See text for discussion.

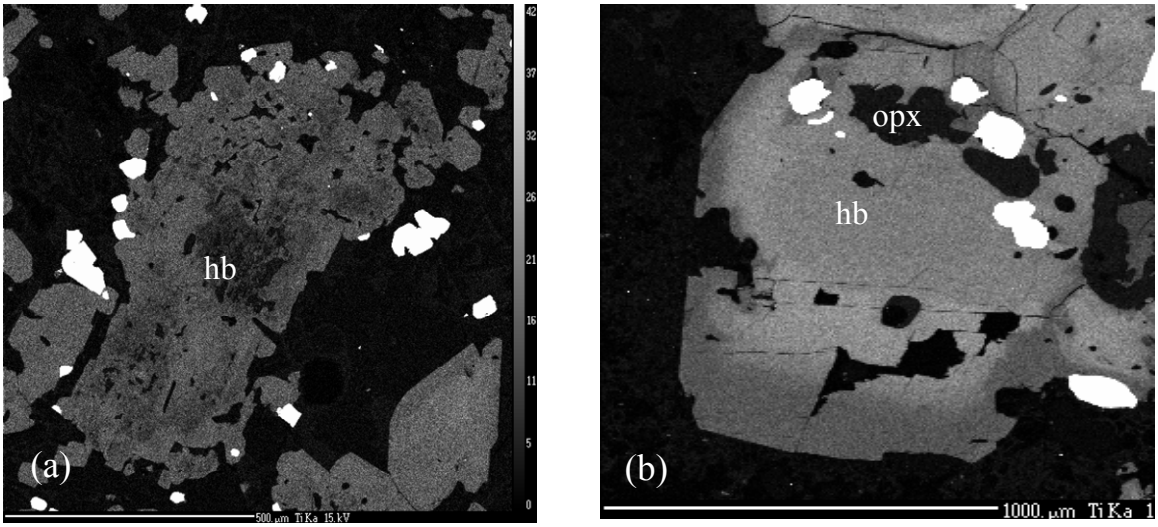

Fig. 4.8. Scanning electron microprobe element maps; Ti-concentrations are proportional to the degree of brightness and considered a proxy for temperature. Several distinct bands of higher Ti-content are observed in many hornblende: (a) over orthopyroxene (opx) cores within glomerocrysts in andesite, and (b) within large hornblende in basalt.

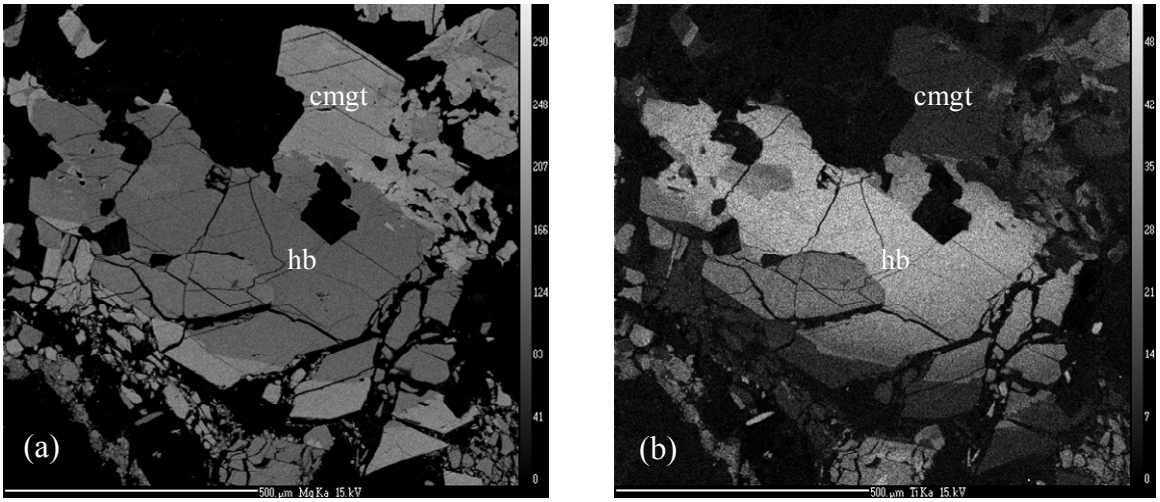

Fig. 4.9. Scanning electron microprobe element maps (sample: UC1239_4amph2; mingled andesite); Mg- and Ti-concentrations are proportional to the degree of brightness. (a) Variation in Mg-content of elongate (~1.0mm long axis), tschermakite (hb) with an irregular, abrupt transition to a cummingtonite (cmgt) overgrowth. (b) Variation in Ti-content of same grain as (a) illustrates the decrease in Ti from the core of tschermakite to the cummingtonite overgrowth boundary.

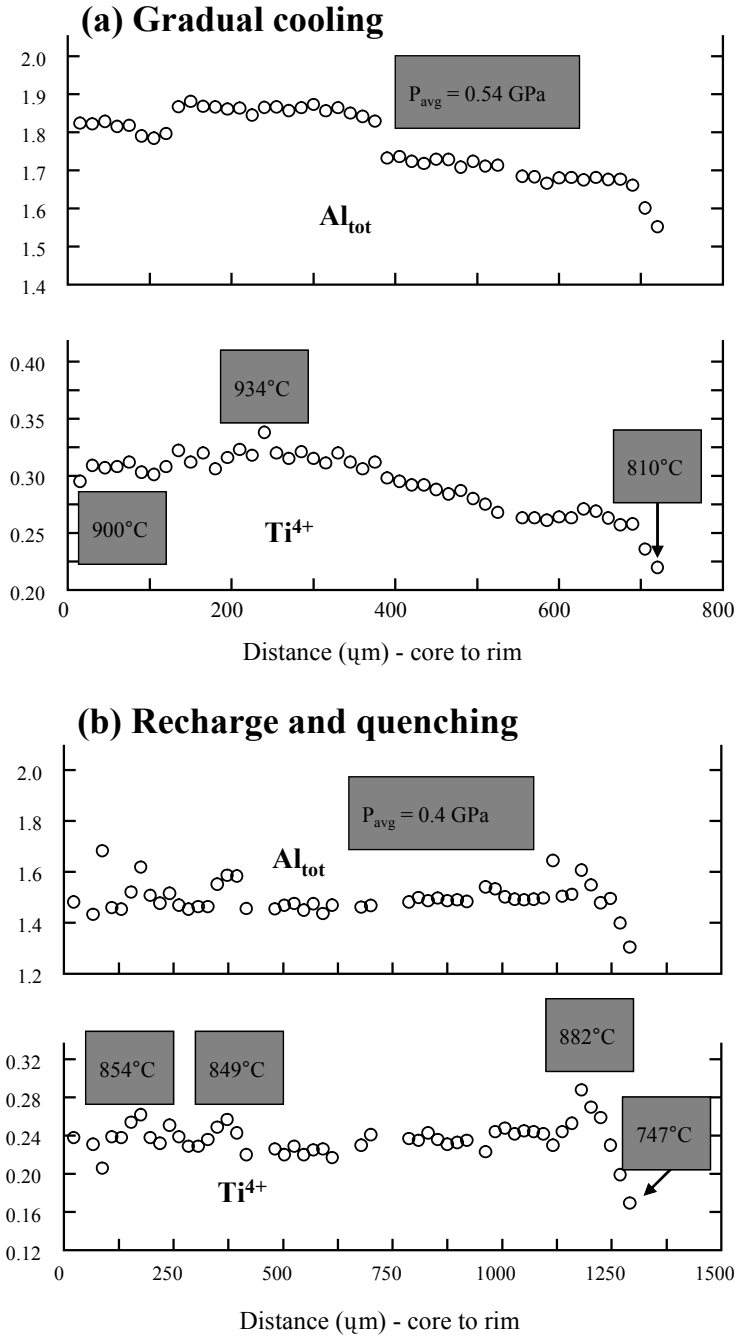

Fig. 4.10. Detailed microprobe profiles on Matahina hornblende. (a) A large basaltic-andesite hornblende (UC816_1amph1) displaying an early heating event (up to 934°C) followed by a gradual cooling (to 856°C) and rapid quench to 810°C, at relatively high-P (0.54 GPa). (b) Andesitic cumulate hornblende (UC1100_2amph1) displaying several discrete, moderate-T increases (up to 60°C), followed by a rapid quenching to 748°C.

4.14 TABLES

Table 4.1. Phenocryst assemblages of selected Matahina basalt to rhyolite clasts.

Sample	Map	Deposit	SiO_2 (wt. %)	G'mass	Plag	Amph	Amph: type/size(mm)	Oxides/Mgt	Ilm	Opx	Cpx	Biot	Qtz	Phenocryst total	$\sum r^2$
UC839	2	PDC	51.29	57.4	0.1	38.3	stub-bld/<0.5	4.1		0.1	-		-	42.6	
					0.2	*89.9*		*9.6*		*0.2*	-		-		
UC520	2	PDC	58.66	72.2	18.2	4.9	glom-bloc-tab-stub/<3.0	2.0		2.4	0.2		-	27.8	
					65.6	*17.8*		*7.2*		*8.7*	*0.7*		-		
UC832	2	PDC	66.33	83.7	9.8	4.1	tab-stub-glom-bloc/<1.5	0.3		1.8	0.1		0.2	16.3	
					60.1	*25.2*		*1.8*		*11.0*	*0.6*		*1.2*		
UC498	2	PDC	71.16	94.4	3.2	1.4	tab-stub/<1.0	0.3		0.4	-		0.4	5.7	
					55.8	*24.8*		*5.3*		*7.1*	-		*7.1*		
UC816	1	PDC	56.79*	73.0	11.0	11.8	glom-bloc-tab-stub/<2.0	2.0		1.9	0.3		-	27.0	
					40.7	*43.7*		*7.4*		*7.0*	*1.1*		-		
UC1100	1	PDC	57.65	51.8	28.0	16.9	glom-bloc-tab-stub/<3.5	1.6		1.1	0.6		-	48.2	
					58.1	*35.0*		*3.3*		*2.2*	*1.3*		-		
UC1123	1	PDC	63.75	76.9	13.2	5.9	glom-bloc-tab-stub/<2.0	1.1		2.7	0.2		-	23.1	
					57.0	*25.4*		*4.8*		*11.8*	*0.9*		-		
UC813	1	PDC	72.80	91.6	6.2	1.5	stub-bld/<1.5	0.4		0.4	-			8.4	
					73.2	*17.3*		*4.8*		*4.8*	-				
UC811	1	PDC	72.63	80.9	5.7	0.2	bld/<0.3	0.3		1.0	-	0.8	11.3	19.2	
					29.8	*0.8*		*1.3*		*5.0*	-	*4.2*	*59.0*		
UC175	3	ash-flow	72.68	0.79	0.167	0.001	tab-bld/<1.5	0.013	0.003	0.027	-	-	-	21.0	0.08
					79.5	*0.3*		*6.0*	*1.3*	*12.9*	-	-	-		
UC168	4	ash-flow	75.17	0.89	0.068	0.009	bld/<1.0	0.004	0.002	0.011	-	-	0.016	11.0	0.15
					61.5	*7.9*		*3.9*	*2.2*	*9.6*	-	-	*14.9*		
UC649	5	ash-flow	76.94	0.95	0.015	0.006	bld/<0.8	0.005	0.0001	0.001	-	-	0.024	5.0	0.02
					29.9	*12.1*		*9.1*	*0.4*	*1.1*	-	-	*47.5*		
UC887	6	plinian	77.85	96.7	1.1	-		0.1		0.1	-	-	2.2	3.3	
					31.8	-		*1.5*		*1.5*	-	-	*65.2*		

Modal phenocryst abundances for basalt to dacite acquired by counting 1000 pts. and rhyolite 2000 pts. per thin section or calculated by least-squares methods using glass, phenocryst, and bulk-rock compositions (Deering et al., 2008; author unpublished). *SiO_2 determined by mass balance using glass and phenocryst compositions. For point counts all oxides are given as magnetite. Map refers to localites in Fig. 1.

PDC = pyroclastic density current. Plagioclase: plag; Amphibole: amph; Magnetite: mgt; Ilmenite: Ilm; Orthopyroxene: opx; Clinopyroxene: cpx; Biotite: biot; Quartz: qtz. Stubby: stub; bladed: bld; glomerocryst: glom; blocky: bloc.

Table 4.2. Average of amphibole major element analyses and structural formulae of Matahina sensu stricto rhyolite and post-collapse basalt-rhyolite magmas

Sample	Basalt	Basaltic-andesite	Andesite	Dacite	Low-silica rhyolite	Rhyolite	Cummingtonite
n =	39	121	375	108	87	327	23
SiO_2	47.43	44.10	45.64	45.99	45.37	46.82	53.78
TiO_2	1.39	2.61	1.99	1.75	2.23	1.53	0.29
Al_2O_3	7.10	9.47	8.53	7.93	8.65	7.22	2.40
FeO	15.17	12.96	14.08	14.08	14.27	16.02	19.40
MnO	0.40	0.30	0.34	0.33	0.32	0.41	0.58
MgO	13.99	14.24	14.06	13.87	13.71	13.28	19.46
CaO	10.81	11.26	11.08	11.22	11.09	10.92	2.23
Na_2O	1.62	2.33	1.76	1.61	2.16	1.66	0.32
K_2O	0.14	0.32	0.27	0.27	0.33	0.33	0.02
F	0.13	0.22	0.16	0.18	0.27	0.28	0.14
Cl	0.12	0.04	0.06	0.15	0.06	0.12	0.03
Sum	98.30	97.88	97.97	97.38	98.46	98.58	98.64
Structural formulae							
Si	6.796	6.402	6.585	6.688	6.561	6.761	7.686
Al_{iv}	1.187	1.593	1.410	1.311	1.435	1.211	0.314
∑(T site)	8	8	8	8	8	8	8
Al_{vi}	0.004	0.023	0.036	0.049	0.036	0.012	0.090
Ti	0.150	0.285	0.216	0.192	0.243	0.167	0.031
Fe^{2+}	0.702	0.786	0.752	0.834	0.912	0.925	2.242
Mn	0.049	0.037	0.042	0.041	0.040	0.050	0.071
Mg	2.987	3.082	3.024	3.006	2.955	2.857	4.147
Fe^{3+}	1.108	0.786	0.947	0.879	0.814	0.990	0.076
∑(M,1,2,3 sites)	5	5	5	5	5	5	5
Ca	1.659	1.751	1.712	1.748	1.719	1.689	0.341
Na	0.341	0.249	0.288	0.252	0.281	0.311	1.659
∑(M4 site)	2	2	2	2	2	2	2
Ca	-	-	-	-	-	-	-
Na	0.108	0.407	0.228	0.217	0.324	0.155	0.000
K	0.025	0.060	0.050	0.050	0.060	0.061	0.003
∑(A site)	0.133	0.467	0.278	0.267	0.384	0.216	0.003
F	0.058	0.099	0.074	0.084	0.125	0.126	0.062
Cl	0.029	0.011	0.015	0.037	0.014	0.029	0.006
OH*	1.914	1.890	1.919	1.879	1.861	1.845	1.932
∑(OH site)	2	2	2	2	2	2	2
Sum cations	15.136	15.525	15.294	15.267	15.379	15.240	16.660
$(Ca+Na)_B$	2.00	2.00	1.98	1.99	2.00	2.00	0.35
$(Na+K)_A$	0.13	0.47	0.28	0.27	0.38	0.22	0.09
$Mg/(Mg+Fe^{2+})$	0.81	0.80	0.80	0.78	0.76	0.76	0.65

Table 4.3. Matahina geothermometry comparison

Method	*Fe-Ti oxides*	Hb-Pl	Ti-content	Opx-cpx
Sample				
Rhyolite (UC649)	773	742	723	-
Rhyolite (UC645)	756	754	730	-
Rhyolite (UC354)	746	770	724	-
Rhyolite (UC808)	773	748	721	-
Low-silcia rhyolite (UC175)	830	877	864	-
Low-silcia rhyolite (UC173)	-	-	-	859
Andesite (UC520)	-	-	-	877
Andesite (UC1100)	-	-	-	890
Basaltic-andesite (UC816)	-	-	-	1063

Fe-Ti oxides: Ghiorso and Sack (1991) Hb-Pl: Holland and Blundy (1994) and
Ti-content: Féménias et al. (2006)

CHAPTER 5

Development and the eventual destruction of an andesitic to rhyolitic compositional and thermal gradient: a case study of the caldera-forming Matahina eruption, Okataina Volcanic Complex

Development and the eventual destruction of an andesitic to rhyolitic compositional and thermal gradient: a case study of the caldera-forming Matahina eruption, Okataina Volcanic Complex

Deering, C.D.[1], Cole, J.W.[1], Vogel, T.A.[2], Baker, J.[3]

[1]Dept. of Geological Sciences, University of Canterbury, PB 4800, Christchurch 8020, New Zealand
[2]Dept. of Geological Sciences, Michigan State University, 206 Natural Sciences Bldg., East Lansing, Mi, 48824-1115, USA
[3]School of Geography, Environment and Earth Sciences, PO Box 600, Wellington, New Zealand
[1]cdd21@student.canterbury.ac.nz

Manuscript prepared for submission to Contributions to Mineralogy and Petrology.

Contributions

Jim Cole and Tom Vogel reviewed the drafts of this manuscript. Juvenile pumice clasts were analyzed for Sr-Nd isotope contents at Victoria University by Joel Baker.

5.1 ABSTRACT

The Matahina Ignimbrite (~160 km^3 rhyolite magma, 330 ka) was deposited during a caldera-forming eruption from the Okataina Volcanic Centre (OVC), Taupo Volcanic Zone (TVZ), New Zealand. The outflow sheet is distributed primarily to the northeast to southeast of the OVC and consists of a basal plinian fall member and three ash-flow members. Pumice clasts are separated into three groups defined by differences in bulk geochemistry and mineral contents: high CaO, MgO, Fe_2O_{3T}, TiO_2, and low Al_2O_3, +hornblende (A2), low CaO, MgO, Fe_2O_{3T}, TiO_2 ±hornblende (A1), and a subset to A1, which has high-K, +biotite (B). Two types of crystal-rich mafic clasts were also deposited during the final stages of the eruption. The distinct A and B rhyolite magma types are petrogenetically related to corresponding type A and B andesitic magma by up to 50% crystal fractionation under varying fO_2-fH_2O conditions. Further variations in the low- to high-silica rhyolites can be accounted for by up to 25% crystal fractionation, again under distinct fO_2-fH_2O conditions. Reconstruction of the P-T-fO_2-fH_2O conditions of the andesite to rhyolite magmas are consistent with the existence of a compositional and thermal gradient prior to the eruption. Magma mingling/mixing between the basalt-andesite and the main compositionally zoned rhyolitic magma occurred during caldera-collapse, modifying the least-evolved rhyolite at the bottom of the reservoir and effectively destroying the pre-eruptive gradients.

5.2 INTRODUCTION

Determining the processes governing the generation and maintenance of silicic magma reservoirs is an important area of research in igneous petrology. Variations of two end-member processes are typically presented: (1) partial melting of crust (Clemens & Wall, 1984; Pichavant *et al.*, 1988a, 1988b; Riley *et al.*, 2001; Smith *et al.*, 2003), or (2) crystal fractionation of a mafic progenitor (Bacon & Druitt, 1988; Hildreth *et al.*, 1991; Hildreth & Fierstein, 2000; Clemens, 2003). Each of these petrogenetic models has been tested in the Taupo Volcanic Zone (TVZ), New Zealand, over several decades. Available evidence has been used to suggest that the origin of the rhyolites is linked to partial melting or crystal fractionation of mafic magmas in the lower-middle crust accompanied by some degree of assimilation of continental crust (Graham *et al.*, 1992; McCulloch *et al.*, 1994; Graham *et al.*, 1995; Price *et al.*, 2005; Deering *et al*., 2008). Several variations of crystal fractionation models have been proposed that invoke the development of an intermediate (andesite-dacite) crystal mush zone (up to 60 vol. % crystals), where crystal-poor, silicic interstitial melt is periodically removed and stored in the upper crust (e.g. Bacon and Druitt, 1988; Sisson & Bacon, 1999; Hildreth & Fierstein, 2000; Bachmann & Bergantz, 2004).

However, the characteristics, development, and maintenance of such a reservoir or reticulated magma zone capable of producing large volumes of rhyolite still remain unresolved. Despite the evidence that these systems may have evolved dominantly by crystal fractionation in New Zealand, a potential mafic progenitor rarely appears at the surface, either as a primary erupted magma or co-magmatic/eruptive with a rhyolitic magma. For example, evacuation of ~530 km^3 of rhyolitic magma during the 26.5 ka Oruanui eruption included both tholeiitic and

calc-alkaline mafic magmas, but these were crystal-poor and represented late stage interaction with the main rhyolitic magma body (Wilson *et al.*, 2006). Several detailed studies of smaller TVZ rhyolitic eruptions (<150 km^3) have revealed the presence of slight compositional gradients within rhyolitic magma reservoirs prior to eruption (e.g. Milner *et al.*, 2001; Beresford, 1997). Brown *et al.* (1998) demonstrated that the voluminous (~2000 km^3 of magma, ~340-320 ka) Whakamaru eruption, although consisting of several rhyolitic compositions that could be related by fractional crystallization, was probably comprised of physically separate magma bodies that had individual evolving histories. Co-magmatic mafic components from each of these eruptions were also typically crystal-poor and apparently interacted with the main rhyolitic magma reservoir during eruption. Hence, the preservation of evidence in eruptive materials of any chemical, physical and thermal stratification into a more mafic mush zone is rare, implying that the intermediate mush zone either: 1) resides physically separate from the main rhyolitic magma reservoir, or 2) the magma rheology and/or accompanying caldera collapse hinders the exhumation of significant amounts of this magma.

This paper documents the petrology and geochemistry of an extensive representative sample suite of primary rhyolitic and subordinate crystal-rich mafic components from the 330 ka Matahina eruption. We include an evaluation of the pre-Matahina eruptive products, collectively termed the Murupara Subgroup, which consists of eight units of tephra deposits extending back to the Whakamaru eruption ~340 ka. However, our focus is on the three units that immediately precede the Matahina eruption, which share mineral and compositional characteristics with the Matahina deposits. Our model for the eruption of the Matahina *sensu stricto* provides

insight into the development of a compositional and thermal gradient, and the eventual destruction of that magmatic system induced by caldera collapse.

5.3 REGIONAL GEOLOGIC BACKGROUND

The TVZ in the North Island of New Zealand is a rifted arc (Wilson *et al.*, 1995) and can be divided into segments of dominantly andesitic cone-forming volcanism in the north and south, and a central region characterised by rhyolitic caldera-forming and dome-building eruptions (Healy, 1962; Wilson *et al.*, 1984) (Fig. 5.1). Since the inception of volcanism in this central region, 1.6 Ma, >6,000 km^3 of rhyolitic magma has erupted from eight major eruptive centres. The Okataina Volcanic Centre (OVC), located at the northern extent of the TVZ (Fig. 5.1), is defined as a complex of coalescing collapse structures, which formed during numerous pyroclastic eruptions over > 400 kyrs. (Nairn, 2002).

5.4 MURUPARA SUBGROUP

The Murupara Subgroup consists of a series of tephra deposits found throughout the eastern Bay of Plenty, which overlie the Tablelands Subgroup (terminology from Manning, 1996). The Murupara Subgroup (equivalent to the Bonisch pyroclastics of Nairn, 2002) is an obsidian-rich tephra, and includes the Matahina eruptives from the OVC. In the eastern Bay of Plenty these deposits are found up to 5 meters thick, but are dominantly made up of the uppermost, Matahina, eruptive unit. A generalized tephrostratigraphy is presented in Fig. 5.2.

Field observations of the clast size and deposit thickness proximal to the caldera boundary led Nairn (2002) to conclude that the Bonisch pyroclastics were likely OVC sourced. Manning (1995) also suggested that the Murupara-B through H

units were OVC sourced based on: 1) the thickness and distribution of the tephra deposits on the coast; 2) the similarities in deposit characteristics; and 3) the similarities in glass chemistry and mineral contents. The recently dated rhyolite dome, 350 ka (Leonard *et al.*, in prep), which outcrops north of Lake Rotoiti (Fig. 5.1; locality 8), also has similar mineral abundances and contents as the Murupara tephras.

Nairn (2002) suggested that local biotite-bearing rhyolitic pyroclastics, which lie stratigraphically underneath the Matahina ignimbrite, were also OVC sourced. Dense clasts and the absence of foreign lithic material are indicative of a dome-associated proximal deposit. The clasts contain abundant biotite+quartz and are similar to biotite+quartz-bearing rhyolite lithics that represent a significant portion of the clast type in Matahina lag breccias. Together this evidence supports the existence of biotite + quartz-bearing rhyolite domes within the Okataina caldera boundary prior to the Matahina eruption.

The age of the Murupara Subgroup, estimated by Manning *et al.* (1996) using paleoclimatic data, is between 340 and 330 ka. The final deposit in this sequence, the Matahina (Murupara-H), consists of a ca. 30 km^3 plinian style eruption followed by the voluminous expulsion of greater than 160 km^3 of rhyolitic magma during a catastrophic, caldera-forming event (Bailey and Carr, 1994; Manning, 1995). The Matahina ignimbrite lies mainly to the northeast, east, and southeast, extending radially up to 30 km from the caldera margin (Fig. 5.1; Bailey and Carr, 1994). The ignimbrite is thickest and most densely welded to the east where it ponded within the ancestral Rangitaiki river valley along the Ikawhenua Range (Fig. 5.1). Bailey and Carr (1994) separated the ignimbrite sequence into three cooling units termed the lower, middle, and upper members that represent three eruptive pulses estimated to have occurred over 20 to 60 days (Fig. 5.2a). These subcooling units are recognized in

the field by variations in the welding, and specifically, the upper member by a pinkish vapor-phase altered color; presence of clinopyroxene, orthopyroxene and hornblende; and denser more angular pumice. Lag breccias are found within the upper ignimbrite member capped by pyroclastic density current (PDC) deposits (Fig. 5.2b). A single, lithic-rich flow breccia, found along the shores of Lake Okataina (Fig. 5.1; locality 1), contains recycled Matahina ignimbrite clasts, lies stratigraphically below post-Matahina tephra deposits, and contains large (<25cm) pumice (some amphibole rich) and lithic clasts consistent with an OVC source. The presence of Matahina recycled ignimbrite and stratigraphic position below a thick post-Matahina plinian fall deposit (termed Torere by Manning, 1996) indicate that the flow breccia was emplaced contemporaneously with the Matahina upper ignimbrite member.

5.5 SAMPLING AND ANALYTICAL TECHNIQUES

Pumice, fiamme, ignimbrite clasts, rhyolite lava and rhyolite lithics were sampled from the upper Murupara Subgroup pyroclastic fall and flow deposits (Units E-H; Fig. 5.2) in an attempt to best represent the full distribution of the Matahina eruption and lead-up volcanic activity from the OVC (Fig. 5.1). Fiamme were cut out of welded ignimbrite and trimmed to remove the attached matrix. Small (<2 cm) pumice clasts were removed from 'recycled' Matahina type ignimbrite clasts from within the Matahina outflow sheet. The most abundant rhyolite lithics found in the Matahina plinian fall deposit and lag breccias were sampled for analysis to explore their relationship to the Matahina magma(s). A total of 200 representative samples were analyzed by X-ray fluorescence (XRF) and laser ablation – Inductively Coupled Mass Spectrometry (LA-ICP-MS).

Samples were trimmed using a diamond grinder and saw to remove any weathered rind or organic matter. Sample fragments were then cleaned in a sonic bath of distilled water for 10 minutes to remove any surface contaminants from the grinder and saw, then placed in an oven at 100ºC for a minimum of 24 hours. These dry fragments were rough crushed using a tungsten-carbide, pneumatic press. Any additional weathered fragments were removed from the sample aggregate prior to milling in a Frisch Planetary agate mill.

For the XRF and LA-ICP-MS analyses, three grams of the milled rock powder and 9.0 g of lithium tetraborate ($Li_2B_4O_7$), along with 0.5 g of ammonium nitrate (NH_4NO_3; used as an oxidizer), were fused in platinum crucibles at 1000 °C for 20-30 minutes on an orbital mixing stage. The melt was then poured into platinum molds, making a glass disk that was analyzed using a Bruker S-4 X-ray fluorescent (XRF) spectrograph. XRF major-element analyses were reduced by a fundamental parameter data reduction method using Bruker Spectra Plus® software, while XRF trace-element (Rb, Sr, and Zr) data were calculated using standard linear regression techniques using the ratio of the element peak to the Rh Compton peak, which corrects for mass absorption. Prior to any calculations, the background signal was subtracted from the standards and samples. Major- and trace-element concentrations in the samples were calculated based on a linear regression method using BHVO, W-2, STM-1, MRG-1, SY-2, SY-3, DNC-1, PCC-1, JA-2, JA-3, BIR, QLO-1, and RGM-1 standards.

The rare-earth elements and Nb, Ta, Hf, Ba, Y, Th, U and Pb were determined by LA-ICP-MS on the same glass disks as used for XRF analyses. A Cetac LSX200+ laser ablation system was used, coupled with a Micromass Platform ICP-MS, using strontium determined by XRF as an internal standard. Trace element data reduction was done using MassLynx software. Element concentrations in the samples were

calculated based on a linear regression method using well-characterized standards. All major- and trace-element whole rock analyses reported here were conducted at Michigan State University. Precision and accuracy of both XRF and LA-ICP-MS chemical analyses are reported in Vogel et al. (2006).

Mineral and glass compositions were determined using a Cameca SX 100 EPMA equipped with five wavelength spectrometers at the University of Michigan. For the minerals, we used an accelerating potential of 15 kV, a focused beam with a 0 μm spot size, counting time of ~3 min/ mineral, and a 10 nA beam current. The beam was defocused and the spot size increased to 10 μm for glass analyses to reduce Na loss. Standards used were natural fluor-topaz (FTOP); natural jadeite (JD-1); natural grossular, Quebec (GROS); natural adularia, St. Gothard, Switzerland (GKFS); synthetic apatite (BACL); synthetic Cr_2O_3; and synthetic $FeSiO_3$ (FESI).

The $^{87}Sr/^{86}Sr$ and $^{143}Nd/^{144}Nd$ isotopic ratios were measured on the Victoria University of Wellington, Geochemistry Laboratory Nu-Plasma Multi-Collector ICP-MS (MC-ICP-MS), Wellington, New Zealand. Mass spectrometric and laboratory techniques used are a modified version of those described in detail in Waight *et al.* (2002). The ratios were corrected for mass spectrometric fractionation using exponential law and normalized to $^{86}Sr/^{87}Sr = 0.710248$ (SRM987) and $^{143}Nd/^{144}/Nd = 0.512980$ (BHVO-2). Precision (2σ) is ±0.00002.

5.6 MURUPARA GEOCHEMISTRY

5.6.1 Rhyolite

Bulk-rock compositions

Juvenile rhyolite pumice and fiamme, pre-Matahina rhyolite lava dome clasts, rhyolite lithics, and recycled ignimbrite have been analyzed to represent the full

spectrum of eruptive deposits and magma types. Representative data are provided in Table 5.1, and the full dataset is available as Electronic Appendix 5.1.

Clasts display several distinct and coherent major and trace element trends and can thus be separated into groups. In general, there are two subparallel trends in most major elements that vary with SiO_2 content (Fig. 5.3). One group is defined by high CaO, MgO, Fe_2O_{3T}, TiO_2, and low Al_2O_3 trends, hereafter termed 'Group A2', and extends to the lowest SiO_2 contents (71.16 wt. %; Fig. 5.3). The other group is defined by low CaO, MgO, Fe_2O_{3T}, TiO_2, and high Al_2O_3 trends, hereafter termed 'Group A1', and is subparallel to A2, but extends only to 75.23 wt. % SiO_2 (Fig. 5.3). There is also a subset to Group A1, which has high-K contents (Fig. 5.3) and is hereafter referred to as Group B rhyolites. The Murupara units E-G and the 'recycled' ignimbrite pumice fall geochemically within the A1 and A2 Matahina groups, but individual pumice tend to share characteristics of both groups or overlap with the two types (Fig. 5.3). The 350 ka rhyolite dome, exposed along the northern margin of the present day caldera (Fig. 5.1), is included in Group A1.

Trace element variations further define the three distinct groups (Fig. 5.4). Group B has distinctive Th and Rb, but falls within the A1-group in all other trace element plots (Fig. 5.4). Group A1 has lower Zr, Sr, and Hf than A2, but overlaps with the A1 and B in Rb, Y, and Th. Group A2 has some of the lowest Rb contents, but also overlaps with groups A1 and B. Yttrium shows significant scatter among all groups. Rare-earth element (REE) contents are broadly similar with enriched LREE, slight depletion in MREE, and a negative Eu anomaly (Fig. 5.5).

Petrography and mineral contents

Phenocryst contents were determined by least squares mass balance using bulk-rock, glass, and mineral chemistry and point counting on thin sections of selected samples and yield total crystallinities ranging from 3-21 % for Matahina pumice and rhyolite lithics (Table 5.2). Samples within the A1, A2, and B geochemical groups each correspond with distinct mineral assemblages: A1) crystal-poor (<5 %), containing quartz + plagioclase + magnetite + orthopyroxene ± hornblende + ilmenite; A2) crystal-poor/moderate (5-21 %), containing plagioclase + quartz + hornblende + orthopyroxene + magnetite + ilmenite ± clinopyroxene ± biotite; and B) crystal-poor/moderate (4-17 %), containing quartz + plagioclase + biotite + magnetite + ilmenite. Accessory zircon, apatite, and pyrrhotite are present as microphenocrysts and mineral inclusions. Total crystal contents are negatively correlated with bulk-rock SiO_2 wt. % in the Matahina *sensu stricto* pumice clasts, but not with those from the PDC deposits (Table 5.2).

Plagioclase is the dominant felsic mineral in group A, but is generally less abundant than quartz in group B rhyolite. Phenocrysts are subhedral to euhedral and typically < 2 mm with subtle zoning. Quartz are subhedral to euhedral, and up to 2 mm in the A1 and 6 mm in the B group. The quartz/plagioclase ratio increases with increasing SiO_2 in the group A (Table 5.2). In contrast, the group B rhyolite always have high quartz/plagioclase ratios compared to the A group with no apparent relationship to bulk-rock SiO_2 wt. %. Hornblende in the high-silica A2 and A1 group are subhedral to euhedral and almost exclusively elongate and bladed up to 1 mm. Crystal habits are more varied in the low-silica, A2 rhyolite, including blocky and tabular euhedral types up to 1.5 mm, in addition to the bladed type. The abundance of hornblende is inversely proportional to total crystallinity and bulk-rock SiO_2 wt.% in the group A2 from the Matahina *sensu stricto* and is rarely present in the A1 group

(Table 5.2). Orthopyroxene are subhedral to euhedral and up to 1 mm in the A2 rhyolite, although mostly < 0.5 mm. Clinopyroxene are rare and only found in the A2 rhyolite pumice. Biotite are dominantly found in the group B rhyolite as flakes and books up to 1.2 mm. In contrast, the rare biotite in A2 clasts are flakes <0.5 mm in length. Magnetite and ilmenite are ubiquitous in the Matahina rhyolite pumice and are typically found included in orthopyroxene and less commonly in hornblende. Magnetite also occurs as individual phenocrysts and are anhedral to euhedral up to 0.4 mm. Exsolution lamellae were identified in magnetite from all groups.

Phase chemistry

Phenocrysts from 44 rhyolite samples were analyzed. These samples were selected to reflect the range of SiO_2 content from Murupara tephrostratigraphy (E-H; Fig. 5.2), and the full distribution of the Matahina outflow sheet (Fig. 5.1). The complete dataset of mineral chemistry is available in Electronic Appendix 5.2.

Plagioclase range in composition from An_{53} to An_{21} and $Or_{4.5}$ to $Or_{0.8}$ (Fig. 5.6a). The highest Or contents are observed in Group B and form a divergent trend from Group A1-2 plagioclase. The FeO_T increases with An content and decreases with K content (Fig. 5.6b). The A1- and B-group plagioclase are typically the lowest An % and A2 the highest and are, therefore, correlated with bulk rock SiO_2 (Fig. 5.8a). Rare sanidine is found in Group B, but appears only as microlites (< 50 μm). Calcic amphibole are tschermakite to magnesiohornblende, using the classification of Leake *et al.* (1997). Al_{iv} contents correlate well with Ti, $(Na+K)_A$, and Ca (e.g. Fig. 5.7a). Potassium is positively correlated with Cl (Fig. 5.7b). Hornblende Al_T is variable with respect to bulk rock SiO_2, but those from the low-silica A2 rhyolite have two distinct populations (Fig. 5.8c). Orthopyroxene compositions range from En_{60} to

En_{40} and $Wo_{3.3}$ to $Wo_{0.9}$ for all of the rhyolite types (Fig. 5.6c). Group A2 orthopyroxene encompass the entire En and Wo range, but are dominantly higher than the Group A1 (Fig. 5.8b). The low Mn contents in the A2 also distinguish them from Group A1 orthopyroxene, although several A1 orthopyroxene also have low Mn (Fig. 5.6d). Clinopyroxene compositions are ~En_{35} and ~Wo_{43}. Biotite from Group B rhyolite lithics and juvenile pumice clasts from the PDC deposit along the western caldera margin (Fig. 5.1; locality 1) are similar in composition (Fig. 5.7). However, the orthopyroxene+amphibole+biotite bearing rhyolite, also from locality 1, also includes a much higher MgO biotite.

Glass compositions range from 74 to 79 wt. % SiO_2 and mostly overlap with the high-silica rhyolite type. The lowest SiO_2 glass analyzed follows the bulk rock trend of the A2 group rhyolite. Although the K_2O content of glass from Group B is the highest among the rhyolites, distinct glass compositions also overlap with those from the A2 group (Fig. 5.9).

Intensive parameters and water content

Pre-eruptive temperatures and oxygen fugacities were estimated by Fe-Ti oxide equilibrium using the method of Ghiorso and Evans (2008), which has an uncertainty of ±30°C. Magnetite and ilmenite grains in direct contact were preferred for calculations; however, most were not actually touching, but included in single orthopyroxene phenocrysts. Therefore, the equilibrium test of Bacon and Hirschmann (1988) was used to determine the suitability of oxide pairs for temperature-oxygen fugacity estimates. Temperatures of low-silica, A2-types were also estimated by clinopyroxene-orthopyroxene equilibrium using the method of Ghiorso and Sack (1991). Results are given in Table 5.3.

The average pre-eruptive temperature and oxygen fugacity calculated for the high-silica rhyolite compositions, which include A1 and A2 groups, is 766°C and log units (ΔNNO; relative to the nickel-nickel oxide buffer) = -0.12, respectively. The temperature estimated for the low-silica, A2 rhyolite is 866°C (log units ΔNNO = 0.18), whereas clinopyroxene-orthopyroxene yields 853°C. These low-silica, A2 pumice clasts are only found in the PDC deposit overlying the lag breccia outside of the eastern caldera margin, in 'upper member' pyroclastic flow deposits to the east-southeast and southwest of the caldera margin, and within the Lake Okataina biotite-bearing PDC deposit within the western caldera margin (Fig. 5.1). While the Group B Fe-Ti oxide estimates yield temperatures within error of the high-silica A1 group (778°C), the oxygen fugacity is distinctly higher (log units ΔNNO = 0.50) than either of the Group A rhyolites. The range of estimated oxygen fugacities also correlates with orthopyroxene En-content (Fig. 5.10), consistent with changes observed in experiments (e.g. Sisson *et al.*, 2005).

Pressure estimates using Al-hornblende are inherently difficult for volcanic rhyolite compositions from the TVZ as they typically lack the full buffering assemblage (plagioclase + quartz + biotite + sanidine + hornblende + sphene) that is required, allowing the composition to change freely with temperature and oxygen fugacity. Only the group B pumice have the appropriate phase assemblage (with the exception of sphene), restricting quantitative interpretations of pressure to this group. However, Deering (in press) showed that the Al-Tschermak coupled exchange between Al_{vi} and Al_{iv} in hornblende, which is pressure dependent, accounted for some of the changes in Matahina hornblende compositions, concluding that Al-geobarometers (e.g. Schmidt, 1992; Smith and Anderson, 1995) could provide a relative indication of pressure among rhyolite groups. The results of that study

showed that the low-silica rhyolite (A2) crystallized at ~300 MPa (10-12 km depth) and the high-silica rhyolite (A1-B) at ~100-200 MPa (4-6 km depth).

Blundy and Cashman (2001) showed that in silica- and water-saturated melts pressure and temperature could be estimated from glass compositions projected into the synthetic Qz-Ab-Or-H_2O system and for relative pressures from silica-undersaturated melts. Quartz is present in the Matahina rhyolites (although rare in pumice <73 wt. % SiO_2), indicating silica-saturation. Water-saturation has not yet been determined using volatile abundances, but Johannes and Holtz (1990) demonstrated that in water-undersaturated experiments the cotectics are not significantly different than in water-saturated melts. Glass compositions of Group A1, A2, and B rhyolites plot between 100 MPa and 300 MPa (4-12 km depth), with the low-silica A2 rhyolite at the highest pressures from 200-300 MPa (up to 12 km depth). These results are similar to those determined by Al-hornblende geobarometry, indicating that the low-silica rhyolite crystallized at greater depths than the high-silica rhyolite. Although we recognize the limitations of both these methods, we suggest they provide useful relative estimates of crystallization depths among the different magma groups.

Water contents were estimated using plagioclase rim and glass compositions, assumed to be in equilibrium by the method of Housh and Luhr (1991). Estimates range from 2.77 to 5.42 wt. % H_2O (An method) and 3.61 to 5.70 wt. % H_2O (Ab method), from the low-silica to high-silica rhyolite type (samples: UC175, UC649, UC555, UC808). The increase in H_2O contents from low- to high-silica rhyolite types also coincides with an increase in the abundance of modal hornblende in Group A2 (Table 5.2).

5.6.2 Basalt-dacite

Bulk-rock compositions

Dense basalt to dacite pumice clasts were found at two localities: 1) along the western caldera margin (Fig. 5.1; locality 1) within the lithic rich pyroclastic flow deposit, which contains the biotite-bearing Group B pumice, and 2) directly above a lag breccia within a PDC deposit east of the caldera margin (Fig. 5.1; locality 2), which contains A1-2 group pumice. Representative data are provided in Table 1, and the full dataset is available as Electronic Appendix 5.1.

Andesite to dacite clasts are calc-alkaline and the basalt is tholeiitic. Similar to the rhyolite groups, these clasts can be divided into two groups based on differences in their bulk geochemistry. These groups are also related to the two geographically separate localities 1 and 2. Group B clasts erupted at locality 1 with the biotite-bearing, group B rhyolite pumice. The andesite to dacite clasts of Group B are similar to Group A in K_2O, MgO, and TiO_2 with the exception of sample UC1123; however, Group B has lower Al_2O_3 and Fe_2O_3 and higher CaO and Na_2O (Fig. 5.11).

Similar to the rhyolites, some trace element variations in the basalt-dacite further define Groups A and B. Group B is distinct in having lower Y and higher Sr than Group A (Fig. 5.12). Rubidium, Th, and Zr are similar in both groups, but the Hf shows significant scatter (Fig. 5.12). In both groups, Sr, Y, and Zr decrease only slightly with increasing SiO_2 and show scatter, whereas Th and Rb increase along a coherent trend (Fig. 5.12). Rare-earth element patterns are similar in both groups with slight enrichments in LREE and a slight depletion in MREE (Fig. 5.13). The Eu anomaly varies from slightly positive in the most crystalline andesite (UC1100; Table 5.1) to negative in the dacites, indicating a correlation with bulk-rock SiO_2; the basalt has a negative anomaly (Fig. 5.14).

Petrography and mineral content

Phenocryst contents were determined by point counting thin sections and yield crystallinities from 16-49 vol. % (Table 5.4). Group B has higher crystal contents than Group A pumice at comparable andesite and dacite compositions. Crystallinity decreases in both groups, relatively, from andesite to dacite. However, the rare basaltic clasts are fine-grained, hornblende-rich (up to 90 % modal), and crystal-rich (~43 vol. %). Another distinct clast type is the least evolved basaltic-andesite clast (bulk composition determined by mass balance), which shows obvious signs of distinct felsic and mafic glasses in hand sample, and has a lower crystallinity than the andesite. Although varying in abundance, the mineral assemblage for the basalt-dacite pumice is: plagioclase + amphibole + orthopyroxene ± clinopyroxene + magnetite + ilmenite ± quartz.

Textures such as glomerocrysts, embayed plagioclase, and corroded plagioclase with overgrowths are common features in the mafic clasts (Fig. 5.15). Glomerocrysts include all phases in the assemblage, but those with adcumulate textures (sutured grain boundaries) are typically dominated by hornblende, although a few are orthopyroxene dominated, and are up to 2.5 mm in diameter. Amphibole are anhedral within some of the glomerocrysts as a function of the adcumulate texture, but are more commonly intergrown with oxides and plagioclase and are euhedral up to 3 mm. Clinopyroxene are anhedral and commonly enclosed within large (2 mm) hornblende phenocrysts, but also occur as subhedral individual phenocyrsts (<2.0 mm). Most plagioclase (up to 3.5 mm) display deep embayments, with almost skeletal surfaces where melt has infiltrated the grain into the center (Fig. 5.15). Although not seen on all of the large, near skeletal, plagioclase, overgrowths occur and range in size

from ~50 μm to 150 μm. Orthopyroxene are subhedral to euhedral phenocyrsts up to 1.8 mm in length. Oxides are anhedral to euhedral up to 0.4 mm. Quartz are found in dacitic pumice and are subhedral to euhedral, bipyramidal, and up to 0.5 mm in length.

Phase chemistry

Phenocrysts from basalt-dacite samples were analyzed from samples that were selected to reflect the range of SiO_2 contents. Average compositions of minerals are given in Table 5.5, and the full dataset is available in Electronic Appendix 5.2.

Plagioclase compositions form a continuous range from An_{15} to An_{94} and $Or_{0.01}$ to Or_{11}; however, group B plagioclase are restricted from An_{34} to An_{90} (Fig. 5.16a). The FeO_T is positively correlated with An% and negatively correlated with K (Fig. 5.16b). Anorthite content (An%) does not clearly correlate with bulk-rock SiO_2 (Fig. 5.17). Intermediate pumice compositions have a wide range of An, but the basaltic clast has a narrow range of the highest An content. Calcic-amphibole are classified as Ti-magnesiohastingsite, magnesiohastingsite, Ti-tschermakite, tschermakite, magnesiohornblende, and cummingtonite. Cummingtonite occurs as hornblende overgrowths and as smaller individual groundmass phenocrysts. Al_{iv} contents correlate well with Ti, $(Na+K)_A$, and Ca (e.g. Fig. 5.16c). Orthopyroxene range from En_{47} to En_{78} and $Wo_{1.8}$ to $Wo_{4.0}$ (Fig. 5.16d). There is a slight negative correlation between Wo content and Mn and two opposing trends between En and Wo, with one outlier grain of the highest En content (Fig. 5.16e). Clinopyroxene range from En_{41} to En_{44} and Wo_{42} to Wo_{47} (Fig. 5.16d). En content does not correlate with bulk-rock SiO_2 (Fig. 5.17). Group B magnetite generally have higher Mg contents than group A and both are correlated with Al. Rhyolitic glass compositions

from the andesite to dacite overlap with those analyzed from the rhyolitic pumice (Fig. 5.18). However, the andesite to dacite glass compositions diverge slightly from the dominant high- to low-silica glass of the rhyolite. Glass from Groups A and B overlap and, noticeably, some fall within a low-K_2O group (Fig. 5.18).

Intensive parameters

Pre-eruptive temperatures and oxygen fugacity were estimated using several geothermometers: Fe-Ti oxides equilibrium, clinopyroxene-orthopyroxene, Ti-hornblende. The results of these calculations are summarized in Table 5.3. Iron-titanium oxide equilibrium calculations yield temperatures for the group B andesite and group A dacite within error of the eruptive temperatures determined for the Matahina rhyolite (~785°C). Temperatures estimated for basaltic-andesite to andesite hornblende cores, using the Ti-hornblende geothermometer of Féménias *et al.* (2006), average ~850°C, which is within error of those determined by clinopyroxene-orthopyroxene pairs (~920°C). Similar to the temperatures estimated using Fe-Ti oxide equilibria for the andesite to dacite pumice, the hornblende rims yield ~765°C. The fine-grained basalt temperature is 727°C, slightly less than the eruptive temperature of the other mafic clasts. Oxygen fugacity in the mafic group B is similar to that estimated for the group B rhyolite and higher than the mafic and felsic group A magmas.

5.6.3 Sr-Nd isotopes

Strontium and Nd isotopes are broadly within the field of other TVZ rhyolites (Fig. 5.19). Pre-Matahina biotite+quartz-bearing rhyolite lithics from the lag breccia and biotite+quartz-bearing pumice from the PDC deposit along the western margin of

the caldera (Fig. 5.1; localities 1 and 2) have Sr-Nd isotope compositions within analytical error of one another (Fig. 5.19). Murupara-E pumice and rhyolite dome clasts from the northern exposure along Lake Rotoiti (Fig. 5.1; locality 8) have Sr isotopes that are within error of one another, but different Nd isotopes. The Group A and B andesite are distinct from one another with respect to both Sr and Nd. The isotopic composition of Matahina pumice is negatively correlated with indicators of differentiation (e.g. SiO_2; Fig. 5.19) and the Group A andesite, but the Group A2, low-silica rhyolite is similar to the Group B andesite.

5.7 INCREMENTAL ASSEMBLY AND GROWTH OF THE MATAHINA MAGMA

5.7.1 Development of intermediate crystal-mush

Many silicic magma eruptions have been recorded that represent evacuation of a reservoir, which is zoned from crystal-poor to crystal-rich (up to 25% crystals). However, few intermediate 'mushes (25-55% crystals)' appear to accompany the extraction of voluminous crystal-poor rhyolite (only e.g. Hildreth and Fierstein, 2000). Marsh (1996) defined a rheological transition at ~25% crystals from a viscous fluid suspension to a high viscosity mush of reticulated crystals. This increase in viscosity was characterized as a 'viscosity barrier' by Smith (1979) preventing efficient extraction; barring energetic disruption – possibly by caldera collapse.

Despite the absence of copious amounts of intermediate crystal 'mush' in eruptive deposits, a growing body of evidence indicates that large rhyolitic magma reservoirs evolve via silicic melt extraction from intermediate mushes (see Bachmann and Bergantz, 2004; Hildreth and Wilson, 2007), rather than separation of crystals within the rhyolitic chamber. Hildreth and Wilson (2007) prefer a model for the well

studied Bishop Tuff (~600 km^3 rhyolitic magma), whereby secular escape of interstitial melt from these mushes would be favoured in extensional environments. Rift related faulting would repeatedly disrupt the mush column allowing the low viscosity hydrous rhyolitic melt (<10^4-$10^{5.5}$ Pa s at 700-800°C; Scaillet et al., 1998) to be incrementally extracted. This model appears to be consistent with the following observations of the pre-eruptive Matahina magma reservoir, obtained directly from clasts representing the intermediate mush extending to high-silica rhyolite, all exhumed during the eruption and accompanying collapse.

Pressure and temperature estimates indicate that the Matahina mafic magmas resided at greater depths than the rhyolites prior to eruption (Table 5.3), within the mid-crust at and just below the brittle-ductile transition at 10-12 km (Heise et al. 2007). Estimates of the pre-eruptive magma P-T-fO_2 conditions of the Group A and B andesite to dacite are consistent with pre-eruptive storage temperatures between 950°C and 850°C. Although the storage temperatures of Group A and B magmas are similar, several other features are distinctly different: 1) Group A oxygen fugacity is +0.05 (ΔNNO), whereas Group B is +0.49 (ΔNNO); 2) the hornblende/orthopyroxene ratio is higher in Group B compared to Group A andesite; and 3) although crystal contents decrease in both groups from andesite to dacite, the total crystal contents are different at comparable bulk rock compositions.

Therefore, although the major element trends from andesite to rhyolite indicate a potential genetic relationship (Fig. 5.20), the distinct compositional features and mineral contents of the two different crystal-rich andesites and geographic separation of the deposits suggest that two crystal mushes existed and would presumably produce distinct rhyolite compositions. Within this context we explore, in detail, the origin of compositional variations of the more evolved Matahina magma(s).

Trace elements are particularly sensitive to fractionation of mineral phases and, therefore, provide a good indicator of magma differentiation. Although the bulk composition of the andesite to low-silica rhyolite may have been influenced by magma mingling/mixing, as will be discussed in detail later, some of the trace element variations associated with primary crystal fractionation processes have been preserved. In detail, the trace elements show scatter among andesite to rhyolite clasts that otherwise follow coherent major element trends. We modelled crystal fractionation from the group A and B andesites to the rhyodacite/low-silica rhyolite compositions, using the mineral contents and modal percentages determined by mass balance and point counting. We targeted several trace elements that are preferentially partitioned into hornblende and plagioclase as these are the primary phases that vary in abundance between Group A and B andesite to rhyolite.

The results of our simplified models show that the array of trace element patterns observed in the rhyodacite/low-silica rhyolite can be explained by up to 15% fractionation of the distinct andesitic progenitors (Fig. 5.21). Crystal fractionation of the Group B andesite, which has the higher oxygen fugacity and hornblende/orthopyroxene ratio, produces liquids similar in trace element composition to the A2 low-silica rhyolite with high hornblende/orthopyroxene ratios. Whereas, the Group A andesite, which has the lower oxygen fugacity and hornblende/orthopyroxene ratio, produces liquids similar to the A2 low-silica rhyolite with likewise low hornblende/orthopyroxene ratios. These variations, therefore, can be reasonably explained by differences in the modal abundance of fractionating hornblende that are presumably associated with the amount of water in the system and, consequently reflect oxygen fugacity.

5.7.2 Rhyolite magma from intermediate mush

The broadly coherent major element trends that can be traced from each of the distinct andesitic progenitors provide first order indicators of the magmatic processes that were involved in the assembly of the Matahina rhyolite prior to eruption. In addition, hornblende, orthopyroxene, magnetite, and plagioclase form a continuous range of compositions from andesite to rhyolite (Fig 5.16). Consequently, the range of rhyolite compositions from a water-rich to water-moderate type are best explained as being generated by crystal fractionation from two distinct intermediate mushes. Together the following observations of the andesite-dacite and rhyodacite-high-silica rhyolite magmas erupted, support the existence of a compositional and thermal gradient from mid- to upper-crust: 1) The order of appearance of the mafic component and the pressure estimates for mafic to felsic magmas allow the construction of a compositional profile from crystal-rich andesite to rhyolite, and 2) The P-T estimates from basaltic-andesite/andesite to rhyolite ranged from 950°C to 760°C and from 400 MPa to 100 MPa, respectively.

5.7.3 Pre-Matahina rhyolitic magmatism

The bulk rock, mineral compositional overlap, and isotopic similarities among the Murupara E, F, and G units, Lake Rotoiti dome, Group B lithics, and the Group A1-2 and B Matahina magmas provide some temporal constraints on the assembly of Matahina magmas prior to the catastrophic event. Extrusive dome construction apparently extended out to the northern caldera boundary, probably similar to the dome complex that occupies the current OVC. Although the glass compositions and some bulk rock compositions of biotite-bearing rhyolite pumice from the post-collapse PDC deposit on the west of the caldera (Fig. 5.1; locality 1) are similar, the

higher K_2O indicates they may be a distinct magma batch or derived from a less-evolved composition. Further discussion of the rhyolite petrogenesis, therefore, refers to the pre-Matahina and Matahina compositions collectively within their respective groupings outlined earlier (Groups A1, A2, and B).

5.7.4 Upper-crustal fractionation (4-8 km)

The paucity of disequilibrium textures in the Matahina *sensu stricto* low- to high-silica rhyolite permits a more comprehensive evaluation of the geochemical diversity. The andesite to rhyodacite modeling can be used to suggest a model in which distinct mushes existed in the mid-crust prior to the Matahina eruption, and these fed several distinct rhyolite magma reservoirs within the adjacent upper crust. Similar to the andesite to rhyodacite major element trends, there are coherent trends from low-silica to high-silica rhyolite consistent with crystal fractionation (Figs 5.3 & 5.4). However, the subparallel trends that define Groups A1 and A2 rhyolites and the distinct high-K_2O of the Group B rhyolite require additional model refinements. In addition, significant scatter in Y and the range of variation in REE are also evaluated.

One important feature of the andesite to rhyodacite model is the difference in hornblende/orthopyroxene ratios between the Group A and B andesites that produced distinct liquid compositions with respect to key trace elements (e.g. Dy, Y, Sr). In a second stage, we model crystal fractionation extending from rhyodacite compositions, where each has distinct hornblende/orthopyroxene ratios along separate trends. As hornblende and plagioclase are the dominant phases present in the rhyodacites we chose to model using Y, Dy, and Sr, which are highly partitioned into those phases. Similar to the andesite to rhyodacite model, ~15% crystal fractionation of the high hornblende/orthopyroxene rhyodacite to rhyolite produces the A1 and A2 low Y and

Dy melts (Fig. 5.22). Group B high-silica rhyolite can be produced by ~20% crystal fractionation of the lowest-silica group B rhyolite generating the observed trends to higher Y values (Fig. 5.22).

Several additional features are also consistent with the first stage of andesite-rhyodacite modelling. First, trace element contents of melts, derived from crystal fractionation, and oxygen fugacity are well correlated (Fig. 5.22). For example, Dy is quantitatively well correlated with oxygen fugacity (Fig. 5.23) and qualitatively with the presence and abundance of hydrous phases consistent with derivation from discretely differing fO_2 and fH_2O conditions throughout the magma reservoir. Second, the decrease in crystal contents with increasing bulk-rock SiO_2. Third, P-T estimates of low- to high-silica rhyolites are consistent with a thermal gradient from ~850°C to ~750°C with depth from ~8 km to ~4 km depth, respectively.

5.7.5 Magma mingling/mixing

Although P-T constraints and compositional variations can predominantly be explained by fractionation from an andesitic progenitor to produce the rhyolite, the following characteristics of deposits derived from the final eruptive phase indicate that mingling/mixing during or slightly before eruption was an important process and modified the composition of a subordinate volume of the Matahina rhyolite *sensu stricto*. First, the ubiquitous disequilibrium textures (e.g. deeply embayed plagioclase, spinel exsolution lamellae) found in pumice clasts from the PDC and upper member deposits indicate a late stage mixing event occurred. Second, some magnetite, hornblende and glass are bi-modal, but only in the upper member low-silica rhyolite and in the PDC deposits. In contrast, most mineral and glass compositions from the Group A and B andesite to rhyolite overlap suggestive of complex mixing prior to

eruption that included both types of mush and rhyolite types. Third, using ratio-ratio comparisons, mingled dacite to low-silica rhyolite clasts, which also display bimodal mineral chemistry (e.g. UC175 opx and mgt), have distinct Zr contents offset from the dominant rhyolite fractionation trend (Fig. 5.24a). Although a simple mixing line cannot be drawn from rhyolite to andesite (Fig. 5.24b), the pumice with distinct Zr form a trend towards the andesite-dacite. Fourth, Deering (in press) showed, using detailed compositional traverses of amphibole crystals, that the basalt to dacite compositions quenched against the cooler rhyolite, and coupled with the distinct glass compositions presented here, implies that crystal + melt exchange occurred across the lower extent of the rhyolite magma chamber.

Another aspect of the amphibole chemistry that is consistent with both crystal fractionation and mingling/mixing models is related to volatile concentrations. Distinct trends in volatile contents in hornblende are consistent with differences also observed in glass contents. There is an increase in volatile contents from andesite to rhyolite reflected in both hornblende and glass (Figs. 5.16d & 5.25). In contrast, the fine-grained basalt, which has low K and high Cl glass, has low K and Cl hornblende similar to the other mafic clasts (Figs. 5.16 & 5.25). Most mantle-derived basalts are dense and would stagnate in the lower crust crystallizing and assimilating to feed the middle crust with intermediate magma (Annen et al., 2006; Dufek and Bergantz, 2005). However, the fine-grained texture and mineral assemblage (hornblende + plagioclase + oxides) of the basalt reflects significant undercooling due to direct interaction with the main rhyolitic magma body (e.g. Oruanui eruption; Wilson et al., 2006) following penetration of the intermediate mush (Wiebe and Collins, 1998). Consequently, we interpret the trend to higher volatile contents (Cl, F) as indicative of a combination of two processes 1) volatile transfer during crystal fractionation of the

andesitic progenitors producing the dominant andesite to rhyolite trend, and 2) the mingling of a volatile rich melt from the basalt with parts of the rhyolitic magma; analogous to mafic sheets preserved in plutons (e.g. Wiebe and Collins, 1998).

Additionally, if we consider the evidence from basaltic-andesite/andesite amphibole chemistry that there were several recharge events recorded during the mush evolution Deering (in press), perhaps these recharge events were coincident with basalt-rhyolite interaction and triggering of earlier Murupara events. Basaltic triggering of rhyolitic eruptions in Okataina has been documented for more recent volcanic activity (e.g. Leonard et al. 2002; Shane et al. 2007), and monogenic basalt eruptions are closely temporally associated with other rhyolitic eruptions (e.g. Schmitz and Smith 2004).

5.7.6 Eruptive model

Pre-Matahina volcanism

The eruptive activity that preceded the Matahina eruption signified the early stages of magma assembly and indicates that distinct magma batches resided geographically within the current trace of the caldera. A schematic of the pre-eruptive magmatic system beneath the OVC is provided in Fig. 5.26. Periodic venting of the Group B biotite-bearing, Group A2 orthopyroxene + hornblende-bearing, and Group A1 orthopyroxene ± hornblende-bearing magma types occurred prior to the climactic Matahina eruption. The frequency, style, and volume could be compared to the current activity within the OVC, which has erupted smaller volumes of rhyolite that are distinctly different along the two linear vent zones. The distribution of these magmas within the current trace of the caldera complex and the timing of the Group B biotite-bearing rhyolite dome building remain unclear, but the exposures of the Group

A1-2 rhyolite dome remnants (Fig. 5.1; locality 8) are consistent with the existence of a magma reservoir that extends even to the northwestern caldera margin. Ar-Ar age dates (Leonard et al. in prep) coupled with paleoclimate dating of associated Murupara tephra deposits indicate that the Matahina magma assembly began at least 25 kyrs. prior to the 330 ka eruption.

Matahina eruption

The early plinian phase of the Matahina eruption only evacuated the type A1, high-silica rhyolite, which contains rare hornblende. Although the A2 rhyolite appears in the first flow deposit the low-silica A2 rhyolite was only found to the southeast in one pinkish ash-flow deposit, which would be considered the upper member of the Matahina by Bailey and Carr (1994). Therefore, the distribution of the final phase of the eruption appears to be primarily along an array from east/southeast to west and includes not only the Group A1 and A2 rhyolitic magma types, but also the Group B rhyolite and Groups A and B andesite to dacite from the PDC deposits. Importantly, the A1 rhyolite is still mixed within the PDC deposit. Consequently, we infer that the collapse corresponded with unzipping of the crust along ring faults tapping the uppermost portion of the magma reservoir unevenly through time. The exhumation of the andesite to dacite mush likely represents mid-crustal aliquots, which are squeezed out along the ring faults as the crust founders. Late stage interaction with the foundering crust is also evidenced by the increase in Sr-Nd isotopes (Fig. 5.19), and hence assimilation from rhyolite to andesite compositions. A similar model was proposed for caldera collapse induced late stage mixing and exhumation of mafic mush along the Ossipee ring dyke, New Hampshire, USA (Kennedy and Stix 2007).

The eruption of more than one compositionally distinct rhyolitic magma is not unique in the TVZ. Several eruptions have also had several compositionally distinct magma bodies erupt that could be related by crystal fractionation (e.g. Whakamaru, Brown et al. 1998; Rerewhakaaitu, Shane et al. 2007; Rotoiti, Schmitz and Smith 2004; Shane et al. 2005). Even the eruption of two distinct mafic magma types is not unique as Wilson et al. (2006) showed both a calc-alkaline and tholeiitic type interacted with the Oruanui rhyolitic magma. What is unique is the crystal content (phenocrystic hornblende) and abundance within the mafic clasts, which represent a zone within the mid-crust that has rarely been sampled.

5.8 CONCLUSIONS

The chemical characteristics of distinct crystal mushes, erupted within 15-20 km of one another, strongly support a model whereby variable amounts of fluid are contained within the melt column within the OVC. This variation can give rise to the production of different magma types, which range from those that are wet-oxidizing to those that are relatively dry-reducing rhyolites. These rhyolites coexist as incompletely mixed magmas within a single reservior. Although the caldera collapse disrupted the compositional and thermal gradient that had formed, collectively, the phase chemistry, crystal contents, and bulk-rock compositions retain some clues to the structure of the magmatic profile. Mixing was only important in influencing the composition of subordinate aliquots of the main Matahina rhyolite magma body, modifying the stratified dacite to low-silica rhyolite compositions in the late stages of the eruption, and were probably induced by the caldera collapse. Therefore, this case study of the Matahina eruption may provide our first insight into the deeper processes

that drive production of the highest volumes of rhyolite erupted on earth over the past two million years.

5.9 ACKNOWLEDGEMENTS

We would like to thank the Marsden Fund administered by the Royal Society of New Zealand (UOC0508) and the Department of Geological Sciences, University of Canterbury, Mason Trust Fund for financial support. Electron microprobe analysis at the University of Michigan was supported by NSF grant #EAR-9911352. Rose Turnbull is thanked for help preparing samples for Sr-Nd isotope analyses.

5.10 REFERENCES

Bachmann, O. & Bergantz, G.W. (2004). On the Origin of Crystal-poor Rhyolites: Extracted from Batholithic Crystal Mushes. *Journal of Petrology* **45**, 1565-1582.

Bacon, C.R. & Druitt, T.H. (1988). Compositional evolution of the zoned calcalkaline magma chamber of Mount Mazama, Crater Lake, Oregon. *Contributions to Mineralogy and Petrology* **98**, 224-256.

Bacon, C.R. & Hirschmann, M.M. (1988). Mg/Mn partitioning as a test for equilibrium between coexisting Fe-Ti oxides. *American Mineralogist* **73**, 57-61.

Bailey, R.A. & Carr, R.G. (1994). Physical geology and eruptive history of the Matahina Ignimbrite, Taupo Volcanic Zone, North Island, New Zealand. *New Zealand Journal of Geology and Geophysics* **37**, 319-344.

Beresford, S.W. (1997). Volcanology and Geochemistry of the Kaingaroa Ignimbrite, Taupo Volcanic Zone, New Zealand. *Unpublished PhD thesis*, *University of Canterbury Library*.

Blundy, J. & Cashman, K.(2001). Ascent-driven crystallisation of dacite magmas at Mount St. Helens, 1980-1986. *Contributions to Mineralogy and Petrology* **140**, 631-650.

Brown, S.J.A., Wilson, C.J.N., Cole, J.W., Wooden, J.L. (1998). The Whakamaru Group ignimbrites, Taupo volcanic zone, New Zealand: evidence for reverse tapping

of a zoned silicic magmatic system. *Journal of Volcanology Geothermal Research* **84**, 1-37.

Clemens, J.D. (2003). S-type granite-petrogenetic issues, models and evidence. *Earth-Science Reviews* **61**, 1-18.

Clemens, J.D. & Wall, V.J. (1984). Origin and evolution of a peraluminou ignimbrite suite: the Violet Town Volcanics. *Contributions to Mineralogy and Petrology* **88**, 354-371.

Deering, C.D., Cole, J.W., Vogel, T.A. (2008). A Rhyolite Compositional Continuum Governed by Lower Crustal Source Conditions in the Taupo Volcanic Zone, New Zealand. *Journal of Petrology* **49**, 2245-2276.

Deering, C.D. (in press). Cannibalization of an amphibole-rich andesitic progenitor induced by caldera-collapse during the Matahina eruption: Evidence from amphibole compositions. American Mineralogist.

Féménias, O., Mercier, J-C. C. Nkono, C., Diot, H. Berza, T., Tatu, M. Demaiffe, D. (2006) Calcic-amphibole growth and compositions in calc-alkaline magmas: Evidence from the Motru Dike Swarm (Southern Carpathians, Romania). American Mineralogist, 91, 73-81.

Gamble, J.A., Smith, I.E.M., McCulloch, M.T., Graham, I.J., Kokelaar, B.P. (1993). The geochemistry and petrogenesis of basalts from the Taupo Volcanic Zone and

Kermadec Island Arc, S.W. Pacific. *Journal of Volcanology and Geothermal Research* **54**, 265-290.

Ghiorso, M.S. & Evans, B.W. (2008). Thermodynamics of rhombohedral oxide solid solutions and a revision of the Fe-Ti two-oxide geothermometer and oxygen-barometer. American Journal of Science **308**, 957-1039.

Ghiorso, M.S. & Sack, R.O. (1991). Fe-Ti oxide geothermometry: thermodynamic formaulation and estimation of intensive variables in silicic magmas. *Contributions to Mineralogy and Petrology* **108**, 485-510.

Graham, I.J., Cole, J.W., Briggs, R.M., Gamble, J.A., Smith, I.E.M (1995). Petrology and petrogenesis of volcanic rocks from the Taupo Volcanic Zone: a review. *Journal of Volcanology Geothermal Research* **68**, 59-87.

Graham, I.J., Gulson, B.L, Hedenquist, J.W., Mizon, K. (1992). Petrogenesis of late Cenozoic volcanic rocks from the Taupo volcanic zone, New Zealand, in the light of new lead isotope data. *Geochimica et Cosmochimica Acta* **56**, 2797-2819.

Healy, J. (1962). Structure and volcanism in the Taupo volcanic zone, New Zealand. *Geophysical Monograph* **6**, 151-157.

Heise, W., Bibby, H.M., Grant, C.T., Bannister, S.C., Ogawa, Y., Takakura, S., Uchida, T. (2007). Melt distribution beneath a young continental rift; the Taupo Volcanic Zone, New Zealand. *Geophysical Research Letters* **34**, 28.

Hildreth. W. & Fierstein, J. (2000). Katmai volcanic cluster and the great eruption of 1912. *Geological Society of America Bulletin* **112**, 1594-1620.

Hildreth, W. & Wilson, C.J.N. (2007). Compositional zoning of the Bishop Tuff. *Journal of Petrology* **48**, 951-999.

Hildreth, W., Halliday, A.N. & Christiansen, R.L. (1991). Isotopic and chemical evidence concerning the genesis and contamination of basaltic and rhyolitic magma beneath Yellowstone Plateau volcanic field. *Journal of Petrology* **32**, 63-137.

Housh, T.B. & Luhr, J.F. (1991). Plagioclase-melt equilibria in hydrous systems *American Mineralogist* **76**, 477-492.

Johannes, W. & Holtz, F. (1990). Formation and composition of H2O undersaturated granitic melts. In: Ashworth, J.R., Brown, M. (Eds.), *High-Temperature Metamorphism and Crustal Anatexis. Unwin Hyman, London*, 87-104.

Kennedy, B. & Stix, J. (2007). Magmatic processes associated with caldera collapse at Ossipee ring dyke, New Hampshire. *Geological Society of America Bulletin* **119**, 3-17.

Leake, B.E., Wooley, A.R., Arps, C.E.S., Birch, W.D., Gilbert, M.C., Grice, J.D., Hawthrone, F.C., Kato, A., Kisch, H.J., Krivovichev, V.G., Linthout, K., Laird, J., Mandarino, J.A., Maresch, W.V., Nickel, E.H., Rock, N.M.S., Schumacher, J.C., Smith, D.C., Stephensen, N.C.N., Ungaretti, L., Whittaker, E.J.W., and Youzhi, G.

(1997). Nomenclature of amphiboles: Report of the Subcommittee on Amphiboles of the International mineralogical Association, Commission on New Minerals and Mineral Names. *American Mineralogist* **82**, 1019-1037.

Leonard, G.S, and Begg, J., (in prep). Geology of the Rotorua area: scale 1:250,000. Lower Hutt: Institute of Geological & Nuclear Sciences. Institute of Geological & Nuclear Sciences 1:250,000 geological map 5. + 1 folded map.

Leonard, G.S., Cole, J.W., Nairn, I.A., Self, S. (2002). Basalt triggering of the c. AD 1305 Kaharoa rhyolite eruption, Tarawera Volcanic Complex, New Zealand. *Journal of Volcanology and Geothermal Research* **115**, 461-486.

Leonard, G.S., Calvert, A.T., Wilson, C.J.N., Gravley, D.M., Deering, C.D., (in prep). Taupo Volcanic Zone $^{40}Ar/^{39}Ar$ geochronology illuminates 550 ka volcanism at Okataina Volcanic Centre, coastal uplift and sea level fluctuations.

Manning, D.A. (1995). Late Pleistocene tephrostratigraphy of the Eastern Bay of Plenty region, New Zealand. Unpublished PhD thesis, Victoria University.

Manning, D.A. (1996). Middle-late Pleistocene Tephrastratigraphy of the Eastern Bay of Plenty, New Zealand. *Quaternary International* **34-36**, 3-12.

Marsh (1996). Solidification fronts and magma evolution. *Mineralogical Magazine*, **60**, 5-40.

McCulloch, M.T., Kyser, T.K., Woodhead, J.D., Kinsley, L. (1994). Pb-Sr-Nd-O isotopic constraints on the origin of rhyolites from the Taupo volcanic zone of New Zealand; evidence for assimilation followed by fractionation from basalt. *Contributions to Mineralogy and Petrology* **115**, 303-312.

Milner, D.M., Cole, J.W., Wood, C.P. (2001). Mamaku Ignimbrite: a caldera-forming ignimbrite erupted from a compositionally zoned magma chamber in Taupo Volcanic Zone, New Zealand. *Journal of Volcanology Geothermal Research* **122**, 243-264.

Nairn, I.A. (2002). Geology of the Okataina Volcanic Centre, scale 1:50 000. *Institute of Geological & Nuclear Sciences geological map 25. 1 sheet + 156 p. Lower Hutt, New Zealand: Institute of Geological & Nuclear Sciences*, 20.

Pichavant, M., Kontak, D.J., Briqueu, L., Herrera, J.V. & Clark, A.H. (1988a). The Miocene-Pliocene Macusani Volcanics, SE Peru, 1. Mineralogy and magmatic evolution of a two-mica aluninosilicate-bearing ignimbrite suite. *Contributions to Mineralogy and Petrology* **100**, 300-324.

Pichavant, M., Kontak, D.J., Briqueu, L., Herrera, J.V. & Clark, A.H. (1988b). The Miocene-Pliocene Macusani Volcanics, SE Peru, 2. Geochemistry and origin of felsic peraluminous magma. *Contributions to Mineralogy and Petrology* **100**, 325-338.

Price, R.C., Gamble, J.A., Smith, I.E.M., Stewart, R.B., Eggins, S., Wright, I.C. (2005). An integrated model for the temporal evolution of andesites and rhyolites and crustal development in New Zealand's North Island. *Journal of Volcanology and Geothermal Research* **140**, 1-24.

Riley, T.R., Leat, P.T., Pankhurst, R.J. & Harris, C. (2001). Origins of large volume rhyolitic volcanism in the Antarctic Peninsula and Patagonia by crustal melting. *Journal of Petrology* **42**, 1043-1065.

Schmitz, M.D. & Smith, I.E.M. (2004). The Petrology of the Rotoiti Eruption Sequence, Taupo Volcanic Zone: an Example of Fractionation and Mixing in a Rhyolitic System. *Journal of Petrology* **45**, 2045-2066.

Shane, P. Martin, S.B., Smith, V.C., Beggs, K.F., Darragh, M.B., Cole, J.W., Nairn, I.A. (2007). Multiple rhyolite magmas and basalt injection in the 17.7 ka Rerewhakaaitu eruption episode from Tarawera volcanic complex, New Zealand. *Journal of Volcanology and Geothermal Research* **164**, 1-26.

Shane, P., Nairn, I.A., Smith, V.C. (2005). Magma mingling in the approximately 50 ka Rotoiti eruption from Okataina Volcanic Centre; implications for geochemical diversity and chronology of large volume rhyolites. *Journal of Volcanology and Geothermal Research* **139**, 295-313.

Sisson, T.W. & Bacon, C.R. (1999). Gas-driven filter pressing in magmas. *Geology* **27**, 613-616.

Smith (1979). Ash-flow magmatism. *Special Paper – Geological Society of America* **10**, 487.

Smith, I.E.M., Stewart, R.B. & Price, R.C., (2003). The petrology of a large intra-oceanic silicic eruption: the Sandy Bay Tephra, Kermadec Arc, Southwest Pacific. *Journal of Volcanology and Geothermal Research* **124**, 173-194.

Vogel, T.A., Flood, T.P., Patino, L.C., Wilmot, M.S. Maximo, R.P.R, Arpa, C.B., Arcilla, C.A, Stimac, J.A. (2006). Geochemistry of silicic magmas in the Macolod Corridor, SW Luzon, Philippines: evidence of distinct, mantle-derived, crustal sources for silicic magmas. *Contributions to Mineralogy and Petrology* **151**, 267-281.

Waight, T.E., Baker, J.A., Peate, D.W. (2002). Sr isotope ratio measurements by double-focusing MC-ICPMS: techniques, observations and pitfalls. *International Journal of Mass Spectrometry* **221**, 229-244.

Wilson, C.J.N., Blake, S., Charlier, B.L.A., Sutton, A.N. (2006). The 26.5 ka Oruanui Eruption, Taupo Volcano, New Zealand: Development, Characteristics and Evacuation of a Large Rhyolitic Magma Body. *Journal of Petrology* **27**, 35-69.

Wilson, C.J.N., Houghton, B.F., McWilliams, M.O., Lanphere, M.A., Weaver, S.D., Brigges, R.M. (1995) Volcanic and structural evolution of Taupo volcanic zone, New Zealand: a review. Journal of Volcanology and Geothermal Research, 68, 1-28.

Wilson, C.J.N., Rogan, A.M., Smith, I.E.M., Northey, D.J., Nairn, I.A., Houghton, B.F. (1984) Caldera volcanoes of the Taupo volcanic zone, New Zealand. Journal of Geophysical Research, 89, 8463-8484.

5.11 FIGURES

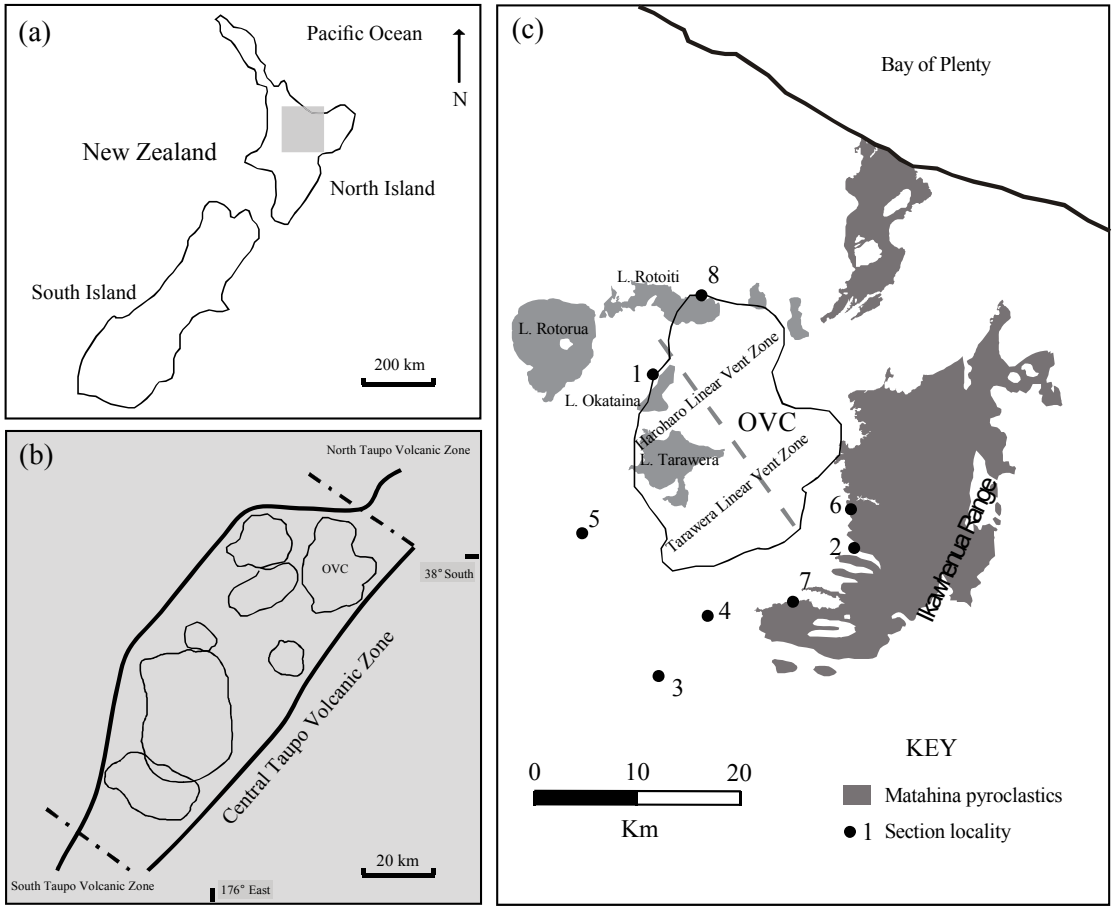

Fig. 5.1. (a) Location of the central Taupo Volcanic Zone (TVZ) North Island, New Zealand. (b) The central Taupo Volcanic Zone and Okataina Volcanic Centre (OVC) as one of seven major caldera-forming volcanic complexes. Inferred caldera boundaries are outlined in bold. (c) Mapped extent of the Matahina outflow sheet *sensu stricto* surrounding OVC and specific sampling localities discussed in the text.

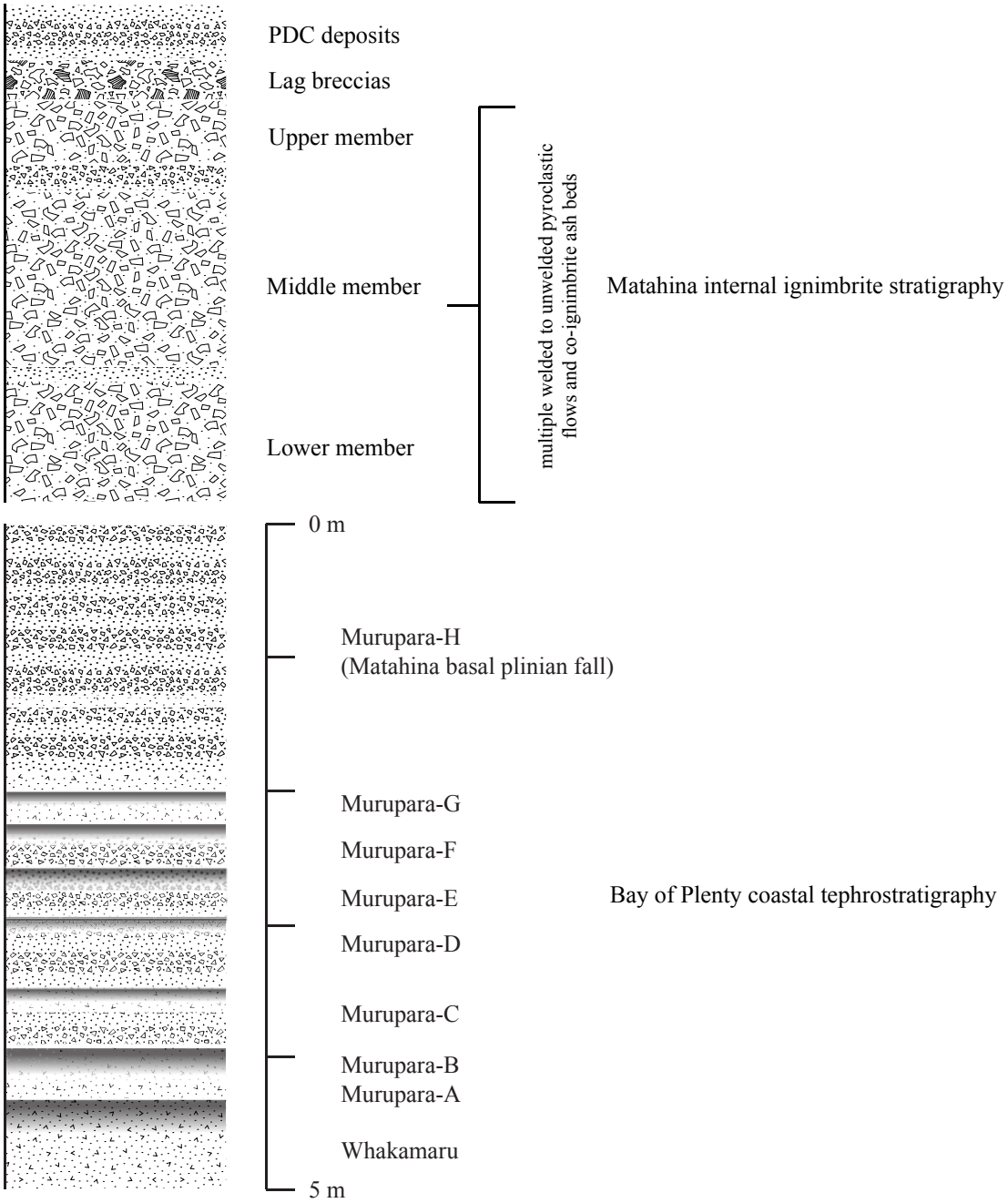

Fig. 5.2. Schematic stratigraphic column of the Murupara Subgroup from the eastern Bay of Plenty (after Manning, 1996; Murupara A-G are equivalent to the Bonisch pyroclastics of Nairn, 2002) and representation of the Matahina ignimbrite internal stratigraphy, including post-collapse PDC deposits from localities 1 and 2 in Fig. 5.1. Weak paleosols in gray separate the units. A Whakamaru-group co-ignimbrite ash marks lowermost boundary of the Murupara subgroup.

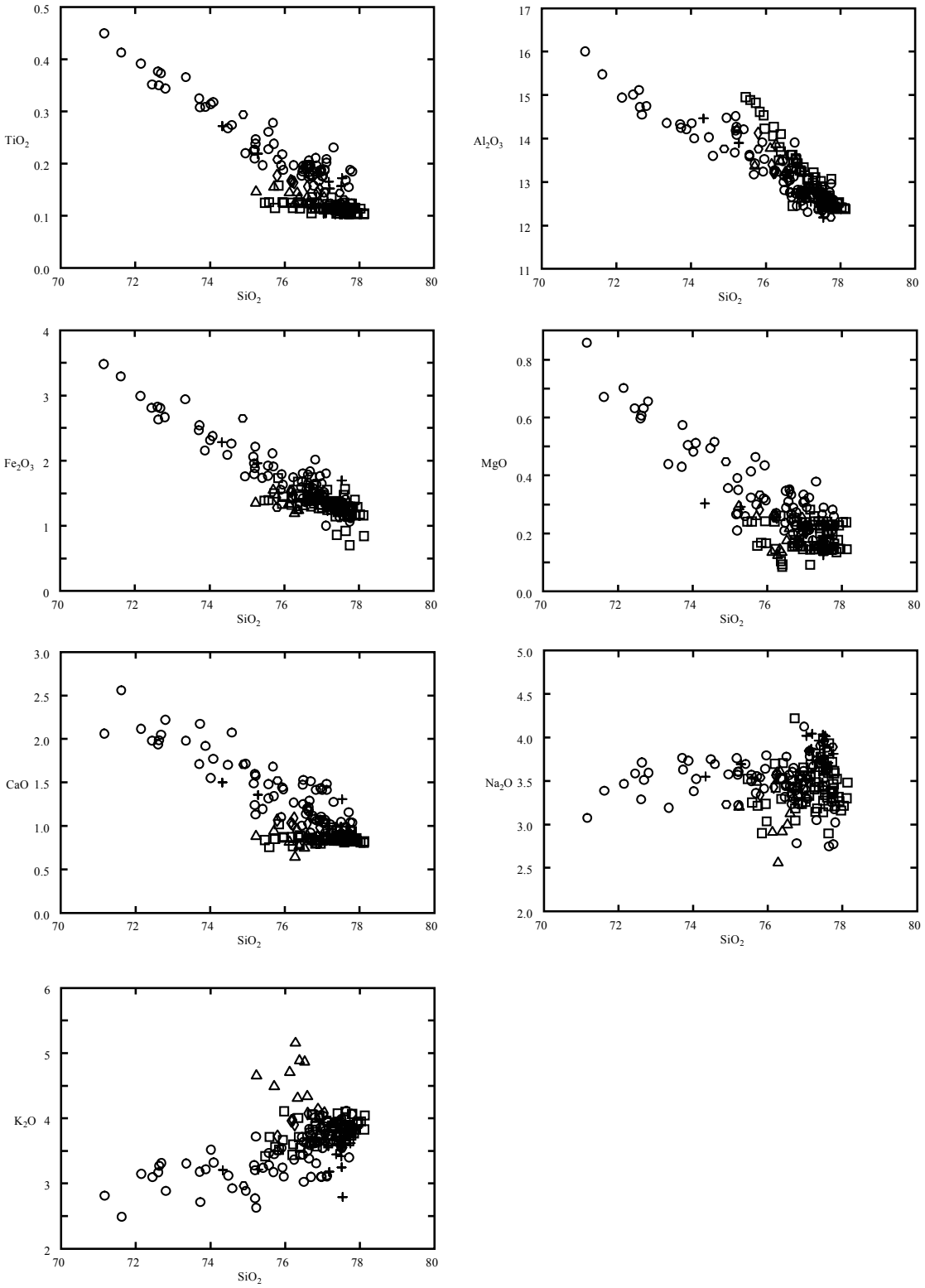

Fig. 5.3. Selected major element oxides vs silica for the Murupara E-H, Matahina ignimbrite, recycled ignimbrite, and rhyolite lithics. Open circles = Group A2 Matahina ignimbrite; open squares = Group A1 Matahina ignimbrite; open triangles = Group B Matahina ignimbrite; crosses = Murupara E-G tephras; open diamonds = Group B rhyolite lithics.

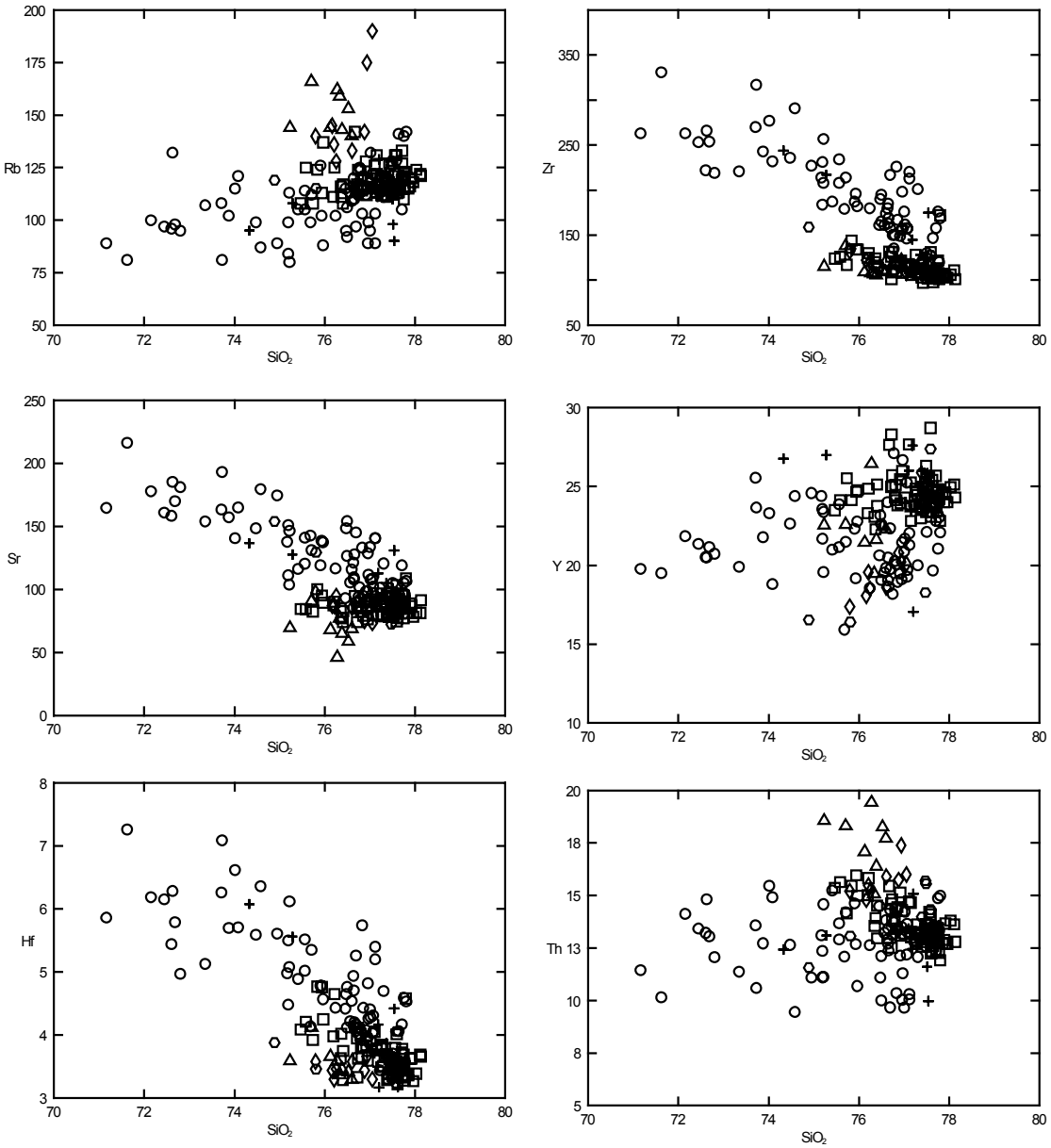

Fig. 5.4. Selected trace elements vs silica for the Murupara E-H, Matahina ignimbrite, recycled ignimbrite, and rhyolite lithics. Symbols same as Fig. 5.3.

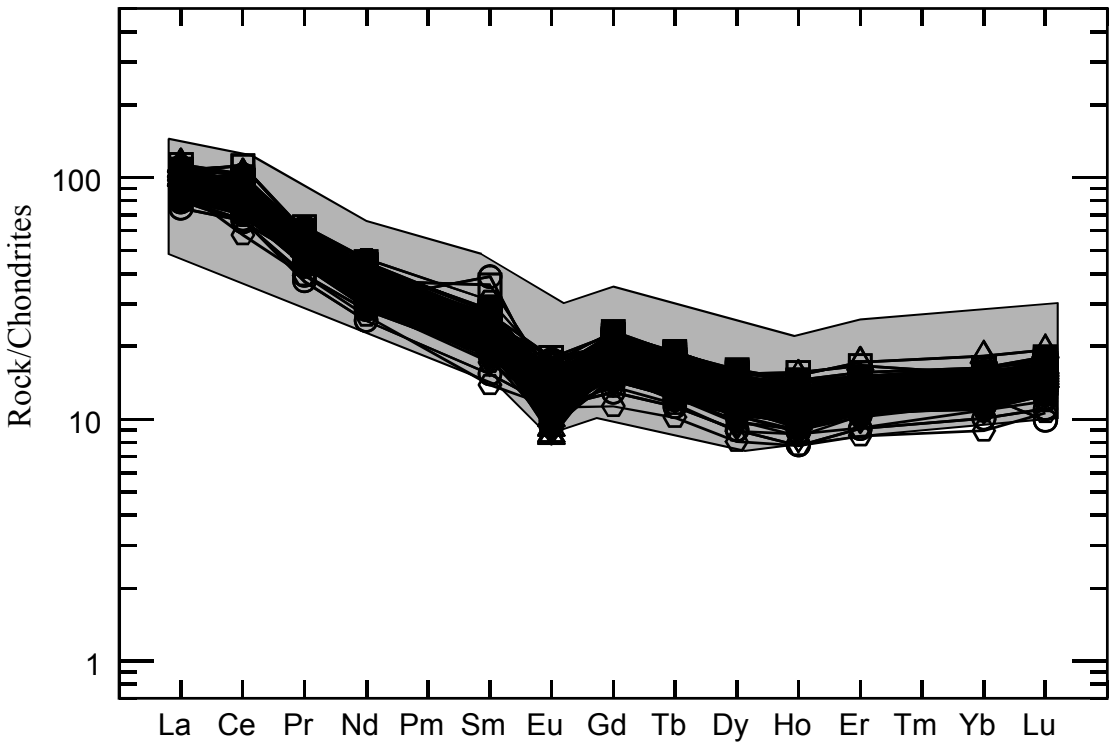

Fig. 5.5. Field of chondrite-normalized REE patterns for the Murupara E-H, Matahina ignimbrite, recycled ignimbrite, and rhyolite lithics. Shaded area represents all TVZ rhyolites (data from Deering *et al.*, 2008).

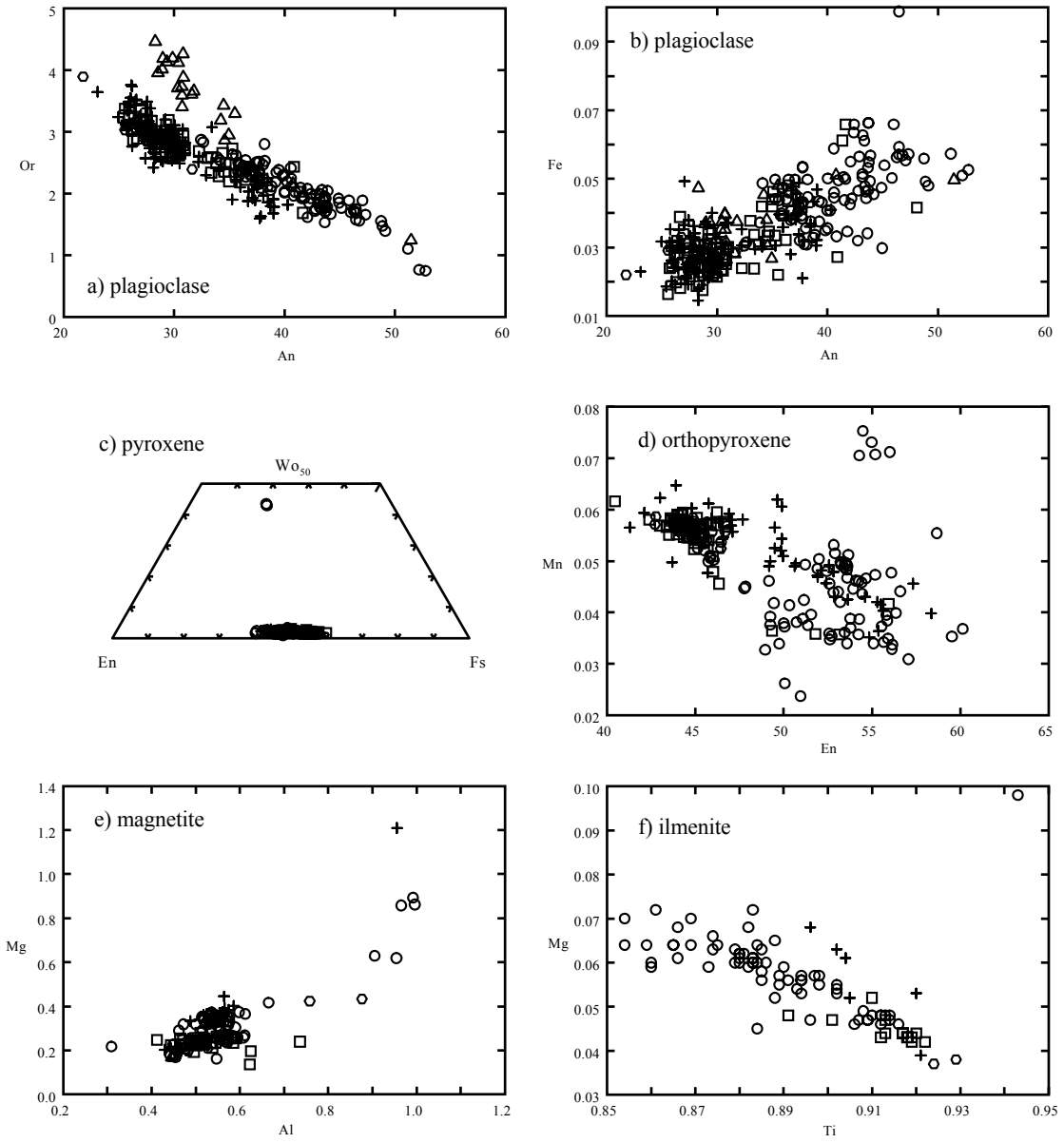

Fig. 5.6. Anhydrous mineral compositions from all rhyolite clasts. Symbols same as Fig. 5.3. Open circles = Group A2; open squares = Group A1; open triangles = Group B; crosses = pre-Matahina; Group B lithics.

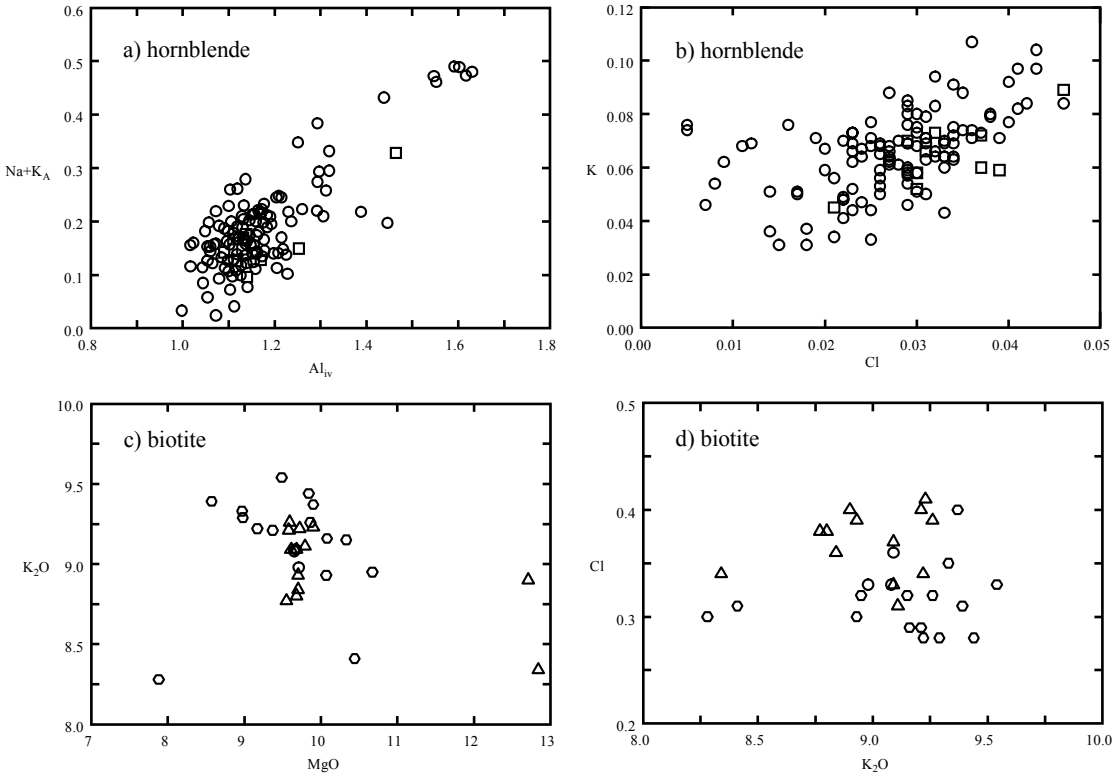

Fig. 5.7. Hydrous mineral compositions from all rhyolite clasts. Symbols as in Fig. 5.6.

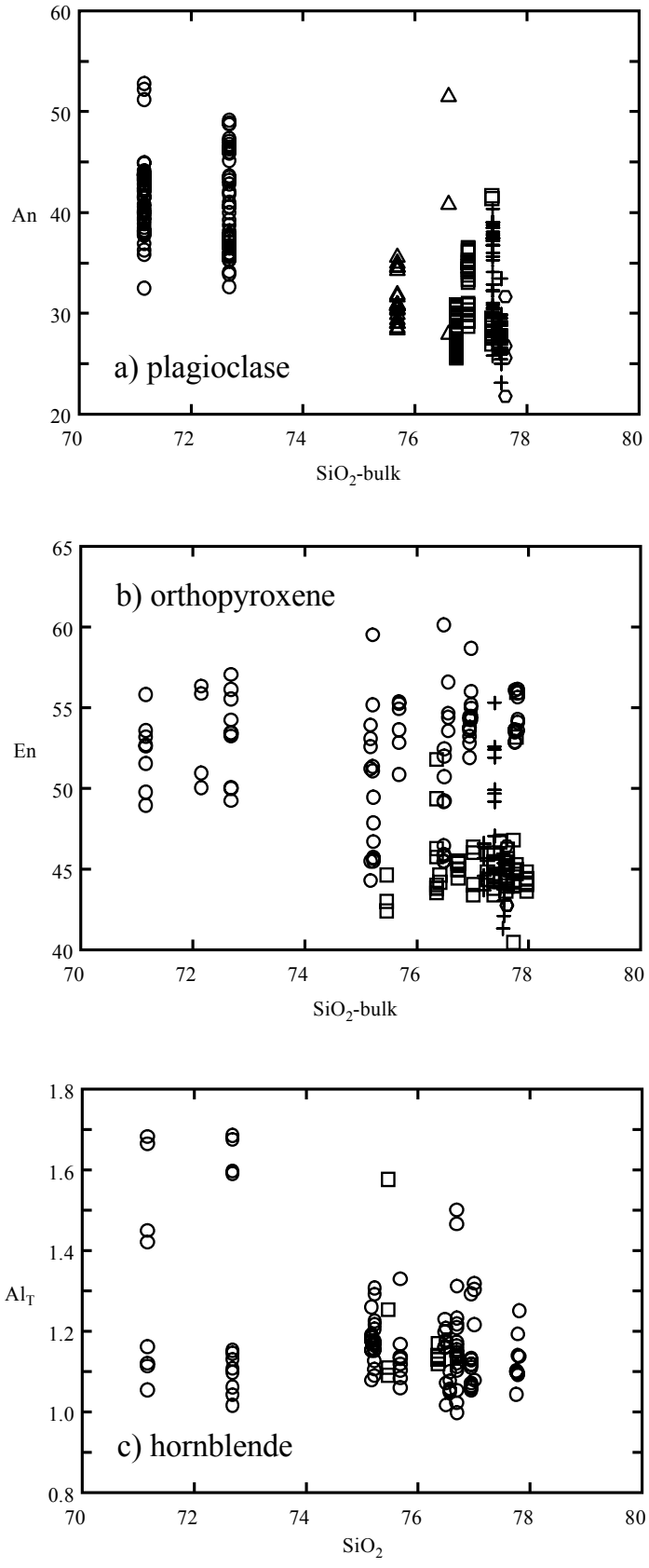

Fig. 5.8. Mineral compositions of Matahina rhyolite vs host rhyolite bulk silica composition. Symbols as in Fig. 5.6.

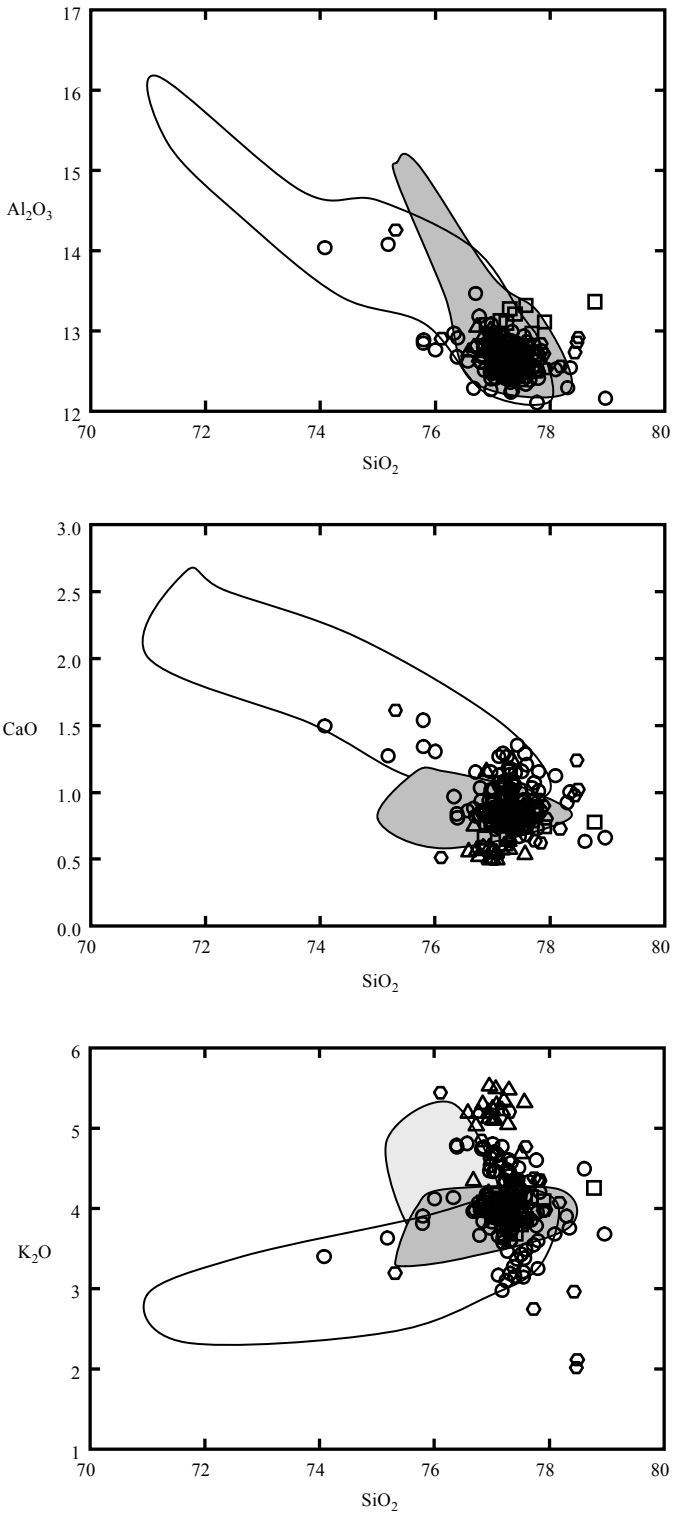

Fig. 5.9. Rhyolite glass compositions of selected major element oxides. (a,b) Open field are Group A2, dark gray field are Group A1, light gray field are Group B rhyolite. Symbols as in Fig. 5.6.

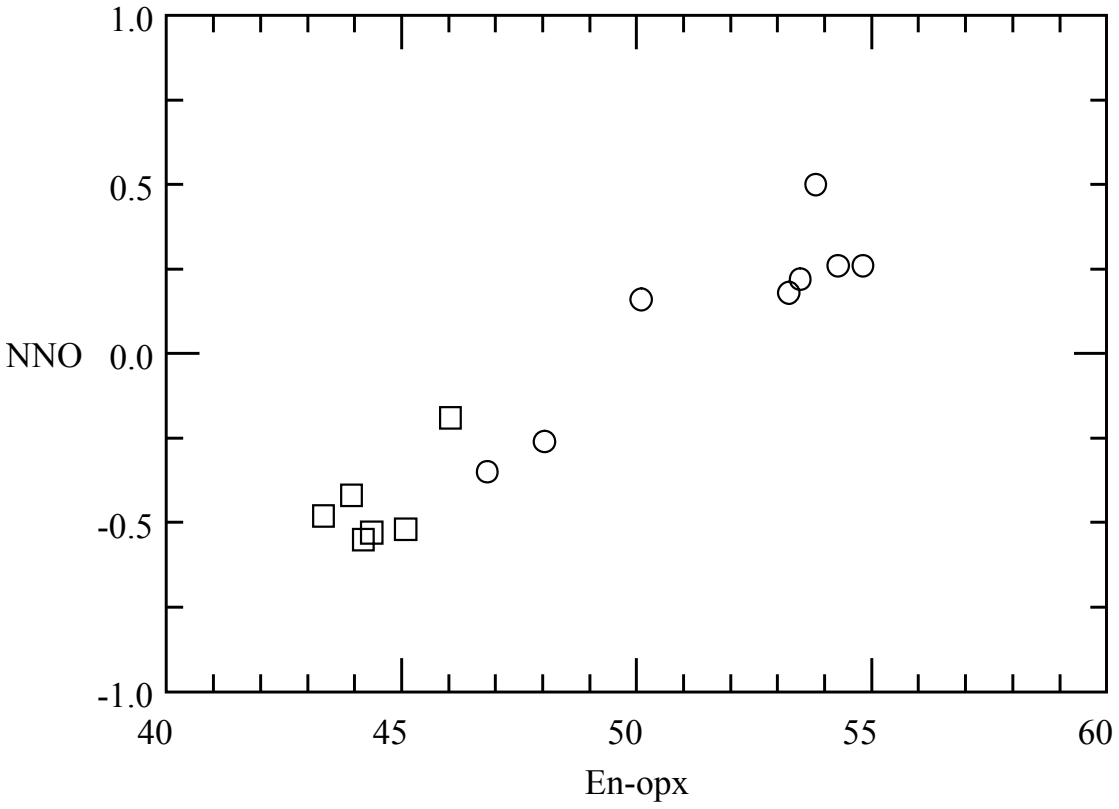

Fig. 5.10. Orthopyroxene En content vs oxygen fugacity (log units ΔNNO). Symbols as in Fig. 6.

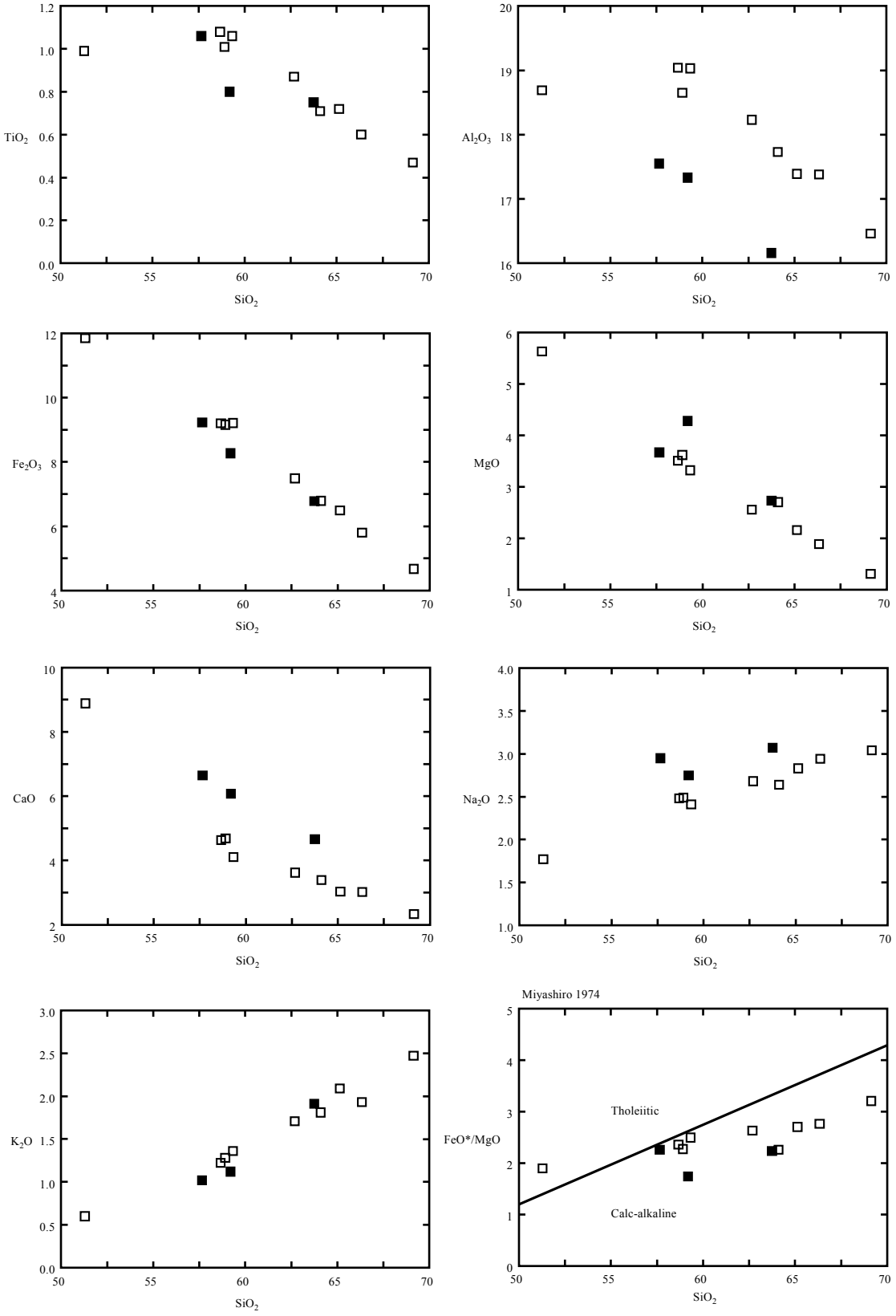

Fig. 5.11. Selected major element oxides vs silica for the basalt to dacite from post-collapse PDC deposits. Open boxes = Group A and closed boxes = Group B.

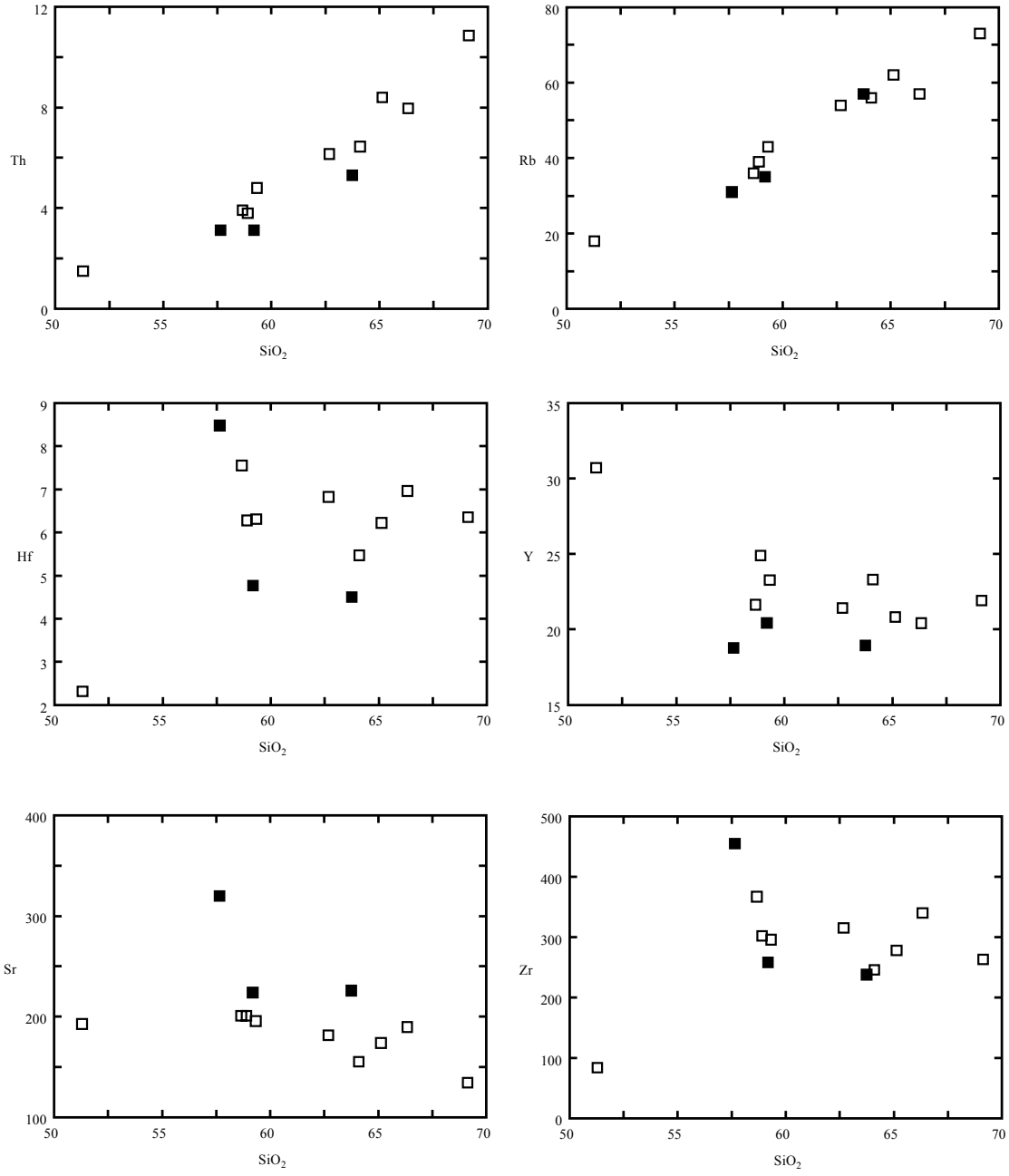

Fig. 5.12. Selected trace element vs silica for the basalt to dacite from post-collapse PDC deposits. Symbols as in Fig. 5.11.

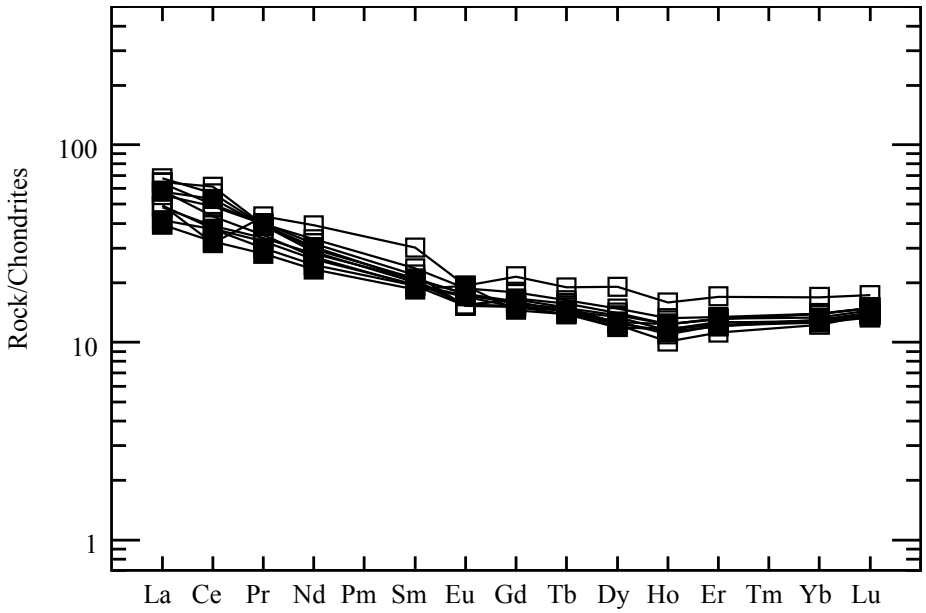

Fig. 5.13. Chondrite-normalized REE patterns for the basalt to dacite from post-collapse PDC deposits. Symbols as in Fig. 5.11.

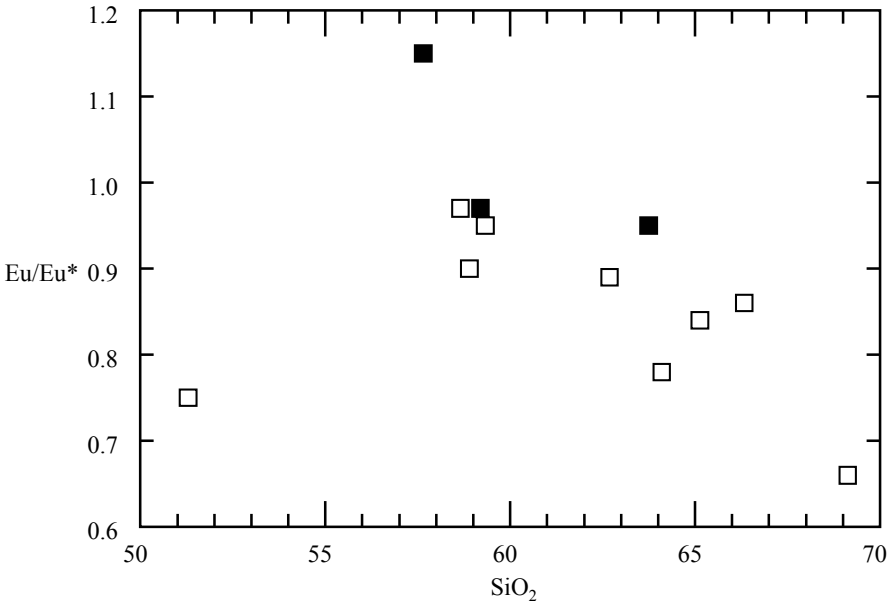

Fig. 5.14. Eu anomaly (Eu/Eu*) vs. silica for andesite to dacite compositions. Eu/Eu* is calculated from the two linear equations $\log_{10}(Sm_N) = (a*62)+b$ and $\log_{10}(Tb_N) = (a*65)+b$.

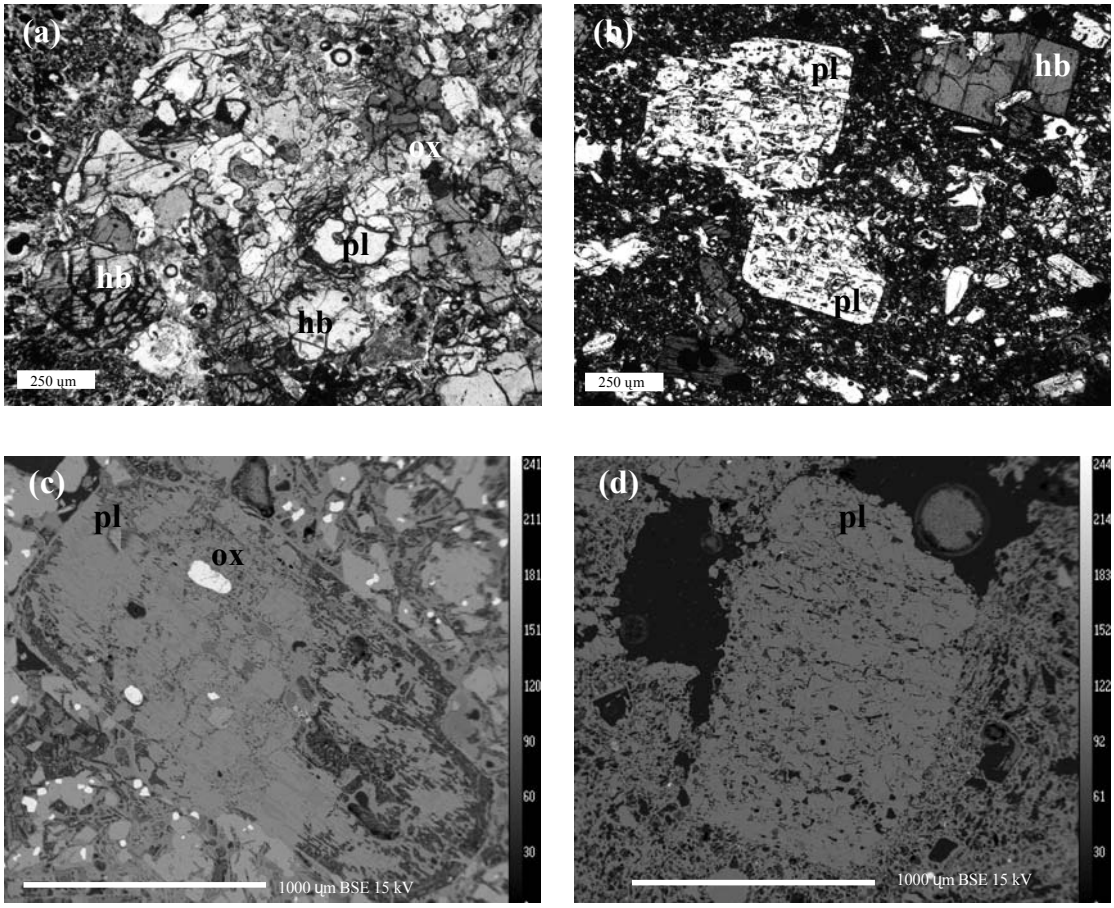

Fig. 5.15. Photomicrographs of (a) typical glomerocrysts of sutured hornblende and plagioclase in andesite to dacite clasts, and (b) embayed and dissolved plagioclase. Backscattered images of (c) large corroded plagioclase with thin overgrowth, and (d) typical, deeply corroded and dissolved plagioclase similar to that displayed in (b). Pl = plagioclase; hb = hornblende; ox = Fe-Ti oxide.

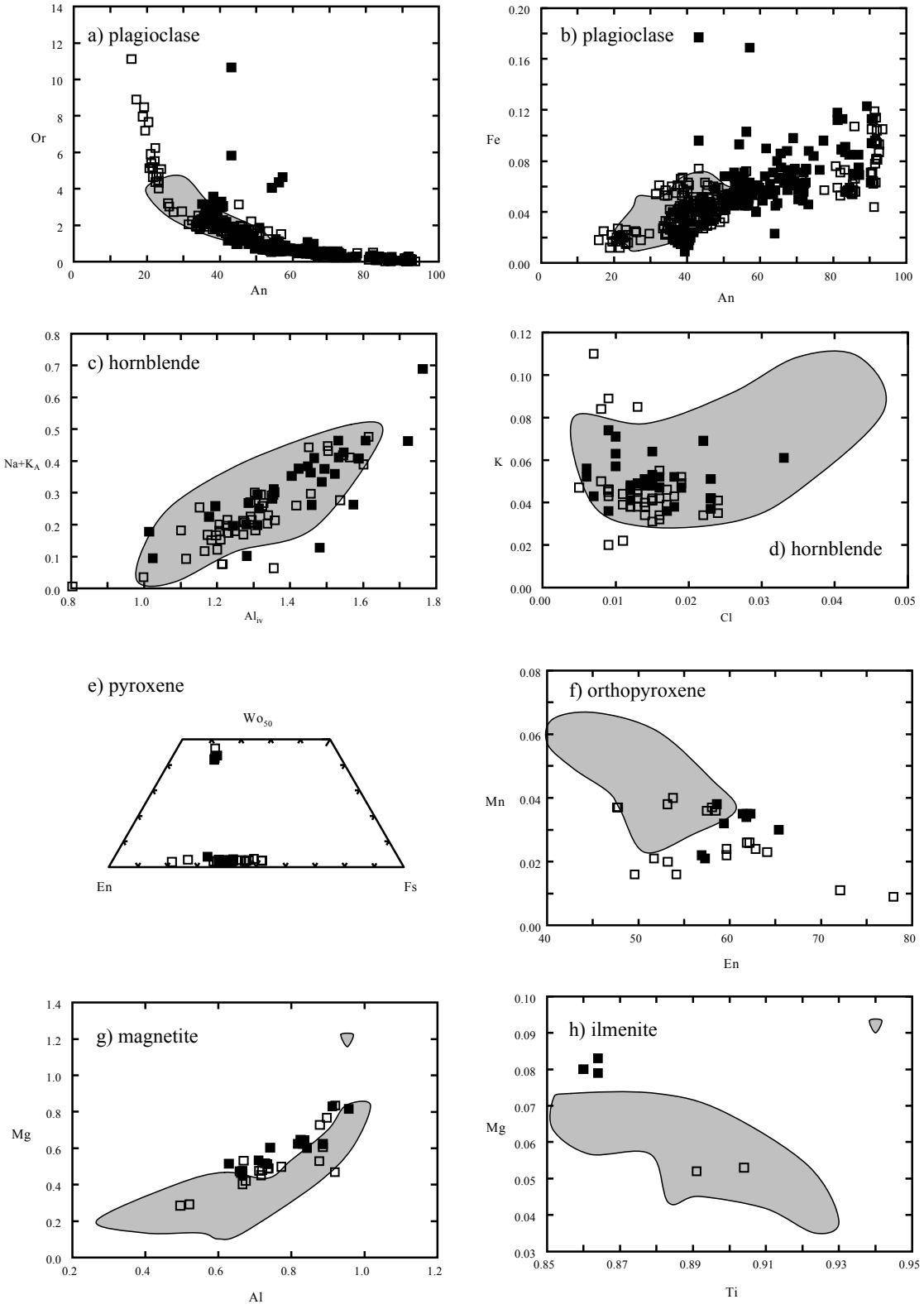

Fig. 5.16. Mineral compositions from Group A and B andesite to dacite compositions. Gray fields represent compositions of rhyolite minerals. Group A are open boxes and Group B are closed boxes.

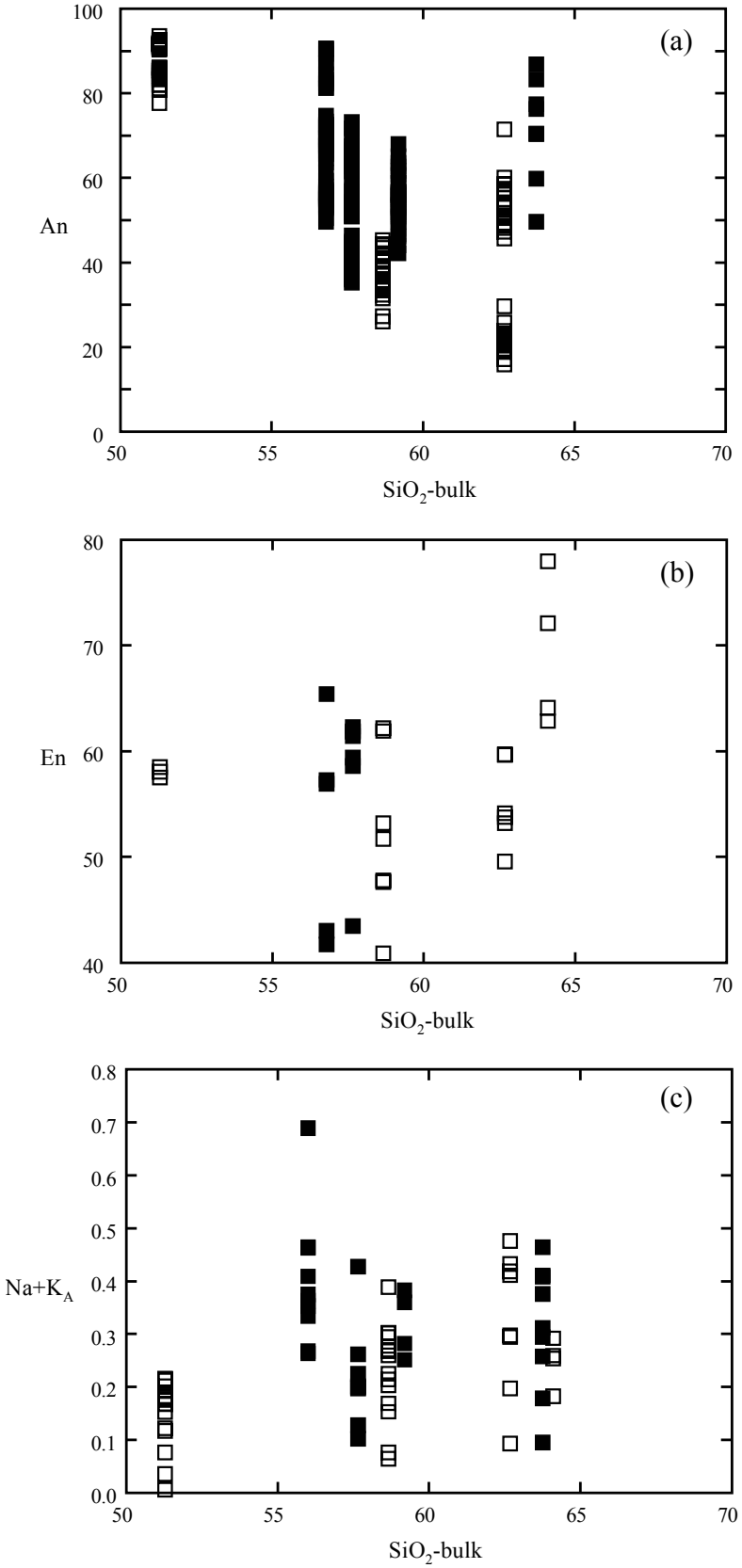

Fig. 5.17. Mineral compositions of Group A and B andesite to dacite vs. host bulk silica contents. Symbols as in Fig. 5.16.

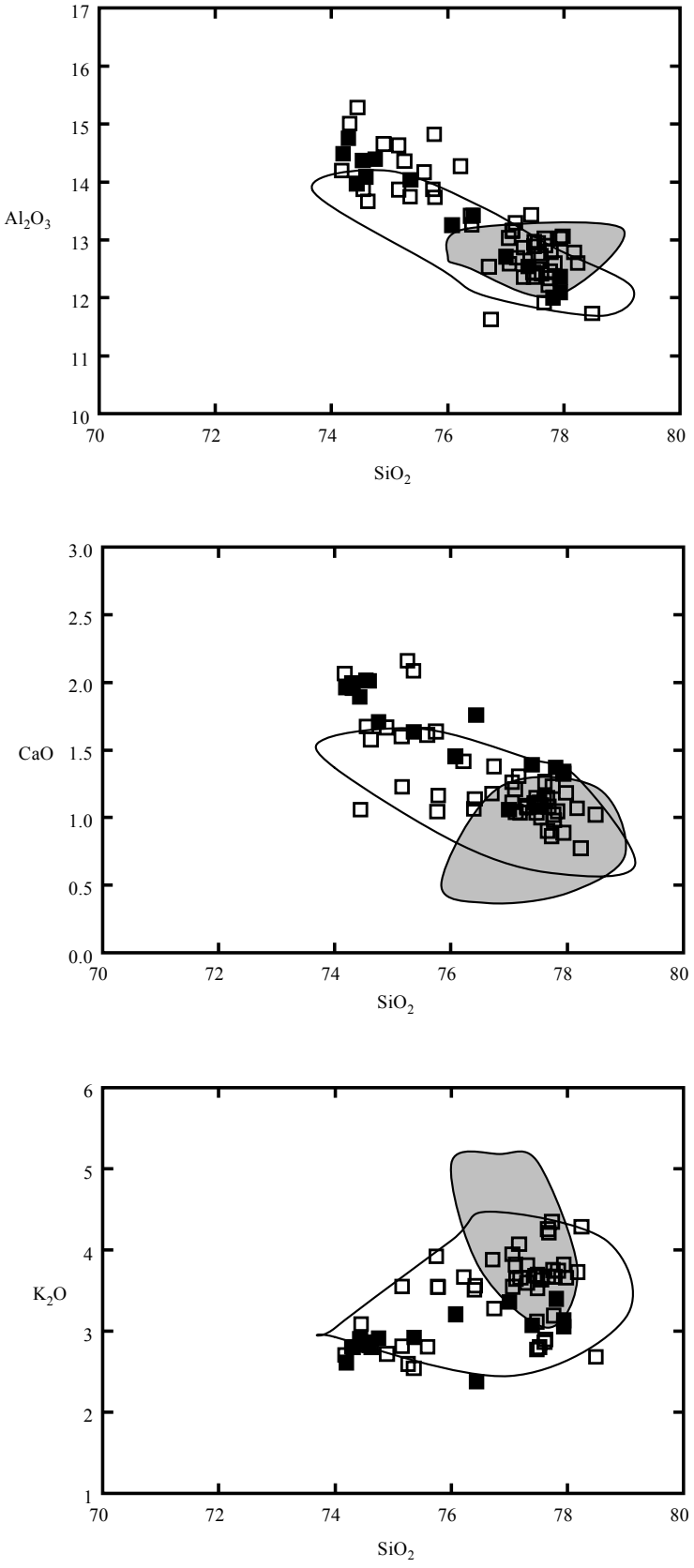

Fig. 5.18. Rhyolitic glass compositions from Group A and B andesite to dacite. Symbols as in Fig. 5.16. Open field represents Group A2 rhyolite and gray field Group A1/B rhyolite.

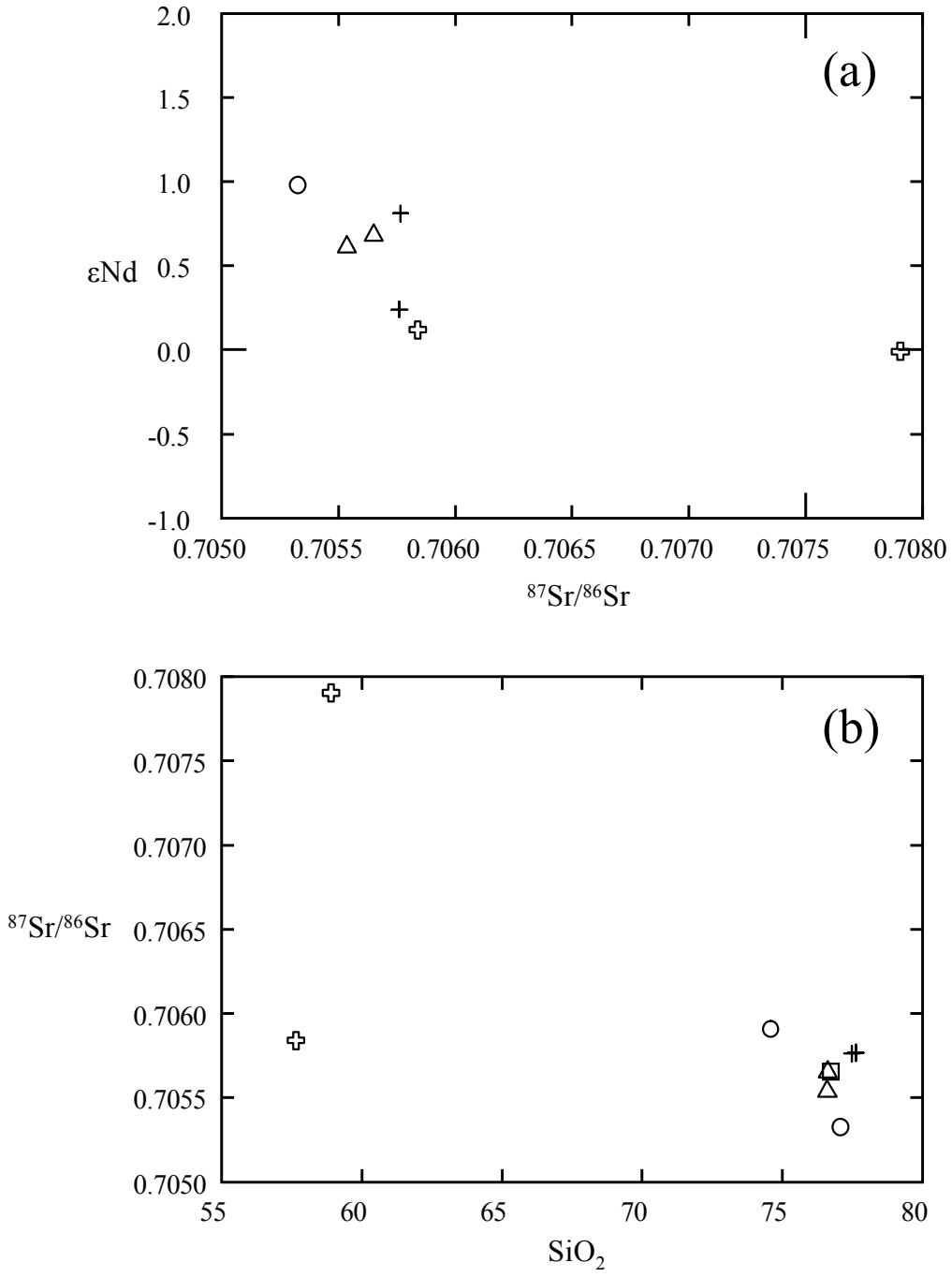

Fig. 5.19. (a) $^{87}Sr/^{86}Sr$ vs. εNd values, and (b) $^{87}Sr/^{86}Sr$ vs. bulk rock SiO_2 for Matahina mafic and felsic compositions. Open crosses = Group A and B andesite; open circles = Matahina A2 rhyolite; open squares = Matahina A1 rhyolite; crosses = Murupara E rhyolite; open triangles = Group B rhyolite.

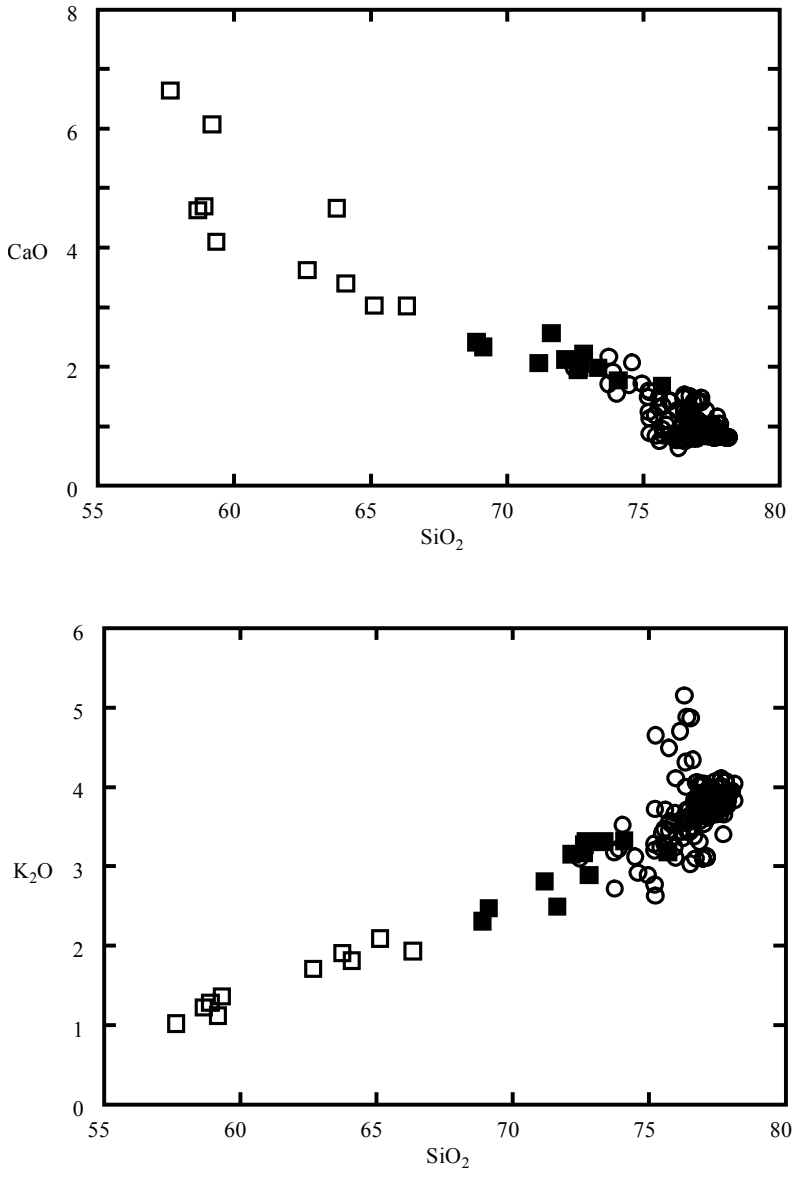

Fig. 5.20. Selected major element oxides vs. silica Matahina compositions from andesite to high-silica rhyolite. Open boxes = andesite-dacite; closed boxes = mingled rhyodacite-rhyolite; open circles = rhyolite.

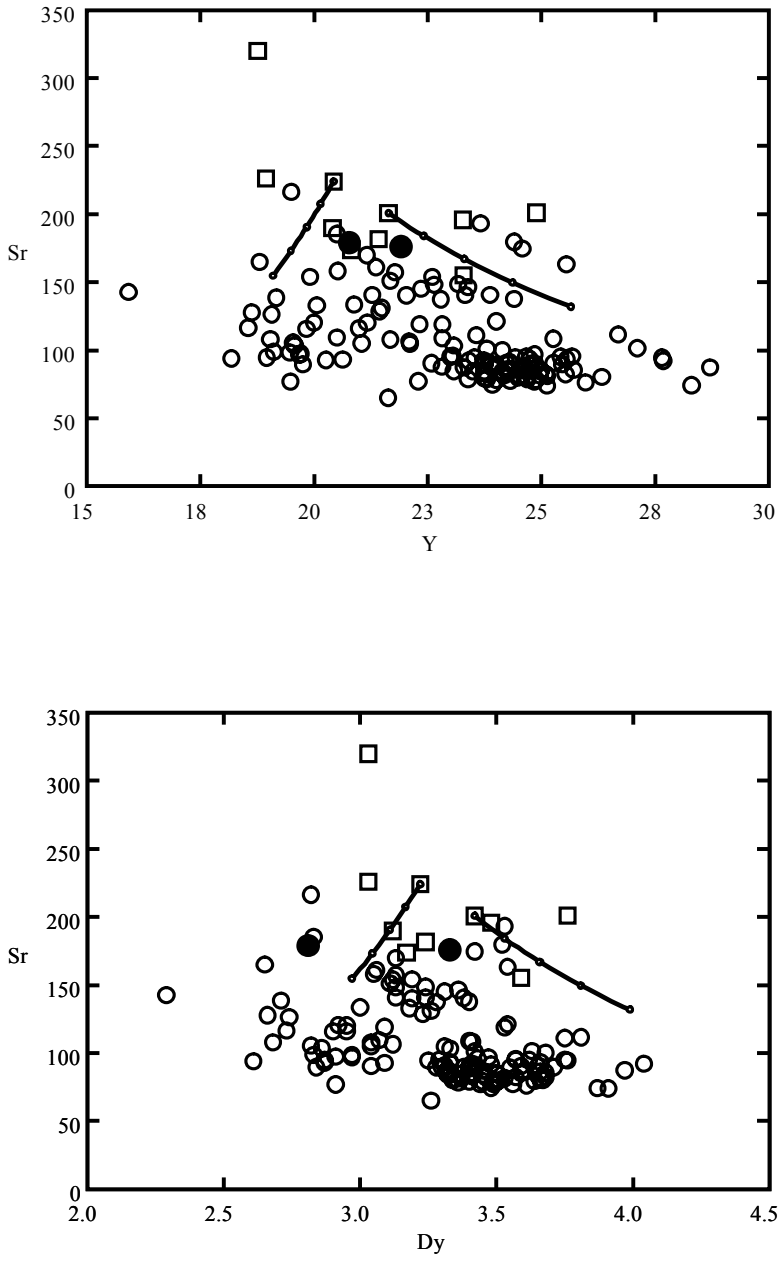

Fig. 5.21. Trace element plots illustrating modeled fractionation trends (increments of 5 %; up to 20%) from andesite to rhyodacite using (1) high hornblende/orthopyroxene ratio and (2) low hornblende/orthopyroxene.

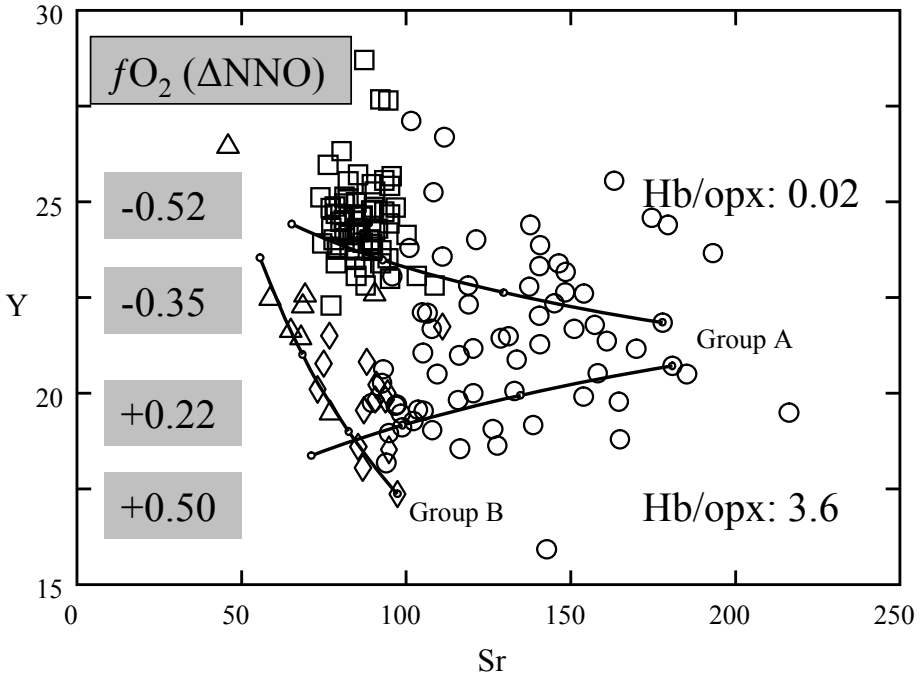

Fig. 5.22. Trace element modeling for rhyodacite to high-silica rhyolite for Group A high and low hornblende/orthopyroxene types. Oxygen fugacity are highest for high hornblende/orthopyroxene rhyolite derivatives and lowest for low hornblende/orthopyroxene rhyolite derivatives. Group B modeling trends from the least evolved to most evolved biotite+quartz-bearing rhyolite. Modeling for both Group A and B is in 5% increments up to 15%. Open circles = Group A2 rhyolite; open boxes = Group A1; open diamonds = Group B rhyolite.

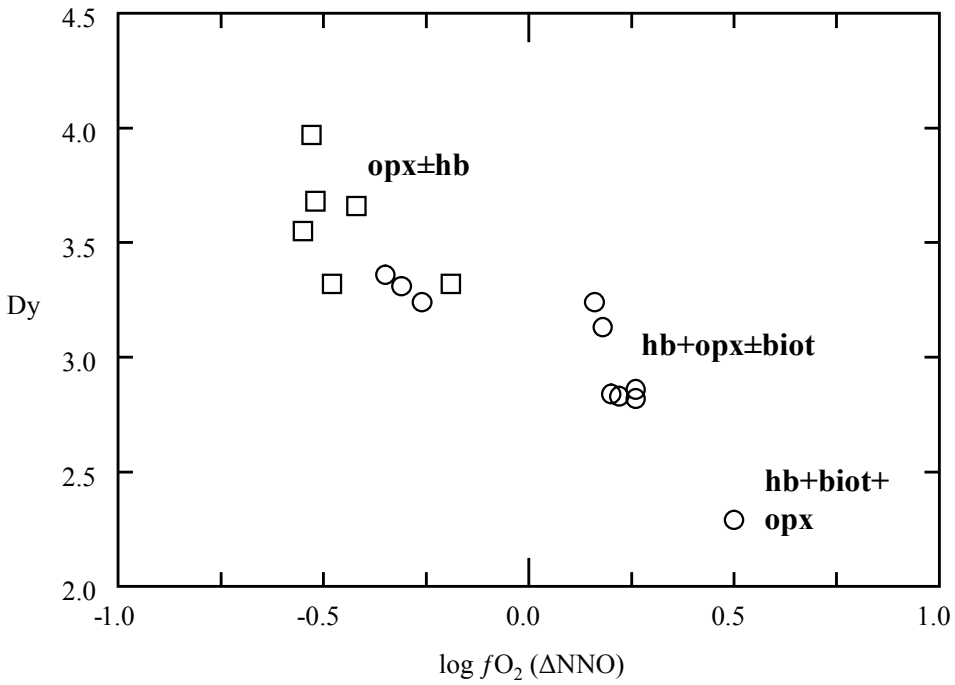

Fig. 5.23. Log fO_2 (ΔNNO) vs. Dy illustrating the correlation between type of rhyolite produced via crystal fractionation governed by the oxidation state of the parental melt. Ferromagnesian mineral contents for each rhyolite type are also correlated with the oxidation state of the magma. Open boxes = A1 and open circles = A2 types. Opx = orthopyroxene, hb = hornblende, and biot = biotite.

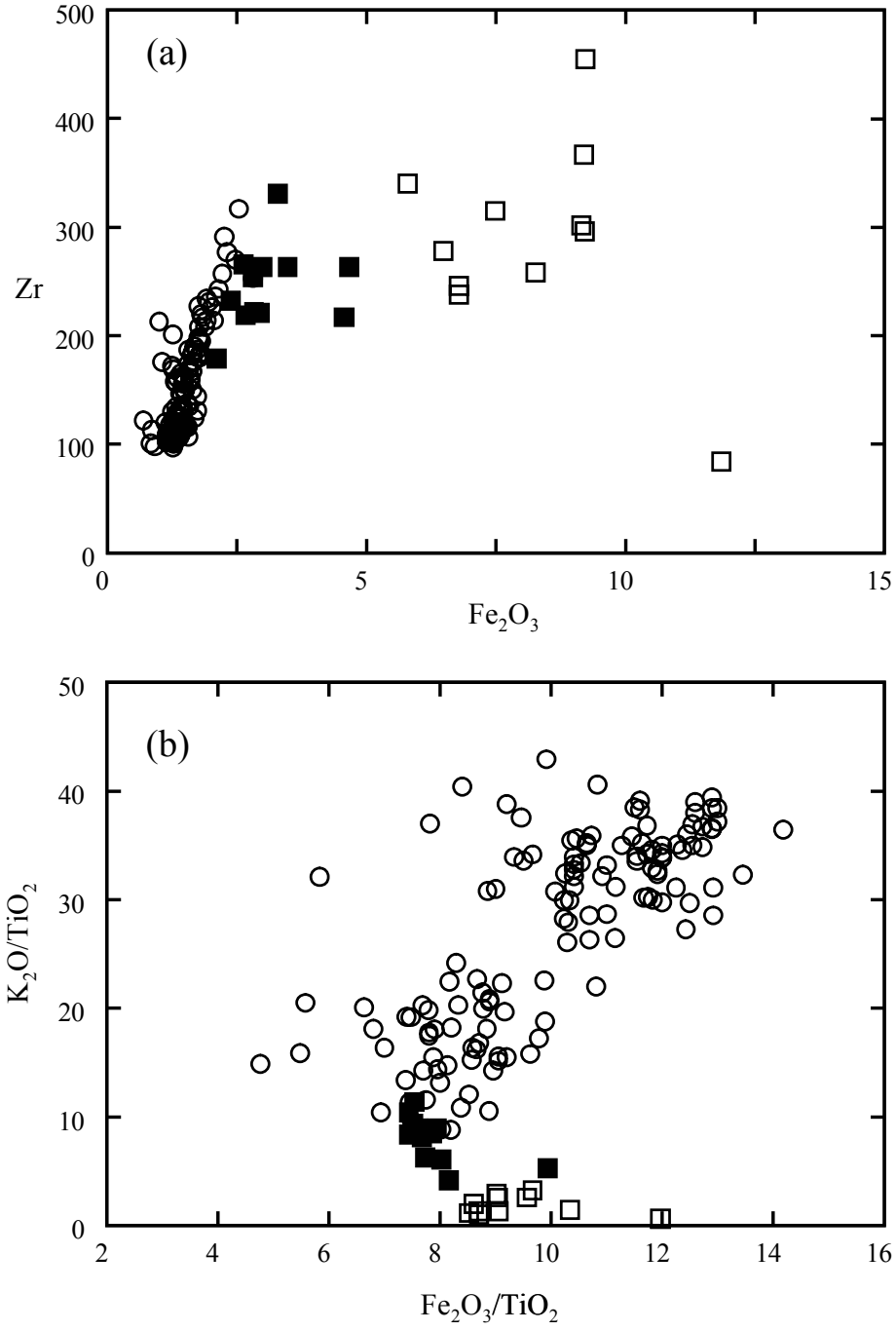

Fig. 5.24. Plots of all Matahina compositions. (a) Zr vs. Fe_2O_3 and, (b) K_2O/TiO_2 vs. Fe_2O_3/TiO_2. Open circles = rhyolite; closed boxes = mingled rhyodacite-rhyolite; open boxes = andesite to dacite.

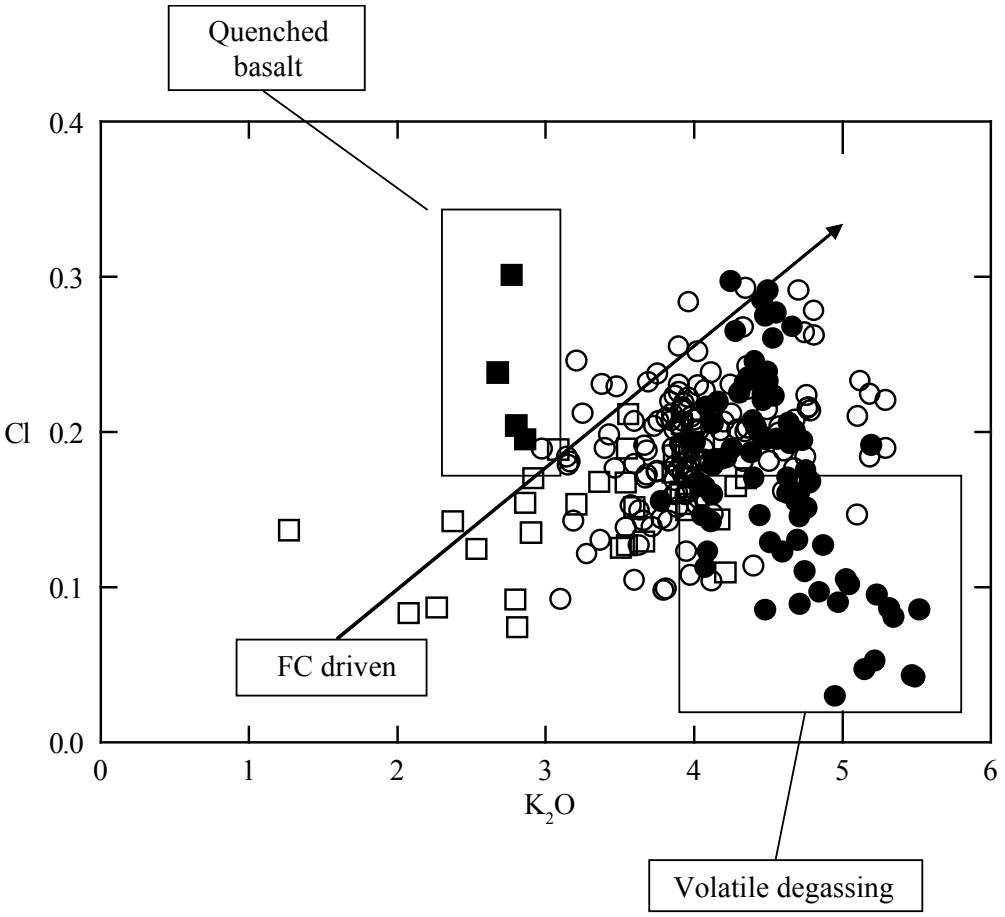

Fig. 5.25. Incompatible elements in glass for all Matahina eruptive types. Dominant trend of increasing Cl and K_2O interpreted as fractionation driven, whereas the trend observed for the population of Group A2 rhyolite with low Cl contents (biotite-bearing dome clasts and biotite-only pumice from locality 1 are consistent with volatile loss during degassing. Fine-grained basalt samples have the highest Cl contents at a given K_2O, indicative of preservation of the undegassed high volatile contents of an undifferentiated basalt. Open boxes = andesite to dacite; closed boxes = fine-grained basalt; open circles = Group A2 rhyolite; closed circles = Group A1 rhyolite.

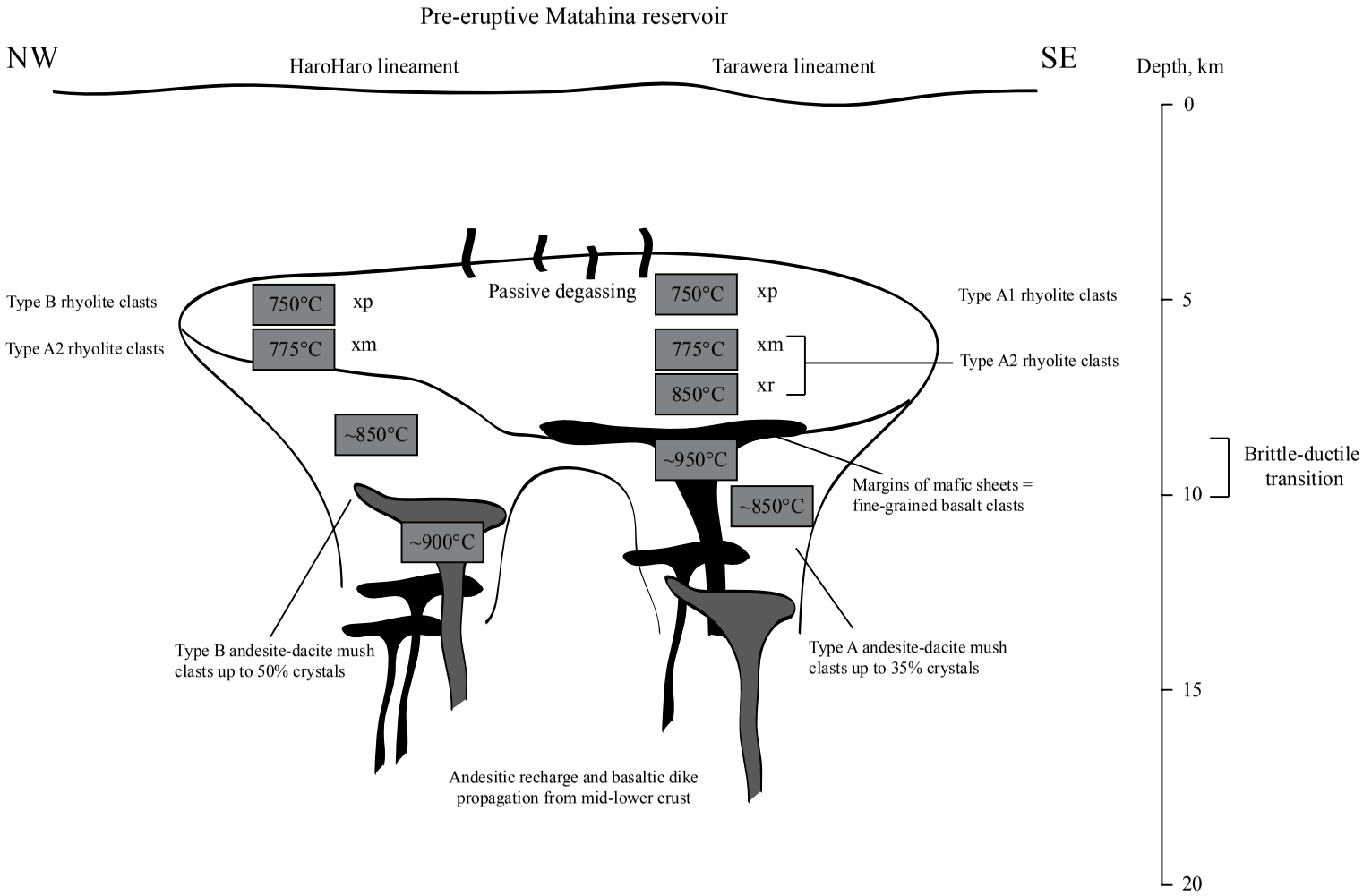

Fig. 5.26. Schematic cross-section from NW to SE through the OVC illustrating the magmatic plumbing system prior to the Matahina eruption. Intruded basalts are sandwiched between crustal greywacke and intermediate intrusives between 15-30 km depth. The compositional and thermal gradient includes the amphibole-bearing cumulate and crystal-rich intermediate magmas up to the brittle-ductile transition at ~8 km depth, whereas the rhyolitic magma reservoirs develop between 4 and 8 km depth.

5.12 TABLES

Table 5.1. Representative Matahina basalt to rhyolite bulk geochemical analyses

Sample	UC813	UC498	UC175	UC181	UC168	UC649
Lithology	Matahina	Matahina	Matahina	Matahina	Matahina	Matahina
Deposit description	PDC	PDC	pinkish tuff	pinkish tuff	gray tuff	pinkish tuff
Type	dense pumice	pumice	pumice	pumice	pumice	pumice
Location	Lk. Okataina	Te Weta Rd.	Reihana Rd.	Reihana Rd.	Pahekeheke Rd.	SH38
Grid reference	U16/079355	V16/300301	U17/092099	U17/092099	V16/356186	V16/113141
SiO_2	72.80	71.16	72.68	74.58	75.56	76.94
TiO_2	0.34	0.45	0.37	0.27	0.23	0.19
Al_2O_3	14.75	16.00	14.55	13.60	13.63	12.82
Fe_2O_3	2.67	3.48	2.81	2.26	1.77	1.46
MnO	0.06	0.07	0.06	0.06	0.05	0.04
MgO	0.66	0.86	0.63	0.52	0.41	0.21
CaO	2.22	2.06	2.05	2.07	1.48	1.07
Na_2O	3.59	3.07	3.51	3.69	3.57	3.41
K_2O	2.89	2.81	3.31	2.92	3.28	3.85
P_2O_5	0.02	0.02	0.02	0.01	0.02	0.01
LOI	3.85	4.26	3.30	4.80	3.22	3.58
Total	96.00	95.61	96.57	95.05	96.65	96.29
V	30.00	66.31	29.21	14.77	12.80	1.31
Cr	4.89	10.63	4.61	3.25	5.23	3.95
Ni	18	18	17	17	17	17
Cu	-	6	3	3	5	1
Zn	45	54	42	41	45	31
Rb	95	89	98	87	105	116
Zr	219	263	254	291	208	156
Sr	181	165	170	180	141	99
Y	20.72	19.78	21.16	24.40	23.87	19.11
Nb	8.60	10.75	8.79	7.76	9.62	8.32
Ba	786	726	686	659	833	839
La	20.60	18.68	19.66	18.98	23.19	21.64
Ce	43.00	49.81	47.76	39.97	49.91	45.87
Pr	4.08	4.10	4.41	4.39	5.57	4.23
Nd	14.13	14.59	15.39	16.11	18.06	14.36
Sm	2.84	3.20	3.05	3.33	3.27	2.92
Eu	0.74	0.92	0.82	0.91	0.80	0.63
Gd	3.00	3.22	3.60	3.80	3.80	3.20
Tb	0.48	0.53	0.55	0.58	0.57	0.50
Dy	2.80	2.92	3.13	3.52	3.24	2.83
Ho	0.52	0.62	0.61	0.71	0.66	0.57
Er	1.77	1.86	1.94	2.18	2.01	1.84
Yb	2.05	2.08	2.19	2.43	2.25	2.01
Lu	0.34	0.32	0.34	0.41	0.37	0.34
Hf	4.97	5.86	5.79	6.36	5.02	3.97
Ta	1.04	1.22	1.42	1.09	2.15	1.65
Pb	21.45	25.34	23.15	22.82	33.15	32.15
Th	12.06	11.45	13.05	9.45	12.90	13.51
U	3.21	3.34	3.10	2.46	3.77	4.21
$^{87}Sr/^{86}Sr$				0.705908		
$^{143}Nd/^{144}Nd$						

Samples are normalized to 100% anhydrous. Major elements given in wt. % and trace elements (ppm).
Trace elements determined by ICP-MS. LOI values are calculated by weight difference. n.d. = not detected.
Grid references refer to sample localities on the New Zealand NZMS 1:50,000 maps.

Table 5.1 cont.

UC650 Matahina pinkish tuff pumice SH38 V16/113141	UC842 Matahina plinian airfall pumice Ohakiri Rd. V16/298277	UC887 Matahina plinian airfall pumice Bonisch Rd. V16/310207	UC702 Murupara-E rhyolite lava obsidian Anaputa Pt. V15/244423	UC1137 ho1 rhyolite dome lava Lk. Rotoiti	UC888 Pre-Matahina lithic lag breccia lava Te Weta Rd. V16/300301	UC812 Matahina PDC dense pumice Lk. Okataina U16/079355
77.07	75.84	77.85	77.48	77.61	76.61	76.60
0.19	0.16	0.11	0.10	0.11	0.16	0.13
12.62	14.62	12.44	12.42	12.50	13.02	13.27
1.48	1.73	1.29	1.29	1.18	1.39	1.37
0.04	0.04	0.04	0.04	0.04	0.05	0.05
0.23	0.17	0.14	0.14	0.07	0.34	0.22
1.07	1.02	0.83	0.83	0.81	1.02	0.89
3.53	2.90	3.52	4.03	4.04	3.33	3.12
3.77	3.52	3.76	3.65	3.62	4.07	4.34
0.01	0.01	0.01	0.01	0.01	0.00	0.01
3.74	4.63	3.94	1.45		3.91	3.23
96.13	95.23	95.93	98.44	98.26	95.97	96.65
1.93	6.18	n.d.	n.d.	3.84	10.98	5.74
2.61	4.86	3.93	5.00	4.84	2.96	5.82
16	19	16	16	-	17	17
2	-	1	4	-	6	2
30	41	30	28	-	27	28
115	124	115	117	116	133	140
158	144	106	107	109	121	109
97	100	81	79	77	85	69
19.71	24.14	24.52	24.35	21.60	18.60	22.27
8.45	10.39	8.88	8.59	10.28	9.76	9.36
838	1052	938	934	879	963	788
21.76	23.98	24.50	24.27	23.13	23.69	24.62
46.06	56.24	56.65	56.26	52.70	53.30	54.82
4.17	5.13	5.25	5.08	5.44	4.59	4.80
14.52	17.86	18.50	17.83	18.60	14.72	16.02
2.88	3.84	3.69	3.79	4.06	2.86	3.06
0.63	0.86	0.71	0.73	0.82	0.57	0.53
3.35	4.35	4.11	4.10	4.12	3.21	3.43
0.51	0.67	0.60	0.62	0.69	0.48	0.51
2.91	3.68	3.34	3.50	3.55	2.62	2.92
0.58	0.74	0.64	0.71	0.81	0.56	0.55
1.84	2.36	2.10	2.22	2.90	1.81	1.83
2.04	2.74	2.37	2.44	2.46	2.04	2.18
0.35	0.41	0.38	0.40	0.39	0.34	0.37
4.05	4.77	3.36	3.28	3.16	3.58	3.29
1.64	2.32	1.98	1.73	1.29	1.73	1.89
32.15	36.15	34.17	31.02	30.47	29.53	25.56
13.26	15.45	12.73	13.39	12.89	15.89	17.71
4.36	5.04	4.06	4.88	4.65	5.25	5.83
0.705326			0.705761	0.705766	0.705652	0.705536
0.512688			0.512654	0.512684	0.512672	0.512668

Table 5.1 cont.

UC839 Matahina PDC pumice Te Weta Rd. V16/300301	UC1100 Matahina PDC dense pumice Lk. Okataina U16/079355	UC520 Matahina PDC pumice Te Weta Rd. V16/300301	UC501 Matahina PDC banded pumice Te Weta Rd. V16/300301	UC1121 Matahina PDC pumice Lk. Okataina U16/079355	UC1123 Matahina PDC pumice Lk. Okataina U16/079355	UC832 Matahina PDC pumice Te Weta Rd. V16/300301
51.29	57.65	58.66	58.90	59.19	63.75	66.33
0.99	1.06	1.08	1.01	0.80	0.75	0.60
18.69	17.55	19.04	18.65	17.33	16.16	17.38
11.85	9.23	9.20	9.15	8.27	6.78	5.80
0.20	0.18	0.16	0.17	0.16	0.12	0.09
5.63	3.67	3.51	3.62	4.28	2.73	1.89
8.88	6.64	4.63	4.69	6.07	4.66	3.02
1.77	2.95	2.48	2.49	2.75	3.07	2.94
0.60	1.02	1.22	1.28	1.12	1.91	1.93
0.09	0.06	0.03	0.05	0.03	0.05	0.02
3.28		4.44	4.48			3.87
96.61	96.36	95.45	95.40	95.86	97.00	95.99
324.69	211.51	212.02	231.41	209.10	189.16	140.32
21.99	13.53	18.01	17.79	34.40	16.26	12.42
21	-	21	21	-	-	19
-	-	-	-	-	-	-
98	-	85	98	-	-	62
18	31	36	39	35	57	57
84	455	367	302	258	238	340
193	320	201	201	224	226	190
30.70	18.76	21.64	24.89	20.43	18.94	20.41
2.65	4.86	5.34	5.58	4.50	6.18	7.73
376	397	343	463	523	556	604
11.74	9.32	11.67	13.17	9.84	13.70	16.05
19.51	19.82	23.05	29.86	22.92	32.52	34.74
4.12	2.67	3.08	3.78	2.84	3.70	3.68
18.29	10.90	12.29	15.51	11.52	13.86	13.39
4.62	2.84	3.00	3.63	2.96	3.22	3.09
1.12	1.12	1.00	1.09	0.99	1.02	0.90
4.43	3.00	3.27	3.69	3.11	3.31	3.15
0.71	0.52	0.54	0.61	0.54	0.53	0.54
4.86	3.03	3.42	3.76	3.22	3.03	3.12
0.90	0.67	0.65	0.75	0.70	0.66	0.57
2.82	2.02	2.08	2.22	2.18	2.10	1.85
2.88	2.14	2.19	2.38	2.27	2.15	2.08
0.44	0.35	0.35	0.38	0.37	0.34	0.35
2.32	8.48	7.55	6.28	4.77	4.50	6.96
0.18	0.34	0.38	0.37	0.32	0.51	0.66
2.76	4.31	5.83	5.75	4.91	8.80	15.31
1.49	3.11	3.91	3.79	3.12	5.31	7.96
0.45	1.23	1.36	1.14	1.29	2.45	2.13
	0.705839		0.707905			
	0.512659		0.512646			

Table 5.2. Phenocryst assemblages of selected Matahina juvenile pumice clasts and rhyolite lava lithics.

Sample	Group	Map	Deposit	SiO_2 (wt. %)	G'mass	Plag	Hb	Oxides/Mgt	Ilm	Opx	Biot	Qtz	Qtz/Plag	Hb/Opx	Phenocryst total	$\sum r^2$
UC175	A2	3	ash-flow	72.68	0.79	0.167	0.001	0.013	0.003	0.027	-	-			21.0	0.08
						79.5	*0.3*	*6.0*	*1.3*	*12.9*	-	-		*0.02*		
UC168	A2	4	ash-flow	75.17	0.89	0.068	0.009	0.004	0.002	0.011	-	0.016			11.0	0.15
						61.5	*7.9*	*3.9*	*2.2*	*9.6*	-	*14.9*	*0.2*	*0.8*		
UC649	A2	5	ash-flow	76.94	0.95	0.015	0.006	0.005	0.0001	0.001	-	0.024			5.0	0.02
						29.9	*12.1*	*9.1*	*0.4*	*1.1*	-	*47.5*	*1.6*	*11.0*		
UC842	A1	6	plinian	75.84	96.9	1.0	-	0.2		0.1	-	2.0			3.1	
						30.2	-	*4.8*		*1.6*	-	*63.5*	*2.1*			
UC887	A1	7	plinian	77.85	96.7	1.1	-	0.1		0.1	-	2.2			3.3	
						31.8	-	*1.5*		*1.5*	-	*65.2*	*2.0*			
UC813	A2	1	PDC	72.80	91.6	6.2	1.5	0.4		0.4					8.4	
						73.2	*17.3*	*4.8*		*4.8*				*3.6*		
UC498	A2	2	PDC	71.16	94.4	3.2	1.4	0.3		0.4		0.4	*0.1*		5.7	
						55.8	*24.8*	*5.3*		*7.1*		*7.1*		*3.5*		
UC812	A1	1	PDC													
UC811	A2	1	PDC	72.63	80.9	5.7	0.2	0.3		1.0	0.8	11.3			19.2	
						29.8	0.8	*1.3*		*5.0*	*4.2*	*59.0*	*2.0*	*0.2*		
UC892	B (lithic)	2	lag breccia	77.48	0.96	0.001	-	0.001	0.000	-	0.017	0.023			4.0	0.01
						2.0	-	*1.6*	*0.2*	-	*40.6*	*55.6*	*27.8*			
UC1091	B (lithic)	4	plinian	77.58	92.5	3.2	-	0.1		-	0.7	3.6			7.5	
						42.0	-	*1.3*		-	*9.3*	*47.3*	*1.1*			
UC853	A (lithic)	6	plinian													

Modal phenocryst abundances were determined by counting 2000 pts. per thin section or calculated by least-squares methods using glass, phenocryst, and bulk-rock compositions. Map refers to localites in Fig. 1. PDC = pyroclastic density current

Table 5.3. Geothermometry comparison

Method	Ti-hb	Plag-hb	Fe-Ti oxide	Cpx-opx	*f*O2 (Δ NNO)
Rock type (group)					
Fine-grained basalt	727	-	-	-	-
Basaltic-andesite (B)	867c/828r	-	-	953	-
Andesite (B)	831c/760r	-	793	882	0.49
Andesite (A)	810c/765r	-	-	885	-
Dacite (A)	784c/756r	-	778	-	0.06
Dacite (B)	813c/780r	-	-	-	-
Low-silica rhyolite (A2)	-	836	866	853	0.18
Rhyolite (B)	-	748	778	-	0.50
High-silica rhyolite (A2)	-	772	770	-	0.00
High-silica rhyolite (A1)	-	774	758	-	-0.38
High-silica rhyolite (A1) *350 ka dome*	-	-	712	-	-0.55

Ti-hb: Féménias et al. (2006); Plag-hb: Holland and Blundy (1994); Fe-Ti oxide: Ghiorso and Evans (2008); Cpx-opx: Ghiorso and Sack (1991). hb: hornblende; plag: plagioclase; cpx: clinopyroxene; opx: orthopyroxene. r: rim and c: core

Table 5.4. Phenocryst assemblages of selected Matahina juvenile basalt-dacite clasts.

Sample	Group	Map	SiO2 (wt. %)	G'mass	Plag	Amph	Oxides	Opx	Cpx	Qtz	Phenocryst total
UC839	A	2	51.29	57.4	0.1	38.3	4.1	0.1	-	-	42.6
					0.2	89.9	9.6	0.2	-	-	
UC816	B	1	56.79*	73.0	11.0	11.8	2.0	1.9	0.3	-	27.0
					40.7	*43.7*	*7.4*	*7.0*	*1.1*	-	
UC1100	B	1	57.65	51.8	28.0	16.9	1.6	1.1	0.6	-	48.2
					58.1	*35.0*	*3.3*	*2.2*	*1.3*	-	
UC1123	B	1	63.75	76.9	13.2	5.9	1.1	2.7	0.2	-	23.1
					57.0	*25.4*	*4.8*	*11.8*	*0.9*	-	
UC520	A	2	58.66	72.2	18.2	4.9	2.0	2.4	0.2	-	27.8
					65.6	*17.8*	*7.2*	*8.7*	*0.7*	-	
UC832	A	2	66.33	83.7	9.8	4.1	0.3	1.8	0.1	0.2	16.3
					60.1	*25.2*	*1.8*	*11.0*	*0.6*	*1.2*	

Modal abundances acquired by counting 1000 pts. per thin section. *SiO_2 determined by mass balance using glass and phenocryst compositions.

Map refers to localites in Fig. 1.

CHAPTER 6

Conclusions and continued research

6.1 CONCLUSIONS

The results of this research have outlined a geochemical framework that has contributed to our understanding of the petrogenetic evolution of the diversity of rhyolite types that have erupted in the TVZ. The models developed are most consistent with fractional crystallization for the origin of the TVZ rhyolite, which is also an important contribution to our broader understanding of the growth of continental crust.

The geochemical database includes over 450 bulk-rock major and trace element analyses and over 5000 mineral analyses, which will be added to the GNS Petlab database.

The following is a brief outline of the major conclusions of this research:

1) The diversity of rhyolite types erupted within the central Taupo Volcanic Zone, New Zealand, can be characterized as a continuum of compositions between cold-wet-oxidizing and hot-dry-reducing end-member magmas. The origin of this diversification is related to changes in the oxidation state and P-T conditions of the intruded basalt in the accumulation and ascent zone where rhyolites are derived. This component of the research also established the importance of amphibole in the parental magmas to the rhyolite using trace element chemistry.
2) Slab-derived fluid is the oxidizing agent governing the rhyolite type (cold-wet-oxidizing vs. hot-dry-reducing) erupted at the surface. Temporal variations in the flux and eventual transfer of that fluid to the lower- to middle-crust are likely dictated by slab heterogeneities, whereas spatial variations in the type

generated are related to the position of the eruptive centre to the central rift axis. Although temporal variations are related to long cycles from wet-oxidizing to dry-reducing magmatism driven by subduction zone processes, these are superimposed over shorter cycles that appear to be related to upper crustal fluid exsolution and degassing following caldera-forming events.

3) Through collaboration with Graham Leonard (GNS) and Andy Calvert (USGS), key ignimbrite and rhyolite dome deposits were dated using Ar-Ar experiments. The age determined for several rhyolite domes, Bay of Plenty coastal tephras, and proximal pyroclastic deposits has revealed a much more extensive volcanic/magmatic history (>550 ka) associated with the OVC. Geochemistry of these dated deposits was used to correlate tephras among different volcanic complexes, which provided key temporal markers for developing the magmatic cycles and distribution models in Chapter 2.
4) The amphibole-rich Matahina andesite-dacite magma, erupted following caldera collapse, represents magma from the accumulation and ascent zone and was identified as a parental candidate for rhyolite petrogenesis. A record of diverse processes that occurred prior to exhumation and quenching against the host Matahina rhyolite during the eruption include in-situ cooling accompanied by periodic hot mafic recharge. This comprehensive evaluation of amphibole compositions further defines the physical characteristics of a mid-crustal 'mush' zone and provides additional support for a crystal fractionation model for the generation of rhyolites.
5) The Matahina eruption of 330 ka evacuated several discrete magma batches rather than one single magma chamber, consistent with the results of other studies of OVC volcanism. In addition, two distinct mafic mushes were also

erupted. The origin of this variation can be related to slab-derived fluid contributions to the mantle melts. Differentiation of these magmas in the lower crust under differing P-T-fO_2-fH_2O conditions produced distinct rhyolite magma batches from wet-oxidizing to relatively dry-reducing types.

6.2 CONTINUED RESEARCH

The following is a summary of manuscripts in preparation, which are pending additional data and/or interpretation to bring studies to completion and will be submitted in the next few months. These projects include data obtained by the author and were conceptualized around hypotheses developed by the author with the exception of the final manuscript presented here (Leonard et al., in prep). Co-authors have contributed to instruction for data analysis and/or the actual collection of data and samples. Collaboration with these co-authors will continue to ensure that their expertise is drawn upon for robust interpretations and they will contribute as such to the manuscripts prior to submittal.

6.2.1

Mantle $\delta^{18}O$ of rhyolites in the Taupo Volcanic Zone, New Zealand

Deering, C.D., Valley, J.W., Vogel, T.A.

Target journal: Earth and Planetary Science Letters

Summary:

Continental-crust/slab-sediment contributions can influence the composition of a rhyolite at each one of, or all, of the following stages of petrogenesis: (1) in the initial stages of basic melt production within the mantle wedge as slab-derived fluid, sediment melt and/or sediment-derived fluid are transported beneath the rifting back-arc; this contaminated basalt fractionates to produce the rhyolite, (2) through crustal anatexis within the lower crustal source zone; mixing or AFC between a primitive basalt and crust, and/or (3) within the upper crustal subvolcanic reservoir just prior to eruption. However, deciphering the timing, source, and volume of input at any one of these stages requires specific knowledge of the composition of the contaminants and a comprehensive dataset of specific geochemical components.

Magmas generated at convergent margins display enrichments in large ion lithophile elements (LILE) and Pb compared to high field strength elements (HFSE) [Gill, 1981; McCulloch and Gamble, 1991; Hawkesworth et al., 1993a; Miller et al., 1994]. In particular, the high mobility of Pb relative to other radiogenic components (e.g. Sr, Nd) suggests a decoupling at the slab-mantle interface, which can allow for discriminating between sediment derived input from the subducting slab and source zone and/or upper crustal contributions.

Interestingly, in the two studies of the TVZ rhyolites, that utilized Sr-Nd-Pb isotopes, Graham et al. (1992) and McCulloch et al. (1994) concluded that the Pb isotopic variation was consistent with anywhere from 15% to 100% contamination of continental crust. Yet, McCulloch et al. (1994) concluded that the Sr-Nd-O isotopes appear to constrain assimilation to between 15% and 25% (e.g. Fig. 6.1). In addition, Graham et al. (1992) suggested the Waipapa Terrane was the dominant assimilant, while McCulloch et al. (1994) suggested the Torlesse Terrane. As Graham et al. (1995) pointed out, the discrepancies in the proposed role

of assimilation vary widely and remain unresolved, partly due to the lack of a comprehensive isotopic dataset that is temporally and spatially representative of the range of TVZ rhyolite types. Graham et al. (1992) had also suggested that the disparity between the stable and radiogenic isotopes might be due to modification from slab-derived sediment as opposed to assimilation of continental crust.

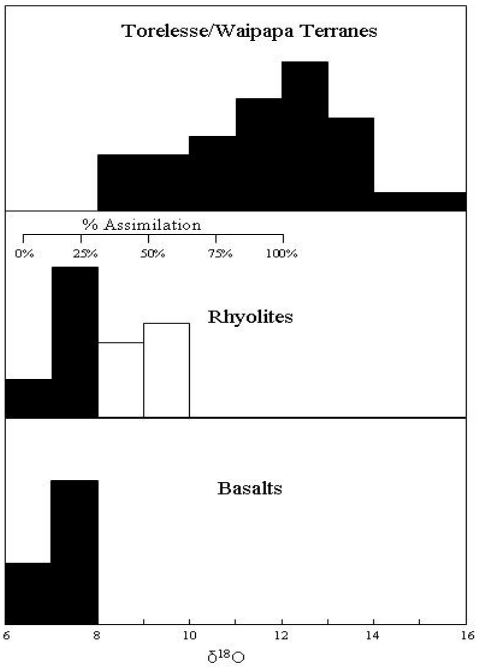

Fig. 6.1. Histograms showing $\delta^{18}O$ values of plagioclase from Maroa rhyolites and bulk-rock samples of basalts, rhyolites and metasediments. Data are from McCulloch et al. (1994) and Blattner and Reid (1982). Open rhyolite symbols are bulk-rock analyses from Blattner and Reid, 1982 and solid symbols are plagioclase separates from McCulloch et al. (1994). Figure modified (from McCulloch et al., 1994).

To date, only two oxygen isotope studies have been undertaken on the TVZ rhyolites. The first, by Blattner and Reid (1982), encompassed not only a broad temporal and spatial range of rhyolites, but also included basalts, andesites, and dacites. This work essentially ruled out crustal anatexis for the origin of the rhyolites and showed a range in the values of the 22 rhyolites analyzed with $\delta^{18}O$ from 6.8‰ to 9.1‰. However, the oxygen isotope measurements were dominantly on whole-rock, and may include the effects of sub-solidus alteration and thus not represent true magmatic values.

McCulloch et al. (1994) used eight plagioclase mineral separates and concluded that a single volcanic center, the Maroa, had little variation ($\delta^{18}O$ (plag) = 6.1‰ to 7.0‰). They concluded that the Sr-Nd isotopes and $\delta^{18}O$ of the plagioclase separates restricted the amount of assimilation to between 15-25%. However, assuming that the plagioclase measurements

represent magmatic values and that melting of a crustal terrane does not produce the rhyolites directly, equilibrium oxygen isotope fractionation in a basalt to produce the rhyolites would increase the $\delta^{18}O$ by approximately 1.5‰. Therefore, the oxygen isotope systematics of the Maroa samples reflect mantle values or lower (Eiler, 2001), which suggests no assimilation of high $\delta^{18}O$ crust.

Our recent study of oxygen isotopes at the University of Wisconsin with John Valley examined the temporal and spatial extent of $\delta^{18}O$ variation within the Okataina Volcanic Centre, one of nine caldera complexes active over the past 600 kyrs. The $\delta^{18}O$ values of quartz and magnetite from individual eruptions were found to be in equilibrium (Fig. 6.2; $\delta^{18}O_{quartz}$: 7.6 to 9.0 and $\delta^{18}O_{magnetite}$: 1.9 to 3.5) and give oxygen isotope temperatures between 740 - 870°C, consistent with those obtained by Fe-Ti oxides (Chapter 3). The oxygen isotope results of this pilot study also reflect mantle values (Fig. 6.2), which is consistent with our new interpretation of the McCulloch et al. (1994) data, but is inconsistent with their estimate of 15-25% assimilation of Torlesse greywackes. These results can only be reconciled by invoking the existence of an as yet unrecognized low-$\delta^{18}O$ component in the source zones of these magmas, such as hydrothermally altered ocean floor gabbros or crustal rocks that interacted with heated meteoric water.

A recent study of the geochemistry of the Central American arc lavas by Eiler et al. (2005) showed that indicators of slab-derived components (e.g. Ba/La and U/Th) correlated with $\delta^{18}O$ (olivine). They concluded that the ~1.0‰ variations in $\delta^{18}O$ across arc were related to differences in slab-derived components. The low-$\delta^{18}O$ component was derived from a solute-rich aqueous fluid as the subducting slab dehydrated and the high-$\delta^{18}O$ component was derived from partial melting of the sediment overlying the plate. Chapter 2 showed distinct spatial and temporal variations in the Ba/La ratio, which is correlated to the specific rhyolite

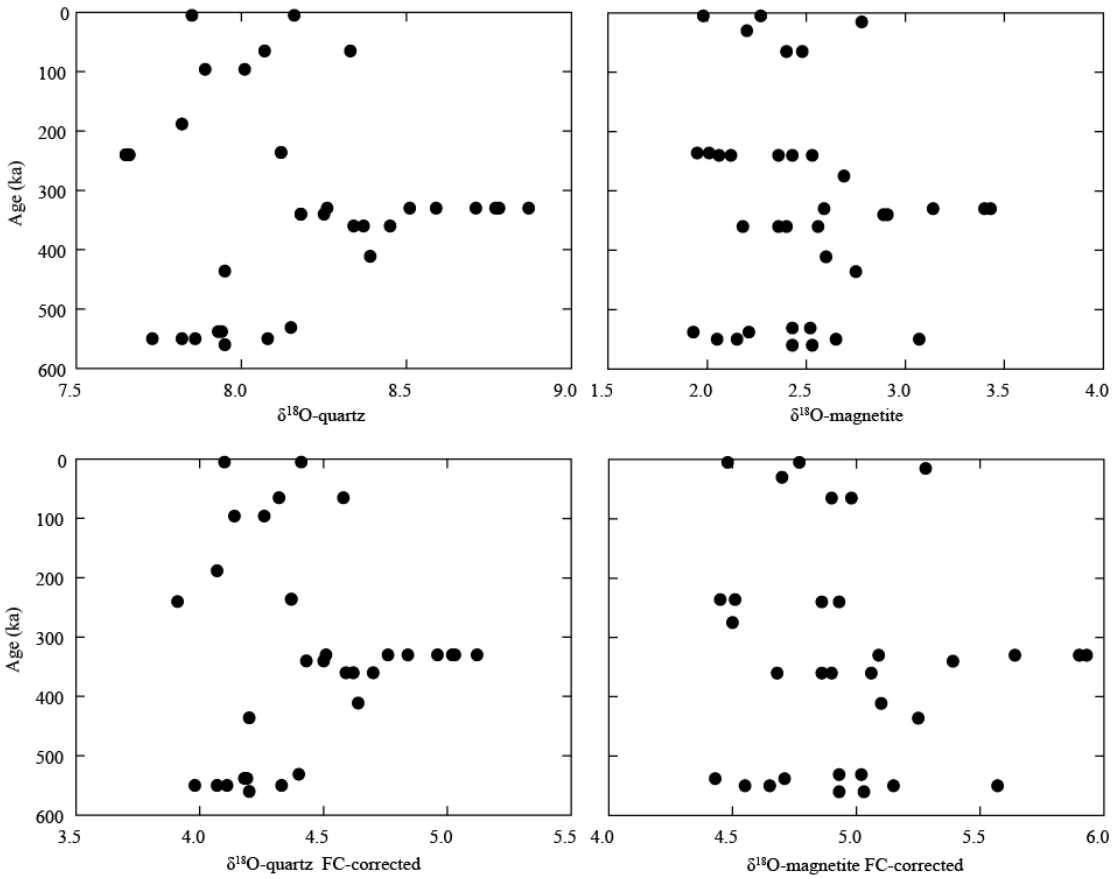

Fig. 6.2. Oxygen isotopes of TVZ rhyolites determined to be in equilibrium and thus representative of magmatic values. (a,b) $\delta^{18}O$ of quartz and magnetite from ~600 ka to present and (c,d) crystal-fractionation 'corrected' $\delta^{18}O$ from quartz and magnetite illustrating the mantle or slightly below mantle values estimated for TVZ rhyolites.

types that are erupted. However, the $\delta^{18}O$ is not inversely correlated with Ba/La, but instead slightly positively correlated with significant scatter (Fig. 6.3).

This supports a possible contribution from a high, rather than low, $\delta^{18}O$ slab component, which is more consistent with the conclusions of Graham et al. (1992), indicating that at least part of the elevated isotopic signature of the rhyolites is related to slab sediment. This indicates that the slab-derived fluid/melt is a complex mixture of components, and determining the origin of the low $\delta^{18}O$ component requires additional investigation. Consequently, pending a comprehensive evaluation of slab-derived trace element components, the origin of the disparity between radiogenic and stable isotopes remains unresolved. We are currently investigating the role of meteoric water circulation in the crust by analyzing plutonic rocks, which will allow us to develop a crustal profile. This may help to

determine the maximum depth of meteoric water circulation and, hence explain the low- $\delta^{18}O$ contribution that is buffering the effects of sediment/crustal contributions.

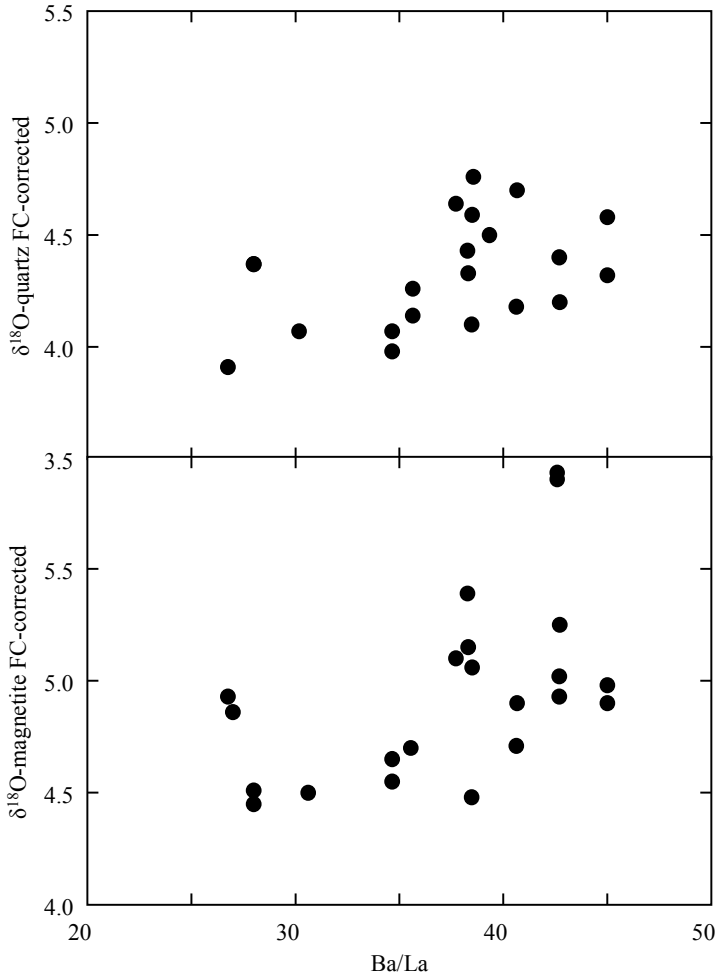

Fig. 6.3. Ba/La ratio vs. FC-corrected $\delta^{18}O$ of quartz and magnetite for OVC rhylites.

References

Eiler, J.M., Carr, M.J., Reagan, M., Stolper, E. (2005). Oxygen isotope constraints on the sources of Central American arc lavas. *Geochemistry, Geophysics, Geosystems – G3* **6**, no. 7.

Eiler, J.M. (2001). Oxygen isotope variations of basaltic lavas and upper mantle rocks. *Reviews in Mineralogy and Geochemistry* **43**, 319-364.

Gill, J.B. (1981). Orogenic Andesites and Plate Tectonics. Springer, New York, pg. 390.

Graham, I.J., Cole, J.W., Briggs, R.M., Gamble, J.A., Smith, I.E.M (1995). Petrology and petrogenesis of volcanic rocks from the Taupo Volcanic Zone: a review. *Journal of Volcanology Geothermal Research* **68**, 59-87.

Graham, I.J., Gulson, B., Hedenquist, J.W., Mizon, K. (1992). Petrogenesis of Late Cenozoic rocks from the Taupo Volcanic Zone, New Zealand; in the light of new Pb isotopic data. *Geochimica et Cosmochimica Acta* **56**, 2797-2819.

Hawkesworth, C.J., Gallagher, K., Hergt, J.M., McDermott, F. (1993a). Mantle and slab contributions in arc magmas, *Annual Reviews in Earth and Planetary Sciences* **21**, 175-204.

McCulloch, M.T., Kyser, T.K. Woodhead, J.D., Kinsley, L. (1994). Pb-Sr-Nd-O isotopic constraints on the origin of rhyolites from the Taupo volcanic zone of New

Zealand; evidence for assimilation followed by fractionation from basalt. *Contributions to Mineralogy and Petrology* **115**, 303-312.

Miller, D.M., Goldstein, S.L., Langmuir, C.H. (1994). Cerium/lead and lead isotope ratios in arc magmas and the enrichment of lead in the continents. *Nature* **368**, 514-520.

6.2.2 Co-genetic basalt and rhyolite reveal volcanic potential

Deering, C.D., Rooney, T., Vogel, T.A.

Target journal: Earth and Planetary Science Letters

Summary:

Identification of wet-oxidizing to dry-reducing rhyolite magma cycles in the Taupo Volcanic Zone, New Zealand (Chapter 3) also show a correlation between the volumes of magma erupted and the type of rhyolite. The highest volume erupted was the wet-oxidizing type and the lowest volume erupted was dry-reducing. Based on these findings, we developed the hypothesis that basaltic eruptions, which coincide with wet-oxidizing rhyolitic magmatism, reflect higher degrees of partial melting in the mantle than those that coincide with dry-reducing rhyolitic eruptions.

Recently, Hughes and Mahood (2008) proposed a correlation between volcanic arc convergence rates and silicic caldera-forming eruptions (CFEs), which inherently suggests that this is the primary control over the basaltic flux (Clift and Vannucchi, 2004). These mafic magmas presumably provide the enthalpy needed for melting of continental crust or some mafic progenitor (e.g. amphibolite) and/or mass via fractionation to produce more evolved magmas. In particular, some workers (Hildreth, 1981; Best and Christiansen, 1991; de Silva and Gosnold, 2007) have hypothesized that an elevated basaltic flux from the mantle is compulsory to maintain large-scale silicic magma systems. Based on this assumption, Hildreth (1981) also proposed that ignimbrite flare-up volcanism results from some increase in the mantle magma productivity over the normal 'steady-state' arc basaltic flux.

The purpose of this study was to augment existing bulk major and trace element data to investigate two hypotheses: 1) that a petrogenetic link exists between

central Taupo Volcanic Zone basalts and rhyolites (e.g. fractional crystallization), and 2) that a relationship exists between rhyolite magma production and slab-derived fluid. It is well established that fluid plays an important role in mantle melting to produce basalts-andesites in convergent settings. Therefore, we are evaluating the potential relationship between slab-derived fluid and a well documented volcanic flare-up event that occurred between 340 and 240 ka (Wilson et al., in press) and the magmatic 'power' of the system.

Recently sampled basalts representing all of the HAB eruptions exposed in the TVZ are currently being analyzed for major and trace element geochemistry. This comprehensive sample suite of over 80 clasts represents 12 different eruptions. The chemistry will be used to evaluate differences in slab-derived contributions, specifically the fluid component, between basalts erupted during wet-oxidizing and dry-reducing rhyolite magma cycles. An evaluation of preliminary results obtained from both this and previous studies indicates that the basalts erupted during wet-oxidizing rhyolite magma cycles were derived from higher degrees of mantle melting (Fig. 6.4a). A correlation between slab fluid (e.g. Ba/La) and mantle melting indicators (e.g. V/Zr), for a dataset restricted to trace elements determined by ICP-MS, supports a direct relationship between mantle productivity and rhyolite magma production *and* the actual erupted volumes (Fig. 6.4b).

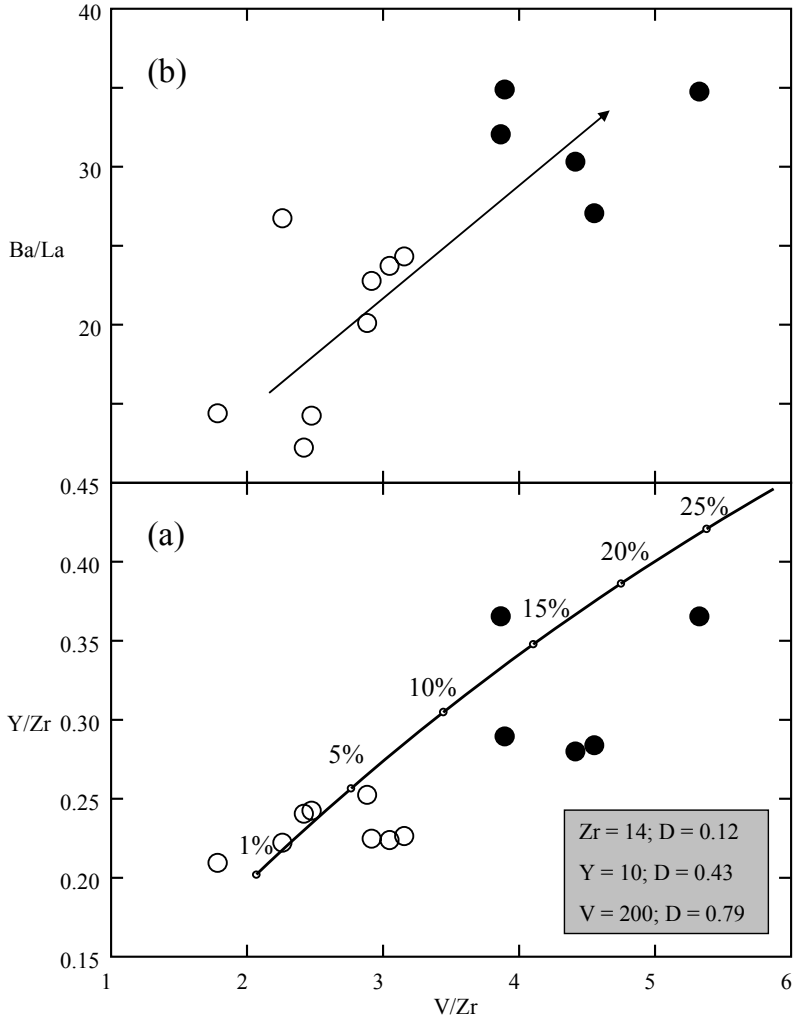

Fig. 6.4. Partial melting of depleted mantle (spinel lherzolite) using starting compositions and distribution coefficients of Gamble et al. (1993). Ba/La ratio as an indicator of slab-derived fluid also shows positive correlation with V/Zr, an indicator of degree of partial melting. Filled circles are basalts erupted during periods of wet-oxidized rhyolitic volcanism and open circles are basalts erupted during periods of dry-reducing rhyolitic volcanism. Data are from Gamble et al. (1993), Hiess et al. (2007), and this study.

References

Best, M.G. & Christiansen, E.H. (1991). Limited extension during peak Tertiary volcanism, Great Basin of Nevada and Utah. *Journal of Geophysical Research* **96**, 13,509-13,528.

Clift, P. & Vannucchi, P. (2004). Controls on tectonic accretion versus erosion in subduction zones; implications for the origin and recycling of the continental crust *Reviews of Geophysics* **42**, 31.

de Silva, S.L. & Gosnold, W.D. (2007). Episodic construction of batholiths; insights from the spatiotemporal development of an ignimbrite flare-up. *Journal of Volcanology and Geothermal Research* **167**, 320-335.

Gamble, J.A., Smith, I.E.M., McCulloch, M.T., Graham, I.J., Kokelaar, B.P. (1993). The geochemistry and petrogenesis of basalts from the Taupo Volcanic Zone and Kermadec Island Arc, S.W. Pacific. *Journal of Volcanology and Geothermal Research* **54**, 265-290.

Hiess, J., Cole, J.W., Spinks, K.D. (2007). Influence of the crust and crustal structure on the location and composition of high-alumina basalts of the Taupo Volcanic Zone, *New Zealand. New Zealand Journal of Geology and Geophysics* **50**, 327-342.

Hildreth, W. (1981). Gradients in silicic magma chambers; implications for lithospheric magmatism. *Journal of Geophysical Research* **86**, 10153-10192.

Hughes, G.R. & Mahood, G.A. (2008). Tectonic controls on the nature of large silicic calderas in volcanic arcs *Geology (Boulder)* **36**, 627-630.

Wilson, C.J.N., Gravley, D.M., Leonard, G.S. & Rowland, J.V. (in press). Volcanism in the central Taupo Volcanic Zone, New Zealand: tempo, styles and controls. *Geological Society London Special Publication*.

6.2.3

Variations in slab-derived fluid contributions to the Taupo Volcanic Zone, back-arc rift: evidence from hydrogen isotopes in hornblende and biotite

Deering, C.D. & Horton, T.

Target journal: Geochimica et Cosmochimica Acta

Summary:

One of the hypotheses/assumptions from Chapter 2 was that the Ba/La ratio is a good indicator of slab-derived fluid contributions to the mantle melts, and consequently to the rhyolites. This ratio was used to relate oxygen fugacity and mineral/melt compositions to variations in slab fluid additions. Although Ba and La are incompatible in the TVZ magmatic evolution, variations are considerable among units and even within units. Therefore, we have used hydrogen isotopes to further evaluate the fluid composition derived from mantle and subducting slab/sediment. Studies have shown that mantle, sediment fluid, and slab-derived fluid contributions to magmas generate distinct hydrogen isotope ratios (Poreda, 1985; Graham et al., 1982; Miyagi and Matsubaya, 1992).

A preliminary evaluation of the Ba/La ratio was undertaken using a suite of hornblende and biotite, which were analyzed for hydrogen isotopes in the stable isotope laboratory at the University of Canterbury. Although the hydrogen isotope contents in hydrous phases are subject to modification due to degassing, studies have shown that the magmatic, 'unmodified' hornblende and biotite hydrogen isotope ratio is preserved in most volcanic rocks. In addition, Chapter 4 evaluated the degassing history of the Murupara Subgroup and Matahina andesitic to rhyolitic magmas, finding little evidence of extensive degassing, except for within glass and biotite analyzed from extrusive dome complexes. The extensive hornblende and biotite

chemical dataset accumulated in this research will be used to evaluate subsequent hydrogen isotope analyses from other TVZ eruptions. Preliminary results, although obviously restricted by the small dataset support the use of the Ba/La ratio as a good indicator of slab-derived fluid (Fig. 6.5). Therefore, I am currently sampling hornblende and/or biotite-bearing ignimbrites dating back to 1.6 Ma to evaluate the changes in slab-derived fluid contributions relative to other wet-oxidizing and dry-reducing rhyolites. The results from this study can potentially provide important insight into the differences in composition of slab-derived fluid contributions from the inception of rhyolitic volcanism in the TVZ 1.6 Ma to present.

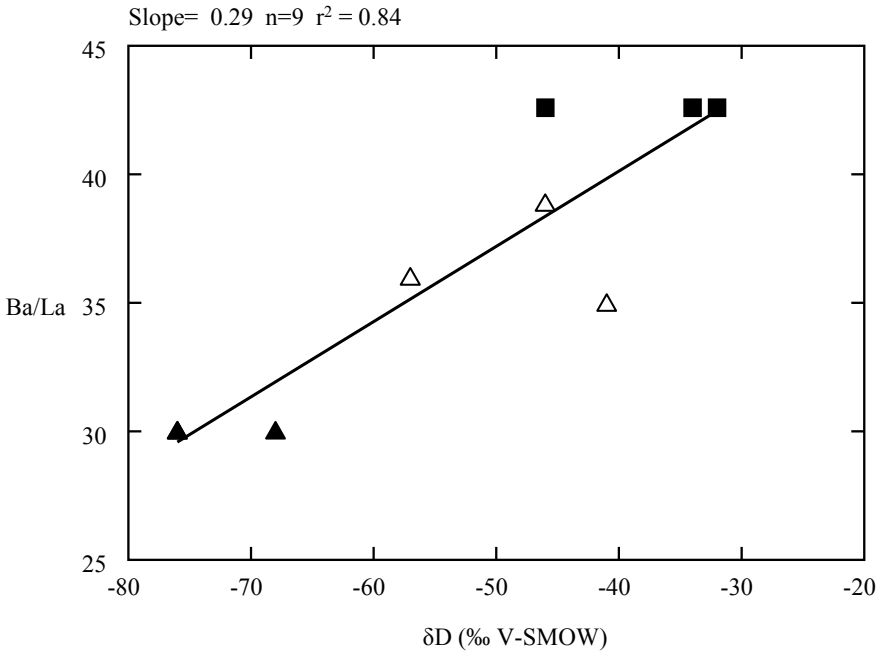

Fig. 6.5. Ba/La ratio as an indicator of slab-derived fluid vs. D/H ratio (relative to V-SMOW) showing a strong positive correlation for this small dataset. Different symbols represent hornblende or biotite from single eruptive units.

References

Poreda, R. (1985). Helium-3 and deuterium in back-arc basalts: Lau Basin and the Mariana Trough. *Earth and Planetary Science Letters*, **73** 244-254.

Graham, A.M., Graham, C.M., & Harmon, R.S. (1982). Origin of mantle waters: Stable isotope evidence from amphibole-bearing plutonic cumulate blocks in calc-alkaline volcanics, Grenada, Lesser Antilles. Proc. 5th Int'l Conf. Geochron. Cosmochron. Isotope Geol., 119-120.

Miyagi, I. & Matsubaya, O. (1992) Hydrogen isotopic ratios of hydrous minerals from Japanese Quaternary volcanoes. Rept. Geol. Surv. Jpn. **279**, 210-211.

6.2.4

Magmatic-volcanic evolution of the Okataina Volcanic Complex

Deering, C.D., Cole, J.W., Vogel, T.A., Leonard, G.

Target journal: Contributions to Mineralogy and Petrology

Summary:

The new geochemical dataset for OVC eruptive deposits and correlations determined through collaboration with Graham Leonard (GNS) during this study will be used to develop a comprehensive magmatic history that includes nearly 600 kyrs. of volcanism. The key finding, which will contribute to our understanding of the OVC magmatic/volcanic evolution, is my discovery of exposures of proximal biotite+amphibole ignimbrites (as evidenced by large lithic and pumice blocks as well as lag breccias) along the Lake Okataina shoreline. Through correlations based on mineral content, size, abundance and chemistry, glass chemistry, and Ar-Ar dating of these proximal pyroclastic deposits and coastal tephras, the temporal extent of volcanism in the OVC is, therefore expanded from 390 ka to over 550 ka. In particular, the quartz+biotite ignimbrite, which was previously dated at ~390 ka was redated and compared to these proximal deposits from Lake Okataina, both yield Ar-Ar dates within error of 550 ka (Leonard et al., in prep.).

Similar correlations have also been made for post-Matahina eruptive activity, which will also provide important new insight into the period between the caldera-forming Matahina (330 ka) and Rotoiti (61 ka) eruptions. These pyroclastic fall and flow beds represent several eruptions of significant volume (>20 km^3).

The combination of tephra correlations and new bulk rock major and trace element chemistry, mineral chemistry, and Sr-Nd-O isotopes will be presented to provide a new magmatic/volcanic evolution for the OVC over greater than 550 kyrs.

6.2.5

Taupo Volcanic Zone $^{40}Ar/^{39}Ar$ geochronology illuminates 550 ka volcanism at Okataina Volcanic Centre, coastal uplift and sea level fluctuations.

Leonard, G., Calvert, A., Wilson, C.J.N., Gravley, D., Deering, C.D, Hikuroa,D.

Target journal: Earth and Planetary Science Letters

My contribution to this manuscript is partly related to the sampling and partial preparation of samples for Ar-Ar dating experiments. However, my primary role in this study was to select, and subsequently correlate coastal tephra deposits, proximal pyroclastic deposits (to the OVC), and extrusive rhyolite domes using geochemical analyses (glass and mineral contents/chemistry). The hypotheses for the correlation of 550 ka deposits developed primarily through field work and my preliminary evaluation of mineral contents and chemistry. These hypotheses correlate a number of coastal tephra deposits with extrusive dome and pyroclastic fall and flow deposits from the OVC, ranging in age from ~400 to 550 ka, some of which were previously thought be Whakamaru-group equivalents.